Infrared Spectroscopy of Interacting and Merging Galaxies

by

René Doyon

A Thesis Submitted for the degree of
Doctor of Philosophy of the University of London
and for the
Diploma of Imperial College

November 1990

A mes parents

Abstract

This thesis presents a study of interacting and merging galaxies exhibiting vigorous star formation activity. Different aspects related to this phenomenon are examined.

New near-infrared spectroscopic observations are presented for selected interacting and merging galaxies. Most of these galaxies show strong recombination lines of hydrogen and helium, a strong evidence for the presence of massive stars. Further evidence that vigorous star formation activity is taking place in these galaxies is provided by the existence of numerous red supergiant stars inferred both from the unusually strong 2.2 μm luminosity and the strength of the CO band absorption at 2.3 μm.

A variety of techniques is used to constrain both the age of the burst and the range of stellar masses present in these galaxies. The use of the He Iλ2.06μm/Brγ line ratio as a constraint of the upper mass limit of the initial mass function is discussed. It is shown that star formation for masses beyond 30 $M_{\odot}$ is apparently suppressed in some galaxies, including the classical starbursts M82 and NGC 253. A stellar synthesis model is constructed and used in combination with a χ^2 analysis technique to determine the age of the burst and the stellar parameters of the initial mass function in a unique way. The age of the burst in most galaxies is found between 10 and 60 million years. This analysis suggests that the initial mass function of NGC 3256 and NGC 2798 is deficient in low-mass ($< 2\ M_{\odot}$) stars, a result which is independent of the knowledge of the mass participating in the burst.

Measurements of molecular hydrogen lines in IC 694, NGC 1614 and NGC 3256 show that a large fraction (>50%) of the H_2 emission is fluorescently-excited by UV photons. Simple theoretical considerations of the physical conditions prevailing in the nuclei of these galaxies show that the copious production of UV radiation by an ensemble of young OB stars provides a viable scenario for explaining the observed H_2 emission.

Acknowledgements

This thesis is the fruit of three years of research during which many people have contributed, through their advice, help or simply their friendship, to make this experience very fulfilling and enjoyable. To these people I would like to express my gratitude.

First, I would like to thank my supervisor, Bob Joseph, for his invaluable guidance and ideas he put into this project. His enthusiasm and attitude towards research will always be a model to follow. This work has greatly benefited from illuminating discussions and advice from Phil Puxley and Gillian Wright. I am particularly grateful to Phil for his careful (and prompt) readings and comments he provided on most of the manuscript. The experience I gained in infrared observing techniques and data reduction is by far due to the devotion of Gillian. These people also gave me their friendship which I valued very much.

It has been a pleasure to work with the many graduate students and the permanent members of the astrophysics group. I give my thanks to everybody but especially to Philip James, Jason Spyromilio and Martyn Wells. I also wish to thank Nicole St-Louis for her love, patience and the many stimulating discussions we had on Wolf-Rayet stars.

This work was financially supported by postgraduate fellowships from the *Conseil de Recherches en Sciences Naturelles et en Génie* of Canada, the canadian national chapter of the *Imperial Order of the Daughters of the Empire* and partly, in the later parts of this work, from the Institute for Astronomy of the University of Hawaii. I am also very grateful to the british *Science and Engineering Research Council* for his generous financial support of so many observing trips. Finally, to whatever goddess on the Mauna Kea who provided me with 80% of photometric weather in the last year of my Ph.D.

Je ne saurais remercier suffisamment tous les membres de ma famille, et plus particulièrement mes parents, pour leur amour, leur support et encouragements constants durant ce long cheminement académique qui m'aura finalement mené jusqu'aux études doctorales. A mes parents, je dédie ce travail.

Table of Contents

Errata

Page 4, paragraph 4, line 5: change to "British".
Page 4, paragraph 4, line 6: change to "its generous".
Page 16, paragraph 2, line 3: change to "referred to as".
Page 16, paragraph 3, line 1: change to "starbursts in M82".
Page 17, paragraph 2, line 7: change to "What is the energy".
Page 20, paragraph 3, line 1: change to "It is with this ".
Page 23, §2.2.1.1 paragraph 1, line 4: change to "arithmetic mean".
Page 23, §2.2.1.1 paragraph 1, line 5: change to "average utilising the individual".
Page 23, paragraph 1, line 5. The last sentence should be changed to: "Further, since the spectra are subject to scan-to-scan variations in atmospheric transmission, the errors obtained from the scatter in the scan-to-scan values are more representative of errors in the absolute flux. For these reasons, the approach involving the arithmetic mean plus the scan-to-scan error was adopted".
Page 26, paragraph 2, line 2: change to "star to remove the".
Page 27, paragraph 1, line 7: change to "star at the wavelength λ'."
Page 27, paragraph 2, line 3: change to "$\log_{10}$ instrumental".
Page 31, paragraph 1, line 5: change to "galaxies (see p. 51-52).".
Page 31, paragraph 2, line 10-11: change to "relative to the difference for αLyrae.". Also on page 194, paragraph 2, line 5.
Page 35, §2.3.2 paragraph 2, line 1: change to "galaxy were obtained".
Page 36, paragraph 1, line 1: change to "next to the line".
Page 60, paragraph 3, line 6: change to "corresponds roughly with the".
Page 64, paragraph 1, line 3-4: change to "prerequisite for the understanding of galaxy evolution and interpretation of the".
Page 81, Equation 3.10: numerator and denominator should be interchanged".
Page 85, paragraph 3, line 4: change to "$\gtrsim 40$),"
Page 88, paragraph 3, line 3: change to "minimize".
Page 104, Equation 4.5: "α" should be changed to "m_l".
Page 123, paragraph 5, line 1: change to "can reproduce".
Page 126, paragraph 1, line 2: change to "Gautier". Also on page 188, line 9.
Page 133, last sentence of the page: change to "H_2 gas in the".
Page 137, paragraph 2, line 2: change to "Figure 5.1".
Page 143, the following new paragraph should be inserted at the bottom of the page: "The wavelength calibration system of the instrument was unavailable at the time of the observations and the spectra had to be calibrated with atmospheric..." (following on page 145).
Page 146, paragraph 2, line 2: change to "spectra are listed".
Page 157, §6.3.4 paragraph 1, line 10: change to "independent of".
Page 161, paragraph 1, line 7-8: change to "demonstrate that both the".
Page 171, paragraph 2, line 4: change to "*via* an".
Page 181, §6.6 paragraph 2, line 6: change to "constrain".
Page 184, §7.1 paragraph 1, line 13-14: change to "will place such observing".
Page 184, §7.1 paragraph 2, line 6: change to "needed. Further".
Page 185, paragraph 3, line 4-5: change to "measurements allowing, for example, the study of the spatial".
Page 185, paragraph 3, line 6, 7: change to "H_2 emission or the investigation of the dependence of the stellar IMF parameters on the physical conditions".
Page 197, Equation A.2 for supergiants: the "+" should be changed by "-".
Page 200, Figure A.3, line 2: change to "solid line".
Page 209, Table B.2: all values in column 4 should be changed from 4.5 to 4.0.
All units (*e.g.*, W for Watt) should be in roman.

List of Tables

Chapter 5

The Excitation Mechanism of the H_2 Emission in Starburst Galaxies

Chapter 6

A Near-Infrared Spectroscopic Study of the luminous Merger NGC 3256

Appendix A

A Spectroscopic Determination of the 2.3 μm CO Band Strength in Stars

Appendix B

Line and Continuum Modelling of Starbursts

List of Figures

Chapter 4

On the Initial Mass Function and the Spectral Evolution of Starburst Galaxies

Chapter 5

The Excitation Mechanism of the H_2 Emission in Starburst Galaxies

Chapter 6

A Near-Infrared Spectroscopic Study of the luminous Merger NGC 3256

Appendix A

A Spectroscopic Determination of the 2.3 μm CO Band Strength in Stars

Appendix B

Line and Continuum Modelling of Starbursts

Chapter 1

Introduction

The subject of this thesis is the study of a class of galaxies which are either interacting or in the process of merging with another system. Unlike "normal" isolated galaxies, it is well-known that some of these systems exhibit vigorous star formation activity *i.e.* the star formation rate is thought to be so high that, given reasonable amount of gaseous material available, it can only be sustained over a short time scale compared with a Hubble time. For these reasons, these galaxies are often described as "starbursts", an expression that we shall retain throughout this thesis to describe vigorous extragalactic star formation activity, even though the time-scale of the burst is not very well constrained in practice.

The starburst phenomenon is by no means restricted to interacting and merging galaxies and has been observed in a variety of objects including dwarf or emission-line galaxies (also referred as "blue compact galaxies"), barred spirals and even the more exotic *active galactic nuclei* (AGN) in which the gigantic energy output is thought to have a non-stellar origin, probably due to accretion of gas onto a black hole in the center of the galaxy. In fact, the frontier between starburst and AGN activity is not always very well defined and there is growing evidence that they may have an evolutionary connection.

Since the seminal study by Rieke *et al.* (1980) of the now classical starbursts M82 and NGC 253, our knowledge of the starburst phenomenon has increased sharply, partly because of the success of the *Infrared Astronomical Satellite* (*IRAS*) but also due to major advances in infrared technology. Since infrared wavelengths are considerably less attenuated by dust compared with the optical, studies in this waveband are particularly important for probing the physical

conditions prevailing in the core of heavily obscured nuclei, where most of the star formation activity is usually taking place.

The present study is concerned with two major aspects related to starburst galaxies. One part is purely observational; new near-infrared *spectroscopic* observations of selected interacting and merging galaxies are presented. These data represent a substantial increase (a factor of three) in resolving power over previous studies of this kind. The second deals with the interpretation and the modelling of the observational properties of these galaxies. The main astrophysical questions addressed by this study are: What is energy production mechanism in these galaxies? What is the shape of the initial mass function (IMF) in starburst galaxies? What is the age and the time-scale of the burst? What should be the observational properties of a "dying" starburst? What is the excitation mechanism of the molecular hydrogen observed in these galaxies?

The main content of this study is divided up into five chapters. Most of the observations are presented in Chapter 2. In Chapter 3, a new technique is described for constraining the upper mass limit of the IMF based on the ratio of the recombination lines He Iλ2.06μm and Brγ. The dependence of the observational properties of starburst galaxies on stellar IMF parameters and the age is described in Chapter 4. The excitation mechanism at the origin of the molecular hydrogen emission is discussed in Chapter 5. Chapter 6 presents a near-infrared spectroscopic study of the merger NGC 3256. All the ideas put forward in the previous chapters have been applied to this specific object. Finally, a summary of the main results of this study is presented in Chapter 7, along with some suggestions for further research. Except for the last one, each chapter is self-consistent with its own introduction and summary section.

Three appendices are also included after the last chapter: (A) A spectroscopic determination of the 2.3 μm CO band strength in stars; (B) line and continuum modelling of starbursts. The details of the model used throughout the thesis are given in this appendix. Finally, the papers published during the course of this work are given in Appendix C.

Chapter 2

The Near-Infrared Spectroscopic Properties of Selected Interacting and Merging Galaxies

2.1 Introduction

It is now well established that interacting and merging galaxies are the sites of vigorous star formation activity. The starburst phenomenon manifests itself at all wavelengths, from the ultraviolet to the far-infrared. In the optical, emission-line surveys (Kennicutt and Keel 1984; Keel *et al.* 1985; Bushouse 1986) have revealed that hydrogen Balmer lines are statistically stronger in paired and interacting systems than in isolated spirals.

Intense star formation activity is particularly conspicuous at infrared (IR) wavelengths (>3 μm) due to emission from warm dust heated by the radiation from young OB stars. Several studies have been devoted to the infrared excess which is a characteristic of starburst activity. From $JHKL$ photometry of 44 interacting galaxies Joseph *et al.* (1984) found that for ~85% of the pairs in the sample, one member of a pair has a significant $K - L$ excess compared with normal spirals. Further studies in the mid-infrared (10-20 μm) (Lonsdale, Persson & Matthews 1984; Graham *et al.* 1984; Cutri & McAlary 1985; Wright *et al.* 1988) confirmed the presence of a steeply rising far-infrared continuum in these galaxies. In particular, Joseph & Wright (1985) (see also Wright, Joseph

& Meikle 1984) showed that merging systems are one or two orders of magnitude brighter than Seyferts and classical starbursts.

That starbursts are conspicuous in the far-IR has been confirmed by the data obtained with the *Infrared Astronomical Satellite (IRAS)*, especially with the discovery of a new class of extremely luminous ($> 10^{12}$ $L_{\odot}$) "infrared" galaxies emitting the bulk of their luminosity at infrared wavelengths (Soifer *et al.* 1984). Follow-up studies revealed that these powerful galaxies are *always* associated with interacting/merging systems (Sanders *et al.* 1988).

However, a vigorous episode of star formation activity is not the only possible mechanism that could explain the large bolometric luminosities observed in ultra-luminous *IRAS* galaxies. A dust-embedded active galactic nucleus (AGN) or quasar could equally be responsible for the tremendous luminosity output observed in the far-IR. NGC 6240 and ARP 220 are probably the most celebrated examples of ultra-luminous *IRAS* galaxies where the energy production mechanism is still controversial (see the following references for different interpretations: Wright, Joseph & Meikle 1984; DePoy, Becklin & Wynn-Williams 1986; DePoy, Becklin & Geballe 1987; Rieke *et al.* 1985). The interpretation of the observational properties of these galaxies in terms of a single energy production mechanism may be misleading if there is a causal or evolutionary link between starbursts and AGN. Theoretical works in this direction (Scoville & Norman 1988; Norman & Scoville 1988) have shown there could be such a link.

Irrespective of the nature of the energy source, the detailed physical processes responsible for the nuclear activity are still poorly understood. Because the infrared is considerably less affected by dust obscuration than the visible, this waveband (especially the K-window) is particularly suited for probing the physical conditions prevailing in the core of these galaxies. Recent advances in infrared technology have it made possible to extend photometric investigations to spectroscopy. Observations in the past few years have revealed that IR spectra of interacting and merging galaxies are very rich, especially in the K-window where strong molecular hydrogen (H_2) emission (1-0 S(1) at 2.1218 μm) is found along with Brγ (2.1661 μm), HeIλ2.06μm and the deep CO band absorption longward of 2.3 μm (*e.g.* Rieke *et al.* 1985; Joseph *et al.* 1987).

These lines provide important astrophysical diagnostics. Recombination lines of hydrogen and helium give information on both the total production rate of ionizing photons and the shape of the UV spectrum, and thus provide

constraints on the population of young massive stars (when the ionization can be shown to have a stellar origin). The strength of the CO band is luminosity-dependent (Frogel *et al.* 1978) and can be used to discriminate between super-giant and giant stars, a property which makes the CO band a powerful tool for identifying starburst activity. The excitation mechanism at the origin of the H_2 emission can be inferred from diagnostic H_2 transitions (*e.g.* 1-0 S(0) and 2-1 S(1) at 2.2233 and 2.2471 μm, respectively) observed in the K-window, to determine whether the H_2 gas is shock or fluorescently-excited.

Given this wealth of spectroscopic information available from the infrared and the difficulties involved in obtaining good quality IR spectra, it is not surprising that most previous extragalactic IR spectroscopic studies have concentrated on a few objects or limited astrophysical problems (*e.g.* excitation mechanism of the H_2 emission). As a result, despite the large number of extragalactic IR spectra in the literature, most spectra obtained thus far are usually restricted to a narrow spectral range, covering one or two lines. And still, amongst the few full window spectra available, several were obtained at the relatively low resolution of a CVF (Joseph *et al.* 1987; Prestwich 1989).

It is in this background that we undertook the extragalactic IR spectroscopy program described in this chapter. The main goals were to substantially increase the resolution over previous CVF observations and to secure near-infrared spectra covering a wide spectral range, assigning the highest priority to the K-window. The rationale for this program was not to determine the IR spectroscopic properties of interacting and merging galaxies in a statistical sense but to study, in as great a detail as possible, a few well known galaxies of this class. The sample includes the three ultra-luminous mergers NGC 6240, ARP 220, NGC 1614 and the interacting systems NGC 3690-IC 694 (source A, B and C) and NGC 2798.

Most of the results presented in this work are based on the observations presented in this chapter. The presentation will be rather descriptive. In general, the interpretation of the data has been left for detailed treatment in the subsequent chapters (three, four and five).

2.2 Observations

Infrared spectra of interacting and merging galaxies were obtained on the 3.8-meter *United Kingdom Infrared Telescope* (*UKIRT*) during two observing trips, on the nights of 12-15th February and 5-8th May 1990. The common-user 7-element cooled grating spectrometer, CGS2, was used for all observations. The instrument was operated with the 637 lines/mm grating, providing a resolving power of ~600 at 2.2 μm. A circular aperture, nominally of 5.5″, was used, but an affective size of 5″ was inferred from a measurement of the beam profile. The spectra were sampled every half-resolution element for the February data. In May, detectors 4 and 5 were defective, and thus, the spectra had to be sampled every quarter-resolution element to ensure a complete sampling at all wavelengths. The telescope was chopped at every grating position between the sky and the target at a frequency of ~0.3 Hz, with a typical chop throw amplitude of 30″. For all galaxy observations, the integration time was set to 15 seconds (10 coadds of 1.5 sec) per grating position. Five to six minutes were required to scan a typical spectral range of 0.3 μm. In general a galaxy observation consisted of 6 scans.

Several photometric and spectroscopic standards were observed during the nights to calibrate and correct the spectra for the imperfect differential response of the detectors and the wavelength-dependent transmission of the atmosphere. The relative air masses of the standard and the galaxy were typically 0.1 and always less than 0.2. Several galaxies were observed more than once on different nights in order to check the reproducibility of the spectra. A log of all galaxy observations obtained at *UKIRT* is given in Table 2.1

Also presented in this chapter is a K-window spectrum of NGC 6240 obtained at the AAT in March 1989 as part of a different observing program on the merger NGC 3256 (see Chapter 6). The grating spectrometer FIGS was used with an aperture of 3.5″×3.5″ and an effective resolving power of 230, slightly less but similar to the resolution of the *UKIRT* spectra after smoothing (see §2.2.1.2).

2.2.1 Data Reduction

The conventional technique for reducing IR spectra comprises the following steps:

Table 2.1

Observing Log

Galaxy	Position	Wavelength (μm)	Integration[1] (mins)	Date	STD # [2]
ARP 220	Nucleus	2.046–2.327	7×5.8	13 Feb '90	14
"	"	2.220–2.490	6×6.0	15 Feb '90	12
"	"	2.044–2.252	9×3.2	6 May '90	19
"	"	2.235–2.498	5×4.6	6 May '90	19
"	"	1.276–1.340	52×0.6	8 May '90	13
MRK 231	Nucleus	2.095–2.381	6×6.0	14 Feb '90	14
"	"	2.165–2.290	13×1.9	6 May '90	11
NGC 1614	Nucleus	2.041–2.323	5×5.8	14 Feb '90	1
"	5″ west of Nuc.	"	6×5.8	14 Feb '90	1
"	Nucleus	2.200–2.483	6×6.3	15 Feb '90	1
NGC 2798	Nucleus	2.021–2.293	6×5.3	14 Feb '90	3
"	"	2.074–2.222	10×2.2	6 May '90	5
"	"	2.200–2.462	6×5.8	15 Feb '90	6
"	"	1.261–1.324	12×0.6	8 May '90	3
NGC 3690	Source A	2.029–2.313	6×5.8	13 Feb '90	9
"	"	"	5×5.8	14 Feb '90	9
"	"	2.210–2.471	6×5.8	15 Feb '90	10
"	"	1.266–1.329	7×0.6	8 May '90	8
"	Source B	2.029–2.313	6×5.8	13 Feb '90	10
"	"	"	5×5.8	14 Feb '90	9
"	"	"	7×5.8	15 Feb '90	10
"	"	1.266–1.329	7×0.6	8 May '90	8
"	Source C	2.024–2.313	4×4.6	9 May '90	9
"	"	1.266–1.329	4×0.6	8 May '90	8
"	5″ east of C	1.266–1.329	4×0.6	8 May '90	7
NGC 6240	Nucleus	2.145–2.497	6×5.3	6 May '90	16

[1] Number of scans times the integration time for each.

[2] Spectroscopic standard used to calibrate and correct the galaxy spectrum, according to the numbering given in Table 2.2.

- Coaddition of individual scans.
- Flatfield (differential response) and atmospheric corrections; removal of intrinsic absorption features in the standard star.
- Flux calibration.
- Wavelength calibration.

The detailed procedure of each step is described below.

2.2.1.1 Coaddition of individual scans

The scans provided by the CGS2 software contain the following information at each spectral point: the wavelength in microns, the instrumental flux (data number per second) and its absolute error. The coadded spectrum can be obtained in two ways, either by taking the geometrical mean at each spectral point or by calculating a weighted average from the individual errors. Because of the small number statistics, the second approach can be misleading. For instance, if a spectral point in a given scan happens to have a small error compared with those in other scans, then the average will be strongly weighted towards the flux of this particular scan, without necessarily increasing the signal-to-noise ratio. This problem was noted several times. Further, since the spectra are not exempt of systematic effects (*e.g.* variation of the atmospheric transmission within one scan), the errors estimated from the scatter around the mean are probably more representative of the "true" errors. For these reasons, the first approach was adopted.

The mean was calculated after normalizing each scan to the same flux averaged over wavelength. The error on each point was then calculated from the square root of the ratio of the variance to the number of scans. If there are N scans and each spectral point has a flux $f_i(\lambda)$, then the final error $E(\lambda)$ on the average flux $\overline{F}(\lambda)$ is

$$E(\lambda) = \left[\frac{1}{N(N-1)} \sum_{i=1}^{N} \left(F_i(\lambda) - \overline{F}(\lambda)\right)^2\right]^{1/2} \tag{2.1}$$

2.2.1.2 Flatfield, atmospheric and stellar feature corrections

The raw spectrum produced by a spectrometer is not truly representative of the intrinsic spectrum for two reasons. First, the transmission of the atmosphere is strongly dependent on wavelength due to molecular band absorption of H_2O and

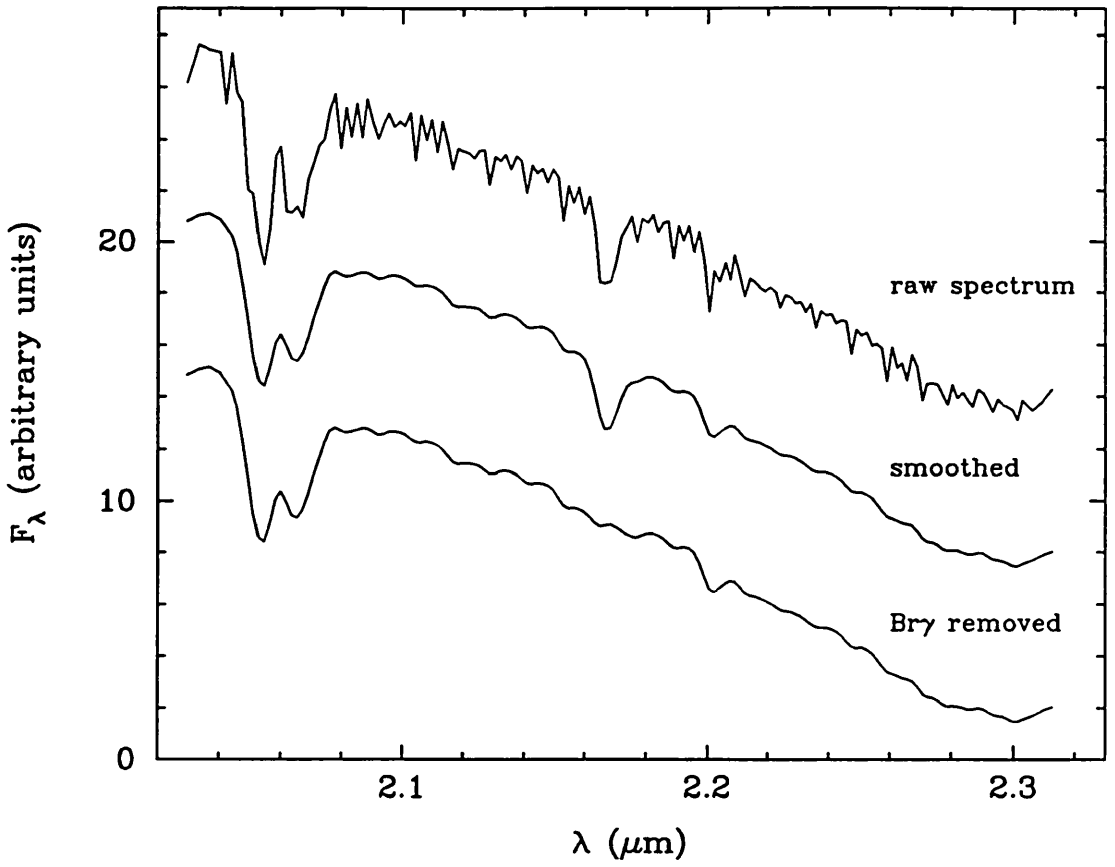

Figure 2.1— K-window spectra of the star BS4554 (A0V). The top one is the original raw spectrum. The middle spectrum has been smoothed with a seven-window triangular filter, removing the instrumental ripples due to the differential response of the detectors, leaving only atmospheric (deep absorption at 2.06 μm) and intrinsic stellar features (Brγ absorption). The bottom spectrum is the same as the middle one after the removal of the Brγ absorption at 2.1661 μm.

CO_2. The instrument also imprints its signature on the spectrum because the sensitivity of the detectors varies (smoothly) with wavelength but also because each detector has a different response relative to others.

The effect of the atmosphere and the differential response of the detectors on the 2.2 μm spectrum of an A0V star is illustrated in Figure 2.1. The most obvious atmospheric feature is found at $\sim$2.06 μm: a strong dip due to a molecular band of CO_2. The periodic ripples (they occur every 7 points) superimposed on the spectrum are due to the imperfect differential response of the 7 detectors.

The standard technique for removing these features is to take the ratio of the object spectrum (in our case a galaxy) with that of a standard star, *if*

one can assume that the atmospheric and instrumental effects are the same in both spectra. In practice, the first requirement is easily met by taking the two spectra at a similar air mass and relatively close in time. Unfortunately, the assumption that the differential response is the same in both spectra is not valid in general. The reason is that the sensitivity also varies *within* the area of the detector itself, which means that the differential response depends on *where* the signal is falling in the aperture and thus, whether the source is point-like (like stars) or extended (like galaxies).

The fact that the amplitude of the ripples was not constant for different stellar spectra can be accounted for by this effect. Amplitude variations as high as a factor of two were noticed, most likely because the stars were not centred exactly at the same place in the aperture. Such an effect would be expected particularly in good seeing conditions, which was observed to be the case on several nights.

Since the ripples are periodic, they could be removed by Fourier analysis, by interpolating out ripple frequencies from the power spectrum and restoring a clean spectrum from its inverse Fourier transform. Although this technique could work on stellar spectra which have high signal-to-noise, the applicability of this technique is very doubtful for noisy galaxy spectra. Instead, the ripples were removed using a simple smoothing technique. The spectra were passed three times in a 1-2-1 triangular filter, corresponding to an effective smoothing window of 7 points. As shown in Figure 2.1 (see middle spectrum), this technique is very successful at removing the ripples, leaving residuals with a typical amplitude of 1-2% of the continuum. Of course, the major drawback of this technique is the degradation of the original resolution but this effect was found to be less than a factor of two, still leaving a resolving power of $\sim$300. All raw spectra (stars and galaxies) were corrected in the same way using this technique.

Finally, before the object spectrum is ratioed with the standard, it must be ensured that there are no (or, at least, negligible) intrinsic absorption lines in the star; otherwise they will appear as spurious emission features in the final spectrum. Early-type stars are best suited for this purpose. Except for hydrogen absorption lines, like Brγ in the K window, they have featureless spectra. The Brγ line can be removed either by interpolating across the line or by ratioing the spectrum with a Gaussian fit of the absorption line. The second

method was adopted. The effect of this correction on the spectrum is shown in Figure 2.1.

When a late-type star must be used as a spectroscopic standard, one can use a rectified template spectrum of the star to removed the intrinsic absorption features. The ratio of the original spectrum with this template should remove the intrinsic absorption lines. Such a technique was used in one case only: for the giant star BS3705 (M0III) (see Table 2.1). A template spectrum was constructed by rectifying and convolving, with the observed instrumental profile, the high resolution spectrum of γSge (M0III) taken from the Kleinmann & Hall (1986) atlas. This template spectrum is shown in Figure 2. Absorption lines due to AlI/MgI, NaI and CaI are the strongest features in the spectrum. As shown in Figure 2.2, such corrections are very small, always less than 3%.

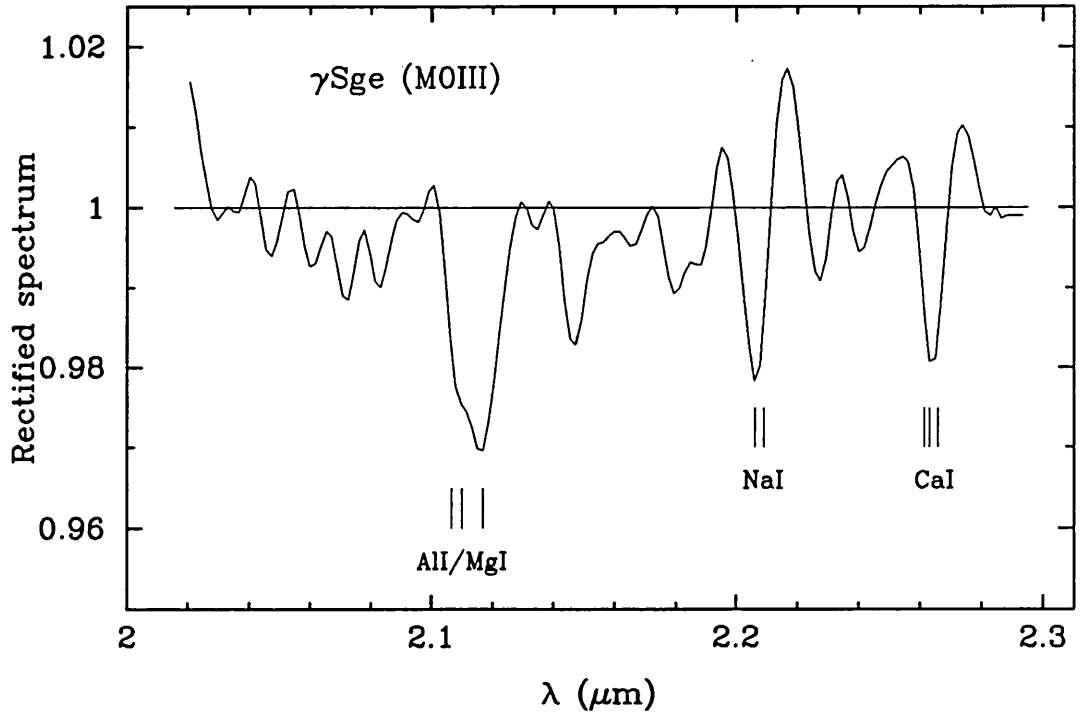

Figure 2.2— Rectified spectrum of a M0III star, obtained by rectifying and convolving the high resolution spectrum of γSge (Kleinmann & Hall 1986) with a Gaussian profile having $\lambda/\Delta\lambda = 300$. The strongest transitions are indicated. The remaining structure in the spectrum is real.

2.2.1.3 FLUX CALIBRATION

A calibrated spectrum is obtained simply by multiplying the ratioed spectrum (*galaxy/standard*) with the absolute energy distribution of the spectroscopic standard, which is well approximated (especially for early-type stars) by a black-body spectrum. If both the source and the standard are observed at approximately the same air mass (< 0.2), this spectrum is given by the following expression:

$$B_\lambda = \frac{k_{\lambda'} F_{\lambda'}(0) 10^{-0.4\, m_{\lambda'}}}{\lambda^5 \exp\big((1.4388/\lambda T_4) - 1\big)} \tag{2.2}$$

where $m_{\lambda'}$ is the magnitude of the star in the waveband λ'. $F_{\lambda'}(0)$ is the flux density of a zero-magnitude star and T_4 is the effective temperature of the star in units of 10^4 K. $K_{\lambda'}$ is a normalization constant equal to $\lambda'^5 \exp\big((1.4388/\lambda' T_4) - 1\big)$ which ensures that $B_{\lambda'} = F_{\lambda'}(0)$. The following zero-points were assumed:

$$\begin{aligned} F_{2.2\mu m}(0) &= 4.03 \times 10^{-10}\ Watt\ m^{-2}\ \mu m^{-1} \\ F_{1.65\mu m}(0) &= 1.17 \times 10^{-9}\ Watt\ m^{-2}\ \mu m^{-1} \\ F_{1.25\mu m}(0) &= 3.03 \times 10^{-9}\ Watt\ m^{-2}\ \mu m^{-1}. \end{aligned} \tag{2.3}$$

Those constants correspond to flux densities (F_ν) of 650, 1060 and 1580 Jy, respectively. When not previously listed, the absolute flux of a spectroscopic standard was determined by comparing with spectra of photometric standards. A list of all the standards used during both observing trips is given in Table 2.2. The spectral types are from the *Bright Star Catalogue* (Hoffleit & Jascheck 1982) or the SAO catalogue. Effective temperatures were taken from the compilation of stellar properties of Landolt-Börnstein (1982). Near-infrared magnitudes are either from the *UKIRT* or the *CalTech* standard list. The specific standard stars used for calibrating and correcting galaxy spectra are given in column 6 of Table 2.1.

The photometric accuracy of the data can be judged from the scatter of the zero points measured during one or several nights. The zero point is defined as the difference between the instrumental magnitude (-2.5 log instrumental flux), and the expected broad-band magnitude, calculated for a given spectral range. The zero points, calculated for different nights and spectral ranges, are given in Table 2.3. It can be seen that photometry better than 3% was achieved around 2.2 μm. The absolute photometry was also very reproducible for different nights and periods of the year.

Table 2.2

Spectroscopic Standards

#	Name	Sp	T_{eff} (K)	J (1.25 μm)	H (1.65 μm)	K (2.2 μm)
1	BS1552	B2III	20300	4.03	4.09	4.14
2	BS2990	K0III	4750	-0.53	-0.99	-1.06
3	BS3705	M0III	3800	-0.39	-0.42	-0.61
4	BS3474	A3V	8720	2.46	1.99	1.88
5	BS3799	A2V	8970	—	—	4.34*
6	BS3881	G1V	5945	4.05	3.78	3.72
7	BS4069	M0III	3800	0.12	-0.68	-0.82
8	BS4518	K0III	4750	1.88*	—	—
9	BS4550	G8VI	6200	4.95	4.46	4.39
10	BS4554	A0V	9520	2.40	2.38	2.37
11	BS4828	A0V	9520	4.83	4.69	4.68
12	BS5634	F5V	6440	4.21	3.96	3.90
13	BS5879	gM1	3720	1.08	0.23	0.03
14	BS5881	A0V	9520	—	—	3.55*
15	BS5947	K3III	4200	2.09	1.45	1.30
16	BS6629	A0V	9520	—	—	3.69*
17	BS7120	K3p	4730	2.73	2.10	2.02
18	BS7615	K0III	4750	2.16	1.70	1.62
19	SAO101682	A2V	8970	—	—	4.38*

* Extrapolated from our own measurements of other standards.

Not surprisingly, the zero point at 2.33 μm is fainter by 0.5 magnitude (factor 1.6) compared with the one at 2.17 μm. The approximate Rayleigh-Jeans nature of stellar spectra ($F_\lambda \propto \lambda^{-4}$; a factor of 1.3 between 2.33 and 2.17 μm) can account partly for this deficit, the rest being due to the relatively smaller transparency of the atmosphere at 2.33 μm, which is also responsible for the higher scatter observed for the zero point at this wavelength. For the same reason, a relatively high scatter (10%) was observed at J (1.25 μm) because the spectra were obtained near the edge of the atmospheric window.

Table 2.3

Zero points

Night	Wavelength range (μm)	λ_{eff} (μm)	Zero point (mag)	N
13 Feb '90	2.05–2.29	2.17	-5.66±0.03	5
14 Feb '90	"	"	-5.70±0.02	7
15 Feb '90	"	"	-5.68±0.03	5
"	2.20–2.46	2.33	-5.19±0.07	7
6 May '90	2.18–2.22	2.20	-5.68±0.02	2
9 May '90	1.28–1.31	1.30	-7.54±0.11	6

* The error is quoted as one standard deviation from the mean, estimated from N measurements taken during the night.

Since some galaxies were observed several times on different nights with overlapping spectral ranges, this provides a more direct way of estimating the uncertainty of the absolute calibration. The spectra were found to differ by 2 to 15% with a typical value of 10%. We adopt 10% as the most likely uncertainty for the absolute calibration.

2.2.1.4 Wavelength calibration

The wavelength calibration of the spectrometer was adjusted at the beginning of each night by setting the center of a strong arc line of Argon at the expected wavelength in the vacuum. The stability of the calibration was checked by measuring the wavelength of Brγ (2.1661 μm) seen in absorption in spectra of early-type stars, obtained several times during a given night. The calibration was found to be constant to within 0.001 μm *i.e.* one sixth of a resolution element at 2.2 μm ($\lambda/\Delta\lambda \approx 300$) which corresponds to an uncertainty of 150 km s^{-1} in velocity.

Non-linearity in the wavelength calibration was also assessed by comparing observed and expected wavelengths of an Argon arc spectrum. Based on 5 lines measured between 2.06 and 2.21 μm, the calibration was found to be linear to within 0.001 μm. However, the variations were not random and systematic differences of up to 0.002 μm cannot be excluded for the relative calibration.

Any line falling within 0.002 μm of its expected wavelength should be regarded as a likely identification.

2.3 Results

All K and J-window spectra are presented in Figures 2.3 to 2.8 and 2.9, respectively. In order to facilitate the presentation and the comparison between galaxies, all spectra have been shifted to their restframe using the recession velocity derived from the strongest emission line observed in the K spectrum, usually the 1-0 S(1) of H_2 (2.1218 μm) or Brγ (2.1661 μm; all wavelengths are quoted in vacuum hereafter). The implicit assumption behind this procedure is that these lines are correctly identified. As shown later, this assumption is proven to be correct as many other absorption and emission lines are also identified in most spectra. When a strong line was not available from the spectrum, redshifts from the literature were used. Within the uncertainties of our wavelength calibration, the recession velocities inferred from the K spectra are consistent with those quoted in the *Second Reference Catalogue of Galaxies* (de Vaucouleurs, de Vaucouleurs & Corwin 1976). The J spectra were shifted using the same velocity inferred from the K lines.

Most K-window spectra cover a wide wavelength interval. In order to illustrate the different spectral features, two versions are presented. The first displays the whole spectrum, and the second shows a continuum-subtracted subset of the 2.0-2.29 μm spectral region. The underlying galaxy continuum was determined by fitting a power-law ($F_\lambda \propto \lambda^\beta$) to featureless sections of the spectrum, defined so as to avoid the spectral range of prominent emission and absorption lines. These include Brγ, HeIλ2.06μm, H_2 transitions (1-0 S(0), 1-0 S(1), 1-0 S(2) and 2-1 S(1)), the CO absorption band longward of 2.3 μm, and NaI, CaI and AlI/MgI absorption features. Power-law indices measured from the K-window spectra are given in Table 2.5. Only the continuum-subtracted versions are presented for the J-spectra. In this case the galaxy continuum was defined either by fitting a second or third order polynomial to the spectrum.

Emission line fluxes were measured from the continuum-subtracted spectra by fitting Gaussian profiles with a fixed FWHM defined by the strongest line (usually Brγ or 1-0 S(1)) observed in a given spectrum. More than one profile was fitted to blended features. Because of the strong CO band absorption at

$\sim$ 2.36 μm, the local continuum around the Q-branch transitions of H_2 (2.40-2.45 μm) is substantially lower than that at 2.2 μm in the continuum-subtracted spectrum. The local continuum around the Q-branch was defined as the average of the continuum-subtracted spectrum over the CO band. Identifications and observed line fluxes are given in Table 2.4 for all galaxies.

Absorption line strengths were measured in equivalent width from the rectified spectrum *i.e.* the ratio of the observed spectrum with the power-law continuum. The strength of the CO band was quantified in a different way, using the following *spectroscopic* CO index:

$$CO_{sp} = -2.5 \log\langle R_{2.36} \rangle \tag{2.4}$$

where $\langle R_{2.36} \rangle$ is the average of the rectified spectrum R_λ between 2.31 and 2.40 μm in the restframe of the galaxy. This definition is similar to the *photometric* CO index used in previous studies of ellipticals (Frogel *et al.* 1978) and bulges of spirals (Frogel 1985). This photometric index is defined as the difference in magnitudes of the flux measured in two narrow-band filters ($\Delta\lambda$ = 0.08 μm) centred on the CO dip at 2.36 μm and the nearby continuum at 2.2 μm, relative to αLyrae.

This photometric technique has the major disadvantage of being sensitive to the *slope* of the continuum between 2.2 and 2.36 μm. High extinction and contamination from non-stellar sources (*e.g.* hot dust)—characteristic features of interacting and merging galaxies— can seriously affect the slope of the continuum. Furthermore, since the wavelengths of the CO and continuum filters are fixed, the photometric CO index is sensitive to redshift. Beyond 3000 km s^{-1}, the K-correction becomes unreliably large (*cf.* Arnaud & Gilmore 1986). Thus, a spectroscopic approach was chosen to minimized these problems. A more detailed description of this spectroscopic approach in presented in Appendix A, along with spectroscopic CO indices for all the stars in the Kleinmann & Hall atlas (1986). Observed equivalent widths and spectroscopic CO indices of the galaxies presented in this work are compiled in Table 2.5. For comparison, we also give spectroscopic CO indices of other spectra obtained with larger apertures at CVF resolution (Prestwich 1989).

Most spectra presented in Figure 2.3 to 2.8 were obtained from merging and coadding a few spectra obtained on different nights and different spectral ranges (see Table 2.1). The error bar of each spectral point was derived from the scatter

around the geometrical mean. These errors are not necessarily representative of the true statistical errors because of the small number of points involved (usually 2 or 3). Nevertheless, they give an objective measure of the systematic variations present in the data. In general, the error bars derived from the scatter around the mean were usually *larger* than those given in the individual spectra, a strong indication that the data is indeed affected by systematic variations. The spectrum of each galaxy is described below.

2.3.1 ARP 220

This galaxy is one of the ultra-luminous ($L > 10^{12}\ L_{\odot}$) *IRAS* galaxies which radiates 98% of its bolometric luminosity in the *IRAS* bands. A considerable number of observations have been secured on this galaxy in last five years. Optical images shows a prominent dust lane (Joy *et al.* 1986) and faint tidal tails (Joseph & Wright 1985, Sanders *et al.* 1988), morphological evidence that the galaxy is the result of a merger involving at least one gas-rich spiral galaxy. The surface brightness profile at 2.2 μm follows a de Vaucouleurs $r^{1/4}$ law (Wright *et al.* 1990) characteristic of elliptical galaxies, showing that this system is dynamically relaxed, which is expected if the galaxy is an ongoing merger. High-resolution 2.2 μm imaging (Graham *et al.* 1990) has revealed the presence of two nuclei in the center, confirming that the galaxy is an evolving merger. The strong 2.6 mm CO emission (Scoville *et al.* 1986) implies an H_2 mass of $10^{10}\ M_{\odot}$ within the central 1500 pc. This concentration of molecular material is $\sim$30 times greater than in a equivalent area of the Galaxy. Along with NGC 6240, ARP 220 is one the brightest extragalactic sources of H_2 emission (Joseph, Wright & Wade 1984).

The K-window spectrum of ARP 220 is shown in Figure 2.3a and 2.3b. The spectrum was obtained from the coaddition of four spectra, each covering roughly half the window (see Table 2.1). The overall shape of the continuum has all the characteristics of late-type stars, the detection of the CO band absorption longward of 2.3 μm being the strongest evidence. Taking into account the uncertainties in the slope of the continuum, we estimate a spectroscopic CO index of 0.18 ± 0.03. For comparison, ellipticals and bulges of spirals have spectroscopic CO indices of $\sim$0.20, as derived from an average photometric CO index of 0.15 (Frogel *et al.* 1978; Frogel 1985) and the transformation between photometric and spectroscopic CO indices given in Appendix A.

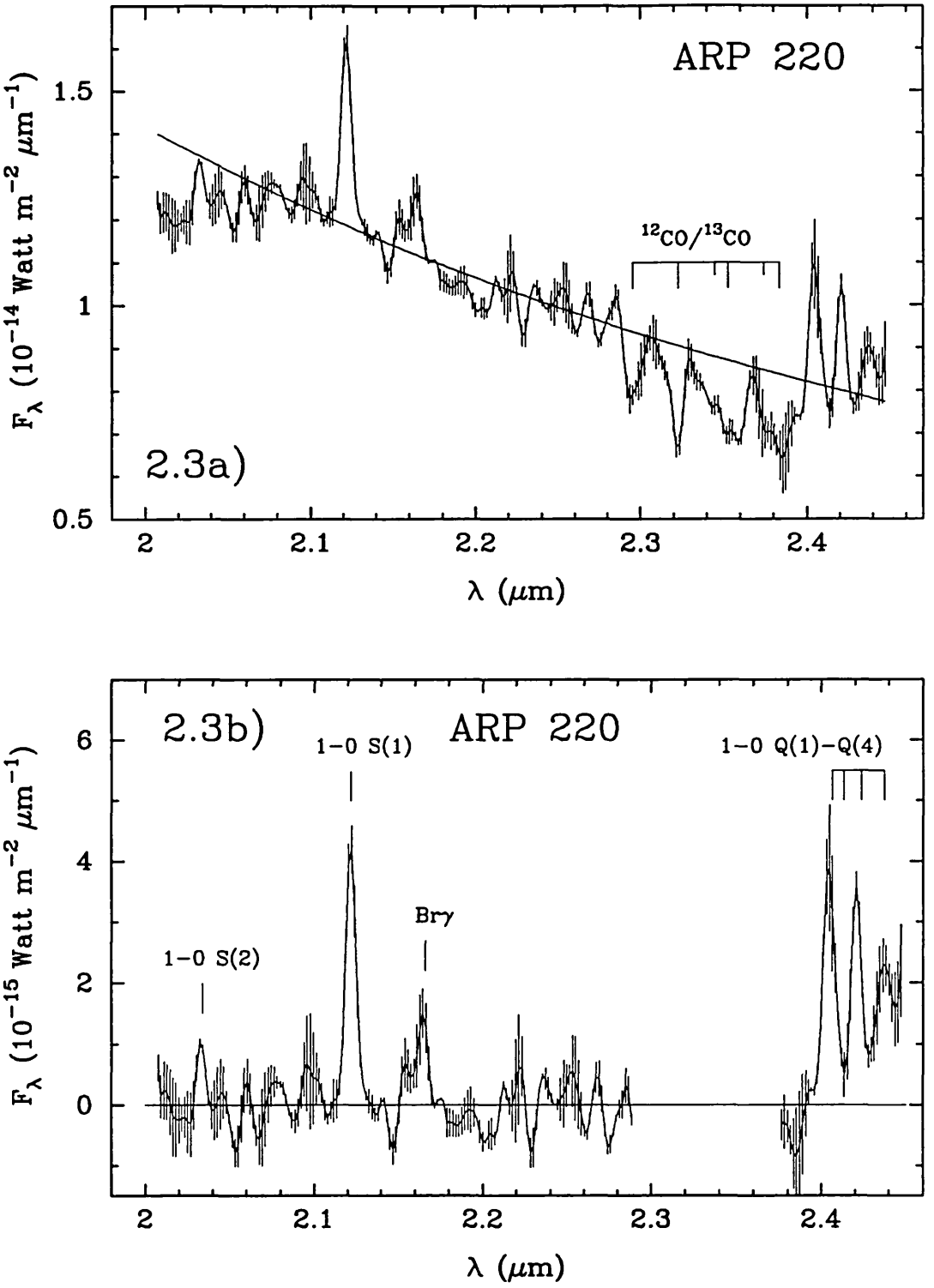

Figure 2.3— a) K-window spectrum of ARP 220, shown in the rest frame. The solid line superimposed on the spectrum is the best fit to a power-law spectrum ($F_\lambda \propto \lambda^\beta$) fitted from featureless sections of the continuum taken between 2.1 and 2.29 μm. b) Continuum-subtracted subset of the spectrum shown in a).

The strength of the CO band in our spectrum may also be compared with the larger aperture (8 and 19″) CVF spectra of Prestwich (1989). As seen in Table 2.5, the spectroscopic CO index of the 5″ spectrum is virtually identical to that measured in the CVF spectra. The CO band of the 8″ CVF is perhaps stronger than in the other spectra but this result is marginally significant. Thus, as far as the strength of the CO band is concerned, *the stellar population in the nucleus of ARP 220 is normal.* This conclusion is in complete disagreement with the study of Rieke *et al.* (1985) who claimed that the strength of the CO band in ARP 220 is much stronger than normal galaxies.

The slope of the K spectrum also provides compelling evidence that the K continuum has a stellar origin. The power-law index of $-3.0^{+1}_{-0.3}$ fitted between 2.1 and 2.29 μm is slightly redder but similar to that of late-type giants which typically have spectral indices of ∼-3.6 (see Appendix A). A puzzling feature of the continuum in ARP 220 is the significant deviation of the spectrum from the power-law shortward of 2.1 μm. As shown in the following sections, a power-law always provide a very good fit to galaxy spectra between 2.0 and 2.3 μm. This feature is unique to ARP 220. Such a deviation could be due to stellar H_2O absorption, a characteristic feature of late-type dwarfs and supergiants (*cf.* the stellar atlas of Kleinmann & Hall 1986). Any contribution from late-type supergiants is unlikely since the CO_{Sp} would have to be well above 0.3, which is inconsistent with the observed strength of the CO band. Alternatively, the nucleus could have a large population of late-type dwarfs, an interpretation which is supported by the relatively small or normal spectroscopic CO index. This is a surprising result because the 2.2 μm radiation of galaxies is generally thought to be dominated by giant stars (typically K5; Frogel *et al.* 1978; Arnaud & Gilmore 1986) which show negligible water absorption.

The emission-line spectrum of ARP 220 is dominated by the 1-0 S(1) of H_2. Within the uncertainties of the absolute calibration, our line flux is consistent with the previous measurement of Joseph *et al.* (1984) obtained with the same instrument and aperture. Other H_2 transitions are clearly present in the spectrum, namely the first four Q-branch lines and the 1-0 S(2). The latter seems marginally detected but this is due to the large errors bars on each side of the line, caused by systematic variations in the local continuum. The smaller errors bars on 1-0 S(2) show that this line was clearly detected in the two original spectra used to produce the coadd. Our spectrum clearly shows significant Brγ

emission which is confirmed by the detection of Paβ (see Figure 2.9). These are probably the first unambiguous detections of these lines in ARP 220. The line flux of Brγ is $1.2 \pm 0.2 \times 10^{-17}$ W m^{-2} which is a factor of three lower than the flux reported by Rieke *et al.* (1985) for an 8.7″ aperture spectrum.

2.3.2 MRK 231

This is another ultra-luminous *IRAS* galaxy but with a far-infrared luminosity twice as large as that of ARP 220. There is morphological evidence (double tails) that this galaxy is a merging system (Sanders *et al.* 1988). These authors reasoned that MRK 231 is the initial dust enshrouded stage of a quasar.

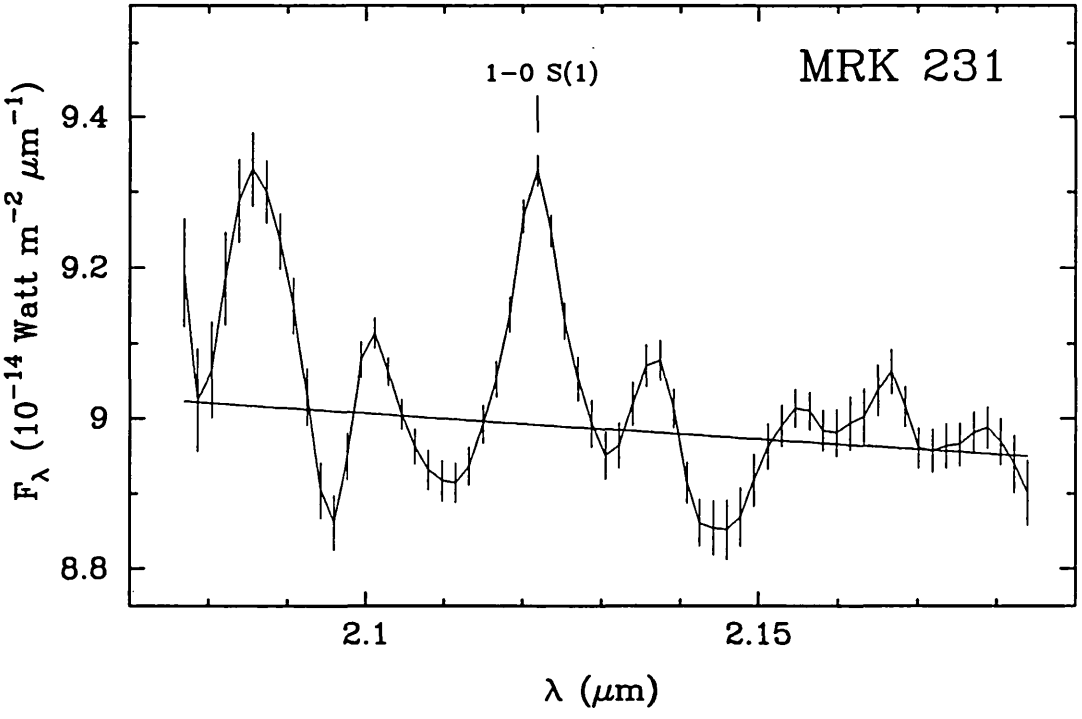

Figure 2.4— K-window spectrum of MRK 231, shown in the restframe.

Two spectra of this galaxy was obtained (see Table 2.1), one in February the other in May 1990. The February spectrum (not shown here) is featureless with a possible detection ($< 2\sigma$) of the 1-0 S(1). The spectrum obtained in May is shown in Figure 2.4. It has been shifted in the restframe using a recession velocity of 12654 km s^{-1} (Sanders *et al.* 1988) and covers only the spectral region encompassing the 1-0 S(1) and Brγ. The errors bars are very small and suggest that the 1-0 S(1) is detected at the 10σ level. However, the apparent

structure in the spectrum next to line is probably not real since its scatter has an amplitude of ~1% of the continuum which is similar to the residuals produced by the imperfect differential response of the detectors, as discussed earlier. Thus, the 1-0 S(1) is detected only at the 3σ level. Although this result needs confirmation, if true, the observed line flux would imply a 1-0 S(1) luminosity four times brighter than ARP 220.

With a power-law index of 0.1 ± 0.2 between 2.1 and 2.3 μm, the overall continuum is extremely red compared with normal stars. For comparison, Seyfert galaxies have infrared power-law indices between -0.1 and 0.5 (Glass & Moorwood 1985). This suggests that the IR continuum of MRK 231 has a non-thermal origin.

2.3.3 NGC 1614

The disturbed and chaotic optical appearance of this galaxy leave no doubt that this system is an ongoing merger. With a bolometric luminosity of $4 \times 10^{11}\ L_{\odot}$, NGC 1614 is amongst the most luminous IR galaxies discovered by *IRAS*, although an order of magnitude less luminous than ultra-luminous objects like ARP 220 and MRK 231. Like ARP 220, this system is characterized by a high concentration of molecular gas in the nucleus (Scoville *et al.* 1989). In their IR study of merging galaxies, Joseph & Wright (1985) argued that its large luminosity is powered by a vigorous episode of star formation, an interpretation which is supported by the extended 10 μm emission (Wright *et al.* 1988). The optical spectrum yields emission line strengths characteristic of H II regions, although close to the boundary between H II regions and LINERS. A recent multi-wavelength study (Neff *et al.* 1990) suggests that there are no signs of Seyfert-like activity in this galaxy.

The K-window spectrum of the nucleus of NGC 1614 is shown in Figure 2.5a and 2.5b. This is probably the best-quality spectrum presented in this chapter. The average signal-to-noise per point is 80 for the whole spectrum and more than 100 around 2.2 μm. The spectrum displayed in 5a is the coadd of two spectra obtained on two different nights with a common spectral range between 2.18 and 2.29 μm. The average signal-to-noise in this spectral region is a factor 1.3 higher than the rest of the spectrum, close to a the factor of $\sqrt{2}$ expected if there are no systematic variations in the spectrum. This suggests that any structure greater than the size of the error bars is probably genuine.

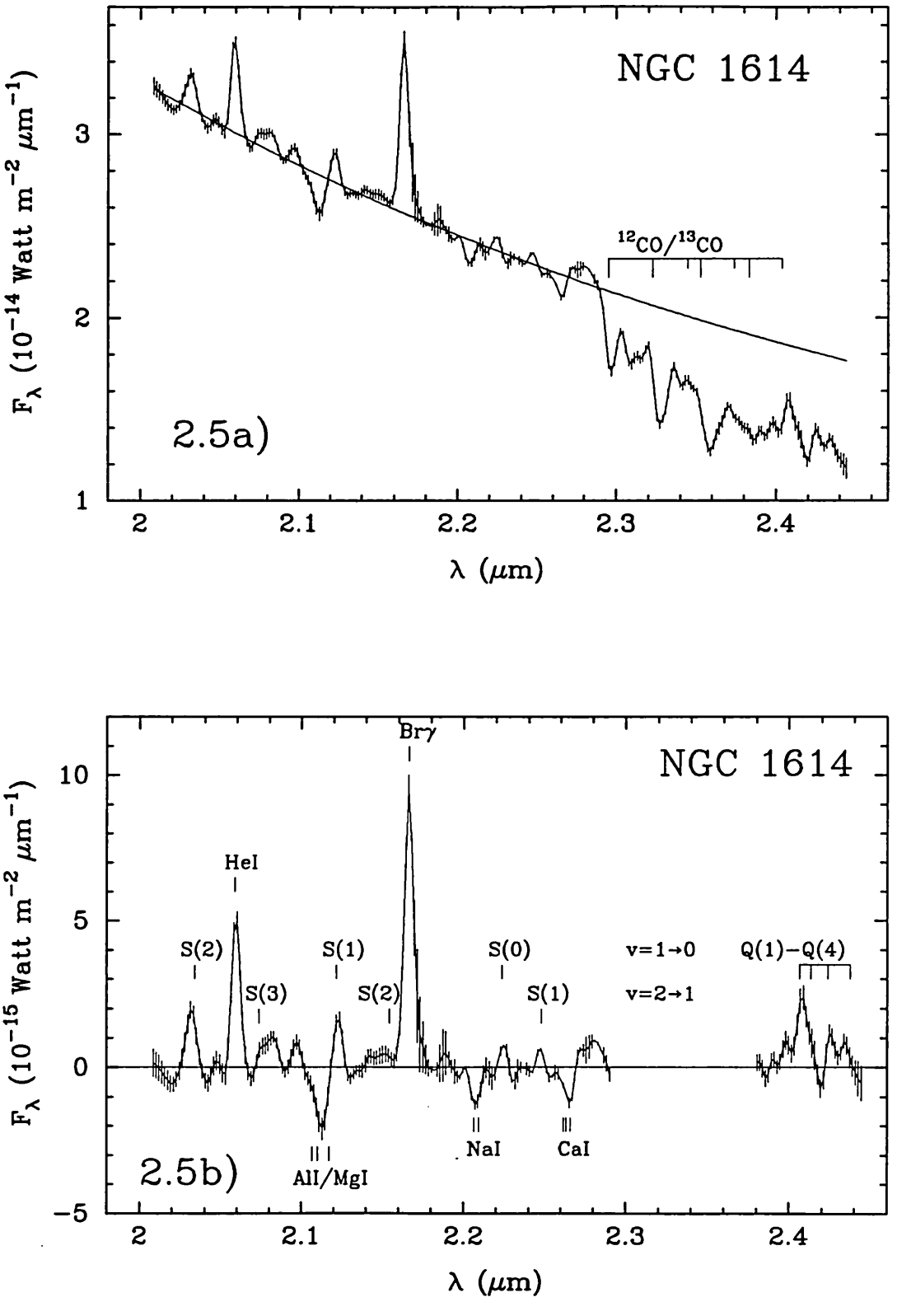
NGC 1614
2.5a)
$^{12}CO/^{13}CO$
F_λ (10^{-14} Watt m^{-2} μm^{-1})
λ (μm)
NGC 1614
2.5b)
Brγ
HeI
S(2)
S(3)
S(1)
S(2)
S(0)
S(1)
v=1→0
v=2→1
Q(1)–Q(4)
NaI
CaI
AlI/MgI
F_λ (10^{-15} Watt m^{-2} μm^{-1})
λ (μm)

Figure 2.5

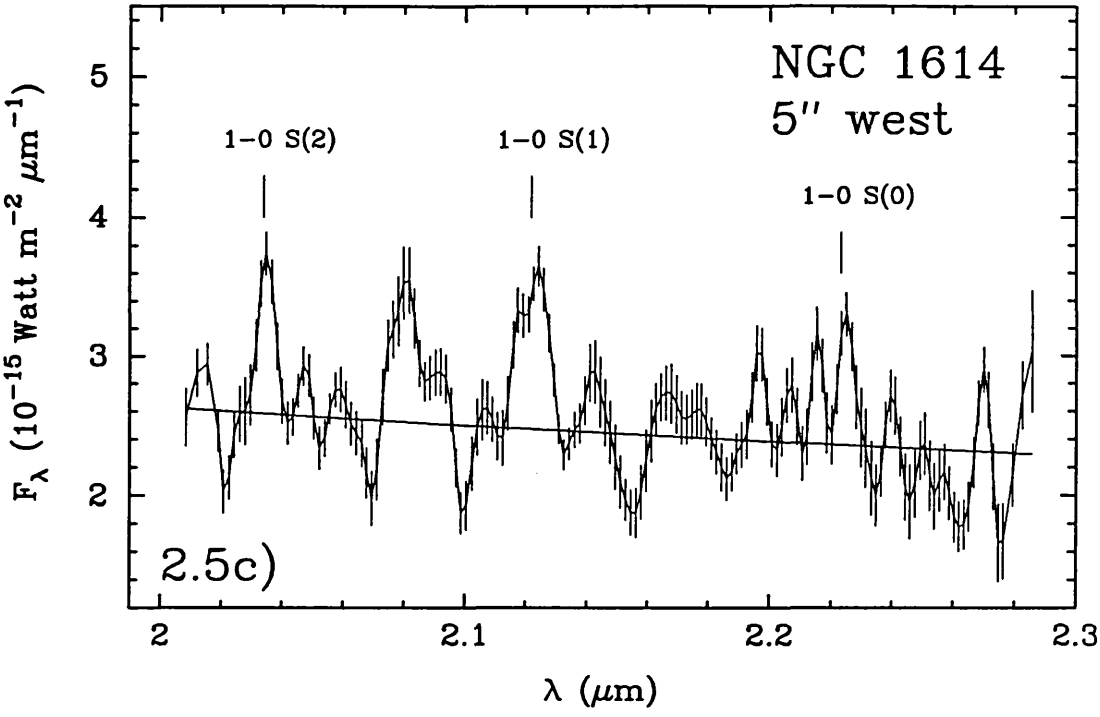

Figure 2.5 a,b) K-window spectrum of the nucleus of NGC 1614. c) Spectrum taken 5″ west of the nucleus. The solid line superposed on the spectrum shown in a) and c) is a fitted power-law ($F_\lambda \propto \lambda^\beta$) continuum.

Brγ and He Iλ2.06μm are the dominant emission lines in the spectrum but several H_2 transitions are also clearly detected. Unambiguous identifications include the 1-0 S(1), 1-0 S(2) and the Q-branch. The Brγ and 1-0 S(1) line fluxes are within the errors consistent with those of Moorwood & Oliva (1988) and Prestwich (1989). The detection of 1-0 S(0) and 2-1 S(1) is very tantalizing and critically depends on the correct assessment of the local continuum around the lines. If correctly identified, these lines are roughly a third of the strength of the 1-0 S(1). This is much stronger than expected for shock excitation and very suggestive that a non-thermal or fluorescent component is contributing significantly to the total H_2 emission. We shall come back to this point later in Chapter 5 when we discuss the excitation mechanism of the H_2 emission.

There is also an emission "bump" around 2.07-2.08 μm. Fitting two Gaussian profiles yields a line at 2.076 and 2.083 μm. We tentatively identify the former with the 2-1 S(3) of H_2 but the second feature is unidentified. Finally, there seems to be an emission line at 2.097 μm for which we cannot provide satisfactory identification.

The power-law index of -3.0 ± 0.1 is slightly redder but consistent with the spectral energy distribution of a late-type star. The presence in the spectrum of

prominent absorption lines is compelling evidence that the continuum is stellar. The strongest feature is the CO band absorption at ~2.35 μm. The spectroscopic CO index of 0.30 ± 0.02 is ~0.1 magnitude stronger than expected for a normal giant-dominated stellar population. Note that the error quoted for the index takes into account the uncertainties in fitting the power-law continuum. If the 2.0-2.5 μm energy distribution of NGC 1614 were represented by a single star, it would be close to the K5I star of the Kleinmann & Hall (1986) atlas which has a spectroscopic CO index of 0.27 (see Appendix A).

The NaI (≈2.206 μm) and CaI (≈2.265 μm) absorptions are also detected in the spectrum. The average equivalent width of the two features is 3.9 ± 0.3 Å, very similar to the value of 3.6 Å measured in the K5I star above. This is a strong indication that the adopted power-law continuum shown in Figure 2.5a is probably not an underestimate. Another dominant absorption feature in the spectrum is the blend of AlI and MgI at 2.09-2.10 μm, a common feature in late-type star spectra. Its equivalent width of 6.3 ± 0.6 Å is 20% stronger than expected for a normal K5I star.

A K-window spectrum was also obtained 5″ west of the nucleus (see Figure 2.5c). Although the spectrum is noisy, the detection of the 1-0 S(1) and 1-0 S(2) of H_2 are significant. It is remarkable that the line flux of the 1-0 S(1) at this position is at least as strong as on the nucleus. At the same detection level as the H_2 transitions, there is also an emission line at 2.080 μm, within the errors at the same wavelength as the line found at 2.083 μm in the nuclear spectrum. The detection of this feature outside the nucleus is further evidence that the line is indeed genuine. Perhaps, the fact that only the molecular lines of H_2 seem to persist outside the nucleus suggests that the unidentified transition 2.080 μm is an unknown molecular line. With a power-law index of -1.0 ± 0.2, the continuum at this position is much redder compared with the nucleus, probably an indication of higher extinction at this position.

2.3.4 NGC 2798

This galaxy forms an interacting pair with NGC 2799. With a 10 μm luminosity of 2×10^9 $L_\odot$ (Wright *et al.* 1988), NGC 2798 is an order of magnitude brighter than normal spirals but also fainter by the same factor compared with merging systems like NGC 1614 and ARP 220. The $JHKL$ photometry study of Joseph & Wright (1985) revealed that NGC 2798 has a high $K - L$ colour relative to normal galaxies, a feature interpreted by the authors as being due to hot dust

heated by young OB stars produced in a starburst. The continuum emission is clearly extended at 10 and 20 μm (Wright *et al.* 1988), strong confirmation that the IR luminosity is powered by vigorous star formation.

This galaxy was observed at K and J. The spectra are shown in Figure 2.6 and 2.9, respectively. The shorter wavelength part of the K spectrum ($\lambda < 2.29$ μm) is the result of the coadd of three spectra obtained on different nights. As evidenced by the variation of the error bars, some parts of the spectrum are clearly affected by systematic variations. The emission lines that can be unambiguously identified are Brγ, He Iλ2.06μm and some transitions of H_2 including the 1-0 S(1) and possibly the blend of the first three transitions of the Q-branch.

Like the other galaxies described thus far, the underlying continuum of NGC 2798 is stellar and dominated by the absorption of the CO band. The spectroscopic CO index of 0.29 ± 0.01 is significantly stronger than expected for a normal giant-dominated stellar population. The NaI and CaI absorption features are also detected. The overall slope of the K continuum is significantly redder (power-law index of -2.5 ± 0.1) than normal late-type stars.

2.3.5 NGC 3690-IC 694

NGC 3690-IC694 is certainly the most extensively studied example of an interacting system. The unusual activity present in this system was first noticed by Gehrz, Sramek and Weedman (1983). They found prominent optical emission-lines and strong 10 and 20 μm continuum emission. In the UV the spectrum shows CIV and SiIV absorption characteristic of young OB stars (Augarde & Lequeux 1985). After NGC 1068, this galaxy was the first to be detected in molecular hydrogen (Fischer *et al.* 1983) and several H_2-related studies have followed since then (Joseph *et al.* 1987; Prestwich 1989; Nakagawa *et al.* 1989).

Although its optical appearance is very disturbed and chaotic, the true mass distribution of this system is unveiled at 2.2 μm, showing three distinct sources (Telesco, Decher & Gatley 1985; Eales *et al.* private communication). Sources A and B are the locations of the nuclei of IC 694 and NGC 3690, respectively, which are separated by $\sim 20''$ in the east-west direction. Another prominent 2.2 μm source (source C) is found $\sim 9''$ north of source B, and is possibly a giant extra-nuclear H II region.

The observational properties of this galaxy are usually interpreted in terms of starburst activity. However, Gehrz, Sramek and Weedman (1983) challenged

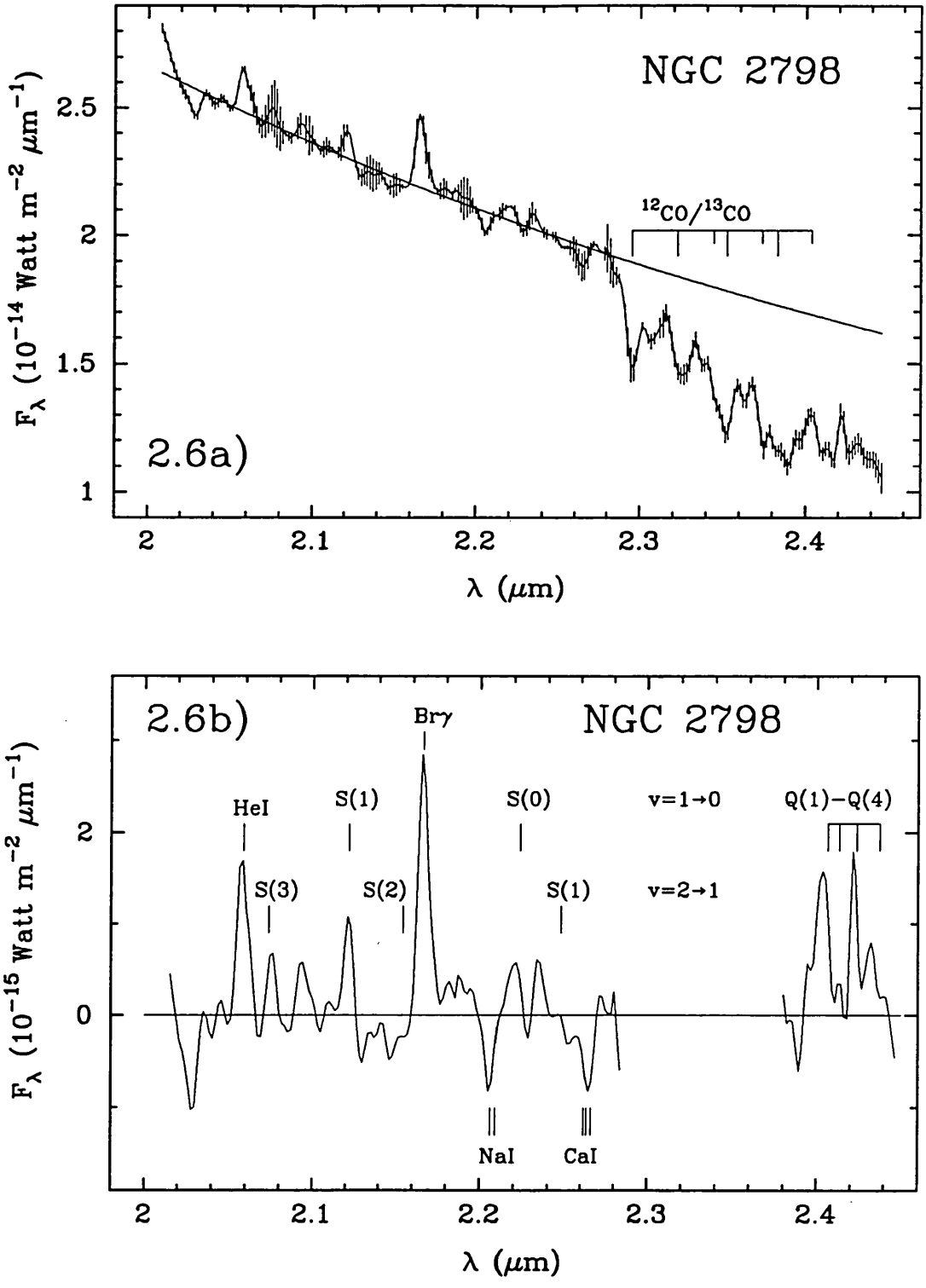

Figure 2.6— a) *K*-window spectrum of NGC 2798, shown in the rest frame of the galaxy. The solid line superimposed on the spectrum is the best fit to a power-law continuum. b) Continuum-subtracted subset of the spectrum shown in a).

this interpretation for IC 694 (source A). They noted that the star formation activity would have to be exceptionally strong in this source in order to generate free-free emission comparable to the observed radio flux. Instead, they suggested that the compact radio source could be associated with a putative active nucleus.

K-window spectra of all three sources are presented in Figure 2.7. As for galaxies discussed thus far, their spectra are also dominated by strong Brγ, He Iλ2.06μm and H_2 emission, but the relative strength of these lines varies appreciably from one position to another. Within the errors, sources A and C have the same Brγ fluxes but the 1-0 S(1), which is very prominent in the former, is barely detected in the latter. It is questionable whether the bump at the position of the 1-0 S(1) represents a detection of the H_2 line. It is even more uncertain, since there is no evidence in the spectrum for other H_2 lines such as the 1-0 S(2), which is clearly detected in sources A and B.

Several other H_2 lines are detected in source A, including the first three transitions of the Q-branch and the two important diagnostic transitions: the 1-0 S(0) and 2-1 S(1). The latter are roughly one third the strength of the 1-0 S(1) which is very similar to the line ratios observed in NGC 1614, again suggestive of non-thermal excitation. There is also a blue shoulder on the Brγ line which we tentatively identify as the 2-1 S(2) transition of H_2.

We measured a 1-0 S(1) line flux of $3.3 \pm 0.3 \times 10^{-17}$ $W\ m^{-2}$ in source A, consistent with the measurement Nakagawa *et al.* (1989) obtained within a similar aperture. The comparison of our line fluxes with those of previous studies obtained using larger apertures is very revealing with regard to the spatial extent of the emission lines. The integrated 1-0 S(1) and Brγ fluxes of sources A, B and C inferred from our spectra are 6 ± 1 and 2.8 ± 0.6 times smaller, respectively, than the measurements Fischer *et al.* (1983) obtained within a beam of 34″ encompassing all three sources. This is strong evidence that the H_2 emission is appreciably more extended than Brγ. This result has already been noted from multi-aperture spectroscopic measurements (Prestwich 1989). Our smaller aperture measurements further reinforce this result. Spectra of Paβ were obtained for all sources (see Figure 2.9). By mistake, an additional position was observed 4″ east of source C.

Only source A was observed beyond 2.3 μm. The stellar CO overtone absorption is clearly detected. With a spectroscopic CO index of 0.21 ± 0.01 the

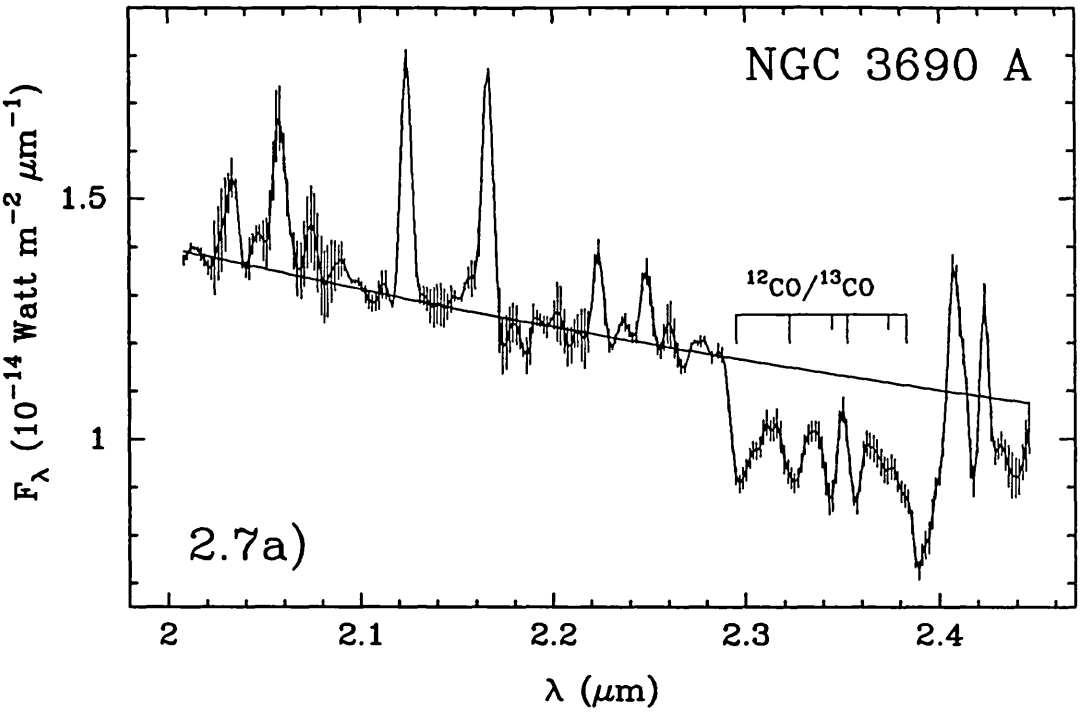
NGC 3690 A
2.7a)
$^{12}CO/^{13}CO$
F_λ (10^{-14} Watt m^{-2} μm^{-1})
1.5
1
2
2.1
2.2
2.3
2.4
λ (μm)

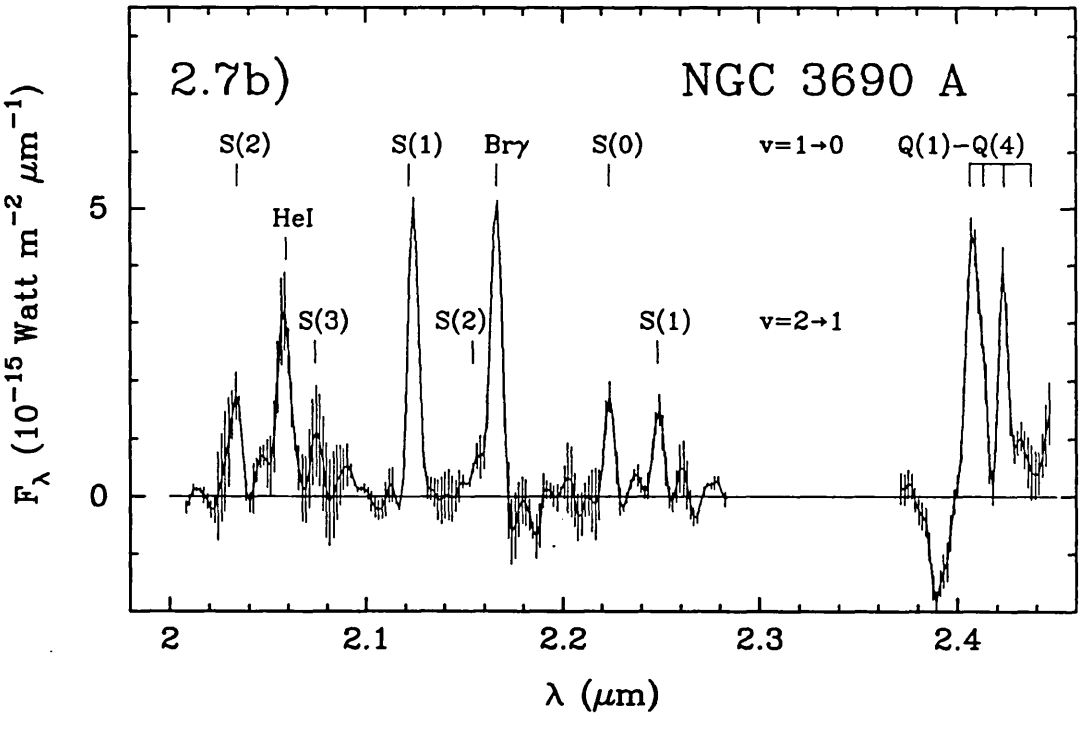
2.7b)
NGC 3690 A
S(2)
S(1)
Brγ
S(0)
v=1→0
Q(1)–Q(4)
HeI
S(3)
S(2)
S(1)
v=2→1
F_λ (10^{-15} Watt m^{-2} μm^{-1})
5
0
2
2.1
2.2
2.3
2.4
λ (μm)

Figure 2.7

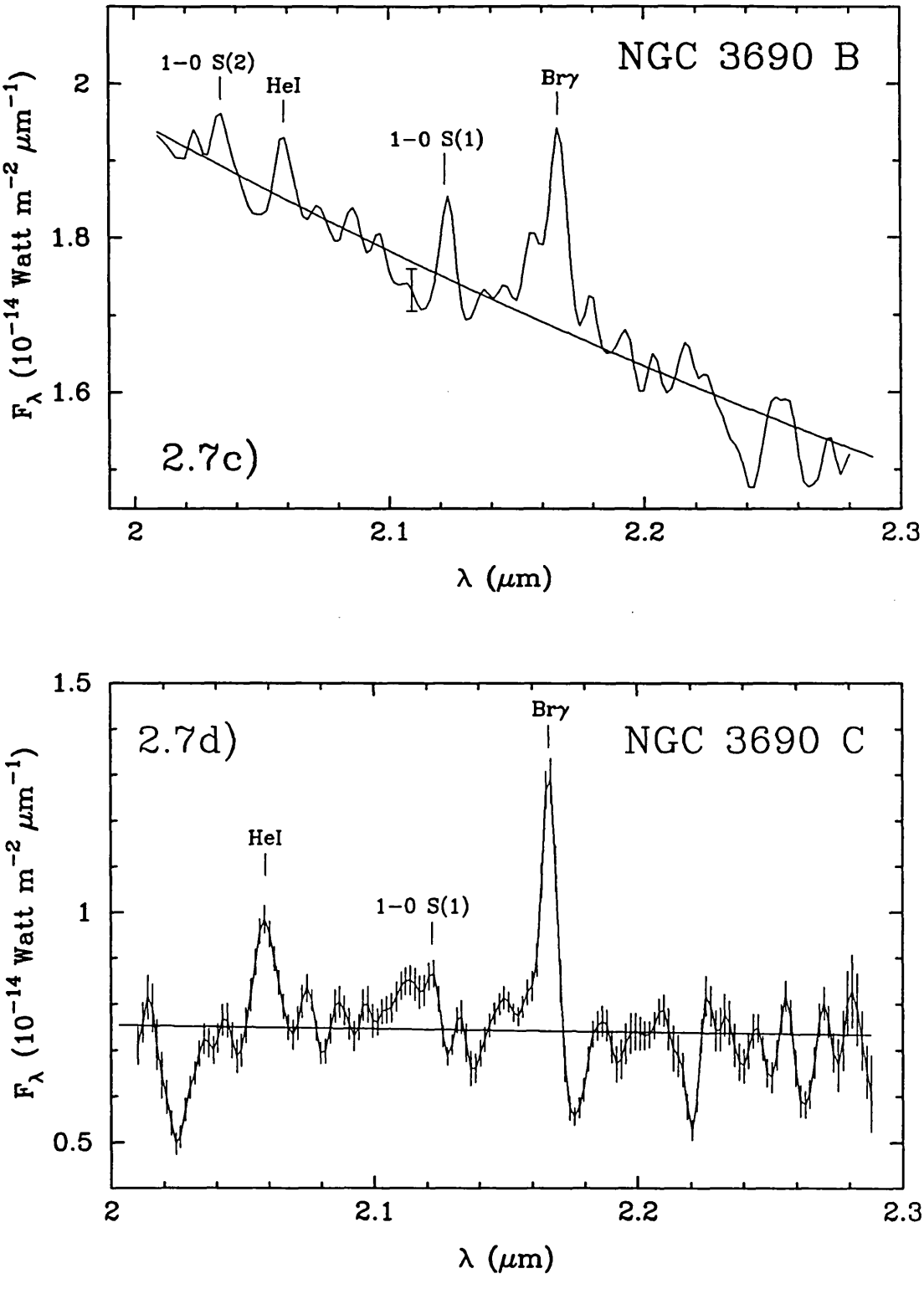

Figure 2.7 K-window spectra of NGC 3690-IC 694. a, b) IC 694 (source A), c) NGC 3690 (source B) and d) source C. The solid line superposed on the spectra shown in a) and c) and d) is the best power-law spectrum ($F_\lambda \propto \lambda^\beta$) fitted to the underlying continuum.

CO band is typical of K5III stars (see Appendix A), as strong as expected for a normal stellar population. The NaI and CaI absorption are barely detected with an equivalent width less than < 2 Å. Given the uncertainty of the continuum level, this is consistent with the equivalent width of 3 Å, typically observed in K5III stars. With power-law indices between -0.2 and -1.9, the spectra of NGC 3690-IC 694 are much redder than normal late-type stars, especially source C which has a K continuum as red as MRK 231.

2.3.6 NGC 6240

NGC 6240 is one of the ultra-luminous *IRAS* galaxies, emitting 90% of its bolometric luminosity beyond 1 μm (Wright, Joseph & Meikle 1984). Two nuclei are clearly revealed by radio VLA maps (Condon *et al.* 1982) and near-infrared images (Thronson *et al.* 1990). This galaxy is particularly well known for its strong H_2 emission (Joseph *et al.* 1984; Rieke *et al.* 1985; DePoy, Becklin & Wynn-Williams 1986; Lester, Harvey & Carr 1988; Elston & Maloney 1990; Herbst *et al.* 1990).

Two K-window spectra of this galaxy were obtained, one at the *AAT* using FIGS with $3.5 \times 3.5''$ aperture, the other at *UKIRT* using CGS2 with a $5''$ aperture. These spectra are shown in Figure 2.8. The *UKIRT* spectrum partially covers the K-window and was obtained up to the edge of the atmospheric window in order to measure the strength of the the Q-branch transitions of H_2.

As shown in Figure 2.8, the K-window spectrum of this galaxy is dominated by the 1-0 S(1) line of H_2. The flux of this line measured from the *UKIRT* spectrum is within the errors identical to that measured by Joseph *et al.* (1984) with the same instrument and aperture. The underlying continuum is not very well defined in this spectrum.

The *AAT* spectrum may be compared with that of Lester *et al.* (1988) since both were obtained with a similar aperture. The 1-0 S(1) line flux measured from the *AAT* spectrum is ~30% smaller than the flux quoted by Lester *et al.* (1988). This discrepancy is probably not significant and due to the uncertainty of the absolute calibration. Our spectrum does show a line coincident with Brγ. Although tantalizing, this detection should be regarded with suspicion since the width of the line is significantly smaller (by a factor of ~ 2) than the profile of the strong 1-0 S(1). Similarly, there seems to be a line close to the wavelength of the 2-1 S(2) transition of H_2 but, like Brγ, this line is very narrow. Assuming

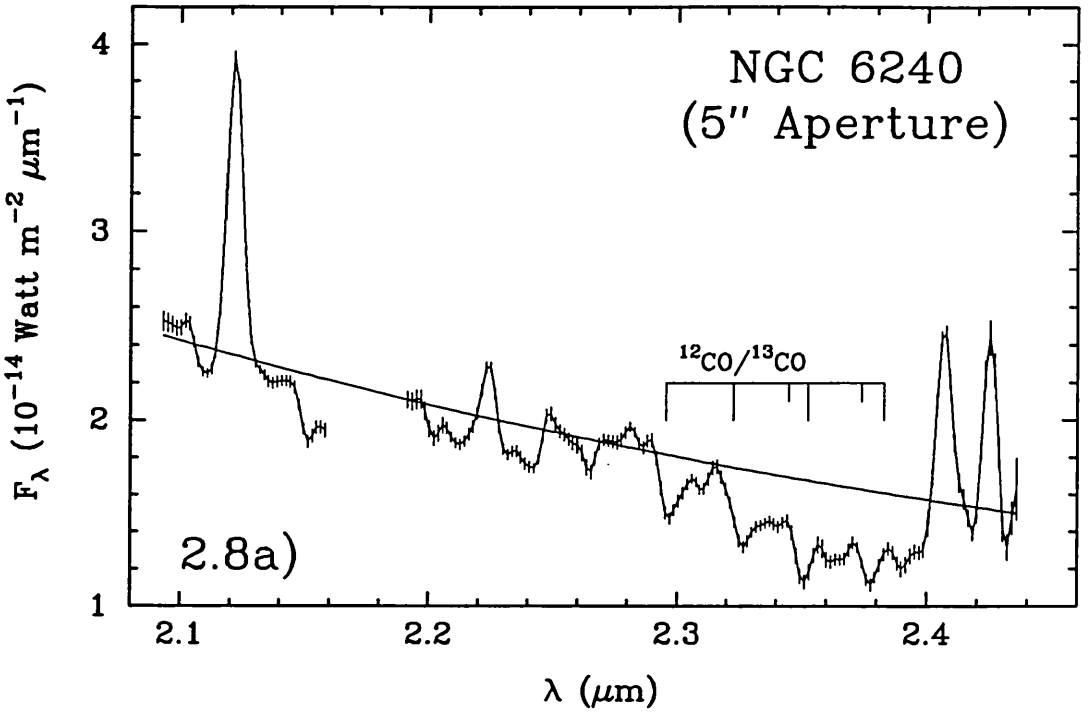
NGC 6240
(5″ Aperture)
$^{12}CO/^{13}CO$
2.8a)
F_λ (10^{-14} Watt m^{-2} μm^{-1})
λ (μm)

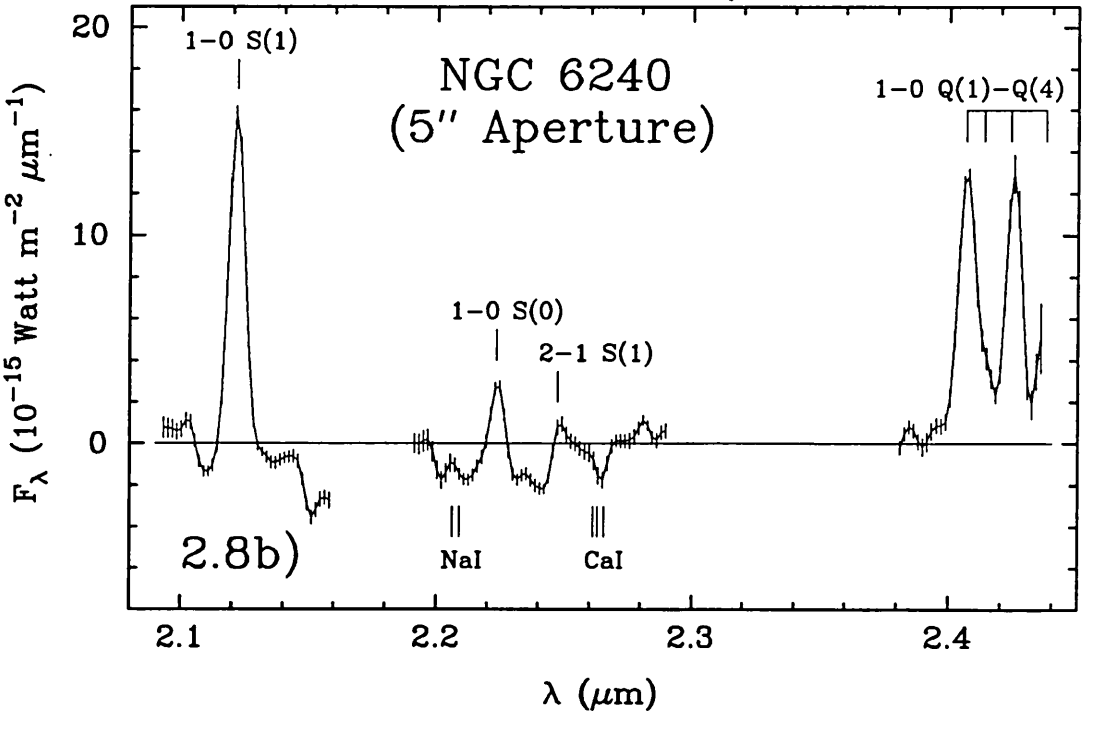
1-0 S(1)
NGC 6240
(5″ Aperture)
1-0 Q(1)-Q(4)
1-0 S(0)
2-1 S(1)
NaI
CaI
2.8b)
F_λ (10^{-15} Watt m^{-2} μm^{-1})
λ (μm)

Figure 2.8

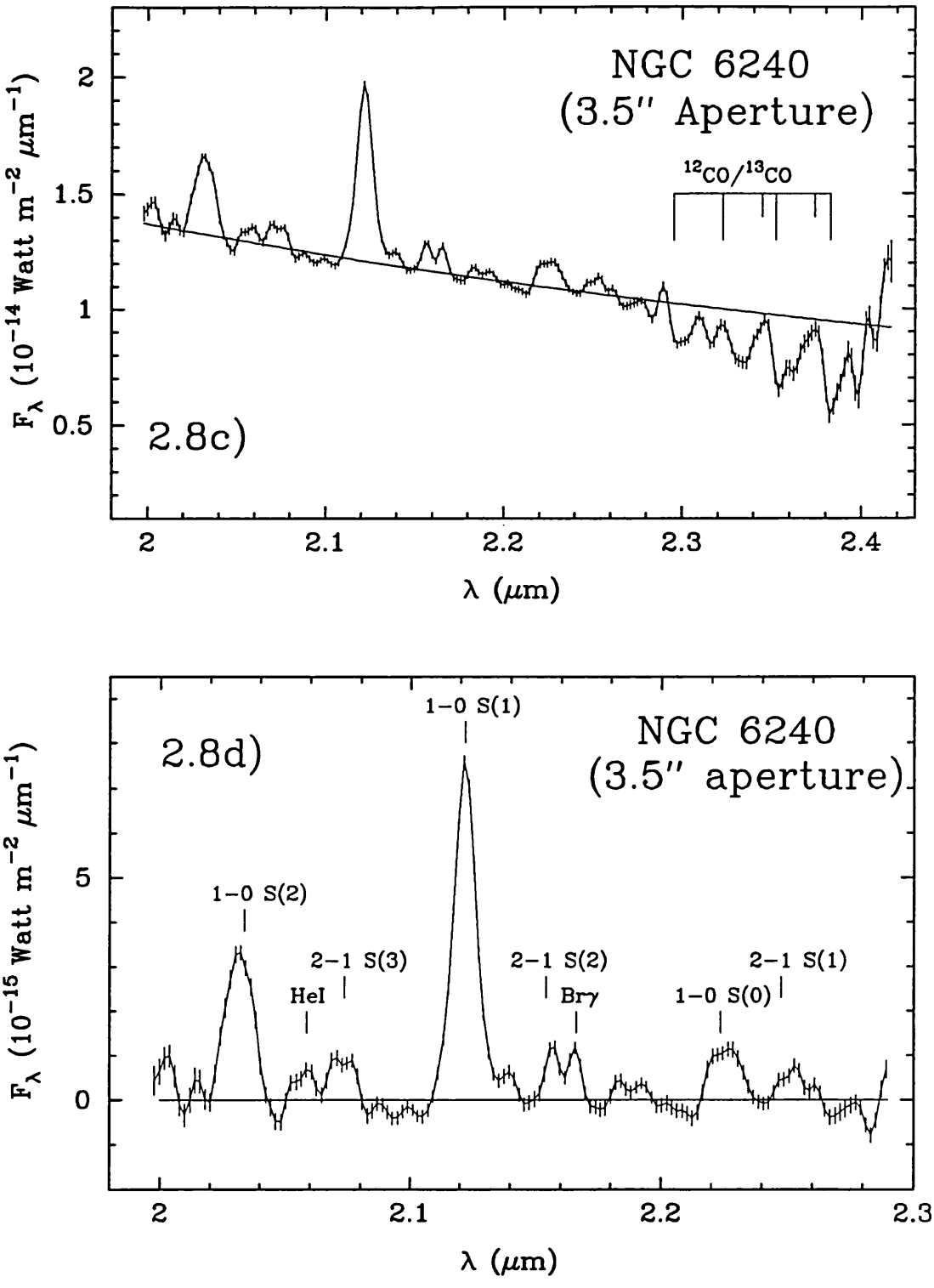

Figure 2.8 a) *K*-window spectra of NGC 6240 obtained at *UKIRT* using a 5″ aperture. b) Continuum-subtracted version of a). c), d) *AAT* spectrum obtained using a 3.5″ aperture. The solid line superimposed on the spectra shown in a) and c) is the best power-law spectrum ($F_\lambda \propto \lambda^\beta$) fitted to the underlying continuum.

that these lines are genuinely detected, we infer line fluxes consistent with those of Lester *et al.* (1988).

The CO band absorption is clearly detected in both spectra. The *UKIRT* spectrum seems to be affected by systematic variations which makes the determination of the continuum slope very difficult. For this reason, the spectroscopic CO index is very uncertain but certainly between 0.19 and 0.27. The continuum slope of the *AAT* spectrum is better defined and yields a spectroscopic CO index of 0.17 ± 0.03 consistent with the lowest value estimated from the *UKIRT* spectrum. The latter value is also consistent with the spectroscopic CO index of 0.18 ± 0.01 inferred from a large aperture CVF spectrum of this galaxy (Joseph *et al.* 1987; Prestwich 1989). Our measurements seem to suggest that the CO band in NGC 6240 is not unusually strong compare with normal galaxies.

This conclusion is somewhat in contradiction with measurements reported before. Lester *et al.* (1988) claimed that the strength of the CO band in their spectrum is as strong as M7-M8 supergiants. An eye estimate of the CO depth from their spectrum yields a spectroscopic CO index of 0.29 ± 0.02, indeed typical of supergiant stars, although not as late as M7-M8 and more like M0 (see Table A.1 in Appendix A). Rieke *et al.* (1985) also reported an unusually strong CO band in their CVF spectra. Their conclusion was based on a comparison with the galaxy M81. Although they quoted the strength of the CO band in magnitudes, they neglected to give details on how this index is defined. Whether they relate (or transform) their CO indices to the Frogel system is not clear. We should mention that any comparison between photometric and spectroscopic CO indices can be misleading. Although there is a good correlation between the two indices (see Appendix A), spectroscopic CO indices are typically 50% stronger than photometric ones.

Thus, the evidence that supergiant stars are contributing significantly to the 2.2 μm continuum in NGC 6240 is marginal, given these contradictory measurements. Higher resolution CO band spectra of this galaxy are needed to fully assess this question.

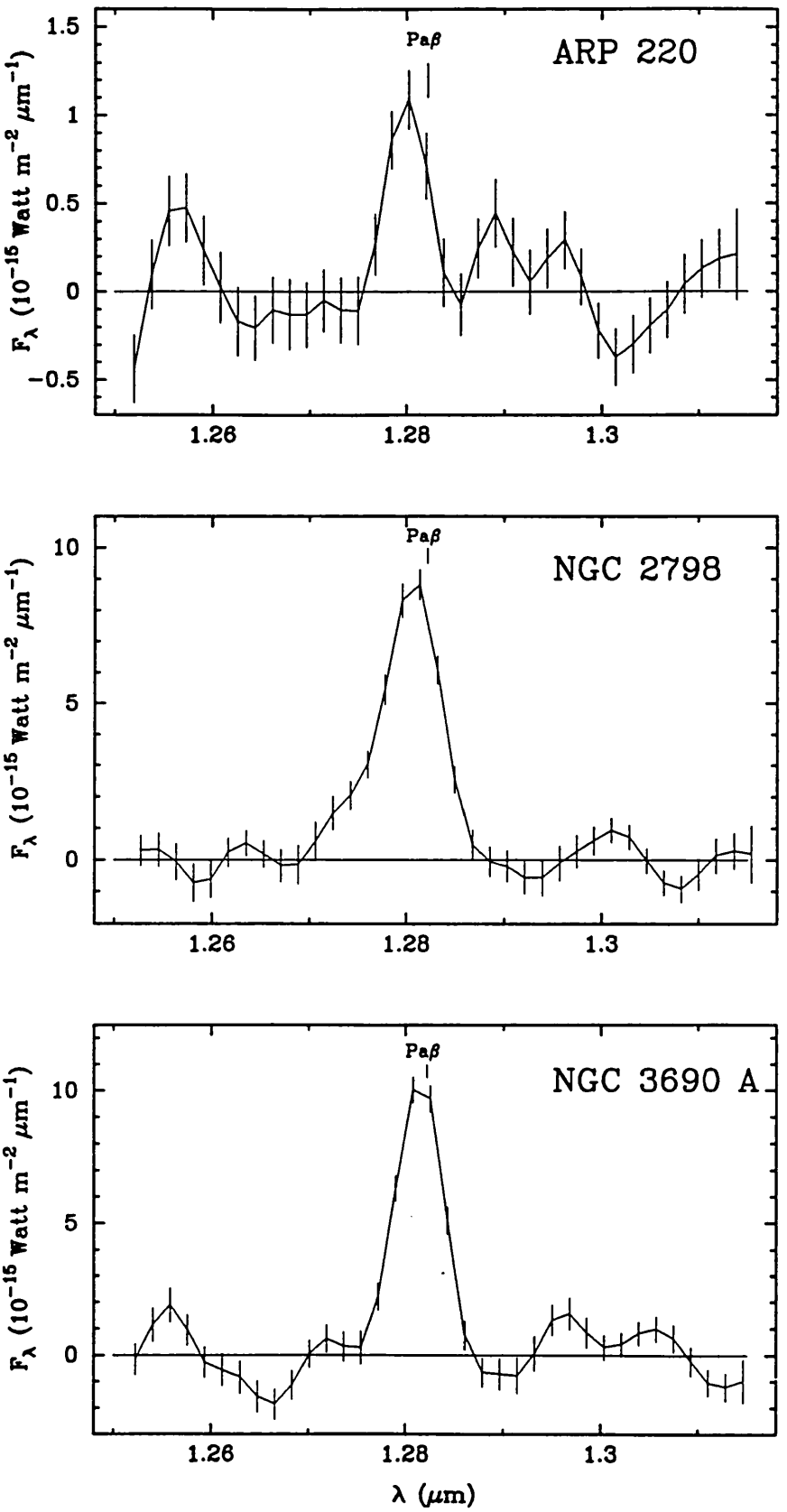
ARP 220
Paβ
NGC 2798
Paβ
NGC 3690 A
Paβ
F_λ (10^{-15} Watt m^{-2} μm^{-1})
λ (μm)
1.26
1.28
1.3

Figure 2.9

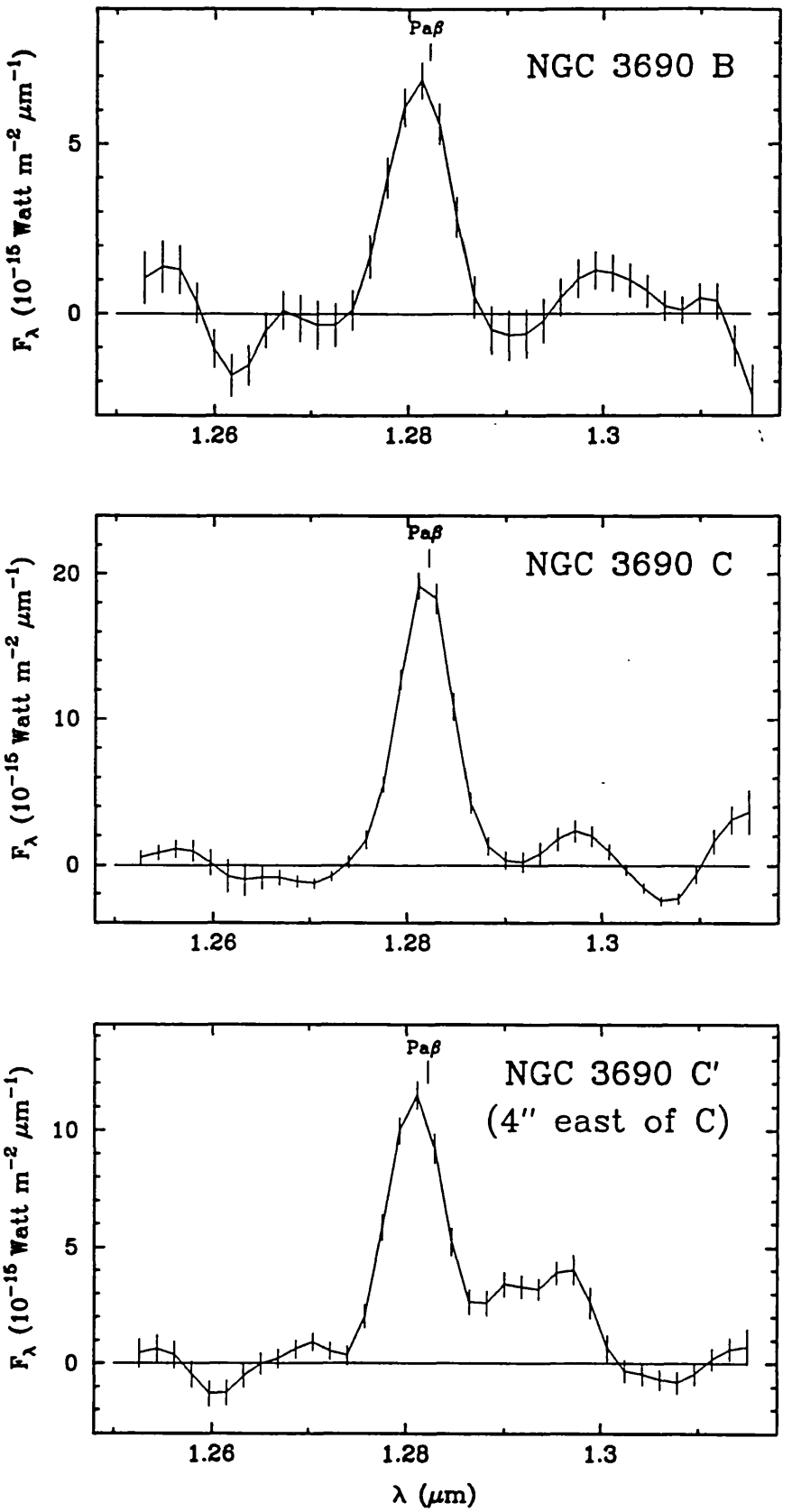

Figure 2.9— Continuum-subtracted spectra of Paβ. The spectra are shown in the restframe, based on redshifts derived from strong K-window emission lines.

Table 2.4
Line Fluxes and Identifications

Observed[1] wavelength (μm)	Integrated Flux (10^{-17} W m^{-2}) observed[2]	dereddened[3]	Identification[4]
	ARP 220		
1.280	0.55±0.10	7.5	Paβ 1.2822
2.033	0.83±0.10	2.7	H_2 1-0 S(2) 2.0338
2.122	3.30±0.15	9.7	H_2 1-0 S(1) 2.1218
2.164	1.18±0.18	3.3	Brγ 2.1661
2.404	3.16±0.47	7.5	H_2 1-0 Q(1) 2.4066
2.421	2.95±0.18	6.9	H_2 1-0 Q(3) 2.4237
2.438	2.21±0.18	5.2	H_2 1-0 Q(4) 2.4375
	MRK 231		
2.121	2.2±0.8	—	H_2 1-0 S(1) 2.1218
2.166	<0.6	—	Brγ 2.1661
	NGC 1614 (Nucleus)		
2.032	1.38±0.15	2.3	H_2 1-0 S(2) 2.0338
2.059	3.35±0.17	5.6	HeI $2^1S - 2^1P^0$ 2.0587
2.076	0.48±0.28	0.8	? H_2 2-1 S(3) 2.0735
2.083	0.69±0.17	1.1	?
2.097	0.55±0.20	0.9	?
2.123	1.06±0.13	1.7	H_2 1-0 S(1) 2.1218
2.164	6.24±0.15	10.0	Brγ 2.1661
2.224	0.54±0.08	0.8	H_2 1-0 S(0) 2.2235
2.247	0.47±0.08	0.7	H_2 2-1 S(1) 2.2477
2.407	1.61±0.18	2.4	H_2 1-0 Q(1) 2.4066
2.413	0.59±0.27	0.9	H_2 1-0 Q(2) 2.4134
2.425	0.80±0.13	1.2	H_2 1-0 Q(3) 2.4237
2.434	0.63±0.12	0.9	H_2 1-0 Q(4) 2.4375
	NGC 1614 (5″ west)		
2.035	0.78±0.25	—	H_2 1-0 S(2) 2.0338
2.080	0.83±0.25	—	?
2.123	1.41±0.25	—	H_2 1-0 S(1) 2.1218
2.225	0.60±0.25	—	? H_2 1-0 S(0) 2.2235
	NGC 2798		
1.281	6.48±0.26	21.2	Paβ 1.2822
2.058	1.34±0.12	2.2	HeI $2^1S - 2^1P^0$ 2.0587
2.121	0.78±0.12	1.3	H_2 1-0 S(1) 2.1218
2.164	2.22±0.11	3.6	Brγ 2.1661
2.404	1.15±0.20	1.7	?H_2 1-0 Q(1) 2.4066
2.423	1.19±0.20	1.8	?H_2 1-0 Q(3) 2.4237
	NGC 3690 C		
1.282	13.2±0.40	43.2	Paβ 1.2822
2.059	1.79±0.12	3.0	HeI $2^1S - 2^1P^0$ 2.0587
2.121	0.81±0.20	1.3	H_2 1-0 S(1) 2.1218
2.166	3.74±0.23	6.0	Brγ 2.1661
	NGC 3690 C′ (4″ east of C)		
1.281	8.58±0.26	—	Paβ 1.2822

Table 2.4—continued

Observed[1] wavelength (μm)	Integrated Flux (10^{-17} W m^{-2}) observed[2]	dereddened[3]	Identification[4]
	NGC 3690 B		
1.281	5.11±0.30	16.7	Paβ 1.2822
2.034	0.46±0.10	0.8	H_2 1-0 S(2) 2.0338
2.059	0.55±0.10	0.9	HeI $2^1S - 2^1P^0$ 2.0587
2.123	0.66±0.13	1.1	H_2 1-0 S(1) 2.1218
2.166	2.00±0.10	3.2	Brγ 2.1661
	NGC 3690 A		
1.281	6.26±0.25	25.9	Paβ 1.2822
2.033	1.22±0.16	2.3	H_2 1-0 S(2) 2.0338
2.059	2.26±0.23	4.2	HeI $2^1S - 2^1P^0$ 2.0587
2.074	0.80±0.30	1.5	? H_2 2-1 S(3) 2.0735
2.124	3.27±0.10	5.9	H_2 1-0 S(1) 2.1218
2.157	0.56±0.11	1.0	? H_2 2-1 S(2)
2.166	3.47±0.10	6.1	Brγ 2.1661
2.224	1.06±0.10	1.8	H_2 1-0 S(0) 2.2235
2.249	0.98±0.10	1.7	H_2 2-1 S(1) 2.2477
2.407	2.74±0.20	4.4	H_2 1-0 Q(1) 2.4066
2.412	1.71±0.20	2.7	H_2 1-0 Q(2) 2.4134
2.423	2.47±0.15	3.9	H_2 1-0 Q(3) 2.4237
	NGC 6240 (5" aperture)		
2.122	12.2±0.5	22.0	H_2 1-0 S(1) 2.1218
2.224	2.12±0.4	3.65	H_2 1-0 S(0) 2.2235
2.250	0.73±0.4	1.24	H_2 2-1 S(1) 2.2477
2.407	9.58±0.2	15.4	H_2 1-0 Q(1) 2.4066
2.414	2.87±0.2	4.59	H_2 1-0 Q(2) 2.4134
2.425	9.66±0.2	15.4	H_2 1-0 Q(3) 2.4237
	NGC 6240 (3.5" aperture)		
2.032	4.2±0.2	7.8	H_2 1-0 S(2) 2.0338
2.057	0.7±0.2	1.3	? HeI $2^1S - 2^1P^0$ 2.0587
2.073	1.3±0.2	2.4	? H_2 2-1 S(3) 2.0735
2.122	9.0±0.2	16.2	1-0 S(1) 2.1218
2.156	1.2±0.2	2.1	? H_2 2-1 S(2) 2.1542
2.166	1.2±0.2	2.1	? Brγ 2.1661
2.226	1.9±0.2	3.3	H_2 1-0 S(0) 2.2235
2.252	1.1±0.2	1.9	H_2 2-1 S(1) 2.2477

[1] Restframe wavelengths as measured from the spectra. The absolute uncertainty on both the absolute and relative wavelength calibration is 0.001—0.002 μm. Laboratory (vacuum) wavelengths are quoted in microns.

[2] The errors are *statistical* only. The absolute calibration is accurate to within 10%.

[3] Based on the average reddening given in Table 2.6 and the extinction curve of Draine (1989).

[4] Unidentified lines are noted by the symbol '?'. Possible identifications are noted by a '?' followed by the suggested transition.

Table 2.5
Continuum Slopes and Absorption line Strengths

Galaxy	Ap (″)	β[1]	NaI (Å)	CaI (Å)	CO_{SP}
ARP 220	5	$-3.0^{+1}_{-0.3}$	< 3	< 3	0.18±0.03
ARP 220 [2]	8	-1.5±0.2	—	—	0.25±0.02
ARP 220 [2]	19	-2.2±0.1	—	—	0.20±0.01
MRK 231	5	0.1±0.2	—	—	—
NGC 1614 (nucleus)	5	-2.9±0.2	3.7±0.4	4.1±0.3	0.31±0.02
" 5″ west	5	-1.0±0.2	—	—	—
NGC 1614 [2]	19	-2.6±0.2	—	—	0.20±0.01
NGC 2798	5	-2.5±0.2	2.4±0.5	3.3±1.0	0.28±0.02
NGC 2798 [2]	19	-2.8±0.2	—	—	0.17±0.01
NGC 3690 A	5	-1.3±0.2	< 3	2.0±0.5	0.21±0.02
NGC 3690 B	5	-1.9±0.2	—	—	—
NGC 3690 C	5	-0.2±0.2	—	—	—
NGC 4565 [2]	8	-3.1±0.2	—	—	0.20±0.01
NGC 4565 [2]	12	-2.8±0.2	—	—	0.20±0.01
NGC 6240	3.5	-2.1±0.3	—	—	0.20±0.02
NGC 6240	5	-3.1±0.4	—	—	0.23±0.04
NGC 6240 [2]	19	-2.8±0.2	—	—	0.18±0.01

[1] Power-law index ($F_\lambda \propto \lambda^\beta$) fitted to the continuum between 2.0 and 2.3 μm.
[2] CVF spectrum taken from Prestwich (1989) (see also Joseph *et al.* 1987).

2.4 Discussion

Combined with the photometry available from the literature, the K-window spectra can be used to draw conclusions about the nature of the physical conditions prevailing in the nuclei of these galaxies.

2.4.1 Extinction

A knowledge of the extinction is a prerequisite for determining the nature of the activity observed in very luminous galaxies. The reddening is very often at the heart of the controversy as to whether the observational properties of a given galaxy are best explained by vigorous star formation or AGN activity.

The reddening estimates given below were derived under the assumption that the extinction is *foreground* only *i.e.* the emitting source is point-like

behind a blanket of dust and gas. In this case, the observed ratio I_2'/I_1' of two lines at wavelength λ_1 and λ_2 with intrinsic ratio I_2/I_1, is simply given by

$$\frac{I_2'}{I_1'} = \frac{I_2}{I_1} \times 10^{-0.4(A_2 - A_1)}, \tag{2.5}$$

where $A_2 - A_1$ is the relative reddening between the two lines in magnitude. The absolute extinction at a wavelength λ was estimated from the reddening curve of Draine (1989), which is given by the following analytical expression

$$\frac{A_\lambda}{E_{J-K}} = 2.4 \left(\frac{\lambda}{\mu m}\right)^{-1.75}, \tag{2.6}$$

where E_{J-K} is the colour excess or the relative extinction between J (1.25 μm) and K (2.2 μm). This expression is valid from 1 to 8 μm and virtually identical to the extinction law of Rieke & Lebofsky (1985).

Our spectra provide three independent methods for determining the reddening. First, the extinction towards the ionized gas can be estimated from the ratio of hydrogen recombination lines, assuming intrinsic ratios predicted from recombination line theory (case B). The weak dependence of the intrinsic ratios on temperature and density ensures that the extinction can be estimated with an accuracy of 10-20%. The extinction was derived from our measurements of Paβ and Brγ assuming an intrinsic Paβ/Brγ ratio of 5.89 ($T_e = 10^4$ K, $n_e = 10^4$ cm^{-3}; Hummer & Storey 1987) and the absolute to relative extinction ratio $A_{2.2}/(A_{Pa\beta} - A_{Br\gamma}) = 0.65$, as derived from Eqn 2.6.

Second, the extinction towards the molecular gas can be estimated from the ratio of the 1-0 S(1) and 1-0 Q(3) transitions of H_2. This method is particularly useful because the lines arise from the same upper level; the extinction derived in this way is independent of the excitation temperature. However, because of the relatively poor atmospheric transmission longward of 2.4 μm, the Q(3) line could be systematically lower than expected. Although we try to correct the atmospheric transmission by ratioing the galaxy spectrum with a standard star, the resolution is too low to resolve the narrow atmospheric features, and thus, a residual fraction of the galaxy emission line can be absorbed. For this reason, the extinction derived from the Q(3) line should be regarded as a *lower limit.* The extinction was derived using an intrinsic 1-0 Q(3)/1-0 S(1) ratio of 0.70 (Geballe, Russell & Nadeau 1982) and $A_{2.2}/(A_{1-0\ S(1)} - A_{1-0\ Q(3)}) = 4.52$.

Finally, the extinction towards the stars can be inferred from the slope of the 2.2 μm continuum, assuming the intrinsic slope is known. As shown in

Appendix A, a power-law index of -3.6 ± 0.2 is a very good approximation for most stars. It can be shown that the power-law index increases by 1.7 for every magnitude of extinction at 2.2 μm. Although the slope of the K spectrum can also be affected by hot-dust contamination, this effect can be quantified by comparison with $H - K$ colours (see Figure 2.10).

The reddenings derived from the three methods are listed in Table 2.6. Except for NGC 2798, the Q(3)/S(1) ratios of H_2 yield reddenings similar to that inferred from other methods. The extinction of 3.8 ± 1.1 magnitudes inferred for NGC 2798 should be regarded with skepticism because the strength of Q-branch in this galaxy is comparable to the amplitude of the bandheads of CO absorption, and thus the 1-0 Q(3) could well have been overestimated (if detected) due to the uncertain continuum. The errors given in Table 7 are statistical only and do not include the uncertainty in placing the continuum level. The same remark applies to NGC 1614. This problem is less serious for the remaining galaxies which have reasonably high line-continuum contrast.

The ratio of Paβ to Brγ observed in ARP 220 yields an extinction at 2.2 μm of 1.8±0.2 mag, somewhat higher than the value of 1.2±0.3 derived from the Q(3)/S(1) ratio but definitely higher than the value of 0.9±0.1 derived from the the slope of the K continuum and the $H - K$ colour excess. Combined with the Brα measurement of DePoy, Becklin & Geballe (1987) our detection of Brγ allows an independent reddening estimate. Using the maximum Brα flux quoted by DePoy *et al.* (1987), we infer an extinction of $A_K \sim 0.5 \pm 0.2$, much lower than the extinction derived from the Paβ/Brγ ratio. The origin of this discrepancy is not clear. Based on these different measurements, we adopt an average extinction of 1.1 magnitude at 2.2 μm for this galaxy.

Our reddening estimates for ARP 220 suggest that the extinction towards the ionized gas is significantly higher, by as much as 10 visual magnitudes, compared with the reddening derived from the 2.2 μm continuum. If real, this effect could be explained if a large fraction of the ionization is due to young massive stars still embedded in their parent molecular clouds. In a such geometry, the 2.2 μm continuum emitted by late-type giants would suffer less extinction since these stars are more likely to be found outside molecular clouds. Alternatively, this effect could be explained by a compact AGN-like ionization source deeply embedded in the core of the galaxy, but the source would have

Table 2.6
Extinction at 2.2 μm

Method	ARP 220 (mag)	NGC 6240 (mag)	NGC 2798 (mag)	NGC 1614 (mag)	NGC 3690 A (mag)	NGC 3690 B (mag)	NGC 3690 C (mag)
Paβ/Brγ	1.8±0.2	—	0.5±0.1	—	0.8±0.1	0.6±0.1	0.4±0.1
Q(3)/S(1)	1.2±0.3	0.6±0.2	3.8±1.1	< 1.1	0.4±0.3	—	—
β, E_{H-K} [1]	0.9±0.1	0.6±0.2	0.1—0.5	0.5±0.1	0.4±0.1	0.4±0.1	0.5—0.9
Adopted	1.1	0.6	0.5	0.5	0.6	0.5	0.5

[1] Extinction calculated from the power-law index ($F_\lambda \propto \lambda^\beta$) of the 2.2 μm spectrum and the $H-K$ colour excess (see also Figure 10). A range of values is given when the contribution from hot dust to the K continuum is uncertain.

to emit very little 2.2 μm continuum radiation, a scenario which is difficult to imagine. Because of its simplicity, we favour the former explanation.

The extinction derived for NGC 6240 (A_K=0.6) is intermediate between the value of 0.3 magnitude adopted by Depoy, Becklin & Wynn-Williams (1986) and the reddening of 1.5 magnitude used by Rieke *et al.* (1985). As shown in Figure 2.10, both the slope of the K continuum and the $H-K$ colour excess exclude any extinction larger than 0.8 magnitude at K. Although the $H-K$ colour of NGC 6240 is ~0.2 magnitude redder than that expected for reddening only, this is not significant given the uncertainty in the slope of the K continuum. As shown in Table 2.5, the power-law index varies from -2.1 to -3.1, depending on the aperture.

2.4.2 Origin of the 2.2 μm continuum

The galaxies discussed in this chapter are known to have high bolometric luminosities compared with normal galaxies. Here, we examine whether this conclusion is also valid for the 2.2 μm luminosity.

The absolute K magnitude of the galaxies, as derived from our spectra, are listed in Table 2.7. To allow a meaningful comparison between the galaxies, we estimated the absolute K magnitude corrected for a linear size of 1 kpc, assuming that the 2.2 μm flux increases linearly with diameter. Such a correction should be valid out to a radius of 2 kpc (Devereux, Becklin and Scoville 1987). There is a clear trend in Table 2.7 that, on average, mergers (ARP 220, NGC

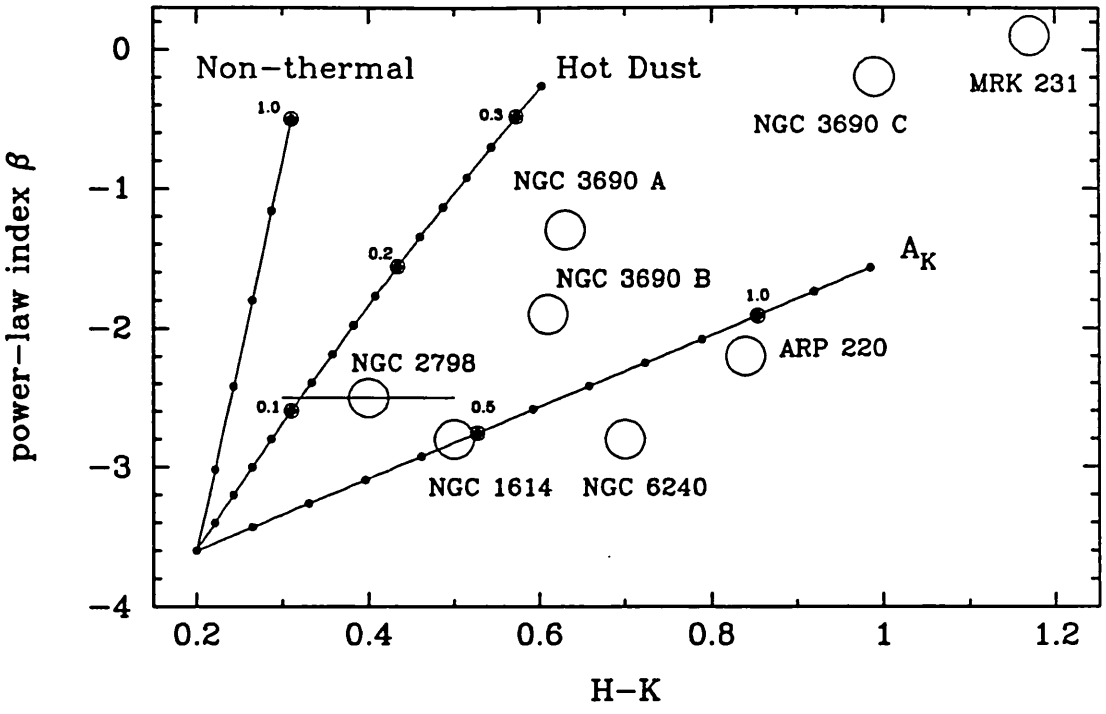

Figure 2.10— Power-law index ($F_\lambda \propto \lambda^\beta$) of the 2.2 μm spectrum against $H-K$ colour. The solid lines shows how the power-law index and the colour of a giant-dominated stellar population ($\beta = -3.6; H-K = 0.2$) are affected by reddening (A_K), contribution to the K continuum by hot dust (grey-body with a temperature of 500 K with emissivity varying linearly with frequency) and an AGN-like non-thermal source ($F_\lambda \propto \lambda^{-0.5}$). The labels on the "hot dust" and "non-thermal" vectors correspond to the fraction of the K continuum contributed by these sources. Source of $H-K$ colours: NGC 3690 (Telesco, Decher & Gatley 1985); ARP 220 (Neugebauer *et al.* 1987); MRK 231 (Sanders *et al.* 1988); NGC 6240 (Rieke *et al.* 1985); NGC 2798 (Joseph *et al.* 1984); NGC 1614 (Neff *et al.* 1990). All measurements were obtained with a 5″ aperture except for NGC 2798 (12″) and NGC 6240 (average of 3.9 and 7.8″).

6240 and NGC 1614) are 3 times brighter than interacting galaxies (NGC 2798, NGC 3690 A and B). However, most of this difference can be accounted for by the fact that the 2.2 μm luminosity of mergers is probably associated with two nuclei. If we decrease their flux by a factor of two, all galaxies (excluding source C of NGC 3690 which is probably an extra-nuclear H II region) yield an average absolute K magnitude of -22.6±0.3 within the central kpc. This value is identical to the cut-off magnitude of the luminosity function of cluster galaxies (Devereux, Becklin and Scoville 1987). In other words, the interacting and

merging galaxies presented in this chapter are not intrinsically more luminous at 2.2 μm than the brightest galaxies in the Virgo cluster.

We should note however that the comparison with the cut-off magnitude is valid as long as the galaxies at the bright end of the luminosity function are "normal" in terms of star-formation activity. Indeed, one cannot exclude the possibility that a large fraction of galaxies near the cut-off magnitude are genuine starbursts which have not been identified before. In support of this hypothesis is the fact that the archetypal starburst galaxy M82 is barely brighter (by only 20%) than the cut-off magnitude (Devereux, Becklin and Scoville 1987). The apparent correlation between the 2.2 μm and 10 μm luminosity (Devereux 1989) also support this hypothesis.

Perhaps the *average* K luminosity of spiral galaxies would provide a more meaningful comparison. Based on the aperture photometry of Devereux, Becklin and Scoville (1987), a typical spiral galaxy in the Virgo cluster has an absolute K magnitude of -20.7 within the central kpc, assuming a distance of 17 Mpc for the cluster. Including only the brightest spirals ($S_{1.65\mu m} > 25$ mJy) brings this estimate up to -21.3 magnitude. Thus, compared with normal spirals, the merging and interacting galaxies discussed in this chapter are intrinsically more luminous at 2.2 μm by a factor of three to six.

Vigorous star formation activity is probably the most likely explanation for this 2.2 μm excess. In all galaxies that were observed beyond 2.3 μm, the CO band absorption was always detected with a strength at least as strong as expected for a normal stellar population. This is very good evidence that the 2.2 μm continuum has a stellar origin. A starburst is expected to produce numerous red supergiants after $\sim$10 million years. Since these stars have stronger CO bands compared with giants (see Appendix A), starburst galaxies should be characterized by unusually strong spectroscopic CO indices. The strength of the CO band observed in galaxies must be corrected for the dilution effect of free-free and hot-dust emission. Because of their featureless K spectrum, any contribution from these sources will systematically decrease the depth of the CO band. The contribution of free-free emission at 2.2 μm can be calculated from the Brγ flux using the Brγ to continuum ratio of Joy and Lester (1988). Although more difficult to quantify, the contribution of hot-dust emission can be judged from the power-law index—$H-K$ colour diagram (see Figure 2.10).

Table 2.7
Observational Properties of the Galaxies

Property	ARP 220	NGC 6240	NGC 2798	NGC 1614	NGC 3690 A	NGC 3690 B	NGC 3690 C
Distance (Mpc) [a]	72	98	23	62		42	
Aperture size (kpc)	1.7	2.4	0.6	1.5		1.0	
m_K(observed)	11.2	10.7	10.7	10.5	11.2	10.8	11.8
M_K [b]	-24.2	-24.9	-21.6	-24.0	-22.5	-22.8	-21.8
$M_K(0)$ [c]	-23.6	-23.9	-22.2	-23.6	-22.5	-22.8	-21.8
$F_K^{HD}(\%)$ [d]	0	0	5	0	15	10	25
$F_K^{ff}(\%)$ [d]	2	1	2	4	4	2	8
CO_{SP}^{corr} [e]	0.18(3)	0.23(4)	0.30(2)	0.31(2)	0.27(2)	—	—
$W_{Br\gamma}$(Å) [f]	-11(2)	-7(2)	-10(1)	-24.7(7)	-29.2(9)	-13.5(7)	-49(3)
$\log L_{IR}(L_\odot)$ [g]	11.93	11.63	10.26	11.51	11.49	11.10	10.92
$\log N_{Lyc}(s^{-1})$ [h]	54.28	53.98	53.32	54.63	54.07	53.79	54.07
$\log N_{Lyc}/L_{IR}$	42.35	42.35	43.06	43.12	42.58	42.69	43.15

Note—All measurements are for a 5″ aperture. When given, the number in parenthesis corresponds to the uncertainty of the last digit.

[a] $H_0 = 75\ km\ s^{-1}\ Mpc^{-1}$.

[b] Absolute K magnitude corrected for extinction. Source of uncorrected magnitudes: ARP 220 (Neugebauer *et al.* 1987); NGC 6240 (this work averaged with the magnitude of DePoy *et al.* 1986); NGC 2798 and NGC 1614 (this work); NGC 3690 (Telesco, Decher & Gatley 1985).

[c] Absolute K magnitude corrected for a linear size of 1 kpc.

[d] Percentage of the K continuum contributed by hot dust (F_K^{HD}) and free-free emission (F_K^{ff})

[e] Spectroscopic CO index corrected for the contribution of featureless K continuum associated with hot dust and free-free emission.

[f] Observed Brγ equivalent width in Å.

[g] Log of the far-infrared luminosity, estimated from the following sources. ARP 220: assuming that 70% of total *IRAS* luminosity is falling within the central 5″, as suggested from a comparison between *IRAS* and ground-based 20 μm measurements (*cf.* Rieke *et al.* 1985); NGC 6240: extrapolated from the 10 μm luminosity (see text) using the extinction-corrected 10 μm measurements of DePoy *et al.* (1986); NGC 2798 and NGC 1614: from extrapolation of the extinction-corrected 10 μm measurements of Wright *et al.* (1988); NGC 3690 A, B and C: assuming that 60% of total *IRAS* luminosity is associated with source A, as suggested by the ground-based far-infrared scanning observations of Joy *et al.* (1989); the rest of the *IRAS* luminosity was distributed to sources B and C according to their relative 20 μm fluxes (Joy *et al.* 1989).

[h] Log of the ionization rate, corrected for extinction.

The percentage of the K continuum contributed by these sources are given in Table 2.7 along with the corrected spectroscopic CO indices.

On can see that three out of five galaxies have spectroscopic CO indices of $\sim$0.3 *i.e.* 0.1 magnitude stronger than expected for normal galaxies. The relatively small CO band in ARP 220 and perhaps NGC 6240 is not necessarily inconsistent with the starburst hypothesis. Given the short lifetime of the red supergiant phase, the enhanced CO band in a galaxy could be very short if the star formation rate is rapidly decreasing. In this scenario, the K luminosity would still be enhanced due to the build up of intermediate-mass stars leaving the main sequence, provided that the burst is sufficiently old. Thus, one could explain (qualitatively) the small CO band and the 2.2 μm excess with a relatively old starburst.

The interpretation of the strength of CO band is further complicated by the fact that it is aperture dependent. As seen in Table 2.5 for NGC 2798 and NGC 1614, the strength of the CO band in the large (19″) aperture is normal, suggesting that the red supergiants responsible for the strong CO band are fairly concentrated in the nucleus. It is worthwhile to note that the 19″ aperture in NGC 2798 correspond to roughly to the same physical area as the 5″ aperture projects at the distance of NGC 6240. This shows that one must be careful in interpreting the strength of the CO band when little spatial information is available.

The stellar origin of the 2.2 μm continuum is also supported by the observed power-law index and $H-K$ colour of the galaxies. As shown in Figure 2.10, the position in this diagram of the ultra-luminous *IRAS* galaxies NGC 1614, NGC 6240 and ARP 220 can be easily explained by reddening only. Sanders *et al.* (1988) argued that ultra-luminous *IRAS* galaxies are the initial dust-enshrouded stage of a quasar. If true, the K continuum should be dominated by non-thermal emission. Our observations are inconsistent with that interpretation, at least for the three galaxies mentioned above. If a non-thermal source is present in the core of these galaxies, the power-law index—$H-K$ diagram suggests that its contribution at 2.2 μm is probably no more than 10% (perhaps 20% for ARP 220). MRK 231 is the only galaxy for which its position in Figure 2.10 could be explained by a combination of relatively high extinction ($A_K \approx 1.4$) and substantial ($\sim$50%) non-thermal emission.

Although the deviation of NGC 3690 A, B and C from the reddening vector in Figure 2.10 could also be explained by a contribution from a non-thermal source, it is more likely that the K continuum is affected by hot dust ($T_{dust} \approx 500\ K$) heated by young massive stars. Unlike MRK 231, Brγ is very prominent in this galaxy, suggesting the presence of numerous H II regions. From their position in Figure 2.10, we estimate that the fraction of the K continuum contributed by hot-dust emission is 10, 15 and 25% for source A, B and C, respectively. These numbers are slightly less but basically in good agreement with those of Telesco, Decher and Gatley (1985) derived from a similar analysis of JHK colours.

2.4.3 Ionization continuum

The production rate of Lyman continuum photons N_{Lyc} can be calculated from the strength of Brγ. From recombination theory (case B), 70 Lyman continuum photons are required to produce one Brγ photon. Assuming that the ionization has a stellar origin, the number of Lyman continuum photons is directly proportional to the present number of high-mass stars in the system and hence, given an initial mass function (IMF), the star formation rate. For a Scalo (1986) IMF extending from 0.1 to 60 $M_\odot$, the star formation rate ψ is given by

$$\psi = 3.44 \left[\frac{N_{Lyc}}{10^{53}\ s^{-1}} \right] \quad M_\odot\ yr^{-1} \tag{2.7}$$

(Puxley 1988). The number of ionizing photons given in Table 2.7 implies star formation rates between 7 $M_\odot\ yr^{-1}$ for NGC 2798 and 147 $M_\odot\ yr^{-1}$ for NGC 1614, with 50 being a typical value. For comparison, the star formation rate within a region of 1 kpc in diameter of the solar neighbourhood is $\sim$0.003 $M_\odot\ yr^{-1}$ (*cf.* Miller & Scalo 1979). It is easy to show that such high star-formation rates cannot be sustained for a long period. An upper limit of the mass in these system can be estimated from the absolute K magnitude (*cf.* Devereux, Becklin & Scoville 1987). Within 1 kpc in diameter, the total mass is of the order of $10^{10}\ M_\odot$. Assuming that 10% of this mass is in gaseous[1] then the star formation rates above imply that all this material will be exhausted in $10^7 - 10^8$ years.

[1] Although typical of normal spiral galaxies, this fraction is probably severely underestimated in ARP 220 because of its unusually high molecular gas content (*cf.* §2.3.1)

If the duration of the burst is very short, one would expect the observational properties of galaxies to vary with time. A useful age indicator is provided by the ratio of the ionization rate to the bolometric luminosity. This ratio should be roughly constant in the early stage of the burst when both the ionization rate and the bolometric luminosity are dominated by young massive stars. It should decrease later because of lower ionization and greater contribution of low-mass stars to the bolometric luminosity. An estimate of the bolometric luminosity within a 5″ aperture may be estimated either from the comparison of ground-based and *IRAS* 20-100 μm observations or from the integrated IR luminosity derived from 10 μm fluxes available from the literature (see Table 2.7), assuming $L_{IR} = 15\, L_{10\mu m}$ (*cf.* Scoville *et al.* 1983; Telesco & Gatley 1984).

As shown in Table 2.7, $\log N_{Lyc}/L_{IR}$ varies appreciably (a factor of five) from one galaxy to another, suggesting that the galaxies are not in the same evolutionary stage. The small ratio inferred for NGC 6240 is well known and led Depoy, Becklin and Wynn-Williams (1986) to conclude that the bolometric luminosity of this galaxy is probably generated by an AGN. This interpretation is valid as long as the comparison between the observational properties of NGC 6240 with that of a "typical" starburst is justified. The small ionization to bolometric ratio could equally be explained (qualitatively) if the age of the burst in NGC 6240 is significantly older than most starburst galaxies. Detailed modelling is needed to determine whether such a scenario is possible in practice.

The equivalent width of Brγ, denoted in Table 2.7 as $W_{Br\gamma}$, is another age indicator since this quantity is proportional to the ratio of massive to cool stars. Because the stellar lifetime decreases with mass, $W_{Br\gamma}$ should decrease with time. The Brγ equivalent width is also expected to vary from one galaxy to another if there is a significant contribution from a pre-existing old stellar population to the K continuum. Given these unknown variables it is not surprising that the Brγ equivalent is observed to vary by a factor of five (see Table 2.7). However, the scatter is reduced by a factor of ~ 2 when NGC 3690 C is excluded. Since this source is probably an extra-nuclear H II region, its continuum should be less affected by a pre-existing stellar population. The fact that the largest equivalent width was found in this source is perhaps an indication that the 2.2 μm continuum of the other galaxies is indeed significantly contaminated by an old stellar population.

2.5 Summary and Conclusions

We have presented new near-infrared spectra of interacting systems NGC 2798, NGC 3690 and the luminous merging galaxies NGC 6240, ARP 220, NGC 1614 and MRK 231. In general, the spectra are dominated by Brγ, He Iλ2.06μm and molecular hydrogen emission. The relative strength of these lines varies considerably from one galaxy to another. We report the detection of molecular hydrogen in MRK 231. The H_2 spectra of NGC 1614 and IC 694 (NGC3690 A) show evidence for non-thermal or fluorescent excitation.

The extinction at 2.2 μm has been estimated using three independent methods which sample the stellar continuum, the ionized and molecular gas. In general, the three methods yield consistent values, typically around A_K =0.5–0.6 mag. We report the detection of Paβ in ARP 220. The ratio of this line with Brγ yields an extinction of 1.8 ± 0.2 mag at 2.2 μm, substantially higher than the value of 0.9 ± 0.2 inferred from the slope of the K continuum and the $H-K$ colour.

When normalized to the same aperture size, the 2.2 μm luminosity of mergers is, on average, approximately a factor of three brighter than the individual members of interacting systems. Most of this difference can be accounted for if the continuum of mergers arises from two nuclei. Their K magnitudes are typically as bright as the cut-off magnitude of the luminosity function of normal galaxies but more luminous than *average* spirals by a factor between three to six.

In all galaxies observed beyond 2.3 μm, the stellar CO band absorption was detected, usually with a strength as strong as expected for a normal giant-dominated stellar population. NGC 1614, NGC 2798 and IC 694 show clear evidence for an unusually strong CO band. Significant spatial variation are noted in the former two. The strength of the CO band provides strong evidence that the 2.2 μm luminosity of these galaxies has a stellar origin. If an AGN-like source is present in these galaxies, its contribution at 2.2 μm is probably no more than 20%. A vigorous episode of star formation provides the most likely mechanism for explaining their near-infrared observational properties.

Chapter 3

The HeI2.06/Brγ Ratio in Starburst Galaxies — an Objective Constraint on the Upper Mass Limit

3.1 Introduction

The initial mass function (IMF) *i.e.* the number of stars formed per unit mass, is a fundamental ingredient of star formation theories. The knowledge of the shape of this function is a prerequisite to understand galaxy evolution and interpret the properties of galaxies experiencing vigorous star formation activity (starburst). The IMF is usually described by a power-law of the mass ($\psi \propto m^{-\alpha}$) and can be inferred from the "present day mass function" derived from star counts in clusters (Mateo 1988) or in the solar neighbourhood (*e.g.* Miller-Scalo 1979). For instance, the Salpeter IMF (1955) is described by an index $\alpha = 2.35$ whereas Scalo (1986) uses a three-segment power-law, the upper end of the IMF ($0.7\ M_\odot \leq m \leq 100\ M_\odot$) having an index $\alpha \approx 2.85$.

Whether the solar neighbourhood IMF is universal and whether it varies with physical conditions (metallicity, star formation rate) are still open questions (see Scalo 1986, 1987 and Zinnecker 1987 for reviews). However, there is growing evidence that the IMF is "unusual" in starburst galaxies. Indeed, observations in the ultraviolet (*e.g.* Sekiguchi & Anderson 1987), optical (*e.g.* Kennicutt *et al.* 1987) and infrared (Rieke *et al.* 1980, Wright *et al.* 1988, Puxley *et al.* 1989) suggest that these galaxies are deficient in low-mass stars, or

equivalently, that the lower mass limit, m_l, is unusually high. Scalo (1989) has reviewed the evidence for a truncated IMF in starburst galaxies and pointed out that the conclusion above is valid only if the upper mass limit, m_u, is not significantly higher than 80-100 $M_\odot$. Unfortunately, the upper mass limit is probably the least constrained parameter of the IMF and only a few studies (Puxley *et al.* 1989; Olofsson 1989) have provided quantitative constraints on this parameter.

In this chapter, we present a new and objective method for constraining the upper mass limit of the IMF which makes use of near-infrared (IR) recombination lines, more specifically, the He Iλ2.06μm/Brγ emission line ratio. New observations and data from the literature are combined to show that the upper mass limit inferred in some galaxies is relatively low. The new data are presented in section 3.2. The dependence of the He Iλ2.06μm/Brγ ratio on spectral type is derived in 3.3 and its implications on the upper mass limit of the IMF are discussed in 3.4. The main conclusions of this study are summarized in 3.5.

3.2 Observations and Results

Near-infrared spectra of star-forming galaxies were obtained on the 3.8 meter *United Kingdom Infrared Telescope UKIRT*. These data were obtained as part of an observing program to determine the IR spectroscopic properties of starburst galaxies. A more detailed presentation of the data is given in Chapter 2. The sample includes interacting, merging and dwarf galaxies for which IR "activity" has been identified in previous studies, either from photometric or spectroscopic observations. Although these galaxies differ in morphologies and bolometric luminosities, they all exhibit strong strong Brγ emission in their K-window spectra.

Except for He 2-10, all galaxies were observed during two observing trips in February and May 1990. The K-window spectra were obtained with CGS2, the common-user seven-element cooled grating spectrometer of *UKIRT*. A circular aperture of 5″ was used for all sources and centred on the galaxy, either by peaking up the signal from the seven detectors or by setting the aperture on the optical nucleus as seen in the TV camera of the guiding system. The telescope was chopped between the target and the sky every grating position at a frequency of $\approx$ 1 Hz with chop throws of 30″. The spectra were sampled every half a resolution element.

In order to take out periodic ripples due to the imperfect differential response of the detectors, the spectra were smoothed with three passes in a 1-2-1 triangular filter [1] (see Chapter 2 for details). Although, this degrades the original resolution by about a factor of two, this procedure insures that no systematics are present in the spectra. A resolving power ($\lambda/\Delta\lambda$) of 300 ± 30 was derived from the width of the Brγ as observed in absorption and emission in early-type stars and galaxies.

Atmospheric absorption features were corrected by dividing the galaxy spectra with the spectrum of a standard star obtained at a similar air mass ($< 0.1 - 0.2$). Early-type stars were used for that purpose since they have a featureless continuum except for the Brγ absorption at 2.1661 μm which was removed by interpolating across the raw spectrum. The spectra were then multiplied by a black-body spectrum with effective temperature and absolute flux specified by the spectral type and the K magnitude of the standard star.

The observations of He 2-10 were made in November 1989 on UKIRT using CGS2 with a 5″ aperture centred on the optical nucleus. The spectrum consisted of 6 coadds, each of 4 samples of 1 second at each grating position. The scans were made in stare mode, running through each grating position on the source and then offsetting 57″ east or west to repeat the scan. The data were sampled at 1/3 of a resolution element with a resolving power of ~700. The spectrum of the galaxy was ratioed with BS3425 (K5III), both obtained at a similar air mass. Because of its higher quality, the spectrum of He 2-10 was not corrected by the smoothing technique described above.

The spectra are shown on a relative scale in Figure 3.1. They were shifted to their restframes using the redshift derived from the position of Brγ in the spectrum. Observed and extinction-corrected He Iλ2.06μm/Brγ ratios are given in Table 3.1. Note that the error quoted for these ratios includes the uncertainty in placing the continuum level. Data for other galaxies, taken from the literature, are also included.

As shown in Figure 3.1, most galaxies have strong He Iλ2.06μm lines in their spectra. The He Iλ2.06μm/Brγ ratios are typically between 0.3 and 0.6. Since the ionization potential of helium (24.6 eV) is twice that of hydrogen, the detection of the He Iλ2.06μm line shows without doubt that an intense and hot UV field is present in these nuclei. Assuming that the ionization has a

[1] Three passes are equivalent to a single pass with a window of 7 pixels.

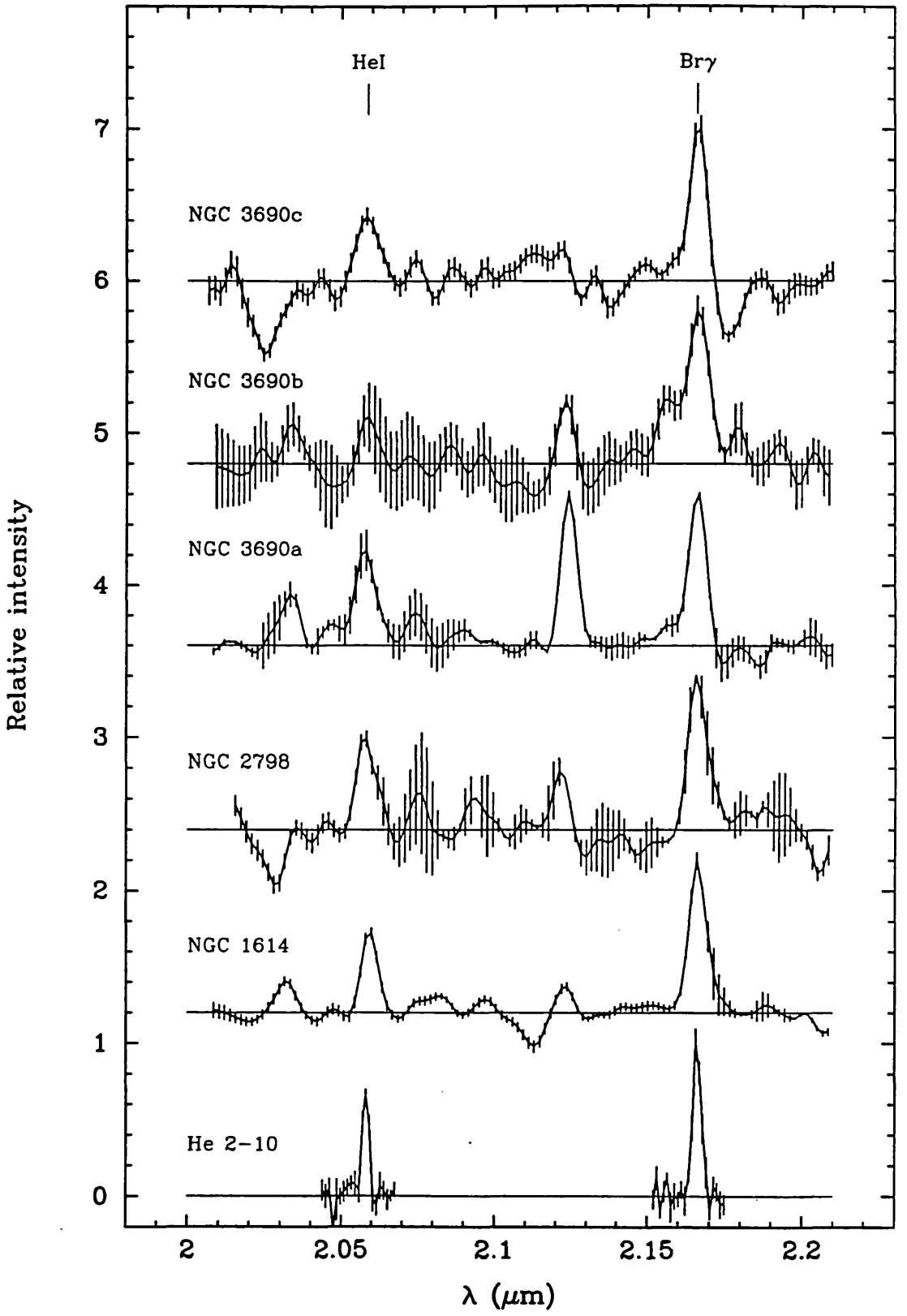

Figure 3.1— K-window spectra of star-forming galaxies. The spectra are shown in their restframe on a relative intensity scale, separated from each other by a unit of 1.2. The spectra have been continuum-subtracted and normalized such that Brγ has a peak intensity of unity.

Table 3.1

HeIλ2.06μm/Brγ Ratio in Starburst Galaxies

Galaxy name	D [1] (Mpc)	Ap ($''$)	A_V [2] (mag)	HeI/Brγ observed	HeI/Brγ dereddened	m_u ($M_\odot$)	Ref [3]
He 2-10	15	5	3	0.64±0.09	0.66	$82^{\geq 18}_{-48}$	1
NGC 253	3	7.8	5	0.38±0.08	0.40	27^{+4}_{-2}	2
M82	3	3.8	5	0.34±0.02	0.35	26 ± 0.5	3
NGC 1614	62	5	5	0.55±0.05	0.56	$33^{\geq 67}_{-3}$	1
NGC 2798	23	5	5	0.60±0.08	0.63	$49^{\geq 51}_{-17}$	1
NGC 3256 A [4]	37	3.5	5.5	0.33±0.04	0.35	26^{+2}_{-1}	4
NGC 3256 B [4]	37	3.5	5.5	0.71±0.15	0.75	> 38	4
NGC 3690 A	42	5	6	0.65±0.08	0.69	> 41	1
NGC 3690 B	42	5	5	0.28±0.05	0.29	25^{+3}_{-2}	1
NGC 3690 C	42	5	5	0.48±0.05	0.50	30^{+12}_{-2}	1

[1] Assuming $H_0 = 75\ km\ s^{-1}\ Mpc^{-1}$.

[2] Source of visual extinction: He 2-10 (D'Odorico, Rosa & Wampler 1983); NGC 253 (Doyon, Joseph & Wright 1991); M82 (Lester *et al.* 1990); NGC 1614, NGC 2798 and NGC 3690-IC 694 (Chapter 2); NGC 3256 (Chapter 6).

[3] Source of HeIλ2.06μm/Brγ ratios: (1) this work; (2) Rieke, Lebofsky & Walker 1988; (3) Lester *et al.* 1990; (4) Chapter 6.

[4] NGC 3256 A: nucleus; NGC 3256 B: average of two positions 5$''$ east and south of the nucleus.

stellar origin, then the UV photons must be produced by a population of young OB stars. The strong HeIλ2.06μm/Brγ ratios provide strong evidence that a episode of vigorous star formation activity is taking place in these galaxies.

Because the ionization rate has a strong dependence on effective temperature (T_{eff}), the HeIλ2.06μm/Brγ ratio, which is basically determined by the ratio of the production rate of UV photons with energy greater than 24.6 and 13.6 eV (the ionization potential of helium and hydrogen, respectively), will also have a strong dependence on spectral type. In principle, this property can be used to constrain the relative number of massive stars in the stellar population of a starburst, and this in turn, can be translated into a constraint on the upper

mass limit of the IMF. However, in order to quantify this constraint, one must first determine the theoretical relationship between the He Iλ2.06μm/Brγ ratio and T_{eff}, and also investigate the possible physical processes that could affect this ratio. This is the subject of the following section.

3.3 The HeI2.06/Brγ Ratio in H II Regions

3.3.1 The He I2.06/Brγ ratio *vs* T_{eff}

Above a certain critical effective temperature T^c_{eff}, the He Iλ2.06μm/Brγ ratio is saturated since the radii of the He^+ and H^+ zones, R_{He+} and R_{H+}, are coincident. In such case, the ratio is independent of the effective temperature of the star and is given by

$$\frac{I_{He\,I2.06}}{I_{Br\gamma}} = \frac{N_{He}}{N_H} \times \frac{\lambda_{Br\gamma}}{\lambda_{He\,I2.06}} \times \frac{\alpha^{eff}_{He\,I2.06}}{\alpha^{eff}_{Br\gamma}} \qquad \text{if} \qquad R_{He+} = R_{H+} \tag{3.1}$$

where N_{He}/N_H is the helium abundance by number. $\alpha^{eff}_{He\,I2.06}$ and $\alpha^{eff}_{Br\gamma}$ are the effective recombination coefficients of the He Iλ2.06μm and Brγ transitions, respectively. Below T^c_{eff}, the line ratio is essentially determined by the relative volume of the He^+ and H^+ spheres. Using Eqn. 2.28 of Osterbrock (1989) relating R_{He+}/R_{H+} with the ionization rates and taking into account the fact that hydrogen contributes to the electron density in the He^+ zone, it is easy to show that, below T^c_{eff}, the line ratio is given by:

$$\frac{I_{HeI2.06}}{I_{Br\gamma}} = \frac{\lambda_{Br\gamma}}{\lambda_{HeI2.06}} \times \frac{\alpha^{eff}_{He\,I2.06}}{\alpha^{eff}_{Br\gamma}} \times \frac{\alpha_B(H^+)}{\alpha_B(He^+)} \times \frac{N^{He}_{Lyc}(T_{eff})}{N^{H}_{Lyc}(T_{eff})} \qquad \text{if} \qquad R_{He+} < R_{H+} \tag{3.2}$$

where $\alpha_B(H^+)$ and $\alpha_B(He^+)$ are the total recombination coefficients for hydrogen and helium in the Case B approximation. $N^{He}_{Lyc}(T_{eff})$ and $N^{H}_{Lyc}(T_{eff})$ are the production rates of ionizing photons with energy greater than 24.6 and 13.6 eV respectively for a star with effective temperature T_{eff}. It can be shown that the He^+ and H^+ zones are coincident when the following criteria is satisfied

$$\frac{N^{He}_{Lyc}(T_{eff})}{N^{H}_{Lyc}(T_{eff})} > \frac{\alpha_B(He^+)}{\alpha_B(H^+)} \times \frac{N_{He}}{N_H} \tag{3.3}$$

The effective recombination coefficient $\alpha^{eff}_{He2.06}$ is the only quantity which is not directly available from the literature. However, this coefficient can be indirectly estimated from other line ratios using the following expressions:

$$\alpha^{eff}_{HeI2.06} = \alpha^{eff}_{\lambda 4471} \times \frac{I_{HeI2.06}}{I_{\lambda 4471}} \times \frac{\lambda_{HeI2.06}}{\lambda_{4471}} \qquad (3.4a)$$

$$\alpha^{eff}_{HeI2.06} = \alpha^{eff}_{Br\gamma} \times \frac{N_H}{N_{He}} \times \frac{I_{HeI2.06}}{I_{\lambda 4471}} \times \frac{I_{H\beta}}{I_{Br\gamma}} \times \frac{I_{\lambda 4471}}{I_{H\beta}} \times \frac{\lambda_{HeI2.06}}{\lambda_{Br\gamma}} \qquad (3.4b)$$

where $I_{\lambda 4471}$ is the intensity of a triplet transition of helium at 4471 Å. Treffers *et al.* (1976) have estimated that the ratio $I_{HeI2.06}/I_{\lambda 4471}$ should be equal to 0.65 if the nebula is optically thick in the $2^1P - 1^1S$ resonant transition of helium at 584 Å (see Figure 3.3). Taking $\alpha^{eff}_{\lambda 4471}$ from Brocklehurst (1972)[1] for an electron temperature and density of 10^4 K and 10^4 cm^{-3}, respectively, Eqn. 3.4a yields $\alpha^{eff}_{HeI2.06} = 4.03 \times 10^{-14}$ cm^3 s^{-1}. For the same conditions, the $I_{H\beta}/I_{Br\gamma}$ ratio is predicted to be 36.4 under Case B (Hummer & Storey 1987). Following Wynn-Williams *et al.* (1978), the $I_{4471}/I_{H\beta}$ ratio can be empirically determined from observations of H II regions. This ratio is typically 0.04 in optically visible H II regions (Peimbert & Torres-Peimbert 1971, as quoted by Wynn-Williams *et al.*). Taking $\alpha^{eff}_{Br\gamma}$ as derived from Hummer & Storey (1987) and assuming an helium abundance of 10%, typical for Galactic H II regions, Eqn. 3.4b gives $\alpha^{eff}_{HeI2.06} = 3.36 \times 10^{-14}$ cm^3 s^{-1} which is slightly lower than the value predicted from Eqn. 3.4a. This probably reflects the uncertainty in this coefficient. We therefore adopt the average of the two values and assign an uncertainty of ~10% on $\alpha^{eff}_{HeI2.06}$.

This coefficient must be corrected for the fact that not all resonant 584 Å photons are recycled by helium. Although these photons are unlikely to escape the nebula, they can ionize hydrogen and this process will compete with the scattering due to helium. As shown by Thompson and Tokunaga (1980), the absorption cross section of helium is 2×10^4 higher than the photoionization cross section of hydrogen at 584 Å. Taking into account the fact that helium is less abundant than hydrogen, 584 Å photons have a probability of 0.0005 of being destroyed by hydrogen atoms. Since the 2^1P state have a probability of 0.001 of decaying to the 2^1S, only 2/3 of the helium atoms in the 2^1P state

[1] Brocklehurst gives the coefficient for Case A only, and we assume the same coefficient for Case B. This should be a reasonable approximation since λ4471 Å is weakly affected by optical depth effects.

will give rise to a 2.06 μm photon. Thus, the effective recombination coefficient $\alpha^{eff}_{HeI2.06}$ must be multiplied by this factor.

Finally, using $\alpha_B(H^+)$ from Hummer and Storey (1987) and $\alpha_B(He^+)$ from Osterbrock (1989) for the same temperature and density as above, Eqn. 3.1 and 3.2 are reduced to

$$\begin{aligned} \frac{I_{He\,I2.06}}{I_{Br\gamma}} &= 7.0 \times \frac{N_{He}}{N_H} \qquad \text{if} \qquad R_{He+} = R_{H+}, \\ \frac{I_{He\,I2.06}}{I_{Br\gamma}} &= 6.6 \times \frac{N^{He}_{Lyc}(T_{eff})}{N^{H}_{Lyc}(T_{eff})} \qquad \text{if} \qquad R_{He+} < R_{H+}. \end{aligned} \tag{3.5}$$

Puxley (1988) (see also Puxley, Hawarden & Mountain 1990) have integrated Kurucz (1979) atmosphere models, using the compilation of stellar properties of Landolt-Börnstein (1982), to calculate the ionization rate $N^H_{Lyc}(T_{eff})$. For consistency, we calculated the ionization rates $N^{He}_{Lyc}(T_{eff})$ in the same way as prescribed by Puxley (1988). These numbers are compiled in Table 3.2 for stars with effective temperatures ranging from 8000 to 50000 K.

The dependence of the He Iλ2.06μm/Brγ line ratio on effective temperature in shown in Figure 3.2. For a Galactic abundance, the He^+ and the H^+ zones are coincident near a temperature of ~38000 K corresponding to an O7V star (Landolt-Börnstein 1982). It is also shown that the helium abundance affects the He Iλ2.06μm/Brγ ratio only when the temperature is lower than $\sim$ 38000 K. Note that the apparent discontinuity at this temperature is just an artefact of the simplistic approach used in calculating the line ratio. In reality, the ratio should turn over smoothly near the point where R_{He+} equals R_{H+}. However, a more detailed treatment of this problem using radiative transfer is not likely to affect the main result of these simple calculations that *the* He Iλ2.06μm/Brγ *line ratio is very sensitive to spectral type.*

3.3.2 Collisional excitation

Beyond a critical density of $(3-5) \times 10^3$ cm^{-3}, the 2^3S metastable level (see Figure 3.3) is preferentially collisionally de-excited to the 2^1S and 2^1P levels rather than by the forbidden single-photon decay at 19.8 eV (626 Å). This, of course, enhances the strength of 2.06 μm transition. Osterbrock (1989) estimates that 17% of all the captures to 2^3S lead to 2^1P. Since 3/4 of all helium recombinations end up to 2^3S and approximately 2/3 of the singlet captures (1/4 of all recombinations) lead to 2^1P, compared with the low-density regime, collisional excitation will overpopulate the 2^1P level by a factor 1.8. Thus, if

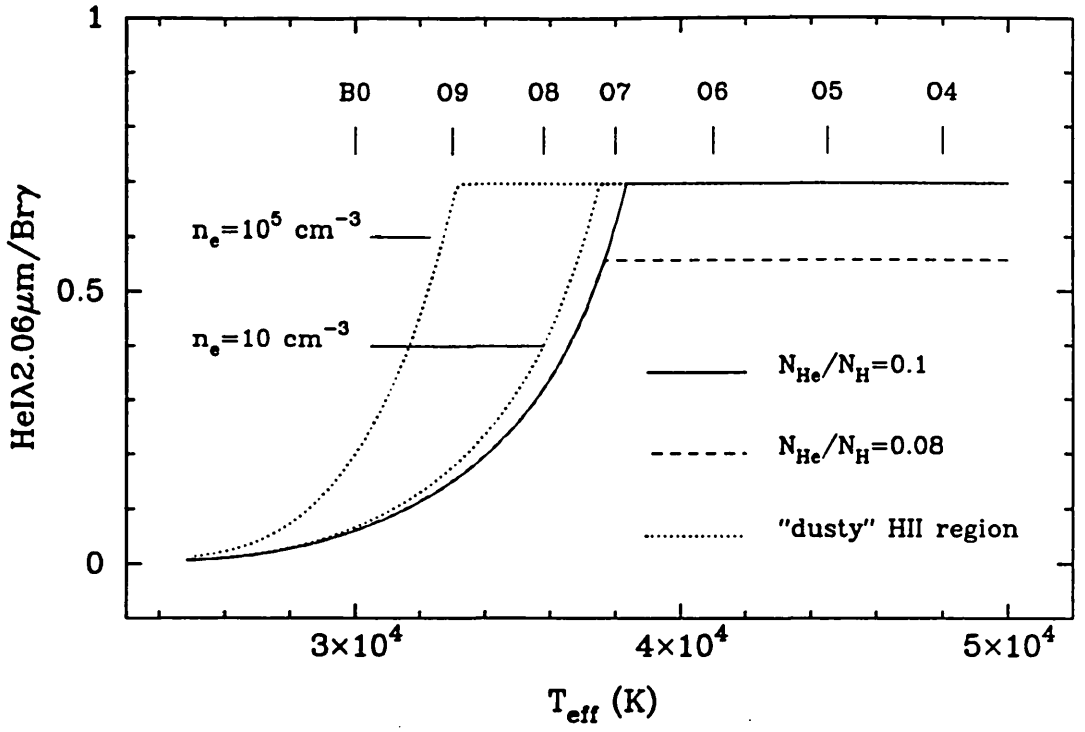

Figure 3.2— He Iλ2.06μm/Brγ ratio *vs* effective temperature, calculated for a Galactic (solid line) and primordial (dashed line) helium abundance. The dotted lines show the effect of internal dust on the line ratio. This was calculated for two electron densities and a Galactic helium abundance. The lower density is typical of optically visible H II regions.

the density is high enough, the theoretical He Iλ2.06μm/Brγ ratio derived earlier will be enhanced by this factor. For typical bright H II regions in which $n_e \lesssim 10^2$ cm^{-3}, this effect should be negligible.

3.3.3 Effect of dust within the H II regions

Dust is certainly present in H II regions. It is clearly evident from their optical photographs but also from the infrared excess inferred in these objects (Wynn-Williams *et al.* 1978; Chini, Krügel & Wargau 1987; Wood & Churchwell 1989a). Dust particles compete with hydrogen in absorbing ionizing photons. The magnitude of this effect can be judged by comparing the ionization rates derived from the bolometric luminosity (from the far-infrared *IRAS* flux) and the free-free radio flux. In their study of compact H II regions, Wood & Churchwell (1989a) showed that between 50 and 90% of the ionizing photons are absorbed by dust. This result is consistent with predictions from models of "dusty" H II regions (*e.g.* Mathis 1986).

Because the dust absorption cross section is not constant beyond 13.6 eV

Table 3.2
Ionization Rates for Dust-free and Dusty HII Regions

			dust-free HII regions		"dusty" HII regions[1]		
Mass ($M_\odot$)	T_{eff} (K)	Sp	$\log N^H_{Lyc}$ (s^{-1})	$\log N^{He}_{Lyc}$ (s^{-1})	$\log N'^H_{Lyc}$ (s^{-1})	$\log N'^{He}_{Lyc}$ (s^{-1})	τ_{eff} [2]
1.9	8000	A6V	34.01	23.41	34.01	23.41	0.00
2.2	8500	A4V	35.08	25.01	35.08	25.01	0.00
2.5	9000	A2V	36.43	26.47	36.43	26.47	0.00
2.9	9500	A0V	37.46	27.73	37.46	27.73	0.00
3.1	10000	B9.5V	38.22	28.94	38.22	28.94	0.00
3.5	11000	B9V	39.24	31.03	39.24	31.03	0.00
3.9	12000	B8V	40.05	32.56	40.05	32.56	0.00
4.5	13000	B7V	40.79	34.12	40.79	34.12	0.00
5.1	14000	B6V	41.43	35.27	41.43	35.27	0.00
5.7	15000	B5V	42.02	36.44	42.02	36.44	0.00
6.2	16000	B4.5V	42.57	37.44	42.57	37.44	0.01
6.7	17000	B4V	43.11	38.30	43.10	38.30	0.01
7.2	18000	B3.5V	43.58	39.04	43.57	39.04	0.01
8.5	20000	B2.5V	44.35	40.37	44.34	40.37	0.02
10.3	22500	B2V	45.17	41.63	45.15	41.62	0.04
12.6	25000	B1V	45.92	42.88	45.89	42.86	0.08
17.5	30000	B0V	47.26	45.22	47.18	45.18	0.20
21.9	35000	O8V	48.34	46.93	48.17	46.85	0.41
34.3	40000	O6.5V	49.03	48.29	48.78	48.18	0.56
63.8	45000	O5V	49.46	48.90	49.17	48.75	0.67
101.2	50000	O3.5V	49.84	49.36	49.50	49.19	0.78

[1] Calculated with $n_H = 10$ cm^{-3}, typical of optically visible HII regions.
[2] Defined such that $N'^H_{Lyc} = N^H_{Lyc} \exp(-\tau_{eff})$.

(Draine & Lee 1984), the relative ionization rates, N^H_{Lyc} and N^{He}_{Lyc}, will be affected by the presence of dust and therefore the He I2.06/Brγ line will also change (see Eqn. 3.5). In this section, we quantify the magnitude of this effect using a simple description of a "dusty" H II region. The following is partly based on the model described by Mathis (1986).

In order to estimate how the ionization rates are affected by the presence of dust, the wavelength dependence of the dust absorption must be determined.

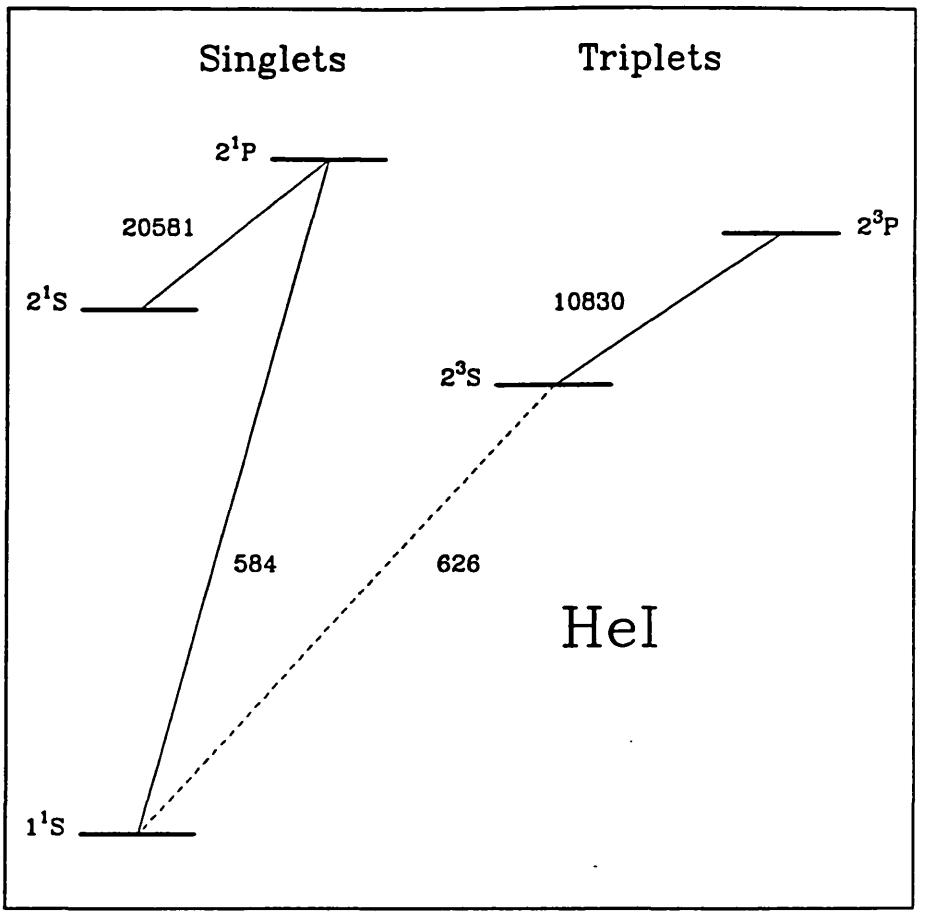

Figure 3.3— Partial energy-level diagram of HeI. Selected transitions are indicated by their wavelength in Å. The vertical axis is not to scale.

The dust optical depth in the wavelength interval $[\lambda, \lambda + d\lambda]$ is given by

$$d\tau_\lambda = \sigma_d(\lambda)\, dn_d\, dr \tag{3.6}$$

where $\sigma_d(\lambda)$ is the dust absorption cross section, n_d the number density of dust particle and r the distance from the source. $\sigma_d(\lambda)$ is related to the grain radius a *via* the following expression:

$$\sigma_d(\lambda) = \pi a^2\, Q_{abs}(a, \lambda) \tag{3.7}$$

where $Q_{abs}(a, \lambda)$ is the absorption efficiency. For dn_d, we adopt the grain size distribution of Mathis, Rumpl and Nordsieck (1977), which includes both silicate and graphite particles:

$$dn_d = (A_{sil} + A_{grap}) n_H a^{-3.5}\, da \qquad a_{min} < a < a_{max} \tag{3.8}$$

where n_H is the number gas density and $A_{sil} = 10^{-25.11}\ cm^{2.5}/H$, $A_{grap} = 10^{-25.16}\ cm^{2.5}/H$, $a_{min} = 0.005\ \mu$m and $a_{max} = 0.25\ \mu$m (Draine & Lee 1984). For a grain density of 3.3 g cm^{-3}, this distribution corresponds to a dust-to-gas mass ratio of 10^{-2}. Eqn. 3.6 may be integrated over grain size and distance r, up to the Strömgren radius R_s, to obtain an expression for τ_λ. It should be noted that R_s is the Strömgren radius in the presence of dust which is related to the dust-free radius, R_0, in the following way: $R_s \approx R_0 \exp(-\tau_{eff}/3)$. τ_{eff} is the effective dust optical depth in the Lyman continuum defined such that $N'^H_{Lyc} = N^H_{Lyc} \exp(-\tau_{eff})$ where N'^H_{Lyc} is the ionization rate modified by the presence of dust. Using the usual definition for R_0, the integration of Eqn. 3.6 yields

$$\exp(\tau_{eff}/3)\,\tau_\lambda \approx 0.27\left(Q^{sil}_{abs}(\lambda) + 0.89\,Q^{grap}_{abs}(\lambda)\right)\left(\frac{n_H}{10\ cm^{-3}}\right)^{1/3} \times \left(\frac{N^H_{Lyc}}{10^{49}\ s^{-1}}\right)^{1/3}. \tag{3.9}$$

In evaluating the integral, we have assumed that all dust particles have the same absorption efficiency Q_{abs} given for grain size of 0.01 μm. This is a reasonable approximation since $d\tau_\lambda/da$ varies as $\lambda^{-1.5}$, and thus only small particles of the order of 0.01 μm will contribute significantly to the integral.

Not surprisingly, τ_λ depends on the density and also on the luminosity of the exciting star *via* N^H_{Lyc}. Eqn 3.9 has the uncomfortable and circular feature that in order to estimate τ_λ, one must also know τ_{eff}. This is due to our simplistic description of an H II region. To be rigorous, radiative transfer equations should be solved at every point in the nebula taking into account Eqn. 3.6, but this is beyond the purpose of this Chapter. We can circumvent this problem by the following approximation. For a given density and ionization rate, the average of the right side of Eqn. 3.9 may be calculated over wavelength. τ_λ on the left side can then be replaced by τ_{eff} which allows the equation to be solved for τ_{eff}.

We have calculated τ_λ for different effective temperatures and a density of 10 cm^{-3}, using the absorption efficiencies tabulated in Draine (1985) and the dust-free ionization rates given in Table 3.2. The dependence of the optical depth on wavelength is shown in Figure 3.4 for an O5 star. Since the optical depth peaks around 800 Å (15.5 eV), the presence of dust will have a stronger effect on N^H_{Lyc} than on N^{He}_{Lyc}. Using the expression for τ_λ, we recalculated the

ionization rates by integrating under Kurucz models, adding a factor $\exp(-\tau_\lambda)$ in the integral. The resulting ionization rates, N'^{H}_{Lyc} and N'^{He}_{Lyc}, are tabulated in Table 3.2 along with the effective dust optical depth τ_{eff}. Typically, between 30 and 50% of the ionizing photons beyond 13.6 eV are absorbed by dust, which is in fairly good agreement with previous models of dusty H II regions (*e.g.* Panagia 1974; Mathis 1986).

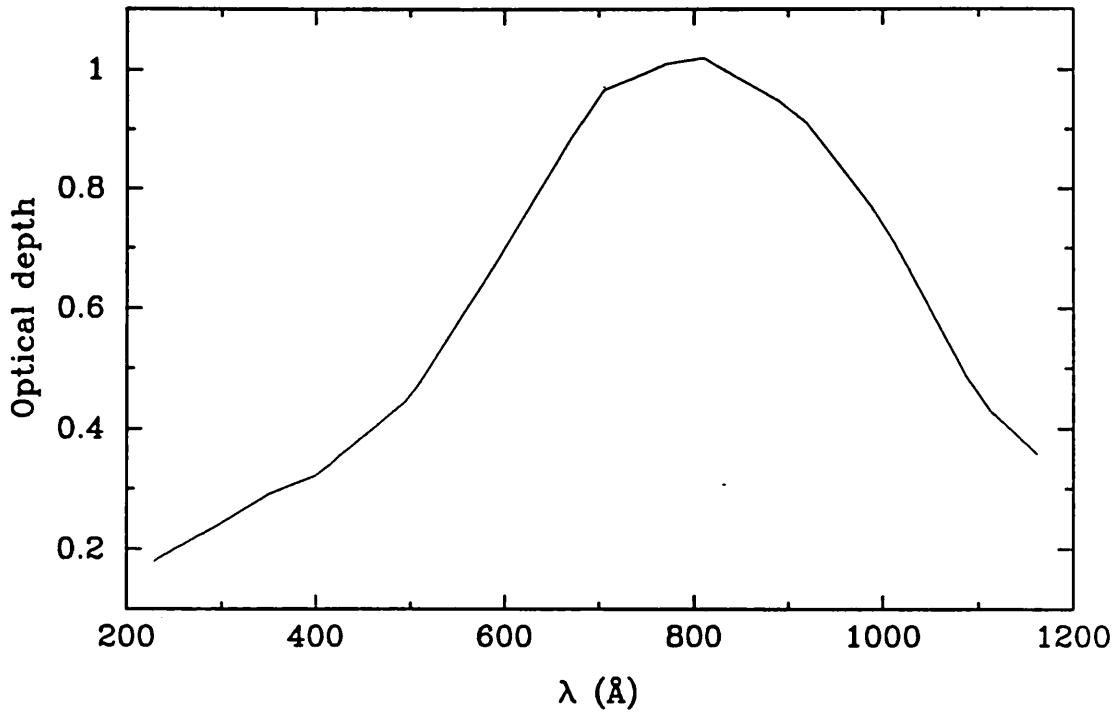

Figure 3.4— Wavelength dependence of the dust optical depth in the Lyman continuum, calculated for an H II region with $n_H \approx n_e = 10$ cm^{-3} and an exciting star with effective temperature of 45000 K (O5).

These new ionization rates can now be used to calculate the He I2.06/Brγ line ratio in dusty H II regions. The results are graphically displayed in Figure 3.2 (dotted lines). The main effect of the dust is to decrease the temperature at which the line ratio saturates, resulting in a steeper dependence between the He Iλ2.06μm/Brγ ratio and the effective temperature of the exciting star. This effect, however, is very small for typical H II regions with densities of ~ 10 cm^{-3} but cannot be neglected for high-density (10^{4-5} cm^{-3}) objects such as compact H II regions.

It is important to note that these results are valid only if we assume that

the dust-to-gas ratio in H II regions is similar to that in the interstellar medium. Although graphite and silicate dust particles can survive the harsh environment of an H II region (Salpeter 1977), the inner region can still be swept clear of dust by radiation pressure (Osterbrock 1989). The dust content of an H II region could be reduced in this way. Dust depletion in H II regions has been noted in some sources (Tielens & de Jong 1979; Churchwell, Wolfire & Wood 1990). A lower dust content would considerably reduce its effect on the He Iλ2.06μm/Brγ ratio. For instance, if $f = 1$ corresponds to a normal dust-to-gas ratio, then a compact H II region with $n_e = 10^5$ cm^{-3} and $f = 0.1$ would have the same He Iλ2.06μm/Brγ ratio as a bright H II region with $n_e = 10^2$ cm^{-3} and $f = 1$, assuming of course they have the same exciting star.

Thus, although internal dust within H II regions can potentially affect the He Iλ2.06μm/Brγ ratio, the magnitude of this effect is difficult to judge without an accurate determination of the dust-to-gas ratio. However, the simple calculations above suggest that this effect should be very small in low-density and bright H II regions.

3.3.4 Comparison with galactic observations

There are few near-infrared spectra of H II regions for which we can test the validity of the theoretical He Iλ2.06μm/Brγ ratio derived in the previous sections. The infrared sources observed thus are: G333.6-0.2 (Wynn-Williams *et al.* 1978; Storey 1983; Landini *et al.* 1984; Moneti and Moorwood 1989), W51 and K3-50 (Thompson & Tokunaga 1980). These objects are known to have exciting stars with effective temperature well above 38000 K, implying that their He Iλ2.06μm/Brγ line ratios should be saturated near 0.7, as suggested by Figure 3.2. Using the highest resolution spectra for these sources and correcting for differential extinction between Brγ and He Iλ2.06μm, we derive an average He Iλ2.06μm/Brγ ratio of 1.07 ± 0.13 (standard error) which is substantially higher than our theoretical prediction of 0.70 for a helium abundance of 10%.

More recently, we have obtained K-window spectra of ultra-compact H II regions, selected from the study of Wood & Churchwell (1989a). Most of the data were obtained as serendipitous observations during poor photometric conditions. The spectra were scanned rapidly to minimized the variable atmospheric transmission. Most of the sources were easily detected within a few minutes of integration. The spectra are shown in Figure 3.5. The noise can be judged from the scatter in the local continuum. In general, the quality of the

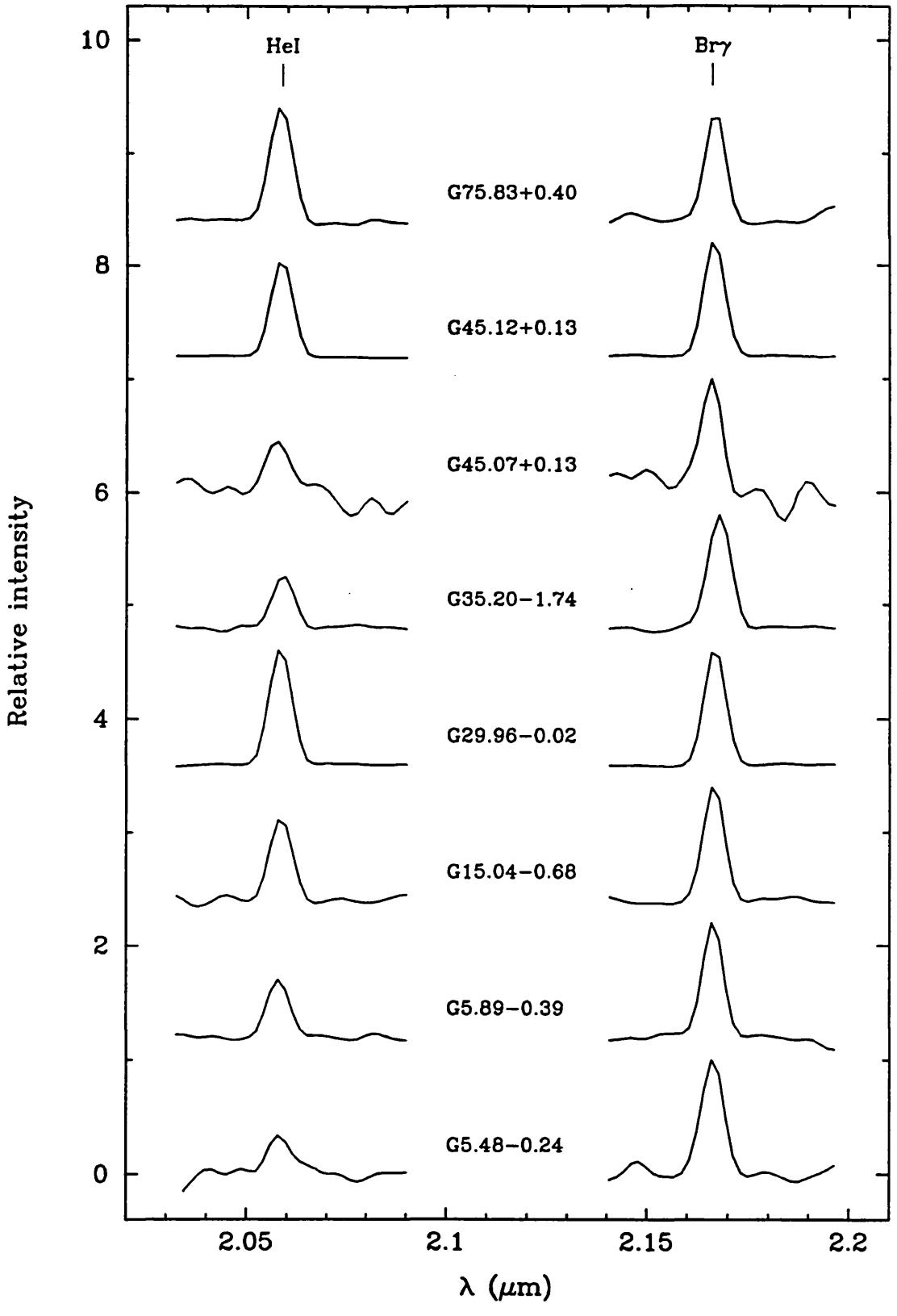

Figure 3.5— K-window spectra of compact H II regions. The spectra are shown on a relative intensity scale, separated from each other by a unit of 1.2. The spectra have been continuum-subtracted and normalized such that Brγ has a peak intensity of unity.

Table 3.3
He Iλ2.06μm/Brγ Ratio in Galactic Compact HII Regions

		Spectral types [2]			
Source	*HeI/Brγ* [1]	*HeI/Brγ*	*IRAS*	free-free	Ref [3]
K3-50	1.02	<O6.7	—	—	1
W51	0.87	<O6.7	—	—	1
G333.6-0.2	1.31	<O6.7	—	—	2
G5.48-0.24	0.41	O8.5	O6.5	O8	this work
G5.89-0.39	0.63	O6.4	O8	O7	this work
G15.04-0.68	0.90	<O6.7	O7.5	B0	this work
G29.96-0.02	1.25	<O6.7	O5	O5.5	this work
G35.20-1.74	0.53	O7	O8	O7.5	this work
G45.07+0.13	0.58	O6.7	O5.5	O6.5	this work
G45.12+0.13	1.04	<O6.7	O5	O5	this work
G75.83+0.40	1.40	<O6.7	O7	O9.5	this work

[1] Extinction corrected (see text).
[2] Spectral type derived from three different methods: 1) the HeI2.06/Brγ ratio (see Figure 2), 2) the *IRAS* flux (see text) and 3) the radio free-free flux.
[3] References: (1) Thompson & Tokunaga (1980); (2) Moneti & Moorwood (1989).

spectra is very good.

The He Iλ2.06μm/Brγ ratio of all the sources are listed in Table 3.3. Since these objects are deeply embedded in a molecular cloud, the ratio were corrected for the differential reddening between Brγ and He Iλ2.06μm assuming a visual extinction of 20 magnitudes and the extinction curve of Draine (1989). Such a high extinction is typical for compact H II regions. For instance, the three sources discussed earlier have visual extinction between 20 and 30 magnitudes.

In order to compare the observe He Iλ2.06μm/Brγ ratio with theoretical predictions, one must know the spectral type of the exciting star in the H II region. Except for very luminous sources such as the three objects mentioned above, the spectral type, or the effective temperature of the exciting star, is difficult to determine. There are essentially two methods. One can use the ionization rate derived from the radio free-free flux, assuming that the distance to the object is known. The spectral type derived in this way is a *lower limit* since dust within the nebula can absorb a significant number of ionizing photons which systematically decreases the observed ionization rate and the free-free

flux. Alternatively, one can use the *IRAS* fluxes to derived the bolometric luminosity of the star, and hence its spectral type. The *IRAS* beam (2′ at 100 μm) is much larger than the size of the compact H II regions, typically or the order of a few arcseconds, and therefore, the spectral type inferred from this method must be considered as an *upper limit.* One can correct for this effect by assuming that the total flux in the beam is associated with a cluster and that the luminosity from the compact H II region is due to the most massive star in the cluster. The spectral type derived in this way is slightly higher than that without correction.

Wood & Churchwell (1989a) have derived the spectral types for all sources in their sample using these two methods. These spectral types are given in Table 3.3 along with those derived from the He Iλ2.06μm/Brγ ratio (see Figure 3.2). Given the uncertainties in the methods used and the extinction, these spectral types should be accurate to within half a sub-class. As expected (see Table 3.3), the spectral types derived from the free-free flux are systematically higher than those inferred from the *IRAS* method, by one or two sub-classes. As pointed out by Wood & Churchwell (1989a), this is indicative of the presence of dust within the nebula. In general, the spectral types derived from the He Iλ2.06μm/Brγ ratio method are earlier that those predicted by the other two methods. Like the three objects mentioned earlier, several sources have ratios exceeding the maximum theoretical value of 0.7. The average ratio of these sources (including the three mentioned earlier) is 1.11$\pm$0.22 *i.e.* a factor 1.6$\pm$0.3 higher than the theoretical maximum.

The most likely explanation for such unusually high He Iλ2.06μm/Brγ ratios is that collisional excitation is not negligible in these sources. Except for the first three objects listed in Table 3.3, all sources have been measured to have electron densities between 10^4 and *a few* $\times$ 10^5 cm^{-3} (Wood & Churchwell 1989a), much higher that the critical density at which collisional excitation becomes important (*cf.* §3.3.2). We predicted above that collisional excitation should enhance the He Iλ2.06μm/Brγ ratio by a factor of 1.8, in reasonable agreement with the factor 1.6$\pm$0.3 inferred from the spectra.

Although a more detailed investigation is needed to fully assessed the infrared spectroscopic properties of compact H II regions, these preliminary results suggest that theoretical predictions of the He Iλ2.06μm/Brγ ratio are in good agreement with the observations.

3.4 The HeI2.06/Brγ Ratio in Galaxies

Having determined the dependence of the He Iλ2.06μm/Brγ ratio on effective temperature, we can now predict the integrated ratio associated with a young stellar population. If we assume that the starburst is very young *i.e.* all the stars are still on the main sequence, then the integrated He 2.06/Brγ ratio, I_{HeI}, is simply given by

$$I_{HeI} = \frac{\int_{m_l}^{m_u} L_{Br\gamma}(m)\,\psi(m)\,dm}{\int_{m_l}^{m_u} L_{Br\gamma}(m)\,I_{He\,I}(m)\,\psi(m)\,dm} \tag{3.10}$$

where $\psi(m)$ is the initial mass function with lower and upper mass limits m_l and m_u respectively. $L_{Br\gamma}(m)$ is the Brγ luminosity of an H II region with an exciting star of mass m, calculated from the ionization rate assuming that one Brγ photon is emitted for every 70 Lyman continuum photons (Hummer & Storey 1987). Thus, in practice, $L_{Br\gamma}(m)$ can be replace by $N^H_{Lyc}(m)$ in equation 3.10.

Because the ionization rate is a steep function of the mass (*cf.* Table 3.2), the integrated He Iλ2.06μm/Brγ ratio should be strongly dependent on the upper mass limit m_u but fairly insensitive to m_l (as long as it is lower than 10 $M_\odot$). The dependence of I_{HeI} on m_u is shown in Figure 3.6. This was calculated using equation 3.10 with a Salpeter IMF ($\psi \propto m^{-\alpha}, \alpha = 2.35$), $m_l = 0.1\ M_\odot$ and the "dust-free" ionization rates given in Table 3.2 and their corresponding He Iλ2.06μm/Brγ ratio from Figure 3.2. Collisional excitation was not included in these calculations since most galaxies have He Iλ2.06μm/Brγ ratios lower than the maximum value of $\sim$0.7 predicted by the theory for the low-density regime (see §3.3.2). This suggests that the average electron density of the photoionized gas in these galaxies is probably lower than $\sim 3 \times 10^3$ cm^{-3}, the critical density beyond which collisional excitation becomes important.

The solid heavy lines in Figure 3.6 represent two different helium abundances, Galactic (upper curve) and primordial (lower curve). In order to take into account the uncertainty of the theoretical He Iλ2.06μm/Brγ ratio, equation 3.10 was also calculated using a Galactic helium abundance and an effective recombination coefficient, $\alpha^{eff}_{He\,I2.06}$, 10% lower than the average adopted in section 3.3.1. This case is represented by the dashed line in Figure 3.6. Despite these uncertainties, Figure 3.6 shows that the He Iλ2.06μm/Brγ ratio provides a reliable measure of the upper mass limit when this ratio is less than $\approx$ 0.5

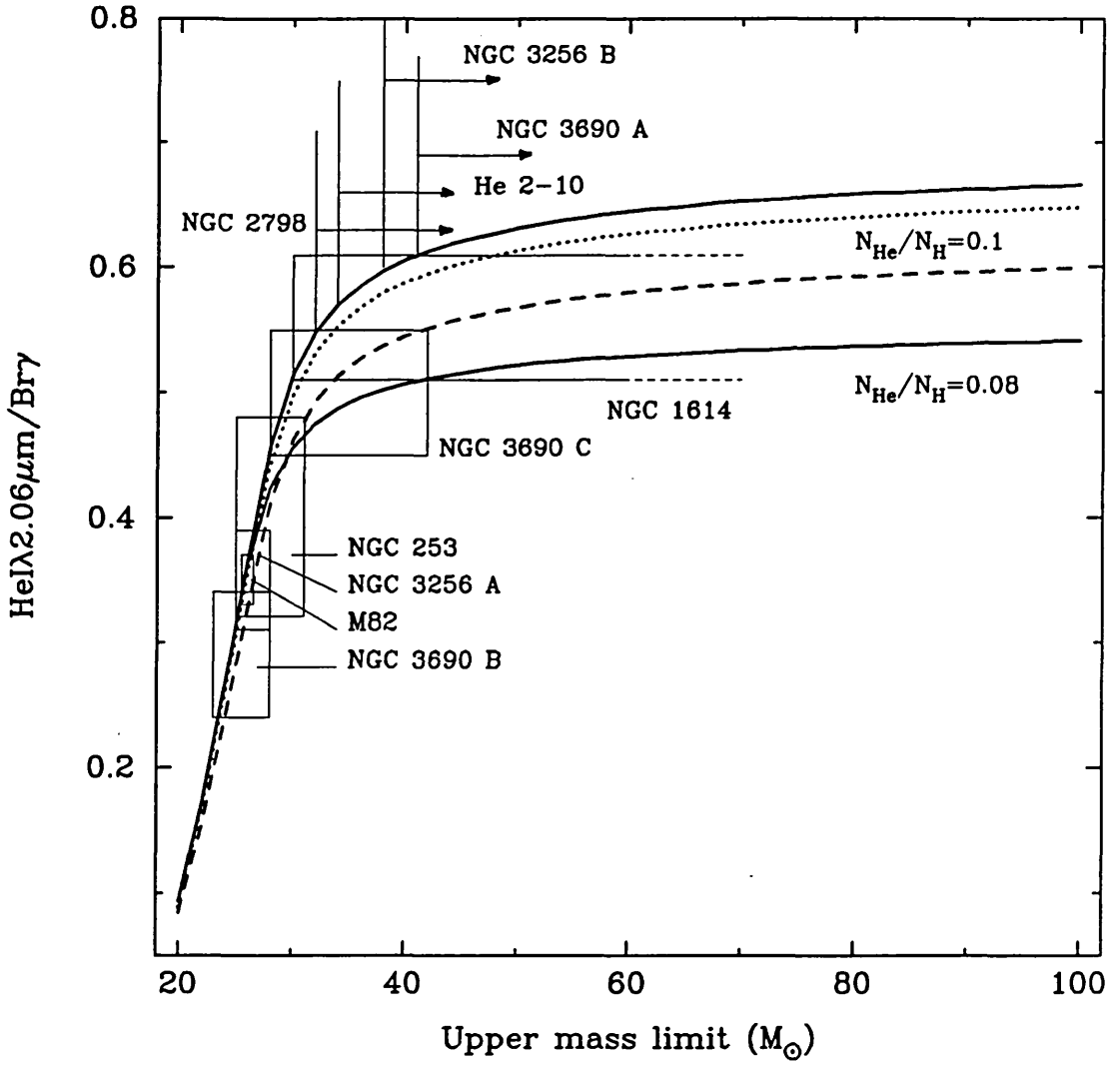

Figure 3.6— He Iλ2.06μm/Brγ ratio *vs* upper mass limit m_u, calculated as described in the text for two helium abundances (solid lines). The dashed line is the lower limit of the line ratio (for Galactic helium abundance) because of uncertainty in the value of $\alpha^{eff}_{HeI2.06}$. The dotted line corresponds to the same parameters as the upper solid line except for the inclusion of an extra term (lifetime of the stars; see text) in equation 3.10. The galaxies are represented either by a box with dimensions of the same size as the errors on both the line ratio and m_u or by an arrow showing the lower limit on m_u.

which is the case for half of the galaxies listed in Table 3.1. Because of the saturation of the ratio, this method is unreliable beyond $m_u \sim 40\ M_\odot$.

The upper mass limits inferred from the He Iλ2.06μm/Brγ ratio are given in column 6 of Table 3.1. The errors on m_u were estimated by taking the widest possible range derived from the uncertainties in both the observed and theoretical He Iλ2.06μm/Brγ ratio. We assumed that all galaxies have a normal

helium abundance. This assumption might not be correct for He 2-10 which is likely to have a low abundance (close to primordial), typical for emission-line and dwarf galaxies. We assumed a normal abundance for this galaxy since it was impossible to derive an upper mass limit value given its high He Iλ2.06μm/Brγ ratio and the loci of the primordial abundance curve (see Figure 3.6). Some galaxies, including the classical starbursts M82 and NGC 253, have relatively modest upper mass limits, between 25 and 30 $M_{\odot}$ but could be as high as 100 $M_{\odot}$ in others. The data obtained on NGC 3256 and NGC 3690-IC 694 also suggest that the upper mass limit is spatially dependent. These results show that *there is no typical value for the upper mass limit in galaxies.*

The He Iλ2.06μm/Brγ ratio calculated with equation 3.10 is valid only for the ideal case of a "zero-age" starburst. In reality, the galaxies are relatively evolved. The strong 2.3 μm CO band absorption observed in some of these galaxies (*cf.* Chapter 2) is strong evidence for the existence of a population of red supergiants. Since these stars appear in the stellar population after $\approx$ 10 million years, this a lower limit for the age of the starbursts. Because the stellar lifetime $\tau(m)$ decreases with the mass as $\tau(m) \propto m^{-0.59}$ for $13 < m < 100\ M_{\odot}$ (Puxley 1988), the most massive stars will leave the stellar population first and thus, the He Iλ2.06μm/Brγ ratio could be affected by the evolution of the galaxy, particularly if the star formation rate is rapidly decreasing.

Analytically, this evolutionary effect can be taken into account by adding the lifetime of the stars $\tau(m)$ in the integrals of equation 3.10. The addition of this term should approximately simulate a stellar population with a constant star formation rate. As shown by the dotted line of Figure 3.6, the resulting line ratios are weakly affected by this term.

Alternatively, we have investigated the evolutionary effect on the line ratio by using a stellar population synthesis model, based on the evolutionary tracks of Maeder and Meynet (1988). The details of this model are presented in appendix B. Using this model, we followed the evolution of the He Iλ2.06μm/Brγ ratio with time for different upper mass limits, assuming a Salpeter IMF and an exponentially decreasing star formation rate with an arbitrary time scale of 20 million years. The results are graphically displayed in Figure 3.7. As expected, the line ratio decreases with time but rapidly reaches an equilibrium after only $\approx$ 10 million years with line ratios similar to those predicted by the analytical model. Since the age of the galaxies are likely to be older than 10

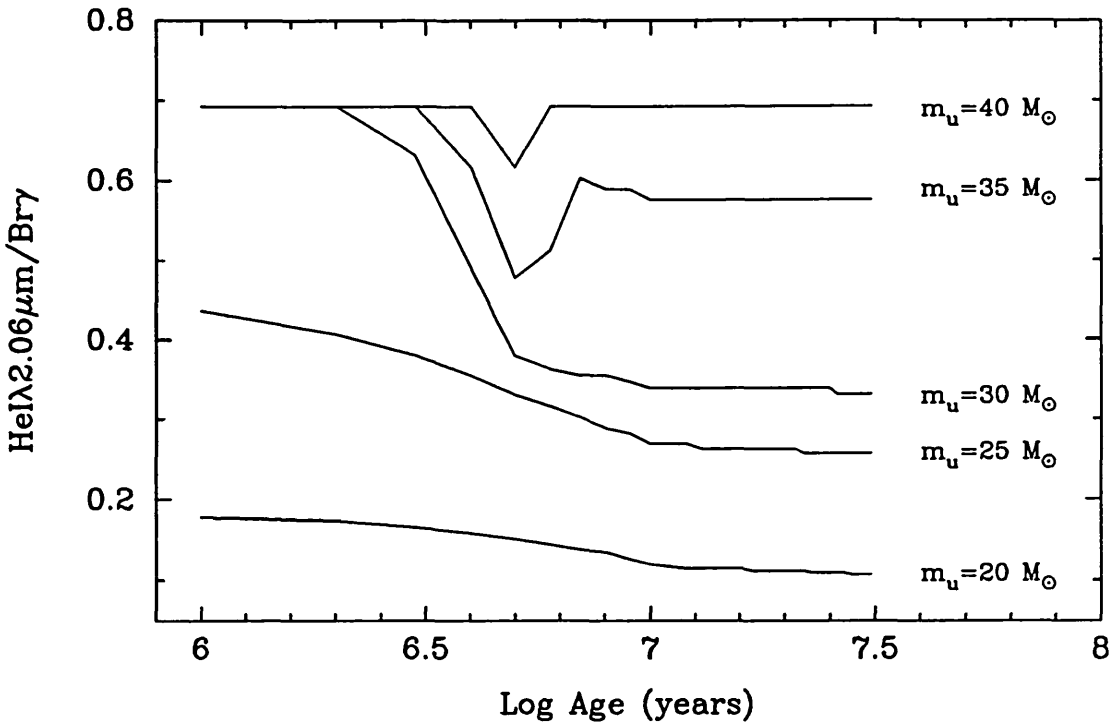

Figure 3.7— Time evolution of the He Iλ2.06μm/Brγ ratio for different upper mass limits, calculated with a stellar synthesis model (see text).

million years, the He Iλ2.06μm/Brγ ratios should have reached an equilibrium. Further, because evolutionary effects are important for upper mass limits less than 30 $M_\odot$—beyond which the He Iλ2.06μm/Brγ ratio becomes saturated—it is unlikely that a high upper mass limit (say greater than 40 $M_\odot$) combined with the evolution of the galaxy could account for the relatively low line ratios observed in some galaxies. Given these calculations, the relatively low upper mass limits ($\sim$25 $M_\odot$) inferred earlier for some galaxies are probably not underestimated by more than $\sim$5 $M_\odot$.

The relatively low upper mass limit of 25-30 $M_\odot$ inferred for some galaxies should have important observable consequences. For instance, Wolf-Rayet (WR) stars should barely exist in these galaxies since the minimum progenitor mass of WR stars is 25 $M_\odot$ for a normal or solar metal abundance ($Z = 0.02$) but as high as 85 $M_\odot$ in low-metallicity ($Z = 0.002$) environments (Maeder 1990). A search of optical WR features (*e.g.* HeII at 4686 Å) would be a good way to determine whether WR stars exist in these galaxies, although high extinction could be a problem in some cases (*e.g.* NGC 253 and M 82).

Interestingly, optical WR features have been reported in He 2-10 (Allen,

Wright & Goss 1976; D'Odorico, Rosa & Wampler 1983) which is consistent with the upper mass limit greater than 34 $M_\odot$ inferred for this galaxy. However, since this object is likely to have a low metallicity, this would require progenitor masses greater than 40 $M_\odot$ (for $Z \lesssim 0.25 Z_\odot$) to account for the existence of WR stars. Within the errors, this high upper mass limit is still consistent with the observed He Iλ2.06μm/Brγ ratio. In fact, an upper mass limit as high as 100 $M_\odot$ cannot be excluded for He 2-10.

Thus far, WR features have been detected in 13 galaxies (Heckman, Armus & Miley 1987; Armus, Heckman & Miley 1988), including He 2-10. It would be interesting to obtain near-infrared spectra of the others. From the existence of a WR population, we can predict that the average He Iλ2.06μm/Brγ ratio should be relatively high (> 0.5) if stars more massive than 30 $M_\odot$ exist in these galaxies. It would at least constrain the range of possible progenitor masses for WR stars.

Although we have presented evidence that the He Iλ2.06μm/Brγ ratio can be used as a reliable probe of the massive stellar population, this technique has serious limitations for predicting the upper mass limit when the ratio becomes higher than $\approx$0.5–0.6 ($m_u \gtrsim 40$, due to uncertainties in both the theoretical ratio and the helium abundance and also because the ratio saturates. Uncertainties in the theoretical ratio should be removed in the near future when reliable calculations of the He Iλ2.06μm recombination coefficient becomes available.

3.5 Summary and Conclusions

We have analysed near-infrared spectra of star forming galaxies which show strong Brγ and He Iλ2.06μm emission. These lines are interpreted as arising from the ionization of recently-formed OB stars. A theoretical relationship between the He Iλ2.06μm/Brγ ratio and effective temperature was derived. The ratio is a steep function of the temperature, a feature that can be used to determine, independently of the distance, the spectral type of the exciting star in H II regions. Preliminary observations of compact H II regions shows that their He Iλ2.06μm/Brγ ratios are in good agreement with those predicted from the theory.

We have shown that the steep dependence between the He Iλ2.06μm/Brγ ratio and temperature can be translated into a strong constraint on the upper mass limit of the IMF in starbursts, but reliable only for m_u less than $\sim$40 $M_\odot$.

The He Iλ2.06μm/Brγ ratios of several galaxies, including the classical starbursts M82 and NGC 253, imply relatively low upper mass limits between 25 and 30 $M_{\odot}$.

Chapter 4

On the Initial Mass Function and the Spectral Evolution of Starburst Galaxies

4.1 Introduction

Although there is compelling evidence for the existence of galaxies experiencing a vigorous burst of star formation (starbursts), the detailed physical processes responsible for this activity are still poorly understood. In order to interpret and translate the observational properties of these galaxies into physical constraints, it is fundamental to have some theoretical description of the starburst phenomenon. Irrespective of the degree of complexity, starburst or population synthesis models always share the same three basic ingredients: 1) the initial mass function (IMF) which specifies the relative number of stars at a given mass interval, 2) a birthrate function or star formation rate (SFR) history which scales the intensity of the burst by specifying how much mass of interstellar gas is converted into stars per unit of time, and 3) the theory of stellar evolution which describes how the luminosity and effective temperature of stars evolve with time in the HR diagram. In general, the stellar evolution is assumed in the model and takes the form of either theoretical evolutionary tracks (tables of luminosity and effective temperature at different ages) or analytical expressions for the lifetime of the stars as a function of mass. The shape of the IMF,

the birthrate function and the age of the system are the free parameters in the model.

In principle, these parameters can be constrained by comparing the observational properties of a given galaxy with the predictions of the model. However, in practice, this task is extremely difficult for normal galaxies because the stellar population is sufficiently old that the past chemical evolution cannot be neglected in the model. As a result, only the age can be reliably constrained, the IMF being assumed in the model.

Starburst galaxies do not suffer from this problem since the bulk of the luminosity is radiated by a stellar population usually not much older 10^8 years, young enough to minimized the effects of chemical evolution. In this case, both the age and the IMF can be constrained. In particular, the unusually high SFR inferred in starburst galaxies offers a unique opportunity to study the IMF in an environment which probably has no counterpart in our galaxy. Is the IMF of starbursts similar to the one derived in star clusters (Mateo 1988) and the solar neighbourhood (Miller and Scalo 1979, Humphreys & McElroy 1984)? Is the IMF universal in time and space? Is it a function of the level of star formation activity? The study of starburst galaxies certainly offers some hope to eventually answer these fundamental questions.

Probably the most important result that has emerged from recent studies is that the IMF in starburst galaxies is apparently deficient in low mass stars. Although there were hints of such result in previous stellar population studies (*e.g.* Huchra 1977), the study of Rieke *et al.* (1980) on the classical starburst M82 and NGC 253 was probably the first to point out this result. Based on the predictions of their population synthesis models, they showed that the observational properties of M82 can be explained only if stars less massive than $\sim 3\ M_\odot$ are not formed. Further studies of these objects and other starburst galaxies, based on different modelling techniques, have followed since then (*e.g.* Wright *et al.* 1988; Puxley *et al.* 1989) in support of this conclusion.

Despite these observational and theoretical efforts, little attention has been drawn to the other important parameter of the starburst: the age. Indeed it is a common procedure in starburst model to ignore or simplify this parameter, usually by feeding the model with a constant SFR. To what extent this simplification affects the constraints inferred for the IMF parameters is not clear. It is the purpose of this chapter is to investigate, from a theoretical point of view,

how the IMF and age-related parameters affect the observational properties of starburst galaxies. We have already described in Chapter 3 the potential application of using the He Iλ2.06μm/Brγ (hereafter referred as HeI/Brγ) ratio for constraining the upper mass limit of the IMF. In this chapter, we investigate further how other infrared observables can be used to constrain *both* the shape of the IMF and the age of the burst.

4.2 Starburst models

The models presented in the following are based on a stellar population synthesis model. This technique consists of following the evolution of stars in the HR diagram according to theoretical evolutionary tracks. The choice of this technique, as opposed to more simple analytical models, was unavoidable in order to predict key quantities which critically depend on stellar evolution. For instance, it would be very difficult to predict the strength of the CO band absorbtion at 2.3 μm from a simple analytical model. Since the CO band arises from cool giants and supergiants, predicting its strength requires the detailed knowledge of how stars evolve off the main sequence and how much time they spend at a given evolutionary stage.

The model is essentially characterized by two parameters: the IMF $\psi(m)$, defined as the number of stars per unit mass interval and the star formation rate history $R_M(t)$, a function which is time-dependent. We adopt the solar neighbourhood IMF of Scalo (1986) which is well parametrized by two power-laws of the mass ($\psi(m) \propto m^{-\alpha}$; see Appendix B for the details of the normalization). The free parameters of the IMF are the lower and upper mass limits, m_l and m_u, respectively. We also assume that the IMF is independent of time.

Three different star formation rate histories will be investigated: constant ($R_M(t) = k$), exponential ($R_M(t) = k\ \exp(-t/\tau_0)$), and "delayed" ($R_M(t) = k\,t\ \exp(-t/\tau_0)$), where k is a normalization constant in $M_\odot/year$ and τ_0 is the time-scale of the burst. Hereafter the three models will be referred as the c-model (constant), e-model (exponential) and d-model (delayed). The three SFR functions are graphically displayed in Figure 4.1. The constant k is defined such that the integral of the SFR function from $t = 0$ to $t = t_0$, the age of the burst, equals the total mass M_0 produced by the starburst *i.e.* the three models were suitably normalized to produce the same total mass after a time t_0. M_0 is another free parameter in the model. Only the first 100 million years

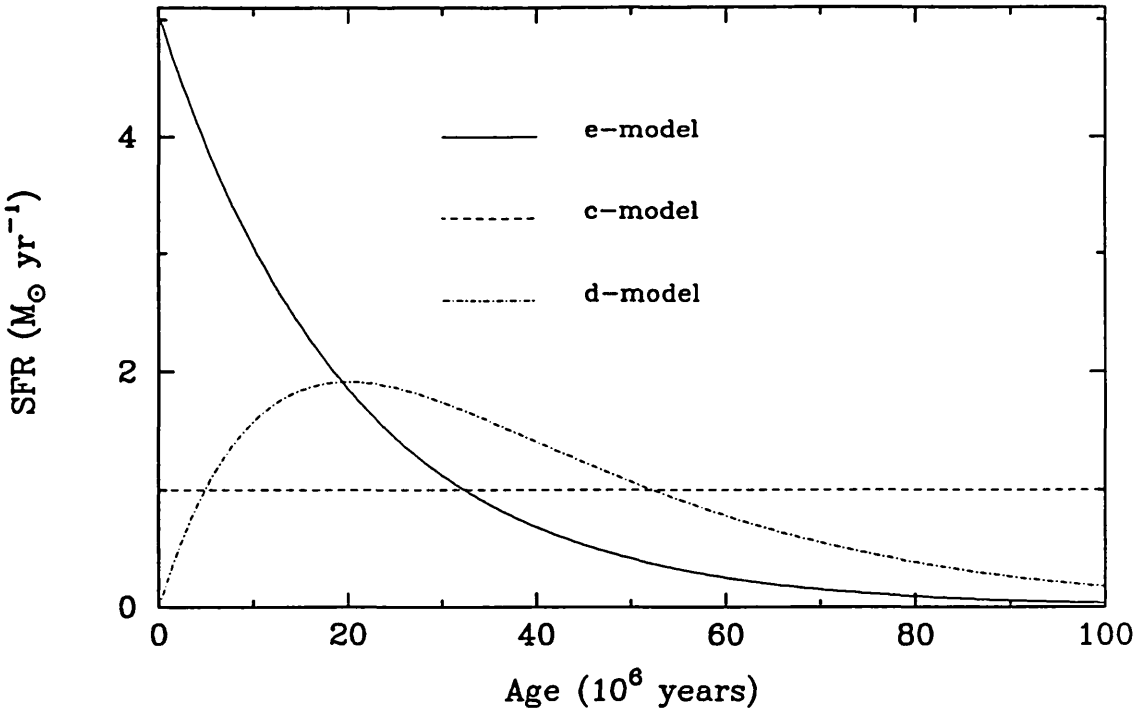

Figure 4.1— Time-evolution of the star formation rate for three different star formation rate histories: constant (c-model), exponential (e-model) and delayed (d-model), the latter two with $\tau_0 = 2 \times 10^7$ years. The normalization has been chosen such that all three models produce a mass of 10^8 $M_\odot$ after 10^8 years.

after the initiation of the burst will be studied. An arbitrary time scale τ_0 of 20 million years will be assumed for e and d-models. There is no physical justification for this particular value except that this choice makes e and d-models significantly different from the c-model over a period of 100 million years. Only the results will be presented and discussed below. For a detailed description of the modelling technique, we refer the reader to Appendix B.

4.2.1 Input observables of the model

The observable quantities that we will use to constrain the parameters of the burst are defined from the K window. Those are: the 2.2 μm luminosity $L_{2.2\mu m}$ (equivalently the absolute K magnitude M_K), the spectroscopic CO index CO_{sp}, the Brγ equivalent width $W_{Br\gamma}$ (in Å), the HeI/Brγ ratio and the ratio of the ionization rate to the bolometric luminosity, N_{Lyc}/L_{bol}. In practice, an estimate of the far-infrared luminosity L_{IR} will be used as it provides a very good approximation of L_{bol}. Except for $L_{2.2\mu m}$, these quantities are distance-independent, and in general, weakly affected (if at all) by reddening. In the

following sections, we examine the time-evolution and the dependence of these observables on the IMF parameters.

4.2.1.1 The 2.2 μm luminosity

Stellar evolution models predict that OB stars evolve into red supergiants. Since the bulk of their luminosity is radiated in the near-infrared, one therefore expects these stars to contribute significantly to the 2.2 μm luminosity of starburst galaxies.

The evolution of the 2.2 μm luminosity of a starburst population is shown in Figure 4.2 for different star formation rate histories. The models were calculated with a Scalo IMF extending from $m_l = 0.1\ M_\odot$ to $m_u = 30\ M_\odot$. In order to allow a meaningful comparison between different models, the luminosity has been normalized to unity at $t = 1$ (hereafter the time is given in units of million years when not specified) for the d-model.

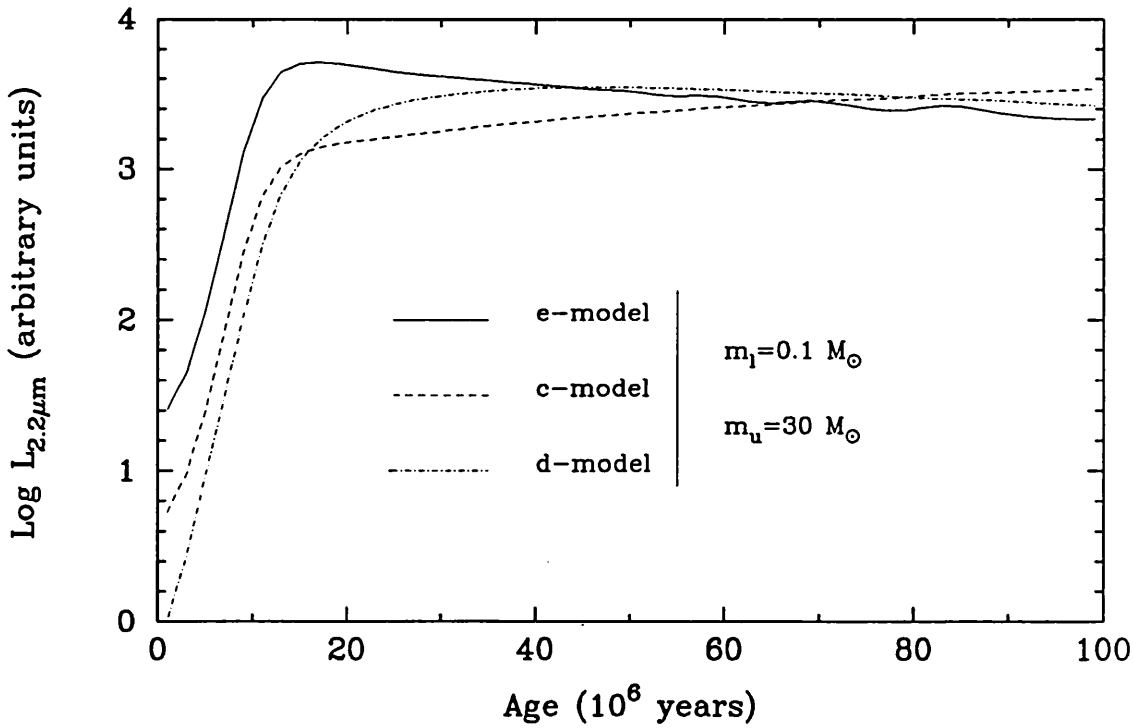

Figure 4.2— Time-evolution of 2.2 μm luminosity for different star formation rate histories. The models were calculated with a Scalo IMF extending from 0.1 to 30 $M_\odot$. The luminosity has been normalized to unity at $t = 1$ of the d-model.

Irrespective of the star formation rate history, the 2.2 μm luminosity experiences a sharp increase until $t \sim 10$. This is due to the rapid formation of red supergiants in the stellar population, mostly from OB stars with initial masses between 10 and 20 $M_{\odot}$ (see evolutionary track tables in Appendix B). As expected, the e-model produces more luminosity in the early stage of the burst compare with the other two models. The luminosity reaches an equilibrium around $t \sim 50$ beyond which the three models become virtually indistinguishable.

Because the 2.2 μm luminosity is directly proportional to the number of red supergiants in the stellar population, this quantity scales directly with the mass participating in the starburst and hence, on the parameters of the IMF. This dependence is graphically displayed in Figure 4.3. Increasing the lower mass limit from 0.1 to 2 $M_{\odot}$ enhances the 2.2 μm luminosity by a factor of $\sim$5, for a fixed total mass participating in the burst. Thus, provided that the mass is known, the 2.2 μm luminosity provides a sensitive way of constraining the lower mass limit of the IMF. However, in practice, it can be very difficult (if not impossible) to obtain a reliable estimate of the mass. Moreover, the 2.2 μm luminosity must be corrected for extinction which is often very uncertain. Despite these uncertainties, the 2.2 μm luminosity still remains an important observable in starburst models. For instance, this parameter was central in the analysis of Rieke *et al.* (1980) leading them to conclude that low-mass ($< 3\ M_{\odot}$) star formation is suppressed in M82.

As shown in Figure 4.3, the 2.2 μm luminosity is not very sensitive to the upper mass limit if a fixed total mass is considered. The reason is that stars more massive than $\sim 30\ M_{\odot}$ never reach, or spend a very short time ($\sim 10^5$ years), in the red supergiant phase (see evolutionary tracks in Appendix B). Although these stars are extremely luminous in the visible, their contribution at 2.2 μm is relatively modest. As a result, the net effect of increasing the upper mass limit is to decrease the number of red supergiants with initial masses between 10 and 20 $M_{\odot}$. We shall see later that the weak sensitivity of the 2.2 μm luminosity to the upper mass limit has an important effect on the Brγ equivalent width.

4.2.1.2 The spectroscopic CO index

Since red supergiants later than K5 are characterized by strong 2.3 μm CO absorption bands compared with giants, the presence of these stars in the young stellar population should be noticeable from the integrated spectroscopic CO

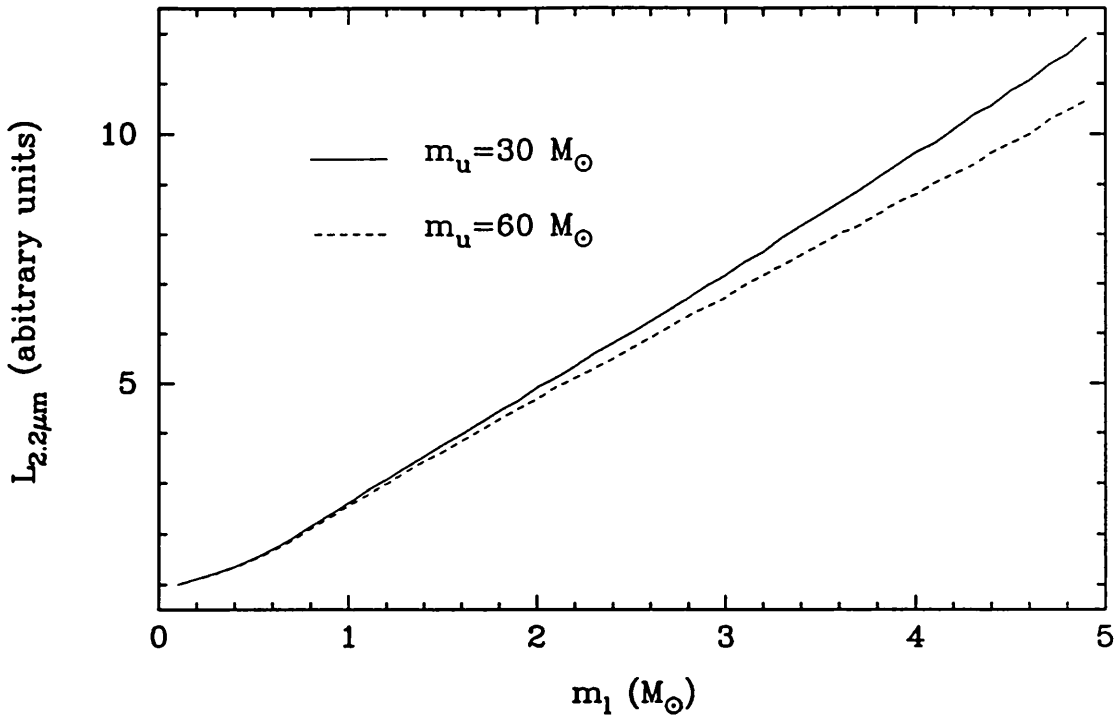

Figure 4.3— Effect of the lower mass limit on the 2.2 μm luminosity, calculated for an e-model at $t = 20$ with two different upper mass limits, 30 $M_\odot$ (solid line) and 60 $M_\odot$ (dashed line). The luminosity is in arbitrary units, normalized to unity at $m_l = 0.1$. The total mass participating in the burst has been fixed.

index. The evolution of CO_{sp} is shown in Figure 4.4. Like the 2.2 μm luminosity, CO_{sp} increases sharply until $t \sim 10$, reaching a maximum of ~0.28 *i.e.* 0.08 mag stronger than a giant-dominated stellar population. The spectroscopic CO index is weakly-dependent on the IMF parameters. Even with an extremely narrow IMF ($m_l = 10$, $m_u = 25\ M_\odot$; dotted line in Figure 4.4), the spectroscopic CO index increases by only 0.02 mag.

The maximum spectroscopic CO index predicted by the stellar synthesis model is critically dependent on the lifetime of the red supergiant phase and hence, on the particular evolutionary tracks used. The tracks of Maeder & Meynet (1988) used in the model predict that the integrated spectroscopic CO index of a starburst population should never exceed ~0.3. It is encouraging that the few galaxies that were found with unusually strong CO bands in Chapter 2 have CO_{sp} between 0.27 and 0.31, in very good agreement with the theoretical prediction. We shall see later, however, that the possible contribution from an old pre-existing population complicates this conclusion. Nevertheless, given the

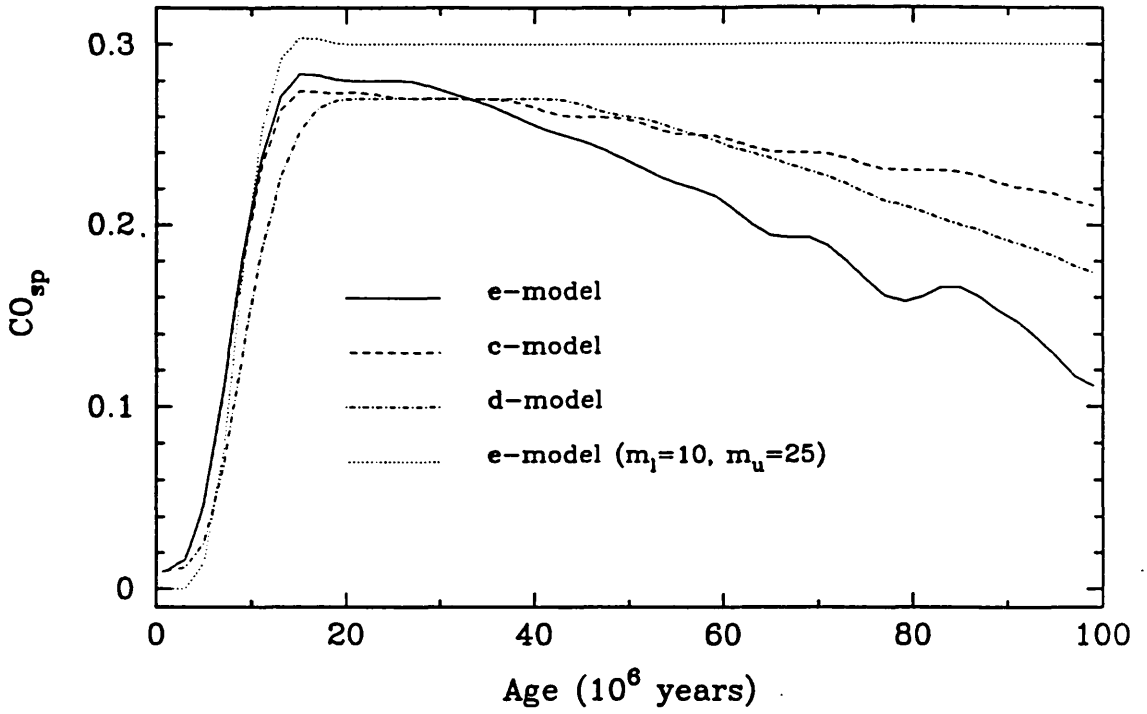

Figure 4.4— Time-evolution of the spectroscopic CO index (CO_{sp}) for different star formation rate histories. Except for the dotted line which was calculated with $m_l = 10$ and $m_u = 25$, all models were calculated with a Scalo IMF extending from $m_l = 0.1$ to $m_u = 30\ M_\odot$.

intrinsic uncertainties in CO_{sp} (~0.02 mag; see Appendix A), the agreement between theory and observations is very satisfactory.

Unlike the K luminosity, the spectroscopic CO index is fairly sensitive to the star formation rate history in the later stages of the burst ($t > 50$). An important result of the model is that the strong CO band phase can be relatively short-lived. As seen in Figure 4.4 for an e-model, after $t \sim 60$ the spectroscopic CO index is marginally stronger than a normal stellar population characterized by a CO_{sp} of ~0.2. It is even predicted to decrease *below* this value later, when the K luminosity is still fairly strong. This behaviour is due to the fact that red supergiants with strong CO bands ($CO_{sp} > 0.2$, later than K5) originate from a very narrow range of initial masses, between 10 and 20 $M_\odot$. With a typical lifetime of 10 to 20 million years, these stars soon disappear from the stellar population, leaving earlier-type supergiants which have relatively small CO_{sp}.

Thus, the general belief that a starburst galaxy should be characterized by a strong CO band must be put in perspective with the age of the system.

Although stellar synthesis models *do* predict a strong CO band phase, a normal (or even small) spectroscopic CO index is conceivable for a starburst galaxy if the SFR is rapidly decreasing and the burst is relatively old. The search of such "dying" starbursts would be particularly important as it would place strong constraints on the lifetime of the burst.

4.2.1.3 THE Brγ EQUIVALENT WIDTH ($W_{Br\gamma}$)

Since the Brγ and K luminosity are directly proportional to the number of OB stars and red supergiants, respectively, the Brγ equivalent width is an good indicator of the relative number of blue and red stars in the stellar population. This observable is particularly useful as it is independent on distance and also on reddening provided that the stellar continuum and the ionized gas are spatially correlated. In practice, this quantity is simply obtained from the ratio of the Brγ line flux to the local continuum flux density at 2.1661 μm. Since the stellar synthesis model can only predict the ionization rate N_{Lyc} and the absolute K magnitude M_K, for the purpose of the model, it is useful to express $W_{Br\gamma}$ in terms of those two quantities.

We define the Brγ equivalent width as the ratio of the "absolute Brγ flux", $F_{Br\gamma}$, to the local flux density $S_{2.166}$. $F_{Br\gamma}$ is defined as the Brγ flux observed at a distance of 10 parsecs, in a similar way as the absolute magnitude. The Brγ flux at a distance d is given by

$$f_{Br\gamma} = \frac{h\nu_{Br\gamma}\alpha^{eff}_{Br\gamma}}{4\pi d^2 \alpha_B} N_{Lyc} \tag{4.1}$$

where N_{Lyc} is the ionization rate, $\alpha^{eff}_{Br\gamma}$ the effective recombination coefficient of Brγ and α_B the total recombination coefficient. Setting $d = 10$ pc in this equation yields

$$F_{Br\gamma} = 1.1 \times 10^{-5} \left(\frac{N_{Lyc}}{10^{54}\ s^{-1}} \right) \qquad W\ m^{-2}. \tag{4.2}$$

The local flux density $S_{2.166}$ is related to the absolute K magnitude by the following expression:

$$S_{2.166} = 10^{-0.4(M_K+23.49)} \left(\frac{2.1661}{2.2} \right)^{-4} \qquad W\ m^{-2}\ \mu m^{-1}. \tag{4.3}$$

The last term corrects for the fact that the flux density at the wavelength of Brγ is slightly higher than at 2.2 μm due to the approximate Rayleigh-Jeans

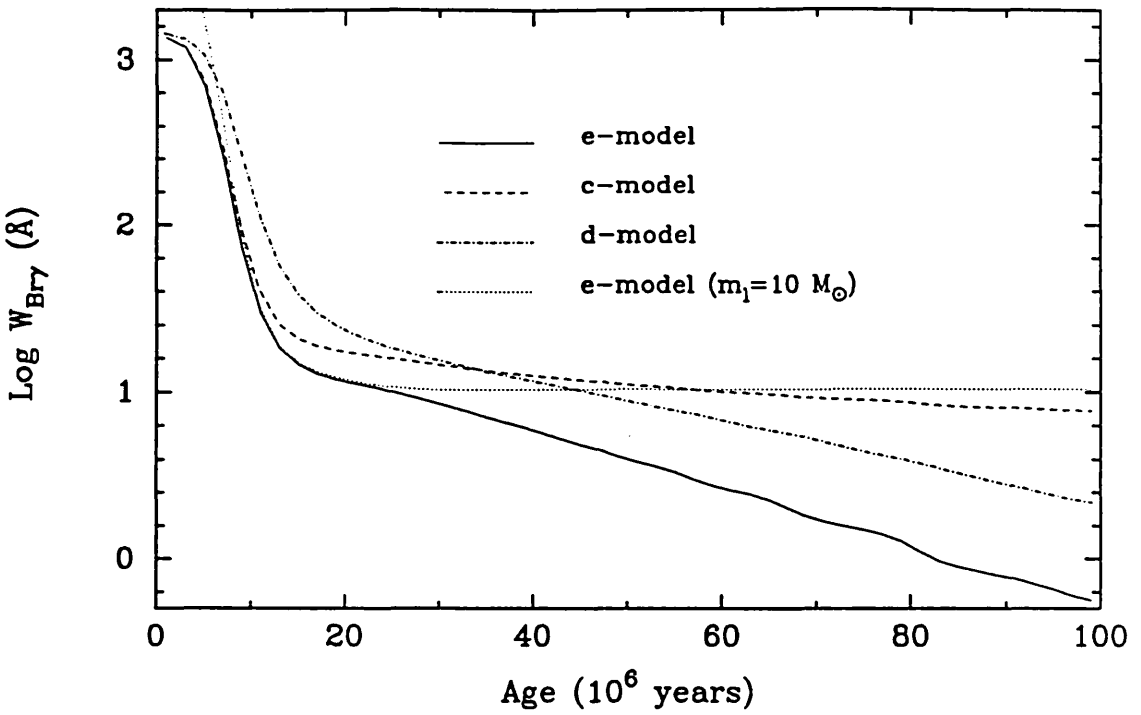

Figure 4.5— Time-evolution of the Brγ equivalent width ($W_{Br\gamma}$) for different star formation rate histories. The models were calculated with a Scalo IMF extending from $m_l = 0.1$ to $m_u = 30\ M_\odot$. The dotted line is an e-model with $m_l = 10$ and $m_u = 30$.

nature of stellar spectra. This expression was calculated using the zero point adopted in Chapter 2 (see Eqn 2.3).

The expression for $W_{Br\gamma}$ is obtained from the ratio of Eqn 4.2 and 4.3. which finally gives

$$W_{Br\gamma}(\text{Å}) = 2.57 \times 10^{10} \left(\frac{N_{Lyc}}{10^{54}\ s^{-1}} \right) 10^{0.4 M_K}. \qquad (4.4)$$

The evolution of $W_{Br\gamma}$ is graphically displayed in Figure 4.5. In the early stage of the burst ($t < 10$), this quantity is very high because of the combined effect of the strong ionization and the small contribution from young OB stars to the 2.2 μm continuum. It decreases sharply until $t \sim 10$ as the red supergiants appear in the stellar population. The subsequent evolution of this observable is greatly affected by the star formation rate history. For instance, at $t = 80$, an e-model predicts a Brγ equivalent width which is an order of magnitude smaller than the c-model. Thus, the Brγ equivalent width can be used both as an age indicator and/or as a discriminant of the star formation rate history.

As shown in Figure 4.5, the Brγ equivalent width is affected by the lower mass limit in the later stages of the burst ($t > 40$) but this dependence is significant only if the IMF is very truncated at the lower end ($m_l > 7\ M_\odot$). For instance, an e-model with $m_l = 5\ M_\odot$ (not shown here) is virtually identical to the corresponding model with $m_l = 0.1\ M_\odot$. On the other hand, the Brγ equivalent width is very sensitive to the upper mass limit. The dependence of this observable on m_u is shown in Figure 4.6. $W_{Br\gamma}$ increases sharply with m_u because the ionization rate is a steep function of the mass whereas the K continuum slightly decreases with m_u, as discussed earlier. This shows that it is crucial to constrain the upper mass limit independently if the Brγ equivalent width is to be used as an age indicator.

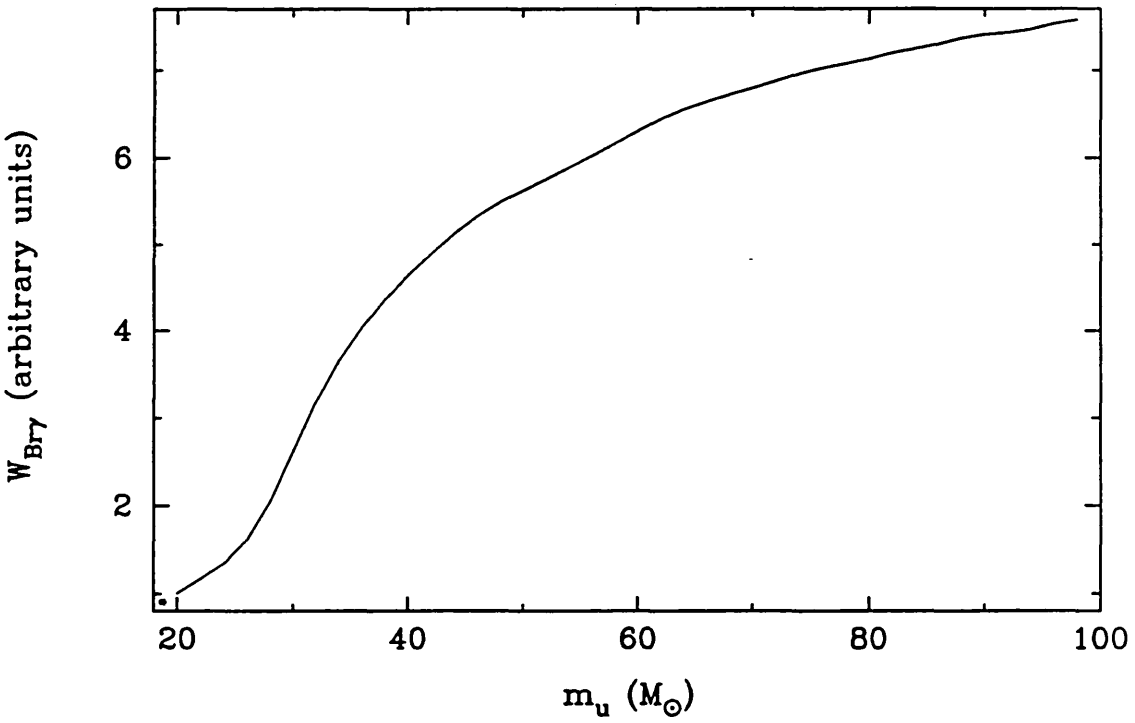

Figure 4.6— Dependence of the Brγ equivalent width on the upper mass limit m_u, calculated for an e-model at $t = 20$ using a Scalo IMF with $m_l = 0.1\ M_\odot$. The $W_{Br\gamma}$ axis is in relative units and normalized to unity at $m_u = 20\ M_\odot$.

4.2.1.4 The ionization rate to bolometric luminosity ratio

In many respects, this quantity is very similar to the Brγ equivalent width. The dependence of N_{Lyc}/L_{IR} on the age and the IMF parameters is graphically

displayed in Figures 4.7 and 4.8. Like $W_{Br\gamma}$, N_{Lyc}/L_{IR} is quite sensitive to the age and provides a good discriminant of the star formation rate history in the later stages of the burst. This quantity is weakly affected by the lower mass limit unless the IMF is very truncated ($m_l > 5\ M_\odot$) but is particularly sensitive to the upper mass limit.

4.2.1.5 THE HeI/Brγ RATIO

As discussed in Chapter 3, this ratio provides a reliable measure of the upper mass limit for $m_u \lesssim 40\ M_\odot$. This quantity is also sensitive to the age but mostly in the early stages of the burst ($t < 20$) after which the ratio reaches an equilibrium. The HeI/Brγ is virtually independent of the lower mass limit.

4.2.1.6 *JHK* COLOURS

Near-infrared colours are not an important constraint in starburst models but they are useful for determining the extinction. Since the method must rely on some assumed intrinsic colours for the underlying stellar population, usually those of normal galaxies, it is interesting to examine theoretically whether starburst activity can affect these colours significantly.

The evolution of the JHK colours of a young stellar population is shown in Figure 4.9. For comparison, ellipticals are characterized by $J-H = 0.68 \pm 0.04$ and $H-K = 0.20 \pm 0.03$ (Frogel *et al.* 1978) similar to the bulges of late-type spirals ($J-H = 0.70 \pm 0.07$, $H-K = 0.25 \pm 0.06$; Frogel 1985). In the very early stage of the burst ($t < 5$), the colours are very blue because the infrared continuum is dominated by OB stars but become much redder until $t \sim 10$ as the first red supergiants appear in the stellar population. However, the colours never become as red as observed in normal galaxies especially for $J-H$ which is always bluer by at least ~0.2 mag, depending on the age. $H-K$ is also bluer but the magnitude of this effect is much smaller (~ 0.05 mag). Unlike $J-H$, $H-K$ is virtually independent of the age and the star formation rate history. This suggests that $H-K$ is probably more suitable for deriving the extinction in starburst galaxies.

4.2.2 EFFECT OF THE PRE-EXISTING POPULATION

Since starburst activity is generally observed in the nuclear regions of the galaxy, it is likely that the underlying giant-dominated stellar population will contribute

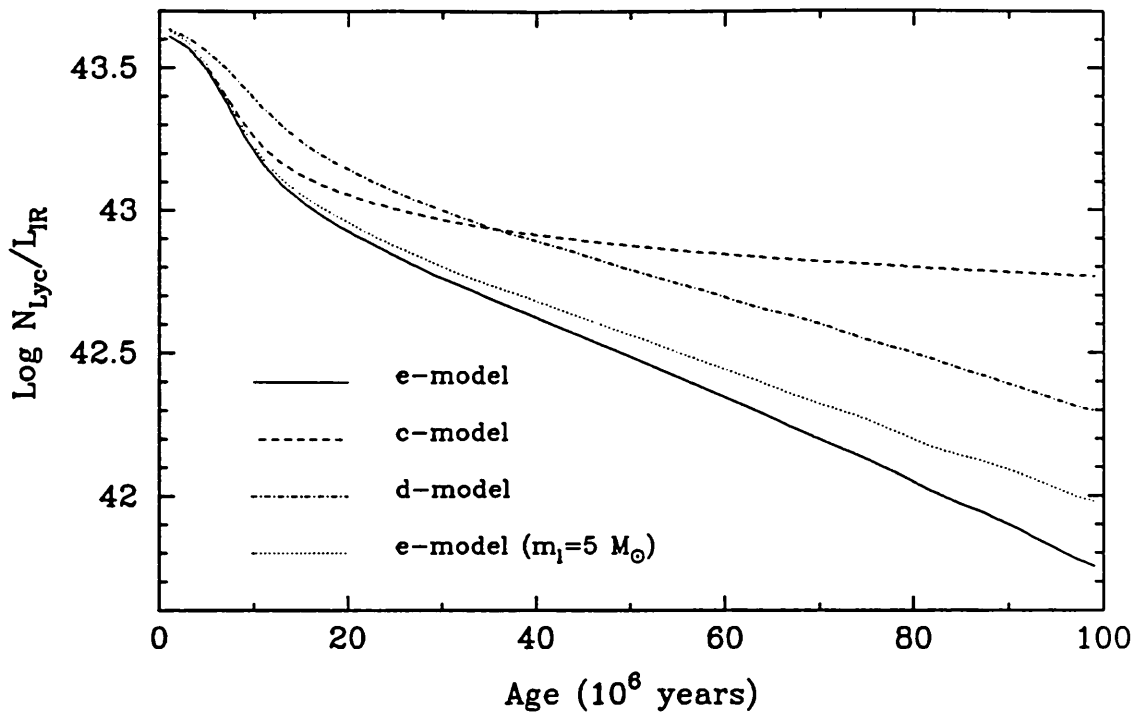

Figure 4.7— Time-evolution of the ionization rate to bolometric luminosity ratio (N_{Lyc}/L_{IR}) for different star formation rate histories. The models were calculated with a Scalo IMF extending from $m_l = 0.1$ to $m_u = 30\ M_\odot$. The dotted line is an e-model with $m_l = 5$ and $m_u = 30$.

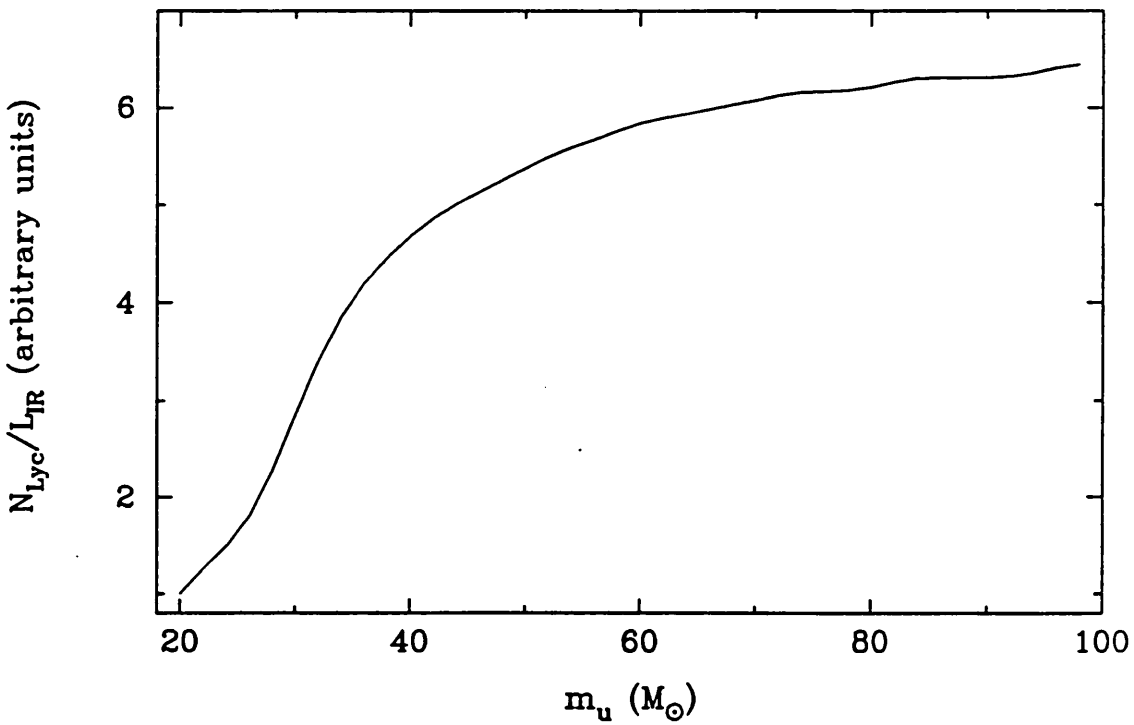

Figure 4.8— Ratio of ionization rate to the bolometric luminosity *vs* upper mass limit m_u, calculated for an e-model at $t = 20$ using a Scalo IMF with $m_l = 0.1\ M_\odot$. The ratio has been normalized to unity at $m_u = 20\ M_\odot$.

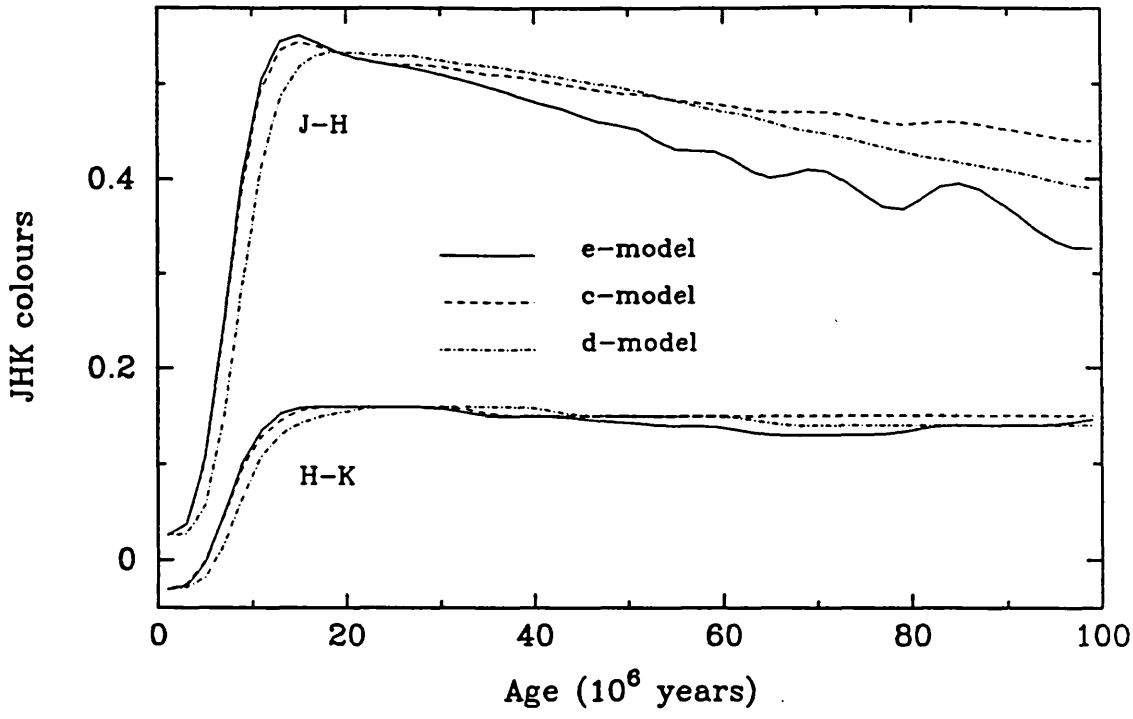

Figure 4.9— Time-evolution of the JHK colours of a young stellar population. The models were calculated with a Scalo IMF extending from $m_l = 0.1$ to $m_u = 30\ M_\odot$.

significantly at 2.2 μm. There is empirical evidence that this contribution is indeed significant. In his study of nearby starbursts, Devereux (1989) showed that these galaxies are brighter at 2.2 μm than normal spirals, typically by a factor of 4. We have also shown in Chapter 2 that some merging and interacting galaxies have their 2.2 μm luminosity enhanced by a similar, or even higher factor. These observations suggest that the pre-existing stellar population contributes roughly 25% of the total 2.2 μm luminosity. Apart from the K continuum, the presence of an old stellar population will also affect the integrated spectroscopic CO index, the Brγ equivalent width and JHK colours.

The pre-existing stellar population can be included in the starburst model by assuming that a certain fraction of the total mass suddenly experiences a burst of star formation. As a fiducial mark, we assume that 10% of the total mass of a galaxy is produced in a single burst after 100 million years according to an e-model. This fraction should be an upper limit for normal spirals since no more than 10% of the mass is in gaseous form. We should remark however that this fraction could be severely underestimated in galaxies which show high

concentration of molecular gas. In fact, we shall see later that in the case of ARP 220, there are approximately equal dynamical and molecular masses. Given this fraction, the rest of the mass associated with the old population is converted into luminosity using typical colours and mass-to-light ratios of normal galaxies *i.e.* $M/L_{1.65\mu m} = 0.7$ in solar units [1] (Devereux, Becklin & Scoville 1987), $J - H = 0.68$, $H - K = 0.23$ (Frogel *et al.* 1978; Frogel 1985) and $CO_{sp} = 0.20$ (as transformed from an average photometric CO index of 0.15; Frogel *et al.* 1978).

The results are shown in Figure 4.10. The 2.2 μm luminosity has been normalized to unity before the occurrence of the burst. With a solar neighbourhood IMF extending from 0.1 to 30 $M_\odot$ the K continuum is enhanced by a factor of $\sim$2, or less, depending on the age. In order to reproduce the 2.2 μm excess of $\gtrsim 4$ observed in starburst galaxies, the lower mass limit must be greater than $\sim 1\ M_\odot$. This suggests that the IMF is biased against the formation of low-mass stars in starburst galaxies.

We have also calculated the effect of the underlying population on the spectroscopic CO index, the Brγ equivalent width and JHK colours, given that $m_l = 1\ M_\odot$ is representative of starburst galaxies. The spectroscopic CO index has a similar behaviour to a pure starburst except for the early stage of the burst ($t < 10$) when the continuum is mostly contributed by the old stellar population. The maximum CO_{sp} is obviously smaller (by 0.02 mag) compared with a pure starburst but still significantly higher than the underlying evolved population characterized by a CO_{sp} of 0.2.

As expected, the Brγ equivalent width ($W_{Br\gamma}$) is mostly affected by the underlying population in the early stage of the burst, decreasing by as much as two orders of magnitudes. Unlike the pure starburst case, the model including the old population predicts that $W_{Br\gamma}$ should increase from onset of the burst and reach a maximum around $\sim$5 million years. After this point, the Brγ equivalent width is 30%-50% smaller than predicted for a pure starburst (see dashed line in Figure 4.10), and decays virtually at the same rate as predicted without the evolved population.

Because only $\sim$25% of the K continuum is contributed by the evolved population, the integrated JHK colours of the starburst remains bluer than

[1] The absolute magnitude of the sun at 1.65 μm is taken as +3.65

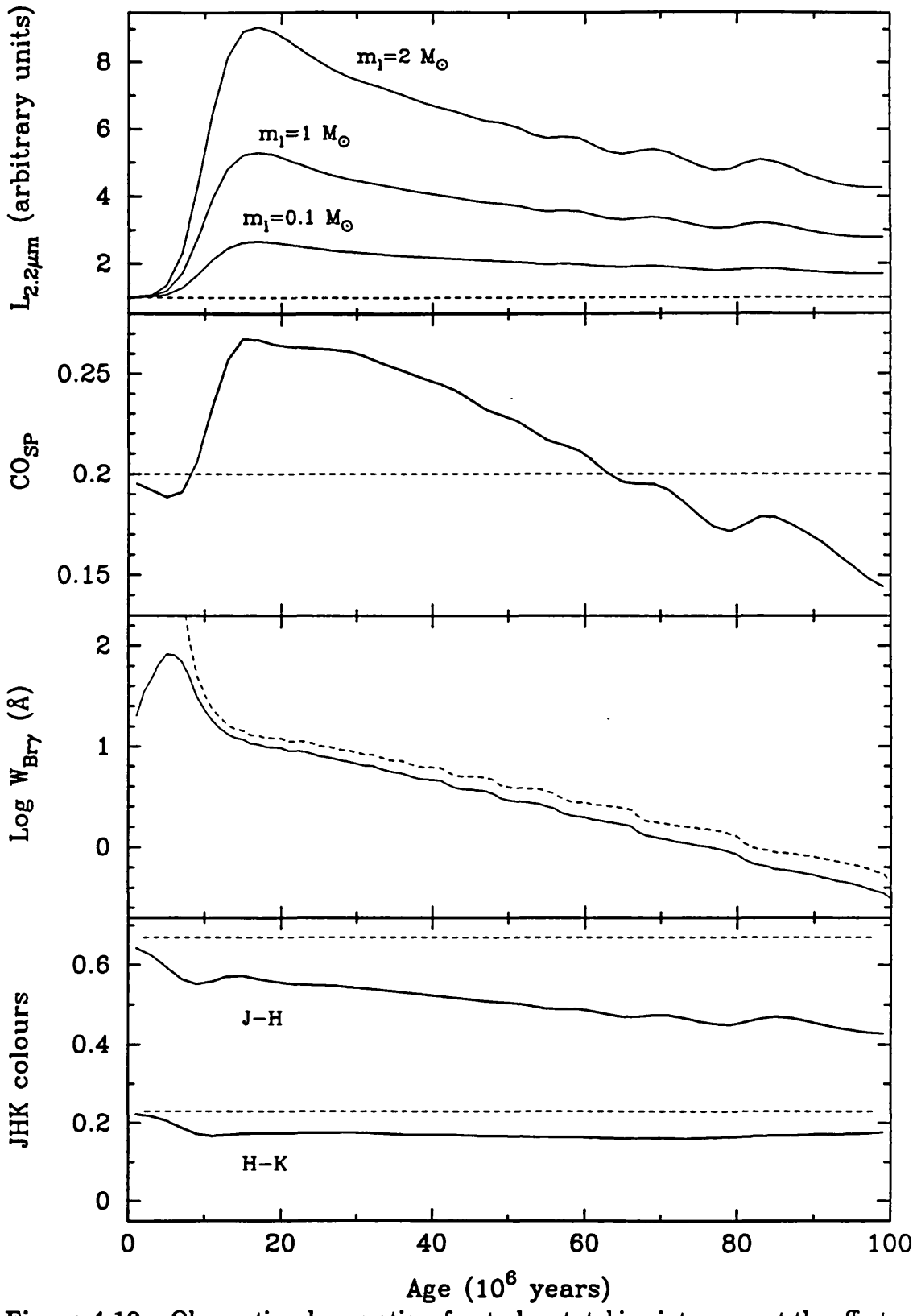

Figure 4.10— Observational properties of a starburst, taking into account the effect of a pre-existing stellar population (see text). Except for $L_{2.2\mu m}$, all quantities have been calculated with an e-model and a Scalo IMF extending from 1 to 30 $M_\odot$. The dashed line in the $L_{2.2\mu m}$, CO_{sp} and JHK plots corresponds to the value observed before the burst. In the plot of $W_{Br\gamma}$ the dashed line has the opposite meaning, representing the model prediction without the pre-existing population.

normal. Like CO_{sp} and $W_{Br\gamma}$, the colours are significantly different from a pure starburst only in the first 10 million years of the burst.

4.3 Comparison with individual galaxies

Having quantified the dependence of several infrared observables on the age and the IMF parameters, it should be possible to constrain the age and the shape of the IMF for a starburst galaxy, given a set of observables. The free parameters of the model that we wish to constrain are: 1) the age of the burst, 2) the star formation rate history and 3) the shape of the IMF. In this section, representative starburst models are presented for the few interacting and merging galaxies discussed in Chapter 2.

The infrared observables that will be used to constrain the model parameters are those referred to earlier: the absolute K magnitude (M_K), the Brγ equivalent width ($W_{Br\gamma}$), the spectroscopic CO index (CO_{sp}), the ratio of the ionization rate to bolometric luminosity (N_{Lyc}/I_{IR}) and the HeIλ2.06μm/Brγ ratio (HeI/Brγ). We shall assume a Scalo IMF leaving the lower and upper mass limits, m_l and m_u, as free parameters. In practice, m_u can be constrained directly from the HeI/Brγ ratio since it is weakly dependent on the other model parameters, as discussed in Chapter 3. Due to computational restrictions, models with only three upper mass limits (25, 35 and 60 $M_\odot$) were investigated. We shall see later that within the errors, the HeI/Brγ ratio observed in a given galaxy can be well represented by one of these upper mass limits. In order to predict the absolute K magnitude, the total mass participating in the starburst, M_*, was also included as a free parameter. Three different star formation rate histories, referred earlier as e-model, c-model and d-model were investigated.

Excluding the star formation rate history and the upper mass limit, the problem is reduced to three parameters: the age t_0, the lower mass limit m_l and the mass M_* participating in the starburst. In order to constrain the age and the lower mass limit of a given galaxy, several starburst models with different combinations of the three parameters above must be generated and compared with the observations. A simple trial and error approach may be used to discriminate (essentially by eye) successful models but this method has the main disadvantage of not providing any information on the uniqueness of the propose solution. This is, for instance, the basis of the method used by Rieke *et al.* (1980, 1985) for modelling several starburst galaxies.

It is possible to assess the uniqueness of a "successful" model with the following χ^2 analysis. Let x_i be one of the five observables of a given galaxy with uncertainty σ_i and $X_i(t_0, m_l, M_*)$ the corresponding quantity predicted by the model for a set of parameters t_0, m_l and M_*. The goodness of a given model may be defined with this χ^2 expression:

$$\chi^2(t_0, \alpha, M_*) = \sum_i \left(\frac{x_i - X_i(t_0, \alpha, M_*)}{\sigma_i} \right)^2 \tag{4.5}$$

Good models are characterized by small values of χ^2. It should be noted that this expression provides only an indication of how good a fit is. Because of the uncertainties inherent to the model and the observations, it is difficult to define a meaningful value of χ^2 (like unity for the usual reduced χ^2) which would quantify and characterize the goodness of the fit. Nevertheless, this quantity is still useful for discriminating different models.

For each of the three star formation rate histories and upper mass limits mentioned above, a total of 1650 starburst models were calculated for different combinations of age and m_l, ranging from 1 to 99 million years (in steps of 2) and 0.1 to 9.7 $M_\odot$ (in steps of 0.3), respectively. The absolute K mag predicted by the models were then scaled with different masses. For a given set of 5 observables (M_K, CO_{sp}, $\log W_{Br\gamma}$, $logN_{Lyc}/L_{IR}$ and HeI/Brγ) a χ^2 was calculated for each combination. A successful solution should be characterized by relatively peaked contours in the [m_l-age] plane.

The results are presented below for all galaxies. Each one is presented with a table summarizing successful models and several χ^2 diagrams of the [m_l-age] plane. The input observables used in the models are summarized in Table 4.1. They were taken from Table 2.7 of Chapter 2, after correction (when appropriate) for the contribution of non-stellar emission to the K continuum. No correction has been made for the potential contribution of an old-stellar population to the K continuum. It can be shown that a contribution of less than 30%, as inferred from the 2.2 μm excess (*cf.* Chapter 2) has small effects on the conclusions. We also emphasise that the results presented below are valid only for the central 5″.

4.3.1 ARP 220

The non-detection of the He Iλ2.06μm transition in this merger (HeI/Brγ<0.3) sets an upper limit for m_u to $\sim$25 $M_\odot$. The total mass present in this system is

Table 4.1
Observational Properties of the Galaxies [1]

Galaxy	A_K (mag)	M_K (mag)	CO_{sp}	$\log W_{Br\gamma}$ (Å)	$\log N_{Lyc}$ (s^{-1})	$\log L_{IR}$ ($L_\odot$)	HeI/Brγ
ARP 220	1.1	-24.2	0.18	1.04	54.28	11.93	< 0.3
NGC 6240	0.6	-24.9	0.23	0.85	53.98	11.63	—
NGC 1614	0.5	-24.0	0.31	1.41	54.63	11.51	0.56
NGC 2798	0.5	-21.6	0.30	1.03	53.32	10.26	0.63
NGC 3690 A	0.6	-22.3	0.27	1.56	54.07	11.49	0.69
NGC 3690 B	0.5	-22.7	—	1.19	53.79	11.10	0.29
NGC 3690 C	0.5	-21.4	—	1.86	54.07	10.92	0.50

[1] All measurements are for a 5″ aperture and corrected for extinction when appropriate.

very uncertain. Assuming that the underlying old stellar population is made of two normal galaxies, the central 5″ (1.7 kpc at the distance of ARP 220) should have a dynamical mass of $\sim 10^{10}$ $M_\odot$ (*cf.* Devereux, Becklin & Scoville 1987), very similar to the H_2 mass of 9×10^9 $M_\odot$ observed in the central $4 \times 6''$ (Scoville *et al.* 1986). Given these estimates, it is unlikely the total mass participating in the starburst should exceed 9×10^9 $M_\odot$.

Because of the He Iλ2.06μm non-detection, the HeI/Brγ ratio was excluded from the χ^2 analysis. The successful models are summarized in Table 4.2. The first set of models, referred as model A, were calculated with the average 2.2 μm extinction of 1.1 mag adopted in Chapter 2. Depending on the star formation rate history, the models yield ages between 23 and 41 million years. It was not possible to uniquely determine the lower mass limit of the IMF without the constraint from the mass. As seen in Table 4.2, provided that between one third and half of the total molecular mass is available for the starburst, models with $m_l = 0.1$ $M_\odot$ are clearly conceivable. However, the lower mass limit would have to be over 1 $M_\odot$ if less than 10% of the total mass is participating in the starburst. Thus, given current estimates of the mass in the core of ARP 220, there is no evidence that the IMF is biased against the formation of low-mass stars in this galaxy.

Although these models are best solutions for the input parameters, they still provide a very poor fit to the observations. As seen in Table 4.2, the models predict a CO_{sp} ~0.1 mag stronger than observed, a Brγ equivalent width weaker by almost a factor of two and too high (by a factor of two) ionization compared

Table 4.2
Model Summary for ARP 220

Age (10^6 yrs)	m_l ($M_\odot$)	m_u ($M_\odot$)	Mass (10^8 $M_\odot$)	SFR	M_K (mag)	CO_{sp}	$\log W_{Br\gamma}$ (Å)	$\log \frac{N_{Lyc}}{L_{IR}}$ (s^{-1} $L_\odot^{-1}$)	HeI/Brγ	χ^2
Model A: starburst only ($A_K = 1.1$)										
23	1.9	25	9	e-model	-24.20	0.29	0.77	42.61	0.24	31.6
23	0.1	25	43	e-model	-24.21	0.28	0.76	42.61	0.24	30.1
39	2.2	25	9	d-model	-24.19	0.28	0.81	42.64	0.25	27.8
35	0.1	25	45	d-model	-24.18	0.28	0.85	42.68	0.25	27.7
53	1.6	25	15	c-model	-24.18	0.26	0.77	42.61	0.26	25.3
47	0.1	25	59	c-model	-24.21	0.26	0.79	42.62	0.26	24.2
Target values			< 90		-24.2±0.1	0.18±0.03	1.04±0.08	42.35±0.1	< 0.3	
Model B: starburst + 30% of non-stellar emission ($A_K = 1.8$)										
11	1.6	25	11	e-model	-24.50	0.26	1.12	42.91	0.25	2.55
11	0.1	25	45	e-model	-24.51	0.25	1.11	42.91	0.25	3.17
19	1.9	25	11	d-model	-24.50	0.28	1.19	42.96	0.28	3.02
13	1.3	25	13	c-model	-24.50	0.29	1.09	42.92	0.27	4.03
29	2.2	35	13	e-model	-24.54	0.28	1.13	42.93	0.53	3.04
29	0.1	35	65	e-model	-24.49	0.27	1.12	42.93	0.53	2.97
Target values			< 90		-24.5±0.1	0.27±0.03	1.20±0.08	42.79±0.1	< 0.3	

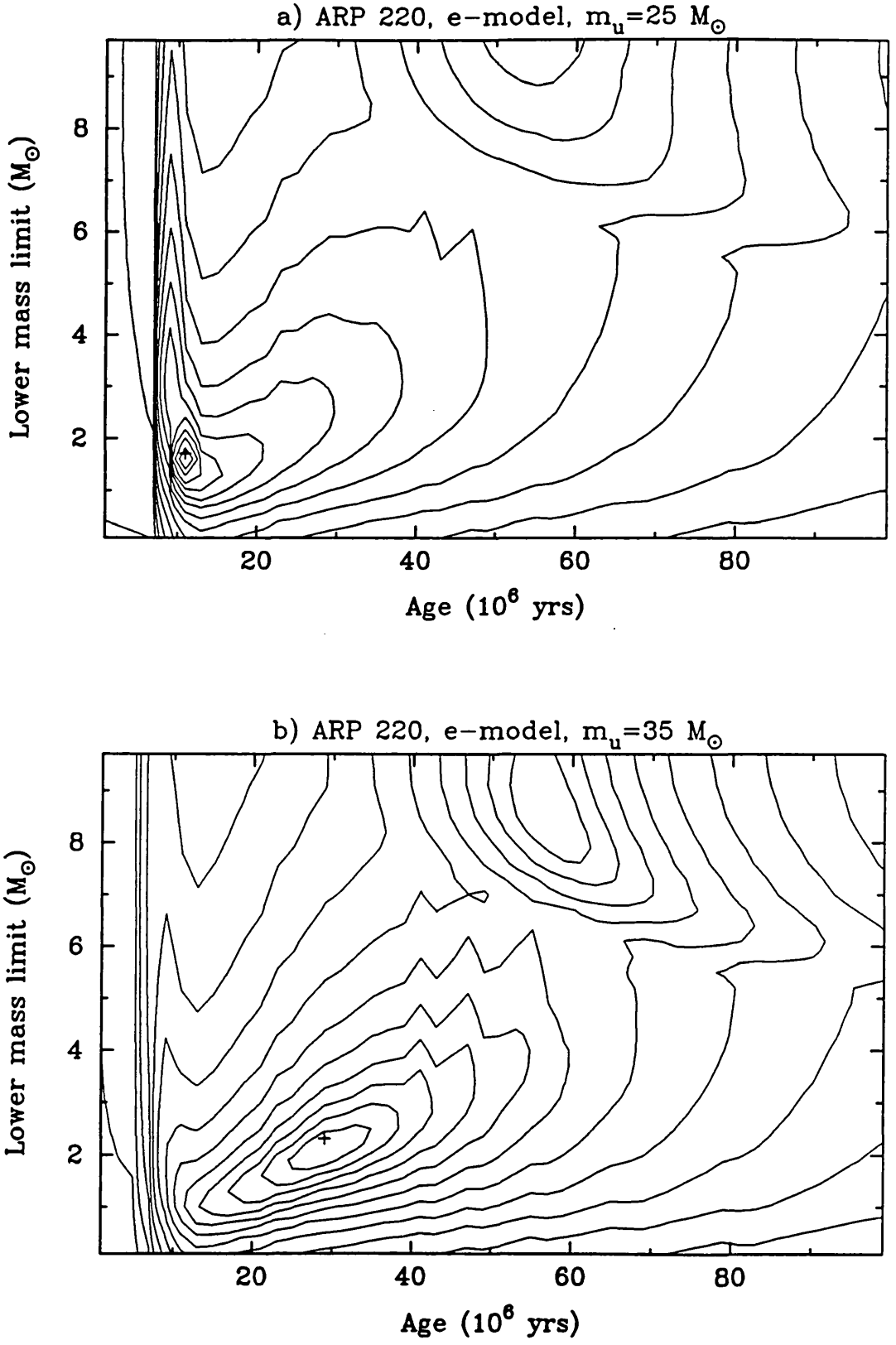

Figure 4.11— χ^2 diagram of ARP 220, calculated with an e-model and two upper mass limits, $m_u = 25$ (a) and 35 $M_\odot$ (b). The contours have been drawn as $1/\chi^2$ on a logarithmic scale, each one separated by "one sigma" ($e^{-1/2}$). The best solution appears as a maximum (marked as a cross) in the diagram.

with the bolometric luminosity. The disagreement between starburst models and observations could be explained if the extinction has been underestimated and a certain fraction of the K continuum and the bolometric luminosity is generated by a non-stellar source, perhaps an AGN. We have calculated another set of starburst models (model B in Table 4.2) assuming that 30% of the 2.2 μm and bolometric luminosity is associated with a non-stellar source. We further assumed an extinction of 1.8 mag at K which is the value inferred from the ratio of Brγ and Paβ (*cf.* Chapter 2). The new set of observables, corrected with the new extinction and the non-stellar contribution, are given in Table 4.2 (model B). The new quantities were derived assuming that the non-stellar source has a featureless spectrum.

It is clear from the χ^2 value (see Table 4.2) that the new models provide a much better fit to the observations. The age of the burst is probably not much older than than 30 million years, depending on the star formation rate history and the upper mass limit. The IMF parameters are not significantly affected by the new models. It would be possible to accommodate starburst models with as much as 50% of non-stellar contribution at 2.2 μm, but if true, this would imply an intrinsic spectroscopic CO index of 0.40 for the starburst population *i.e.* $\sim$0.1 mag stronger than the highest possible value predicted by stellar synthesis models. In order to produce such a strong CO band, characteristic of M2 supergiants (see Appendix A), the IMF would have to be restricted to a *very narrow* range of masses around the progenitor mass of M2Ia stars *i.e.* 15 $M_{\odot}$. Although speculative, the presence of a significant population of red supergiants later than M2 in ARP 220 is qualitatively supported by the detection of water absorption at $\sim$2.0 μm (*cf.* Chapter 2) which is typical of late-type supergiant spectra (*cf.* Kleinmann & Hall 1986).

The uniqueness of the models can be judged from the χ^2 diagram presented in Figure 4.11. The top figure was calculated with e-model, $m_u = 25\ M_{\odot}$ and a mass of $11 \times 10^8\ M_{\odot}$ ($\sim$1/10 of the total mass). The contours are drawn on a logarithmic scale, each one separated by a factor $e^{-1/2}$ ("one sigma"). For this set of parameters, the uncertainty on m_l and the age can judged from the extent of the first contour which is "one sigma" away from the peak. The contours are tightly bounded around a lower mass limit of 1.6 $M_{\odot}$ and an age of 11 million years. As mentioned earlier, this solution is not unique. Varying

the mass participating in the starburst would move the peak up and down in the diagram.

The effect of increasing the upper mass limit to 35 $M_\odot$ is illustrated in Figure 4.11b (see also Table 4.2). Except for the relatively high HeI/Brγ ratio predicted in this case, models with $m_u = 35\ M_\odot$ would be acceptable. However, the contours in the χ^2 diagram are not as tightly bounded as in Figure 4.11a suggesting that the former model with $m_u = 25\ M_\odot$ provides a better fit which is also supported by its slightly smaller χ^2 compared with the model with $m_u = 35\ M_\odot$. (see Table 4.2).

4.3.2 NGC 6240

This merging galaxy is characterised by a weak Brγ equivalent width and a small ionization rate to bolometric luminosity ratio. This suggests that the stellar population is relatively evolved compared with other starbursts showing strong ionization. The detection of the He Iλ2.06μm line in this galaxy is uncertain (*cf.* Chapter 2) and thus, it is difficult to constrain the upper mass limit from the HeI/Brγ ratio. However, given the weak Brγ equivalent with and the small ionization rate to bolometric ratio, we infer that the upper mass limit should be somewhere between 25 and 35 $M_\odot$. The mass of molecular gas in this galaxy is $2 \times 10^{10}\ M_\odot$ within 45″ (Sanders *et al.* 1986). If the molecular gas of NGC 6240 is spatially distributed as in ARP 220, then roughly half of the total mass should fall within the central 5″. Thus, the mass participating in the starburst is probably less than $10^{10}\ M_\odot$.

Successful starburst models of NGC 6240 are presented in Table 4.3. Unlike ARP 220, the age of NGC 6240 is quite sensitive to the shape of the star formation rate and the upper mass limit. Ages between 30 and 95 million years are predicted by the models. The χ^2 diagrams of an e-model and a c-model are compared in Figure 4.12. Although the contours are more tightly bounded in the former, the two models are equally acceptable, as judged from their similar χ^2 values (see Table 4.3).

Models with an IMF extending down to 0.1 $M_\odot$ are possible but would require most of the mass presently available ($10^{10}\ M_\odot$). This conclusion is somewhat in contradiction with the results of Rieke *et al.* (1985) who suggested, based on their starburst models, that the IMF in NGC 6240 is biased against the formation of low-mass stars. This discrepancy is due to the higher extinction ($A_K = 1.5$ instead of 0.6 for this work) and different starburst parameters

Table 4.3
Model Summary for NGC 6240

Age (10^6 yrs)	m_l ($M_\odot$)	m_u ($M_\odot$)	Mass (10^8 $M_\odot$)	SFR	M_K (mag)	CO_{sp}	$\log W_{Br\gamma}$ (Å)	$\log \frac{N_{Lyc}}{L_{IR}}$ (s^{-1} $L_\odot^{-1}$)	HeI/Brγ	χ^2
31	1.6	25	25	e-model	-24.88	0.28	0.65	42.48	0.24	5.1
29	0.1	25	99	e-model	-24.91	0.28	0.68	42.51	0.24	5.3
93	1.6	25	37	c-model	-24.90	0.23	0.63	42.51	0.26	4.7
95	0.7	25	79	c-model	-24.90	0.22	0.62	42.50	0.26	4.7
55	1.0	25	45	d-model	-24.87	0.26	0.62	42.47	0.25	4.4
57	0.4	25	93	d-model	-24.91	0.25	0.59	42.45	0.24	4.3
61	1.9	35	37	e-model	-24.90	0.22	0.60	42.50	0.53	5.1
63	0.7	35	95	e-model	-24.90	0.20	0.57	42.47	0.53	5.5
Target values.....			< 100		-24.9±0.1	0.23±0.04	< 0.85	42.35±0.1	—	

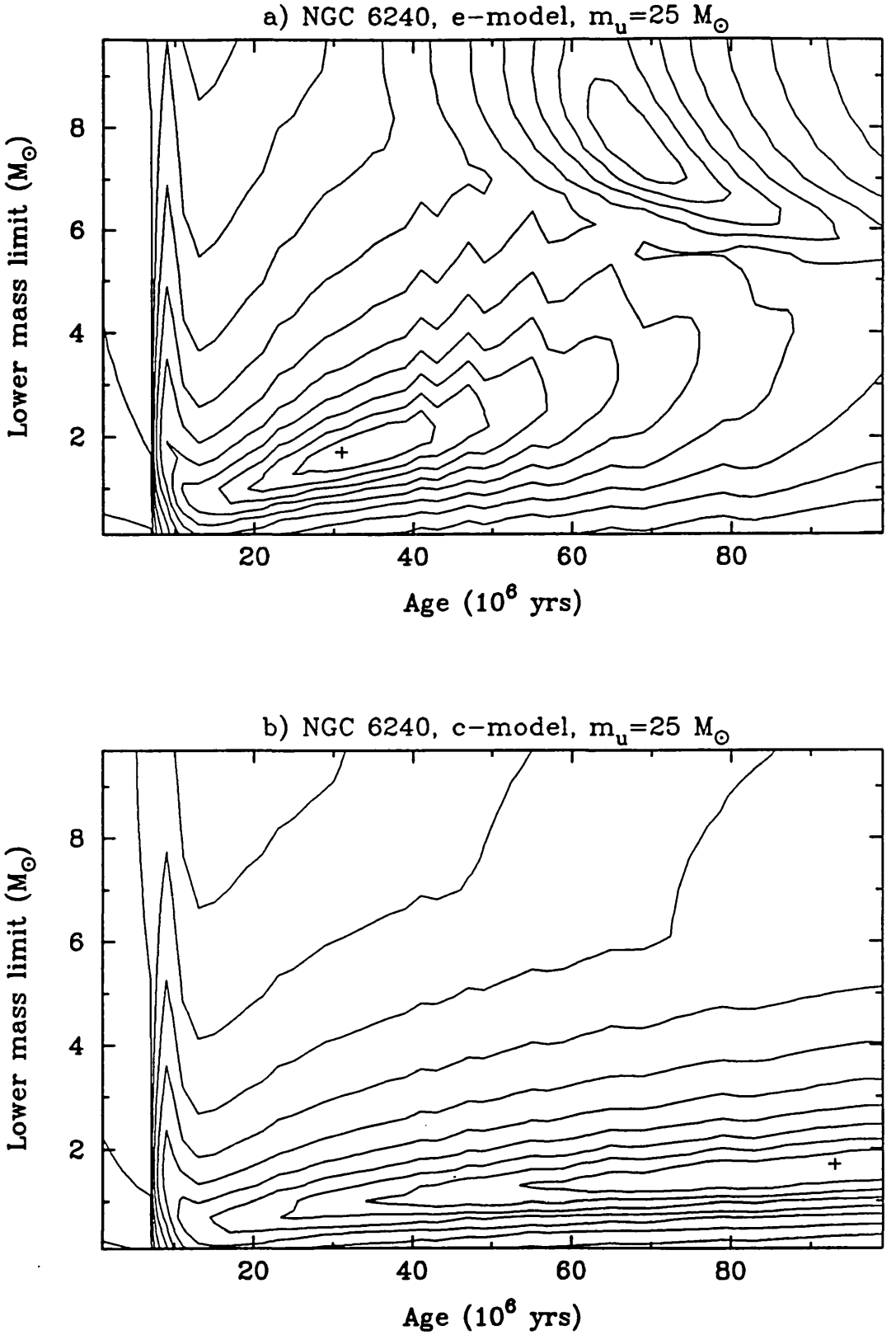

Figure 4.12— χ^2 diagrams of NGC 6240, calculated for two different star formation rate histories (exponential and constant). The contours have been drawn in the same way as in Figure 4.11.

adopted by Rieke *et al.* (1985). Using our model with their parameters (extinction, age and SFR history) yields a lower mass limit of ~3 $M_{\odot}$. The starburst models presented here show that the lower mass limit would be higher than ~1-2 $M_{\odot}$ only if 10%-20% of the total mass is participating in the starburst. Thus, the evidence that the IMF is deficient in low-mass stars in this galaxy is critically dependent on the value of the extinction and the amount of mass present in the nucleus.

Irrespective of the uncertainties in the IMF and the age, the models presented above show that the observational properties of NGC 6240 can be explained by vigorous star formation activity, without any contribution from an AGN-type source. In would be particularly useful to obtain an unambiguous detection of Brγ and He Iλ2.06μm to put stronger constraints on the age and the upper mass limit of this system.

4.3.3 NGC 1614

The HeI/Brγ ratio of 0.56±0.05 yields an upper mass limit of ~ 35 $M_{\odot}$ for this merging galaxy. The dynamical mass of the nucleus may be estimated from the Hα rotation curve of Ulrich (1972). Assuming a distance of 62 Mpc ($H_0 = 75\ km\ s^{-1}\ Mpc^{-1}$), the observed velocity gradient yields a mass of ~ 3×10^9 $M_{\odot}$ within the central 5″. Like ARP 220 and NGC 6240, this merger is characterized by a high concentration of molecular gas. From aperture synthesis mapping of the CO ($J = 1 - 0$) emission, Scoville *et al.* (1989) derived a mass of 1.8 × 10^9 $M_{\odot}$ for the central 4″×6″. We adopt this latter estimate as the maximum mass that could participate in the starburst.

As shown in Table 4.4, the observational properties of this galaxy are well reproduced by starburst models. The χ^2 diagrams presented in Figure 4.13 have well defined peaks. Depending on the star formation rate history, the age of the burst is between 13 and 27 million years. It was not possible to fit the observations with an IMF extending down 0.1 $M_{\odot}$ without violating the constraint that less than the total mass is participating in the starburst. If we assume that ~10-20% of the total mass is available for the burst, then the lower mass limit must be well above 3 $M_{\odot}$ to satisfy the observations. Based on different models and analysis, a similar result was obtained by Wright *et al.* (1988) for this galaxy.

Table 4.4
Model Summary for NGC 1614

Age (10^6 yrs)	m_l ($M_\odot$)	m_u ($M_\odot$)	Mass (10^8 $M_\odot$)	SFR	M_K (mag)	CO_{sp}	$\log W_{Br\gamma}$ (Å)	$\log \frac{N_{Lyc}}{L_{IR}}$ (s^{-1} $L_\odot^{-1}$)	HeI/Brγ	χ^2
13	3.1	35	3	e-model	-24.02	0.29	1.39	43.22	0.54	3.2
13	0.4	35	16	e-model	-24.01	0.28	1.38	43.22	0.54	5.7
27	3.7	35	3.5	d-model	-23.98	0.28	1.41	43.19	0.55	2.8
27	0.7	35	16.5	d-model	-24.01	0.27	1.40	43.18	0.55	4.7
23	3.1	35	4.5	c-model	-24.01	0.28	1.40	43.17	0.55	2.8
23	0.7	35	17	c-model	-24.00	0.27	1.39	43.16	0.55	
Target values			< 18		-24.0±0.1	0.31±0.02	1.41±0.02	43.12±0.1	0.56±0.05	

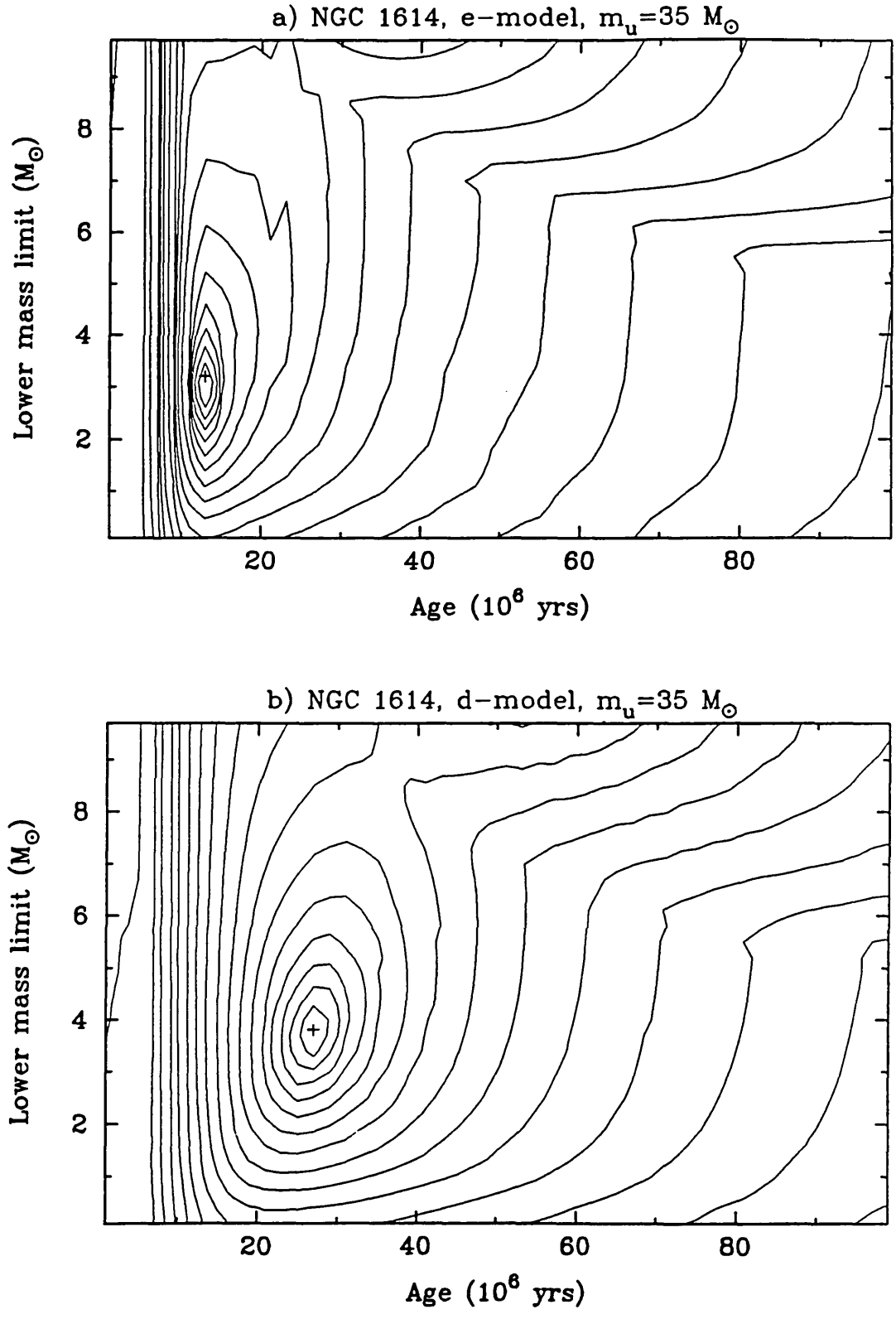

Figure 4.13— χ^2 diagram of NGC 1614, calculated for two different star formation rate histories: exponentially decreasing (e-model) and delayed (d-model). A mass of 3×10^8 $M_\odot$ was assumed for the e-model and 3.5×10^8 $M_\odot$ for the d-model. These masses give the best solutions if roughly 10-20% of the total mass is participating in the burst. The contours have been drawn on a logarithmic scale as described in Figure 4.11.

4.3.4 NGC 2798

The relatively high HeI/Brγ ratio of 0.63±0.06 observed in this interacting galaxy makes the upper mass limit very uncertain, but certainly greater than ~35 $M_{\odot}$. The dynamical mass in this system is also very uncertain but it is possible to obtain a rough estimate by assuming that the underlying stellar population is typical of normal spiral galaxy. Within the central 5″ (600 pc at a distance of 23 Mpc), the expected absolute H magnitude should be ~-19.9 which implies a total mass of 2×10^9 $M_{\odot}$ (*cf.* Devereux, Becklin & Scoville 1987). This estimate is probably an upper limit for the mass participating in the starburst. If the gas content on this galaxy is typical of a normal spiral in which ~10% of the total mass is in gaseous form then a more likely estimate of the mass participating in the burst is 2×10^8 $M_{\odot}$.

Unlike the galaxies discussed thus far, it was possible to constrain the lower mass limit of NGC 2798 *without* the constraint from the mass *i.e.* by excluding the absolute K magnitude from the χ^2 expression. This result is graphically illustrated by the χ^2 diagram of Figure 4.14a. The contours, calculated for an e-model with $m_u = 35$ $M_{\odot}$, are clearly concentrated around a lower mass limit of ~ 8.5 $M_{\odot}$. The age is not uniquely constrained but certainly greater than 35 million years. If we include the absolute K magnitude in the analysis, a similar solution ($m_l = 8.5$ $M_{\odot}$; age=37 million years) is obtained with a mass of 3×10^7 $M_{\odot}$ but this time, the χ^2 diagram shows a relatively well defined peak (see Figure 4.14b).

This particular solution is not unique and depends on the mass participating in the burst. As shown in Table 4.5, increasing the mass to 2×10^8 $M_{\odot}$ yields similar lower mass limits but higher ages around ~70 million years. Models with $m_u = 60$ $M_{\odot}$ also yield high lower mass limits but they tend to predict too small CO bands, an indication that the upper mass limit is probably closer to 35 $M_{\odot}$. Despite the uncertainties on m_u, the age and the star formation rate history, the models all have in common a relatively high lower mass limit, at least 1 $M_{\odot}$ and more likely around 6-8 $M_{\odot}$. The models presented in Table 4.5 also indicate that the best solutions are those with a decreasing SFR, especially e-models. Models with a constant SFR tend to produce too high Brγ equivalent widths and too small CO bands.

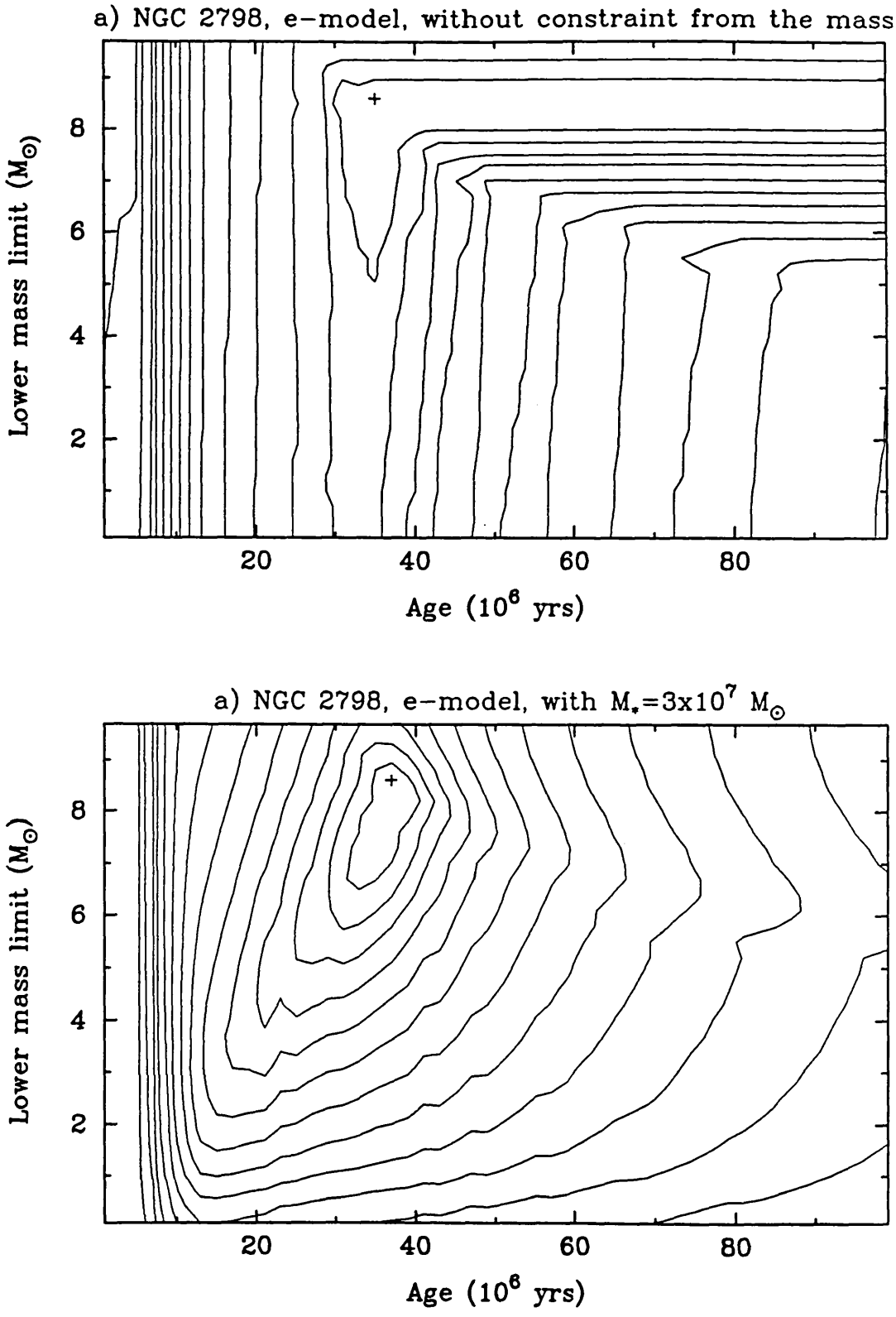

Figure 4.14— χ^2 diagram of NGC 2798, both calculated with an e-model and $m_u = 35\ M_\odot$. The top Figure was calculated without the constraint from the mass *i.e.* by excluding the absolute K magnitude from the χ^2 expression. The bottom Figure was obtained after including M_K and a mass of $3 \times 10^7\ M_\odot$. The contours have been drawn on a logarithmic scale as described in Figure 4.11.

Table 4.5
Model Summary for NGC 2798

Age (10^6 yrs)	m_l ($M_\odot$)	m_u ($M_\odot$)	Mass (10^8 $M_\odot$)	SFR	M_K (mag)	CO_{sp}	$\log W_{Br\gamma}$ (Å)	$\log \frac{N_{Lyc}}{L_{IR}}$ (s^{-1} $L_\odot^{-1}$)	HeI/Brγ	χ^2
37	8.5	35	0.3	e-model	-21.61	0.28	1.06	43.02	0.54	4.0
73	8.2	35	1.9	e-model	-21.57	0.28	1.02	42.99	0.53	4.4
83	7.6	35	0.9	d-model	-21.62	0.27	1.04	43.00	0.54	4.9
99	8.2	35	1.9	d-model	-21.68	0.28	1.09	43.04	0.54	6.1
83	5.5	35	0.5	c-model	-21.61	0.24	1.10	43.03	0.55	13.9
85	1.3	35	1.9	c-model	-21.55	0.23	1.09	42.97	0.55	17.8
75	7.3	60	1.9	e-model	-21.60	0.25	1.06	43.04	0.70	8.2
81	6.4	60	0.7	d-model	-21.56	0.24	1.07	43.04	0.70	11.5
99	1.6	60	1.9	c-model	-21.64	0.22	1.28	43.10	0.70	56.7
Target values			< 2		-21.6±0.1	0.30±0.02	1.03±0.04	43.06±0.1	0.63±0.06	

4.3.5 NGC 3690-IC 694

As described in Chapter 2, there are three sources of activity in this interacting system. All sources show strong Brγ and He Iλ2.06μm emission but the relative strength of these lines varies considerably from one source to another (see Table 4.1). As discussed in Chapter 3, the observed He Iλ2.06μm/Brγ ratios imply upper mass limits of closer to 60, 25 and 35 $M_{\odot}$ for sources A, B and C, respectively.

The high spatial resolution CO ($J = 1 - 0$) mapping of this system has revealed a fairly high concentration of molecular gas in the vicinity of sources A and C (Sargent *et al.* 1987). Within a beam of 5″, they derived an H_2 mass of 1.4×10^9 $M_{\odot}$ in both A and C and an upper limit of 3×10^8 $M_{\odot}$ for source B. We adopt these figures as the highest possible mass that could participate in the starburst. The starburst models of all three sources are listed in Table 4.6.

4.3.5.1 IC 694 (SOURCE A)

Assuming that only 10% of the mass is participating in the starburst, the "best" e-model for source A yields a lower mass limit of $\sim$2 $M_{\odot}$ and an age of $\sim$15 million years. Models with $m_l = 0.1$ $M_{\odot}$ are possible provided that $\sim$1/3 of the observed molecular mass is in the burst.

The major drawback of the "best" models presented in Table 4.6 is that it predicts a N_{Lyc}/L_{IR} of 43.3 dex, which is a factor of 5 higher than the ratio adopted. Part of this this discrepancy could be due to the fact that we have underestimated the extinction. A factor of two would be certainly conceivable if most of the reddening is *internal* and not foreground as assumed. This interpretation is indeed consistent with the larger extinction ($A_K = 1.3$) derived from the $Br\alpha$/Brγ ratio (*cf.* Nakagawa *et al.* 1989). It is unlikely that the remaining factor of two is due to an overestimated bolometric luminosity as there is no evidence for extended emission in IC 694 as suggested by the 20 μm mapping and far-infrared (50 and 100 μm) scanning observations of Joy *et al.* (1989).

Perhaps the most likely explanation is that half of the bolometric luminosity is generated by an AGN-like source. Assuming further that the ionization rate has been underestimated by the same factor, the N_{Lyc}/L_{IR} ratio of the stellar population would then increase to 43.2 dex, in much better agreement with the starburst models presented in Table 4.6. It is unlikely that the AGN

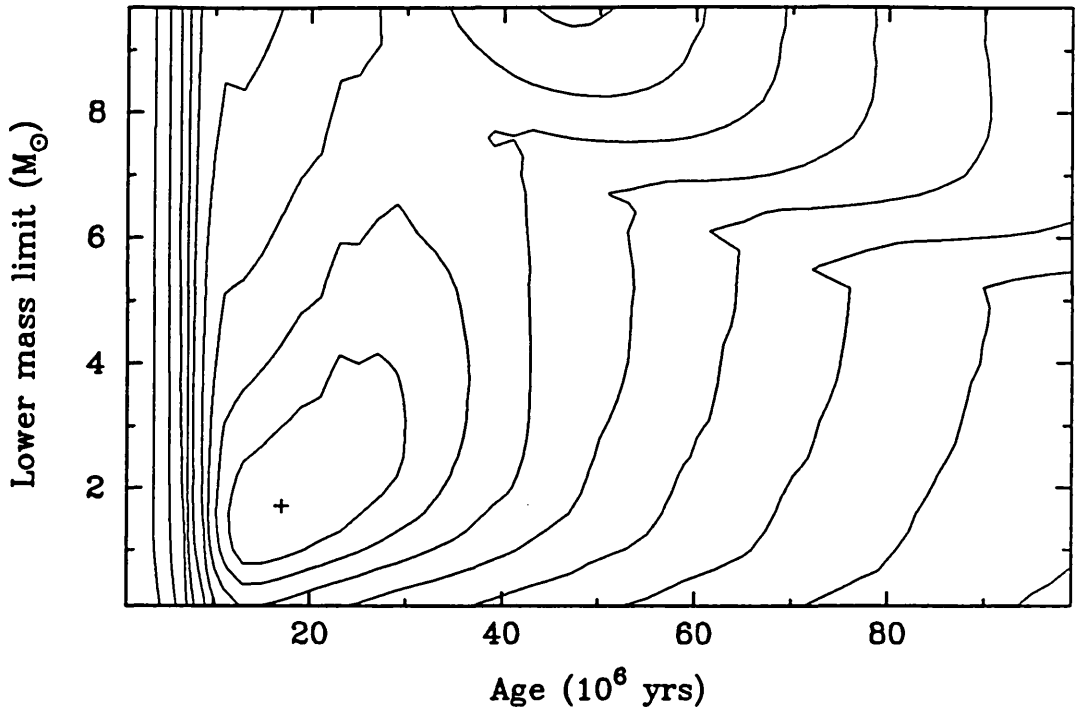

Figure 4.15— χ^2 diagram of IC 694 (source A), calculated with an e-model, $m_u = 60\ M_\odot$ and a mass of $1.3 \times 10^8\ M_\odot$ (~10% of the mass available) participating in the burst. The contours have been drawn on a logarithmic scale as described in Figure 4.11.

source would contribute as much as 50% of the K continuum, otherwise the spectroscopic CO index of the underlying stellar population would have to be 0.47, which is uncomfortably high compared with the maximum value of ~0.3 predicted by starburst models (see section 4.2). However, a contribution of 20-30% is conceivable. Although we argued in Chapter 2 that the $H - K$ excess and the red K continuum of source A is due to a combination of reddening and hot-dust emission, the possibility that the deviation from the reddening vector is due to a combination of *both* non-thermal (AGN) and hot-dust emission cannot be excluded (*cf.* Figure 2.10). The suggestion that a putative AGN is partly responsible for the activity observed in IC 694 is not new. Gehrz, Sramek and Weedman (1983) pointed out that starburst activity alone cannot explain the strong radio flux observed in this galaxy and suggested a contribution from an AGN to make up the deficit. The flat spectrum of the radio source also suggests the presence of an AGN in IC 694 (Condon *et al.* 1982).

This interpretation contrasts with that of Nakagawa *et al.* (1989) and Telesco, Decher and Gatley (1985), who argued that both the ionization rate and

Table 4.6
Model Summary for NGC 3690

Age (10^6 yrs)	m_l ($M_\odot$)	m_u ($M_\odot$)	Mass (10^8 $M_\odot$)	SFR	M_K (mag)	CO_{sp}	$\log W_{Br\gamma}$ (Å)	$\log \frac{N_{Lyc}}{L_{IR}}$ (s^{-1} $L_\odot^{-1}$)	HeI/Brγ	χ^2
					Source A (IC 694)					
17	1.6	60	1.3	e-model	-22.28	0.27	1.49	43.28	0.70	54.5
17	0.1	60	5.1	e-model	-22.30	0.27	1.49	43.27	0.70	53.1
35	1.3	60	2.3	d-model	-22.29	0.27	1.51	43.24	0.70	46.4
35	1.3	60	2.5	c-model	-22.27	0.27	1.52	43.245	0.70	45.4
Target values			< 14		-22.3±0.1	0.27±0.02	1.56±0.03	42.58±0.1	0.69±0.07	
					Source B (NGC 3690)					
11	1.6	25	2.1	e-model	-22.71	0.26	1.11	42.91	0.25	7.4
19	3.1	25	1.3	d-model	-22.75	0.29	1.13	42.92	0.27	7.2
13	2.2	25	1.5	c-model	-22.69	0.30	1.09	42.92	0.27	9.5
Target values			< 3		-22.7±0.1	—	1.19±0.05	42.69±0.1	0.29±0.05	
					Source C					
9	0.1	35	3.5	e-model	-21.36	0.19	1.85	43.36	0.55	5.6
13	0.1	35	3.5	d-model	-21.38	0.23	1.86	43.41	0.57	8.8
9	0.1	35	4.0	c-model	-21.35	0.19	1.94	43.40	0.56	10.6
Target values			< 14		-21.4±0.1	—	1.86±0.05	43.15±0.1	0.50±0.05	

the bolometric luminosity of IC 694 are consistent with simple starburst models. Their analyses were based on an ionization rate estimated from Brγ lines obtained in apertures larger than 5″ (*e.g.* Fischer *et al.* 1983; Beck, Turner & Ho 1986) which is a factor of two higher than the value adopted in this work. This ionization rate yields a N_{Lyc}/L_{IR} ratio of 42.9 dex which is in reasonable agreement with the starburst models presented in Table 4.6. Thus, although starburst activity can account for the observational properties of IC 694 on a large scale (the whole galaxy), the models presented here suggest that this interpretation is inappropriate for the central kpc of the nucleus.

4.3.5.2 Source B and C

Although we have no information on the CO band strength of these sources, it is still possible to constrain the starburst parameters. The best models for source B yield an age similar to the youngest model of source A *i.e.* ~15 million years. The ionization rate to bolometric luminosity ratio predicted by the models is ~60% stronger than observed which is probably not significant given the uncertainties in both the extinction and the bolometric luminosity. No model with an IMF extending down to 0.1 $M_{\odot}$ was possible without exceeding the maximum mass of 3×10^8 $M_{\odot}$. The lower mass limit of this source is certainly higher than 1.3 $M_{\odot}$.

The high Brγ equivalent width observed in source C yields a very young age of 9 million years. Like source B, the models tend to predict too high values of N_{Lyc}/L_{IR} but again, this could be due to uncertainties in both the extinction and the bolometric luminosity. As shown in Table 4.6, models with normal IMFs extending down 0.1 $M_{\odot}$ are certainly possible, requiring masses of $\sim 4 \times 10^8$ $M_{\odot}$ *i.e.* one fourth the observed mass of H_2 gas. It would be interesting to measure the spectroscopic CO index of source C. Our models predict a relatively small CO_{sp} of ~0.20. Combined with the fact that ~30% of the K continuum is due to hot-dust emission (*cf.* Chapter 2; see also Telesco, Decher & Gatley 1985), we predict that the spectroscopic CO index of source C should be ~0.15, significantly smaller than a normal stellar population characterized by a CO_{sp} of 0.2.

If we exclude the N_{Lyc}/L_{IR} ratio from the analysis, the models predict a common age of ~15 million years for all three sources, despite the fact that the Brγ equivalent width varies by as much as a factor of 5. This large scatter in $W_{Br\gamma}$ is not an age effect and results from different upper mass limits adopted

for the three sources. This clearly shows that it is essential to constrain the upper mass limit in order to determine the age of the burst. If the HeI/Brγ ratio provides a reliable measure of the upper mass limit then it is difficult to avoid the conclusion that the starburst in all three sources of activity has started roughly at the same time $\sim$15 million years ago.

4.3.6 THE TIME SCALE OF THE BURST

We have shown in previous sections that in general, it is very difficult to constrain the star formation rate history, whether it is constant, increasing or decreasing with time. We found, however, one example (NGC 2798) in which there was good evidence that the SFR is declining with time.

If we assume that the SFR is declining exponentially, it is possible to determine roughly the time scale τ_0 of the burst ($SFR \propto \exp(-t/\tau_0)$) from a statistical argument. Because of selection effects, it is likely that on average, starburst galaxies are observed at an early stage when the SFR is still relatively high. For an exponentially decreasing SFR, the age of the burst should be of the order of τ_0. Thus, the average age of several starburst galaxies, as derived from the models, should provide a rough estimate of τ_0. Although the age derived from a starburst model depends inevitably on the star formation rate history, one can nevertheless obtain an upper limit by assuming a constant SFR. From the models presented earlier, we find an average age of $\sim$30 million years, as estimated from c-models. Thus, if the SFR is exponentially decreasing in the galaxies modelled earlier, the time scale of the burst is probably lower than 30 million years.

4.4 Summary and Conclusions

An evolutionary model has been developed to predict the observational properties of a young stellar population characteristic of starburst galaxies. The dependence of several near-IR observables on the age and the IMF parameters has been investigated. These observables include the absolute K magnitude, the spectroscopic CO index, the Brγ equivalent width, the HeI/Brγ ratio and the ionization rate to bolometric luminosity ratio. The main results of this theoretical investigation are:

1) The 2.2 μm luminosity of a young stellar population is dominated by red supergiants after only 10 million years. Models including a pre-existing old

stellar population (10% of the total mass in the burst) show that the starburst will enhance the integrated 2.2 μm luminosity by a factor of two if the IMF includes stars as low as 0.1 $M_{\odot}$. In order to produce a 2.2 μm excess greater than 4 as typically observed in starburst galaxies, the lower mass limit of the IMF must be greater than 1 $M_{\odot}$.

2) Provided that the upper mass limit is known, the Brγ equivalent width is a very good age indicator and discriminant of the star formation rate history.

3) The strength of the CO band absorption longward of 2.3 μm is predicted to reach a maximum after ~15 million years, irrespective of the star formation rate history. At the peak, the spectroscopic CO index is predicted to be ~0.1 mag stronger than observed in normal galaxies, a result which is in good agreement with observations. The strength of the CO band remains strong for a relatively short period, of the order of the time scale of the burst. This shows that it is not a necessary condition for a starburst to have an unusually strong CO band.

A χ^2 analysis has been developed to provide an objective way of constraining the age and the parameters of the IMF in starburst galaxies. This technique has been applied to the merging galaxies ARP 220, NGC 6240, NGC 1614 and the interacting galaxies NGC 2798 and NGC 3690-IC 694. The results of this analysis are:

1) In general, starburst activity alone can reproduced the observational properties of the galaxies, except for ARP 220 and IC 694 in which there is evidence for a non-stellar source (perhaps an AGN) contributing a significant fraction (30%-50%) of the bolometric luminosity.

2) The observational properties of NGC 2798 are best explained with an IMF having $m_l \approx 8\ M_{\odot}$ *i.e.* strongly deficient in low-mass stars. This result is independent of the mass participating in the burst. The IMF of other galaxies must also be restricted to stars with mass $\gtrsim 3\ M_{\odot}$ *if* only ~10% of the mass is available for the burst. Solar neighbourhood IMF's with $m_l = 0.1\ M_{\odot}$ are conceivable if a large fraction (50 to 100%) of the observed mass of molecular gas is participating in the starburst.

3) The age of the burst inferred from starburst models is typically ~30 million years. Clear evidence was found in NGC 2798 that the star formation rate is declining with time. Assuming that the star formation rate is exponentially

decreasing, the average age of the galaxies suggests that the time scale of the burst is probably not longer than 30 million years.

Chapter 5

The Excitation Mechanism of the H_2 Emission in Starburst Galaxies

5.1 Introduction

Perhaps the most puzzling feature in near-infrared (IR) spectra of starburst galaxies is the strong quadrupole emission of molecular hydrogen (H_2), the easiest detected transition being the v =1-0 S(1) at 2.1218 μm. Although H_2 lines have been detected in more than 50 galaxies, amongst them interacting and merging systems (*e.g.* Joseph, Wright & Wade 1984; Rieke *et al.* 1985; DePoy, Becklin & Wynn-Williams 1986; Lester, Harvey & Carr 1988; Prestwich 1989; Moorwood & Oliva 1988; see also Chapter 2), Seyferts (Thompson *et al.* 1978; Hall *et al.* 1981; Fischer *et al.* 1987; Kawara, Nishida & Gregory 1987) and bright spirals (Puxley, Hawarden & Mountain 1988), except for a few objects, the nature of the exciting source responsible for the H_2 emission is still unknown.

In general, the H_2 gas can be excited either by collisions or by absorption of ultraviolet (UV) photons in the Lyman and Werner electronic bands (912-1108 Å), followed by a de-excitation cascade to the ground state (fluorescence). In principle, both mechanisms can be discriminated by measuring the 2-1 S(1)/1-0 S(1) and 1-0 S(0)/1-0 S(1) line ratios which are predicted to be 0.1 and 0.2 in thermal spectra (Hollenbach & Shull 1977; Brand *et al.* 1988) but as high as 0.6 and 0.5 in the fluorescent case (Black & Dalgarno 1976; Black & Van Dishoeck 1987). Collisionally excited H_2 emission has been observed in

a variety of Galactic sources including young stellar objects (YSO) and bipolar outflows (*e.g.* the Orion nebula; Gauthier *et al.* 1976), planetary nebulae (Treffers *et al.* 1976), Herbig-Haro objects (Elias 1980), supernova remnants (SNR) (Graham, Wright & Longmore 1987) and the Galactic centre (Gatley *et al.* 1984). Although less numerous, fluorescent H_2 sources have been found in reflection nebulae (Sellgren 1986, Gatley *et al.* 1987), the photodissociation region of the Orion bar (Hayashi *et al.* 1985), the planetary nebula Hubble 12 (Dinerstein *et al.* 1988) and the extragalactic H II region NGC 604 in M33 (Israel *et al.* 1989).

Until recently, the relatively small or undetected 2-1 S(1) line in most galaxies was interpreted as strong evidence for thermal excitation associated with shocks driven by supernova remnants, cloud-cloud collisions or galactic winds. However, recent theoretical development has challenged this interpretation. Sternberg and Dalgarno (1989) showed that at sufficiently high density ($n_H > 10^4$ cm^{-3}), fluorescently-excited H_2 emission will have the characteristics of a thermal spectrum, due to the collisional de-excitation of the high vibrational levels. The situation is even more complicated by the work of Hollenbach and McKee (1989) who showed that fast dissociative J-shocks can produce line ratios characteristic of fluorescent emission if H_2 molecules are reformed, downstream of the shock, in excited vibrational levels. Thus, although H_2 line ratios still provide an important diagnostic for constraining the excitation mechanism, independent information and theoretical considerations of the physical conditions prevailing in H_2 emitting galaxies are also essential for identifying the exciting source of the H_2 emission. The study of Puxley, Hawarden and Mountain (1990; PHM) is a good illustration of this point. They showed, with relatively simple models, that photodissociation regions associated with an ensemble of young stars provide a viable scenario for explaining a wide range of 1-0 S(1)/Brγ ratios observed in starburst galaxies. Although this does not prove that fluorescence is the dominant excitation mechanism in galaxies, it does suggest that this mechanism must be seriously considered when interpreting extragalactic H_2 spectra.

What is clear from an observational point of view is that there is as yet no unambiguous detection of *low-density* fluorescence in a galaxy *i.e.* no galaxy has been found with a large 2-1 S(1)/1-0 S(1) line ratio. The report of such detection in several bright spirals (Puxley, Hawarden & Mountain 1988) is cer-

tainly tantalizing but their spectra were obtained at relatively low resolution ($R \approx 100$) which makes the assignment of the continuum around the 1-0 S(0) and 2-1 S(1) very difficult and this can be misleading for estimating line ratios (Joseph 1989; Moorwood & Oliva 1989). In this chapter, we present strong evidence, at least for two interacting and merging galaxies, that a large fraction of the H_2 emission is produced by low-density fluorescence. This conclusion is based not only upon the observed line ratios but also from theoretical considerations of the physical conditions prevailing in the nucleus of these galaxies.

5.2 Constraints from H_2 Line Ratios

Extinction-corrected H_2 line ratios of four interacting and merging galaxies are presented in Table 5.1. The ratios were derived from the medium resolution ($R \sim 300$) spectra presented in Chapter 2. Only galaxies showing the detection of more than one H_2 transition were included. For ARP 220, NGC 6240 and IC 694, the extinction was derived from the 1-0 Q(3)/1-0 S(1) line ratio of H_2 (see Table 2.6 in Chapter 2) assuming the extinction law of Draine (1989). Because the detection of the 1-0 Q(3) line is very uncertain in NGC 1614, an average extinction was adopted, as derived from other methods. For comparison, line ratios predicted by typical shock and low-density ($< 10^4$ cm^{-3}) fluorescence models are also given in Table 5.1.

It is clear from this table that the shock model fails to explain the H_2 line ratios observed in NGC 1614 and IC 694, particularly in the former. A significant contribution of non-thermal or fluorescent emission is obviously needed to explain the relatively strong 1-0 S(0), 2-1 S(1), 2-1 S(3) and 1-0 Q(1) transitions. *NGC 1614 and IC 694 probably represent the first galaxies in which low-density UV fluorescence is unambiguously detected.*

In NGC 1614, the line ratios are consistent with the H_2 gas being excited by UV fluorescence only. However, the 1-0 S(2)/1-0 S(1) ratio of 1.35±0.2 observed in this galaxy is much too strong compared with the ratio of 0.5 predicted by UV fluorescence. The origin of this discrepancy is not clear but it could be that an unidentified line is contaminating the 1-0 S(2). This hypothetical line would have to be very close to the 1-0 S(2) since the emission spectral feature centred on this line is unresolved. Although the existence of this unknown line is very speculative, it is interesting to note that some unidentified emission features have already been found in the K spectrum of this galaxy (*cf.* Chapter 2).

Table 5.1

H_2 Line Ratios of Interacting and Merging Galaxies

Line	λ^a (μm)	I/I_0^b				Model		
		ARP 220	NGC 6240	NGC 1614	IC 694	shock[c]	UV[c]	mixed[d]
1-0 S(2)	2.0338	0.28±0.04	0.48±0.03	1.35±0.20	0.38±0.04	0.37	0.50	0.44
2-1 S(3)	2.0735	< 0.15	0.15±0.02	0.47±0.24	< 0.25	0.08	0.35	0.22
1-0 S(1)	2.1218	1.00	1.00	1.00	1.00	1.00	1.00	1.00
2-1 S(2)	2.1542	< 0.15	0.13±0.02	< 0.23	0.17±0.03	0.03	0.28	0.16
1-0 S(0)	2.2233	< 0.20	0.20±0.02	0.47±0.08	0.31±0.03	0.21	0.46	0.34
2-1 S(1)	2.2477	< 0.20	0.12±0.02	0.41±0.07	0.29±0.03	0.08	0.56	0.32
1-0 Q(1)	2.4066	0.76±0.11	0.70±0.03	1.41±0.21	0.78±0.06	0.70	0.99	0.85
1-0 Q(2)	2.4134	—	0.21±0.02	0.53±0.25	0.48±0.06	0.23	0.51	0.37
1-0 Q(3)	2.4237	0.70±0.09	0.70±0.13	0.70±0.05	0.70±0.13	0.70	0.70	0.70

[a] Wavelength in vacuum.

[b] Corrected for extinction. 3σ upper limits are given for undetected lines.

[c] Shock and UV line ratios from Black & Van Dishoeck (1987) model S2 and model 14.

[d] Expected line ratios assuming equal contribution from shock and UV excited H_2 gas.

The relatively strong 1-0 S(0)/1-0 S(1) and 2-1 S(1)/1-0 S(1) line ratios in IC 694 are also suggestive of non-thermal excitation although other line ratios are consistent with the shock model. This suggests that the H_2 emission in this galaxy is produced by both thermal and non-thermal excitation. This interpretation is strengthened when we compare the observed ratios with those predicted by a "mixed" model in which half of the H_2 emission is thermally-excited, the rest being produced by UV fluorescence. The expected ratios for this model are given in the last column of Table 5.1. The agreement between these ratios and those observed in IC 694 is reasonably good.

Unlike NGC 1614 and IC 694, the H_2 line ratios observed in ARP 220 and NGC 6240 are consistent with thermal excitation. The line ratios of NGC 6240 presented in this work are generally in good agreement with those measured by Lester, Harvey & Carr (1988). Although thermal or shock excitation provides a good fit to most of the H_2 line ratios of this galaxy, it fails to reproduce the strength of the 2-1 S(3) and 2-1 S(2) lines which are observed to be stronger than expected by at least a factor of two. This result, however, is marginally significant because these transitions are relatively weak. Further, given the relatively small resolution of the spectrum ($R \sim 200$), the transitions are subject to uncertainties is determining the local continuum and potential contamination by unidentified lines. Higher resolution and signal-to-noise observations are needed to determine whether the apparent discrepancy with the shock model is genuine.

5.3 Nature of the exciting source

Although H_2 line ratios provide a strong constraint on the excitation mechanism responsible for the observed H_2 emission, the nature of the exciting source still remains to be determined. Although it is appealing to associate the thermal H_2 emission of ARP 220 and NGC 6240 with shocks driven by young stellar objects (YSO), supernova remnants (SNR), interaction-driven cloud-cloud collisions or an AGN-driven galactic wind, in principle UV fluorescence at high density ($\gtrsim 10^5$ cm^{-3}) cannot be excluded as a potential excitation mechanism. Conversely, although the copious production of UV photons by the young stellar population of a starburst galaxy provides an attractive scenario for producing non-thermal H_2 emission, fast dissociative J-shocks could be equally responsible for the fluorescent H_2 emission observed in NGC 1614 and IC 694. Thus, in

order to identify the exciting source(s) of the H_2 emission, it is fundamental to determine, inevitably from theoretical considerations, the relative contribution of these different sources. This is the subject of the following sections.

5.3.1 H_2 EMISSION CONTRIBUTION FROM A SHOCK COMPONENT

5.3.1.1 YOUNG STELLAR OBJECTS AND SUPERNOVA REMNANTS

Since the most common sources of shock excited H_2 emission in the Galaxy are associated with young stellar objects and supernova remnants, it is natural to suppose that these sources should have a certain contribution to the integrated H_2 luminosity of starburst galaxies. Whether this contribution is significant or not is what we will try to estimate here.

In order to estimate the H_2 contribution of these sources, one needs to know their intrinsic H_2 luminosity and their lifetime. The best studied YSOs are the Orion nebula, DR21, Cepheus A and NGC2071 which have been measured to have a 1-0 S(1) luminosity, corrected for extinction, of 6 $L_\odot$ (Burton & Puxley 1989), 180 $L_\odot$ (Garden *et al.* 1986), 1.2 $L_\odot$ (Doyon & Nadeau 1988) and 1.1 $L_\odot$ (Lane & Bally 1986), respectively. The figure for DR 21 is very uncertain because its distance is known only within 30%. Taking the weighted average of these luminosities, weighting DR 21 with half the weight assigned the other sources, yields an average 1-0 S(1) luminosity $L_{S(1)}^{YSO} \approx 30\ L_\odot$. The lifetime of these sources can be estimated from the ratio of the shock velocity and the spatial extent of the H_2 emission. More sophisticated techniques, based on this principle, yield a lifetime of $(1-3) \times 10^4$ years (Fischer *et al.* 1985; Oliva & Moorwood 1986). We adopt an average value of 2×10^4 years.

There are at present 3 supernova remnants where the H_2 emission have been detected, namely IC 443 (Graham, Wright & Longmore 1987; Burton *et al.* 1988), RCW103 (Oliva, Moorwood & Danziger 1989) and the Crab nebula (Graham, Wright & Longmore 1990). The integrated 1-0 S(1) luminosity of these sources are 70 $L_\odot$ for IC443, 60-90 $L_\odot$ for RCW103 and less than 1 $L_\odot$ for the Crab nebula; all values have been corrected for extinction except for RCW103. These luminosities are somewhat uncertain since a small fraction of the total remnants were mapped. Remnants in the LMC are not plagued by this problem. Oliva, Moorwood & Danziger (1989) detected the [FeII]1.644μm emission in three LMC remnants and provided upper limits for the 1-0 S(1) line corresponding to luminosities between 3 and 70 $L_\odot$. This is consistent with the

luminosities of Galactic remnants. We conservatively adopt a value of 70 $L_\odot$ as the typical 1-0 S(1) luminosity of SNRs. As for the lifetime of the remnants, we adopt the age of IC 443 estimated to 1.3×10^4 years (Parkes, Culhane & Ives 1977).

These numbers can now be used along with the evolutionary model described in previous chapters to estimate the integrated H_2 luminosity associated with YSOs and SNRs. We assume that all stars more massive than 6 $M_\odot$ experience a YSO phase at their formation, emitting a constant 1-0 S(1) luminosity of 30 $L_\odot$ for a period of 2×10^4 years. It also assumed that these stars will become type II supernovae at the end of their life, their remnants emitting a 1-0 S(1) luminosity of 70 $L_\odot$ for a period of 1.3×10^4 years. Since the model also provide the Brγ luminosity from the ionization rate, we can then predict the 1-0 S(1)/Brγ ratio associated with YSOs and SNRs as a function of time.

Although the intrinsic luminosities and time scales of these sources are uncertain, there are reasons to believe that the 1-0 S(1)/Brγ ratio predicted by our simple calculation will probably be overestimated. First, in deriving the 1-0 S(1)/Brγ we implicitly assumed that the extinction towards the molecular and ionized gas is the same. This is probably very conservative since the H_2 emission associated with YSOs and SNRs arises from regions deep in molecular clouds with typical visual extinction of 20 mag whereas the young OB stars contributing to the ionization are mostly located, on average, in the diffuse interstellar medium (ISM). Indeed, comparison of the relative number of compact HII regions and O stars in our galaxy shows that the latter spend only 15% of their lifetime embedded in their parent molecular clouds (Wood & Churchwell 1989b). Thus, it is likely that the Brγ emission suffers less extinction than the 1-0 S(1) line. Furthermore, it is very optimistic to assume that the H_2 luminosity is constant over the lifetime of YSOs and SNRs. The fact that the H_2 luminosity of the Crab nebula is an order of magnitude smaller than the much older remnant IC 443 is probably an indication that the intrinsic H_2 luminosity of SNRs is time-dependent.

The evolution of the 1-0 S(1)/Brγ ratio as a function of time is shown in Figure 5.1. The models were calculated with a solar neighbourhood IMF (Scalo 1986) and a lower and upper mass limit of 0.1 and 30 $M_\odot$, respectively. The effect of the star formation rate (SFR) history was also investigated using three different birthrate functions: constant, exponentially decreasing, and delayed,

the latter two with a time scale of 2×10^7 years. For the first 10 million years, the H_2 luminosity is dominated by YSOs, and apart from the very early stage of the burst (< 5 million years), the 1-0 S(1)/Brγ ratio is $\sim$ 0.05. The ratio begins to rise at $\sim$30 million years because of the increasing contribution of H_2 emission from SNRs and the rapidly decreasing Brγ flux. These calculations show that large 1-0 S(1)/Brγ ratios in the range of 0.5-1, as typically observed in star-forming galaxies (Moorwood & Oliva 1988; PHM) *cannot be explained by starburst models unless the age of the burst is greater than $\sim$60 million years and the SFR exponentially decreasing or delayed. The model also suggests that the contribution from YSOs to the total H_2 emission is relatively small (< 20%) in starbursts younger than < 30 million years.*

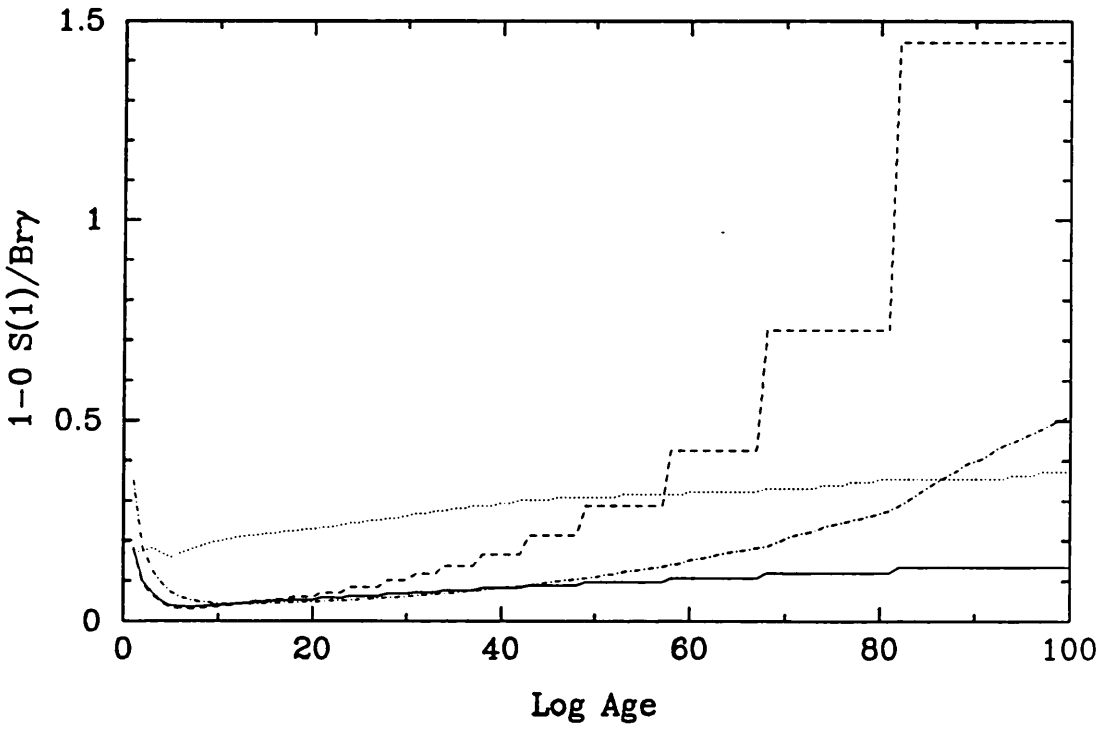

Figure 5.1— Evolution of the 1-0 S(1)/Brγ line ratio with time calculated as described in the text for YSOs and SNRs. Except for the dotted line, the curves correspond to different star formation rate histories: constant (solid line), exponential (dash line) and "delayed" (dash-dot line). The last two SFR were calculated with a time scale of 2×10^7 years. The broken appearance of the dash line is not real but due to the digital nature of the model. The dotted line represents the ratio predicted by a UV fluorescence model (see text).

The 1-0 S(1)/Brγ ratios of the galaxies discussed in Chapter 2 are given

in Table 5.2 along with the age and the upper mass limit (m_u) inferred from the starburst models presented in Chapter 4. Given these starburst parameters, the theoretical S(1)/Brγ ratios associated with YSOs and SNRs were calculated for individual objects, assuming a Scalo IMF and a lower mass limit (m_l) of 5 $M_\odot$. This particular value of m_l was chosen since it is representative of these galaxies (*cf.* Chapter 4). As shown in Table 5.2, the contribution of YSOs and SNRs to the total H_2 emission varies considerably from one galaxy to another. This contribution is less than 5% in NGC 6240 and ARP 220 but as much as 40% in source B of NGC 3690. YSOs and SNRs could be responsible for all of the H_2 emission observed in the relatively old starburst NGC 2798. In particular, these results show that YSOs and SNRs are unlikely to be the source of the shock (thermal) component which apparently contributes half of the total H_2 emission in IC 694. This suggests perhaps that a more exotic mechanism (*e.g.* interaction-driven cloud-cloud collisions, excitation by an AGN wind) is responsible for the thermal component of the H_2 emission in this galaxy.

5.3.1.2 INTERACTION-DRIVEN CLOUD-CLOUD COLLISIONS

Another possible source of collisionally-excited H_2 emission is that associated with large scale shocks driven by the merger of two galaxies. This mechanism is probably responsible for the strong H_2 emission observed in the merger NGC 6240. Recent line imaging of this galaxy (Herbst *et al.* 1990) has revealed that the peak of the H_2 emission is displaced from the two infrared nuclei, a feature that was interpreted as evidence that large scale shocks are responsible for the excitation of the H_2 gas. Thus, in principle, the relative spatial extent of the H_2 emission and the 2.2 μm continuum provides a way of determining whether large scale shocks are responsible for the integrated H_2 emission.

NGC 1614 is the only galaxy for which we have information on the spatial extent of the H_2 emission. A spectrum taken 5″ west of the nucleus shows a 1-0 S(1) line equally strong as on the nucleus but Brγ is not detected at this position (*cf.* Chapter 2). Further, the K spectrum is flatter than on the nucleus, suggesting higher extinction. These observations suggest that, like NGC 6240, the peak of the H_2 emission in NGC 1614 is significantly displaced from the 2.2 μm nucleus, an indication that large scale shocks are responsible for the excitation of the H_2 gas outside the nucleus.

In principle, large scale shocks could be responsible for the excitation of the H_2 gas on the nucleus of NGC 1614 but these shocks would have to be very

Table 5.2
1-0 S(1)/Brγ Line Ratios of Interacting and Merging Galaxies

Galaxy	Age (10^6 yrs)	m_u ($M_\odot$)	S(1)/Brγ	$M_{H_2}/L_{Br\gamma}$ [a] ($M_\odot/L_\odot$)	n (cm^{-3})	R [b]	Theoretical S(1)/Brγ	
							YSOs + SNRs	UV
ARP 220	11	25	2.9±0.4	1700	10^5	1.9	0.13	3.6
NGC 6240	55	35	>7.7	>1600	10^5	1.8	0.21	2.7
NGC 2798	70	35	0.36±0.05	—	—	—	0.51	—
NGC 1614	15	35	0.17±0.03	150	10^4	1.2	0.05	0.23
NGC 3690 A (IC 694)	15	60	0.97±0.04	420	10^4	2.0	0.04	0.37
NGC 3690 B	11	25	0.34±0.07	<170	10^4	1.3	0.13	0.48
NGC 3690 C	9	35	0.22±0.04	430	10^4	2.0	0.04	0.44

[a] Source of H_2 mass: ARP 220 (Scoville *et al.* 1986); NGC 6240 (Sanders *et al.* 1986); NGC 1614 (Scoville *et al.* 1989); NGC 3690-IC 694 (Sargent *et al.* 1987). $L_{Br\gamma}$ was derived from extinction-corrected Brγ fluxes given in Table 2.4 of Chapter 2.
[b] Dimensionless cloud-source separation, calculated as described in the text.

fast and dissociative in order to account for the non-thermal H_2 line ratios. According to the J-shock model of Hollenbach and McKee (1989), a shock velocity in excess of $\sim$150 km s^{-1} would be required to explain the observed 1-0 S(1)/Brγ ratio of less than $\sim$0.3. In this scenario, *all* the ionization would be produced behind shock fronts. Although we cannot exclude that possibility, it is more likely that the bulk of the ionization is produced by young OB stars. The presence of numerous red supergiants (descendents of OB stars) in the nucleus, as evidenced both by the unusually strong 2.2 μm luminosity and by the 2.3 μm CO band absorption (*cf.* Chapter 2), proves without doubt that the ionization is produced by OB stars. In fact, detailed modelling shows that all of the observational properties of NGC 1614 can be easily understood in terms of vigorous star formation activity (*cf.* Chapter 4).

In summary, although large scale shocks provide an appealing mechanism for explaining the strong H_2 emission observed in ARP 220 and NGC 6240, it is unlikely to explain the H_2 emission observed on the nucleus of NGC 1614 but could be responsible for the strong emission emitted off the nuclear region. High-resolution spatial observations are needed to determine whether large scale shocks contribute a significant fraction of the H_2 emission in interacting and merging galaxies.

5.3.2 H_2 EMISSION CONTRIBUTION FROM UV FLUORESCENCE

Copious production of UV photons is a natural consequence of vigorous star formation activity. If there is enough molecular material in the vicinity of young OB stars then the UV radiation field will interact with the molecular gas and produce fluorescent H_2 emission. Fischer *et al.* (1987) and Puxley, Hawarden and Mountain (1988) have used a simple criteria to show that fluorescence is indeed a viable mechanism for explaining the H_2 emission in some AGNs and starburst galaxies. More recently, PHM have used models of star-forming regions to show that a wide range of 1-0 S(1)/Brγ ratios observed in starburst galaxies can be explained by UV fluorescence. In particular, they showed that this ratio is critically dependent on the geometry of the emitting regions. In this section, we use PHM's model (a similar version of it) along with some constraint on the geometrical dilution of the UV radiation field to predict the S(1)/Brγ ratio of the galaxies discussed in this chapter.

We suppose that the emitting region is made of molecular clouds bathed in UV radiation produced by young massive stars. Non-ionizing photons in

the Werner and Lyman bands (910-1108 Å) interact with the molecular gas to produce fluorescent H_2 emission at the surface of each cloud. The H_2 luminosity produced depends on the molecular gas density ($n = 2n_{H_2} + n_H$) and the intensity of the UV radiation incident on the molecular clouds. The latter depends on the average distance between cloud and stars. Following PHM, we express this distance with a dimensionless cloud-source separation R which is in units of the Strömgren sphere R_s. It can be shown that the incident UV intensity at a distance R from the exciting star is given by:

$$\chi = 3113\left(\frac{N_{NUV}}{10^{48}\ s^{-1}}\right)\left(\frac{N_{Lyc}}{10^{48}\ s^{-1}}\right)^{-2/3}\left(\frac{n_e}{10^3\ cm^{-3}}\right)^{4/3} R^{-2} \qquad (5.1)$$

where χ is the photon flux between 912 and 1108 Å, relative to the mean background of $2.7 \times 10^{11}\ photons\ s^{-1}\ m^{-2}$ measured in the solar neighbourhood (Draine 1978, as quoted in Black & Van Dishoeck 1987). N_{Lyc} and N_{NUV} are the ionizing and non-ionizing photon fluxes and n_e is the electron density in the H II region. Values for N_{NUV} as a function of effective temperature were taken from PHM.

For a given gas density n and UV intensity χ, the intensity of the fluorescent 1-0 S(1) line is given by the following analytical expression:

$$I_{S(1)} = 5.1 \times 10^{-10} n \ln\left[90(\frac{\chi}{n}) + 1\right] \quad erg\ s^{-1}\ cm^{-2}\ sr^{-1} \qquad (5.2)$$

(Sternberg 1989). A molecular formation rate of $3 \times 10^{17}\ cm^3\ s^{-1}$ and an effective dust continuum cross section at 1000 Å of $1.9 \times 10^{-21}\ cm^2$ have been assumed in this expression (see Eqn. (3) of Sternberg 1989 for the detailed dependence of $I_{S(1)}$ on these parameters). Assuming that the molecular gas is located at the edge of a sphere of radius R centred on the exciting star, the total 1-0 S(1) luminosity integrated over the surface is $(4\pi R)^2 I_{S(1)}$. Combining the usual expression for the Strömgren sphere and Eqn 5.2 yields

$$L_{S(1)} = 0.2\left(\frac{N_{Lyc}}{10^{48}\ s^{-1}}\right)^{2/3}\left(\frac{n_e}{10^3\ cm^{-3}}\right)^{-4/3}\left(\frac{n}{10^4\ cm^{-3}}\right) \ln\left[90(\frac{\chi}{n}) + 1\right] R^2 \quad L_\odot. \qquad (5.3)$$

These equations were included in the evolutionary model used earlier to predict the integrated 1-0 S(1) luminosity produced by an ensemble of ionizing stars. For every time step and mass interval, the number of stars and the

average ionizing and non-ionizing photon fluxes were computed. For a given set of parameters (n_e, n and R), the UV intensity χ and the corresponding 1-0 S(1) luminosity $L_{S(1)}$ were then calculated using Eqns 5.1 and 5.3.

The evolution of the S(1)/Brγ ratio predicted by the UV fluorescence model is presented in Figure 5.2 (dotted line). This was calculated for an exponentially decreasing star formation rate with a time scale of 2×10^7 years, assuming an electron density of 10^3 cm^{-3} in H II regions, a total gas density of 10^4 cm^{-3} in molecular clouds and a dimensionless cloud-source separation $R = 1$. As expected, the S(1)/Brγ ratio is weakly dependent on the evolutionary state of the starburst. Even though the Brγ emission decreases exponentially, the H_2 luminosity is affected in the same way because its production is intimately related to the number of ionizing photons (equivalently the number of Brγ photons).

For the same parameters (IMF, n_e, n and R) the ratios predicted by our model are systematically smaller, by a factor of two, compared with those of PHM. This discrepancy is due to the use of a different 1-0 S(1) intensity $I_{S(1)}$ in the two models. PHM used the 1-0 S(1) intensities predicted by Black & van Dishoeck (1987) which are a factor of two higher than those of Sternberg (1989) (see also Sternberg & Dalgarno 1989) employed in this work.

We now try to estimate the S(1)/Brγ ratio for the galaxies listed in Table 5.2 assuming that *all* of the observed H_2 emission is fluorescently-excited. We adopt throughout an electron density of 10^3 cm^{-3} in the H II regions. This choice is motivated for two reasons. First, the measurement of the collisionally-excited C^+ emission at 158 μm from M83 suggests that the electron density in the photo-dissociation zones is greater than 10^3 cm^{-3} (Crawford 1985). Second, the He Iλ2.06μm/Brγ ratios observed in several starburst galaxies (*cf.* Chapter 3) never exceed the maximum value predicted for "low-density" H II regions which implies electron densities less than 3×10^3 cm^{-3}. We adopt a total gas density $n = 10^4$ cm^{-3} for all galaxies except for ARP 220 and NGC 6240 which have a thermal H_2 spectrum, implying gas densities of $\gtrsim 10^5$ cm^{-3} if the H_2 emission is fluorescently-excited. We shall discuss later the effect of varying the gas density on the S(1)/Brγ ratio.

The remaining parameter in the model is the dimensionless cloud-source separation R. If ionizing stars are located outside their parent molecular cloud, this quantity depends on the relative number of stars and molecular clouds

in the emitting region. Although it is difficult to constrain this parameter it is nevertheless possible to obtain a rough estimate based on the ratio of the molecular gas mass and the total Brγ luminosity observed in a given galaxy. Let N_* be the total number of ionizing stars which have an average Strömgren sphere R_s and an ionization rate $\overline{N}_{Lyc}$. It is assumed that there are N_{cl} spherical molecular clouds, each of mass M_{cl}, radius R_{cl} and density n. An "effective" cloud-source separation R may be obtained by equating the total area of the molecular clouds with that around the ionizing stars *i.e.* R must satisfy the relation $N_*(R)^2 = N_{cl}R_{cl}^2$ where $R_{cl} = (3M_{cl}/4\pi n m_H)^{1/3}$ with m_H being the mass of a hydrogen atom. N_{cl} is given simply by the ratio of the total H_2 mass $M_{H_2}^{tot}$ and the average mass of each cloud M_{cl}. Similarly, N_* is given by the ratio of the total Brγ luminosity $L_{Br\gamma}^{tot}$ to the average Brγ luminosity of each star, the latter being directly proportional to $\overline{N}_{Lyc}$. It can be shown that R is given by the following expression:

$$R = k\left(\frac{M_{H_2}^{tot}}{L_{Br\gamma}^{tot}}\right)^{1/2}$$

with

$$k = 0.085\left(\frac{M_{cl}}{10^5\ M_\odot}\right)^{-1/6}\left(\frac{\overline{N}_{Lyc}}{10^{48}\ s^{-1}}\right)^{1/6}\left(\frac{n}{10^4\ cm^{-3}}\right)^{-1/3}\left(\frac{n_e}{10^3\ cm^{-3}}\right)^{2/3} \quad (5.4)$$

Observed $M_{H_2}^{tot}/L_{Br\gamma}^{tot}$ ratios are given in Table 5.2. The source-cloud separation R was calculated from Eqn 5.4, assuming $M_{cl} = 10^5\ M_\odot$, the densities mentioned above and and an ionization rate $\overline{N}_{Lyc} = 48.34$ dex. The latter was adopted since it corresponds to an O8V star (*cf.* Chapter 2) which is roughly the average spectral type inferred from the HeIλ2.06μm/Brγ ratio (*cf.* Chapter 3). The inferred value for R is between unity and two. It should be noted that even though R depends on several parameters, it is mostly sensitive to the electron density in the photo-dissociation zones. For instance, decreasing the gas density n by an order of magnitude increases the value of R by only a factor of two.

PHM showed that the S(1)/Brγ ratio also depends on the upper mass limit, decreasing by $\sim$50% when m_u is increased from 30 to 60 $M_\odot$. We adopt the upper mass limits inferred from the starburst models presented in Chapter 4. The predicted S(1)/Brγ ratio for each galaxy is given in the last column of Table

5.2. These predictions are obviously subject to important uncertainties both in the model itself (PHM would predict ratios a factor of two higher) and the parameters adopted (gas and electron densities). For these reasons, one should bear in mind that the theoretical ratios could be affected by as much as a factor of two, if not higher. Despite these uncertainties, it is clear from Table 5.2 that UV fluorescence provides a viable mechanism for explaining the wide range of observed ratios. If the model presented here is correct, then a gas density of 10^4 cm^{-3} provides a very good fit to the S(1)/Brγ ratio observed in NGC 1614. Combining the ratios predicted by the UV fluorescence and shock (YSOs and SNRs) models for this galaxy, we infer than $\sim$70% of the H_2 emission in NGC 1614 is fluorescently-excited. Such fraction is consistent with the observed H_2 line ratios (*cf.* Table 5.1).

In the case of IC 694, the UV fluorescence model predicts a S(1)/Brγ ratio of $\sim$0.4 which is about half of the observed value. Interestingly, the H_2 line ratios of this galaxy are also consistent with UV fluorescence contributing half of the total H_2 emission. Such a good agreement between the model and the observations is somewhat surprising given the uncertainties mentioned above. Perhaps this agreement is just coincidental. If we assume that all the H_2 emission in IC 694 is fluorescently-excited, then the gas density would have be close to the critical density of $(3-5) \times 10^4$ cm^{-3} (Sternberg & Dalgarno 1989) which delineates the non-thermal and thermal regime of fluorescence. Such density would be required since the H_2 line ratios suggest both thermal and non-thermal excitation. If true, the UV fluorescence model should predict a S(1)/Brγ of unity, as observed. Increasing the gas density n to 5×10^4 cm^{-3} would reduce R to 1.2 corresponding to a S(1)/Brγ ratio of 0.5, still a factor of two too small. However, using the 1-0 S(1) intensities of Black & van Dishoeck (1987) in the model (as PHM) would yield a ratio close to unity. Therefore, given the uncertainties in the model, it is conceivable that all the H_2 emission of IC 694 is fluorescently-excited if the gas density is close to $\sim 5 \times 10^4$ cm^{-3}.

For source B and C of NGC 3690, the model predicts too high S(1)/Brγ ratios but this disagreement is not serious as it is possible to obtain a better fit by decreasing the gas density. For instance, decreasing the gas density of source C to 10^3 cm^{-3} would increase R to 4, yielding a new ratio of 0.25, in much better agreement with the observed ratio.

Could high density fluorescence explain the thermal H_2 spectrum of ARP

220 and NGC 6240 ? The S(1)/Brγ ratio predicted for a density of 10^5 cm^{-3} is certainly in good agreement with the ratio observed in ARP 220. However, high-density fluorescence could only explain half of the H_2 emission in NGC 6240. This figure is probably an upper limit since the detection of Brγ is very uncertain in this galaxy. For instance, assuming that the S(1)/Brγ ratio is in fact 20, R would increase by only 60%, yielding a S(1)/Brγ ratio of ~4, in which case, only 25% of the total emission would be produced by high-density fluorescence. This prediction would be consistent with the 1-0 S(1) imaging study of Herbst *et al.* (1990) which suggests that the H_2 emission of this galaxy is produced by large scale shocks driven by the collision of the parent galaxies.

5.4 Summary and Conclusions

We have presented an analysis of H_2 spectra of 4 interacting and merging galaxies. The H_2 line ratios of NGC 1614 and IC 694 show clear evidence that more than half of the H_2 emission in these galaxies is fluorescently-excited. The H_2 spectra of ARP 220 and NGC 6240 are consistent with thermal excitation.

Simple models of star-forming regions have been used to determine the relative contribution of H_2 emission from young stellar objects (bipolar outflows), supernova remnants and molecular clouds excited by the UV radiation of hot stars. The results suggest that, unless the lifetime or the intrinsic H_2 luminosity of YSOs in starburst galaxies is an order of magnitude higher than the corresponding sources of the Galaxy, their contribution to the total H_2 emission should be less than 20%.

Significant contribution of H_2 emission from SNRs is predicted if the age of burst is older than ~60 million years. Depending on the star formation rate history, such systems are predicted to have S(1)/Brγ ratios between 0.3 and 1.5. Except for NGC 2798, all galaxies investigated in this work are usually younger than ~20 million years which rules out any significant contribution of H_2 emission from SNRs.

The contribution of H_2 emission from molecular gas radiatively excited by an ensemble of hot stars has been calculated using models of star-forming regions similar to those used recently by Puxley, Hawarden and Mountain (1990). The models provide a quantitative estimate of the dilution of the UV radiation field based on the ratio of the total H_2 gas to the Brγ luminosity. The models can readily explain the observed S(1)/Brγ ratios in the range 0.2-1 with

gas density of 10^4 cm^{-3}. High-density (10^5 cm^{-3}) UV fluorescence provides a viable mechanism for explaining the thermal H_2 emission observed in ARP 220.

Chapter 6

A Near-Infrared Spectroscopic Study of the Luminous Merger NGC 3256

6.1 Introduction

NGC 3256 is a spectacular example of a merging galaxy. Its optical image shows knotty structures, with two tidal tails (*cf.* Schweizer 1986) indicative that this system was formed by the collision of two galaxies of approximately equal mass (Toomre and Toomre 1972). A kinematic study of the ionized gas has revealed the presence of non-circular motions (Feast and Robertson 1978), probably reminiscent of its violent past history. At a distance of 37 Mpc ($H_0 = 75$ km s^{-1} Mpc^{-1}), NGC 3256 has a total luminosity (8-1000 μm) of 3×10^{11} $L_\odot$ (Sargent, Sanders & Phillips 1989) which makes this merger the most luminous galaxy at redshifts less than 3000 km s^{-1}. This galaxy is a powerful 10 μm source (Graham *et al.* 1984, 1987; Joseph & Wright 1985) and this emission is very extended; half of it is detected outside the central kpc. This feature was interpreted by Graham *et al.* and Wright *et al.* (1988) as strong evidence that its extreme luminosity is powered by a recent episode of vigorous star formation activity, an hypothesis which is also supported by the *JHKL* mapping study of Wright *et al.* (1991, in preparation). Sargent, Sanders and Phillips (1989) have mapped the $J = 2 \rightarrow 1$ CO emission and derived a molecular mass of 3×10^{10} $M_\odot$ which is amongst the highest ever found in a galaxy. However, unlike other ultra-luminous merging galaxies such as NGC

6240 and Arp 220, the molecular gas in NGC 3256 is very extended, suggesting that the merging process is still in its early stage.

This wealth of observations and the relative proximity of NGC 3256 make this galaxy a very good candidate for studying starburst activity associated with merging galaxies. In this chapter, we present new near-infrared (IR) spectroscopic observations of NGC 3256. Two major problems will be treated. In the first part, we present a new method for constraining the age of the burst and the parameters of the initial mass function (IMF). The second part deals with the excitation mechanism of the molecular hydrogen emission (H_2) observed in NGC 3256. It is shown that the bulk of the H_2 emission in this galaxy is fluorescently-excited, which is unexpected since thermal or shock-excited emission is usually the dominant mechanism inferred in other H_2 emitting galaxies, especially in mergers. The main sections of the chapter are divided as follows: the observations are described in 6.2 and the main results outlined in 6.3. Modelling of the observational properties of the galaxy is described in 6.4 and the excitation mechanism of the H_2 emission is discussed in 6.5. The main conclusions of this study are finally summarized in 6.6.

6.2 Observations and Data Reduction

Near-infrared spectra of the nuclear regions of NGC 3256 were obtained at the Anglo-Australian Telescope on the nights of March 24-25 1989, using the infrared grating spectrometer FIGS (Bailey *et al.* 1988). The first position observed was centred on the 2.2 μm nucleus ($\alpha = 10^h25^m42.9^s$, $\delta = -43°38'57''$; 1950.0) using a square aperture of $3.5'' \times 3.5''$. This position is coincident (within 1-2$''$) with the brightest optical region of the galaxy (position 'T' in the notation of Feast & Robertson (1978)). Full window spectra were obtained at J (1.11-1.32 μm), H(1.50-1.80 μm) and K (2.01-2.44) for the nucleus. Two other positions, 5$''$ east and south of the nucleus, were also observed at K using the same aperture. The three positions observed are shown overlayed on the optical image of the galaxy in Figure 6.1. This picture was reproduced from the photograph of Feast & Robertson (1978) and kindly provided by Dr M. W. Feast. Standard chopping and nodding techniques were employed; the chop throw was set to an amplitude of 60$''$ in the north-south direction.

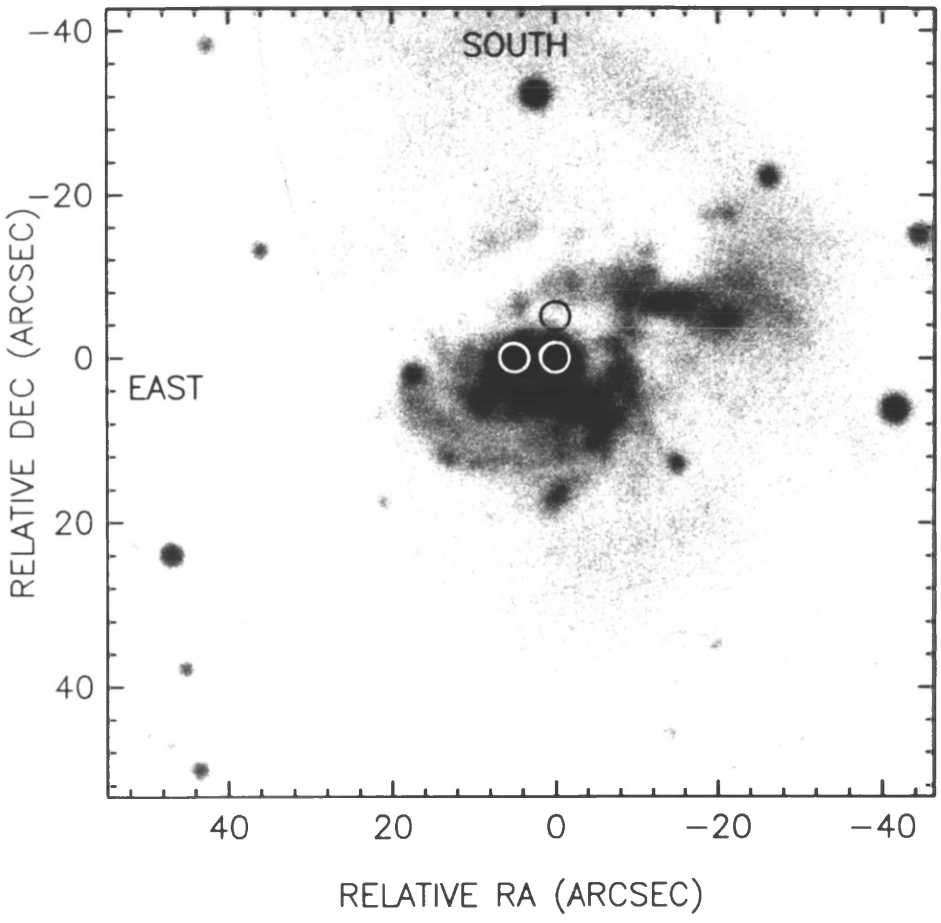

Figure 6.1.— Optical photograph of the central region of NGC 3256 taken by Dr D. S. Evans (*cf.* Feast & Robertson 1978; Figure 1) and kindly provided by Dr M. W. Feast. The three positions observed are shown as circles with diameters of the same size (3.5″) as the side of the square aperture used. The position of the 2.2 μm nucleus defines the origin of the relative coordinates.

absorption and emission lines. Water and CO_2 absorption features at 2.0602 and 1.1346 μm were used for the K and J spectra respectively. The calibration at H was achieved using OH emission bands observed on the sky. The accuracy of this calibration was found to be better than half a resolution element which was good enough to correct the wavelength shift caused by the systematic drift of the grating, observed after moving the telescope to a new position.

A resolving power ($\lambda/\Delta\lambda$) of 220 at K was derived by observing the extended Brγ emission of the planetary nebula IC418. Alternatively, using the width of Brγ observed in the K-window spectrum of NGC 3256 (see Figure 6.2b), we derived a resolving power of 280 assuming that the line is unresolved. The discrepancy between the two estimates is an artefact of the instrument. Because the resolution of FIGS has a strong dependence on aperture size when the source is extended, a lower resolving power was found for IC418 most likely because the Brγ emission is more extended in this source than in NGC 3256. The resolving power derived for the galaxy is probably very close to the experimental one since Moorwood and Oliva (1988) marginally resolved the 1-0 S(1) of H_2 and Brγ lines in NGC 3256 with intrinsic widths of 300-400 km s^{-1} (7% of the total line width at our resolution). Similarly, using the width of Paβ (1.2822 μm) and [FeII]1.644 μm observed in the galaxy, we derived a resolving power of 370 and 400 (both $\pm$50) at J and H respectively.

The atmospheric transmission and the relative sensitivity of the detectors were corrected by dividing all the spectra with the spectrum of the standard star BS4013 (G1V) observed at an air mass similar (<0.05) to the galaxy. The flux calibration was achieved with the same star assuming a K magnitude of 5.01 and an energy distribution as given in the software package FIGARO (*cf.* Allen 1989). Intrinsic K-window absorption lines in the standard were removed by dividing the star with the high resolution rectified spectrum of 16 Cyg A (G3V) taken from the stellar atlas of Kleinmann and Hall (1986) after convolution with a Gaussian instrumental profile with $\lambda/\Delta\lambda = 280$. This correction has virtually no effect on the shape of the galaxy spectrum except for the removal of a spurious emission feature due to Brγ absorption in the standard star. Such correction was not applied for the J and H-window spectra because of the lack of a template spectrum in these bands. The uncertainty of the absolute calibration is $\sim$10% as estimated from the scatter of the mean of several spectra obtained during both nights.

6.3 Results

6.3.1 Emission lines

All the spectra obtained at K are shown in Figure 6.2a to 6.2f. These were obtained after an integration of three hours for the nucleus and one hour for the other two positions. The quality of the spectrum obtained on the nucleus is very good. The average signal-to-noise ratio per point measured for the whole spectrum is ~80 and more than 100 between 2.0 and 2.3 μm. For clarity in illustrating the relative strength of the emission lines, two versions of the spectra are presented for each position, one showing the whole spectrum and the other a subset of the 2.02-2.29 μm region subtracted by a power-law continuum ($F_\lambda \propto \lambda^\beta$). The latter was fitted from featureless sections of the spectrum, defined so as to avoid the spectral range of prominent (or potential) emission and absorption lines. These include Brγ, He Iλ2.06μm, H_2 transitions, the CO band, NaI, CaI and AlI/MgI absorption features. Because the absolute wavelength scale is uncertain, the spectra are shown in their restframe. This was done by shifting the spectra such that either Brγ (2.1661 μm) or the 1-0 S(1) (2.1218 μm)—whichever strongest in a given spectrum—are centred at their respective rest wavelength in the vacuum.

Integrated line fluxes and their corresponding wavelengths as measured from the spectra and listed in Table 6.1. The intensities of strong emission lines were measured by adding all the flux relative to the local continuum and by fitting Gaussian profiles (with a FWHM constrained by the strong lines) for faint lines and blended features. The errors on the flux given in Table 6.1 are *statistical* only and do not include a contribution from the uncertainties in the continuum fit and the absolute calibration.

The dominant emission lines observed in the K spectra are Brγ, the singlet $2^1S-2^1P^0$ transition of HeI (2.0587 μm) and the 1-0 S(1) of H_2, the latter being marginally detected in the 5″ east spectrum. The observed line fluxes on the nucleus for the 1-0 S(1) and Brγ are $1.8\pm0.1\times10^{-17}$ $W\ m^{-2}$ and $5.4\pm0.1\times10^{-17}$ $W\ m^{-2}$, respectively. Adding the flux detected at the other positions off the nucleus, gives line fluxes which are higher (especially for Brγ) by 25-30% compared with the 6″×6″ aperture measurements of Moorwood and Oliva (1988). This discrepancy is probably not significant given the uncertainties in comparing different aperture measurements and possible errors in the relative pointing and absolute calibration of two set of observations.

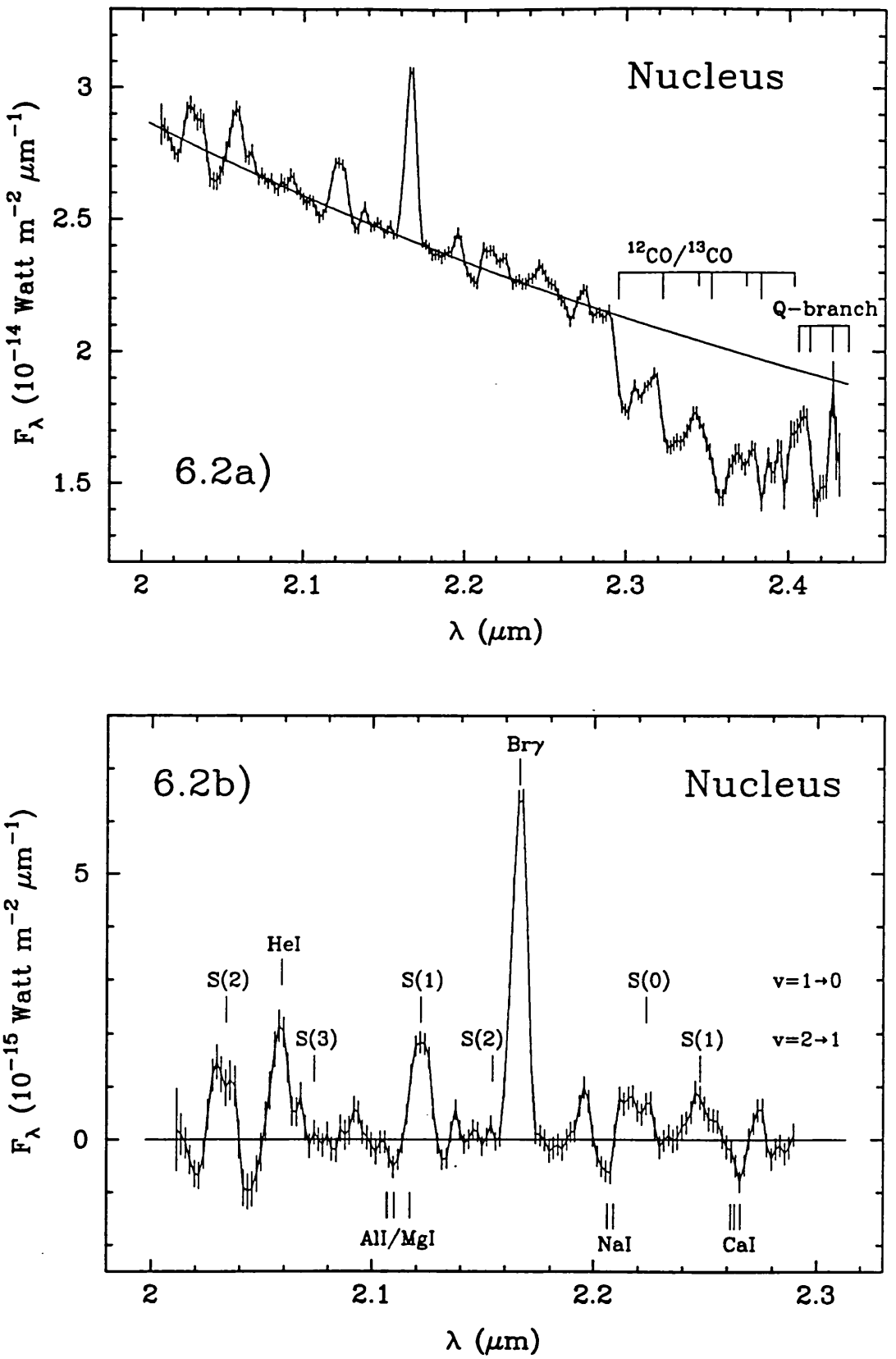
Nucleus
6.2a)
$^{12}CO/^{13}CO$
Q-branch
F_λ (10^{-14} Watt m^{-2} μm^{-1})
λ (μm)
6.2b)
Nucleus
Brγ
HeI
S(2)
S(3)
S(1)
S(2)
S(0)
S(1)
v=1→0
v=2→1
AlI/MgI
NaI
CaI
F_λ (10^{-15} Watt m^{-2} μm^{-1})
λ (μm)

Figure 6.2

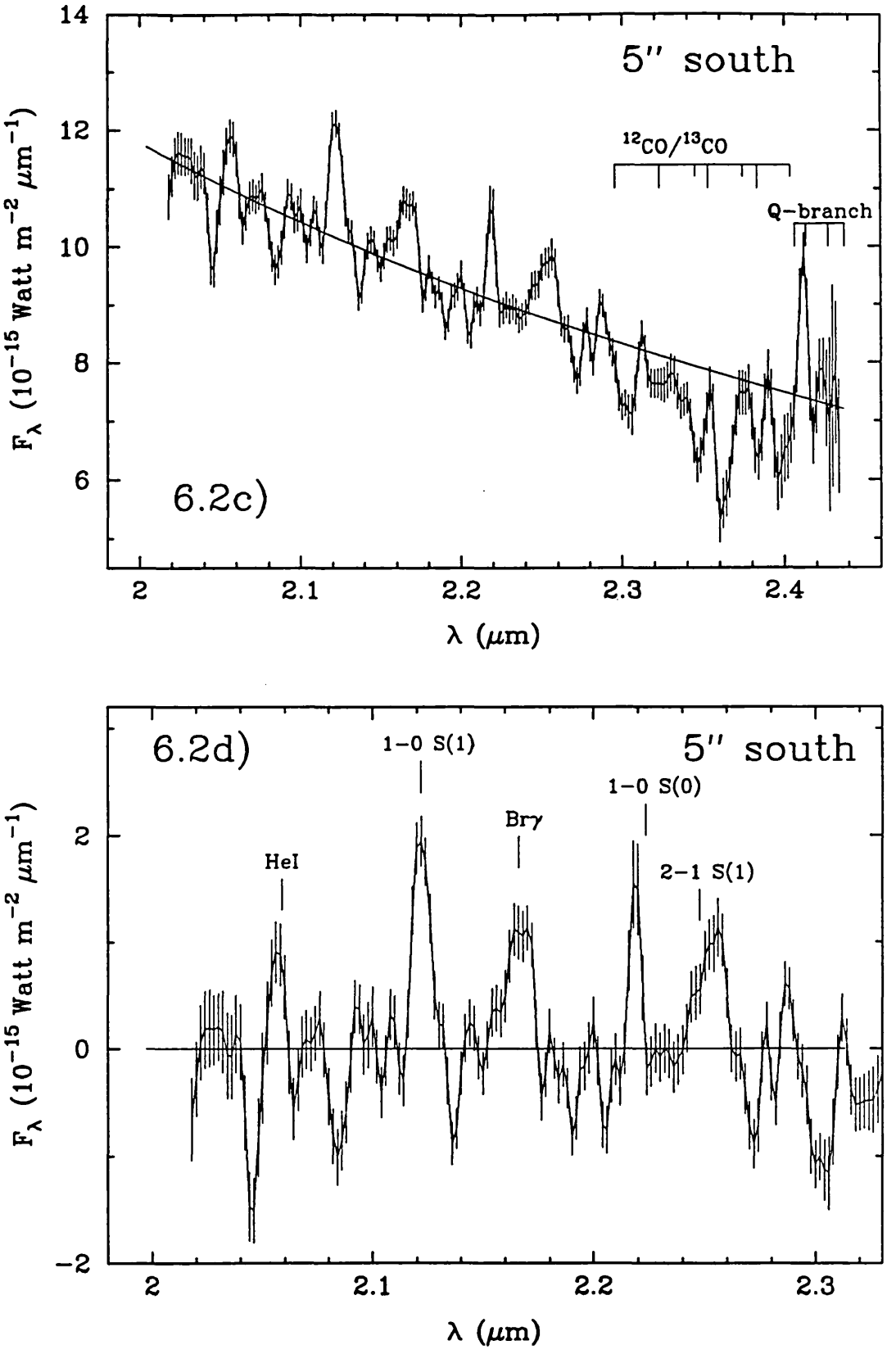

Figure 6.2 (continued)

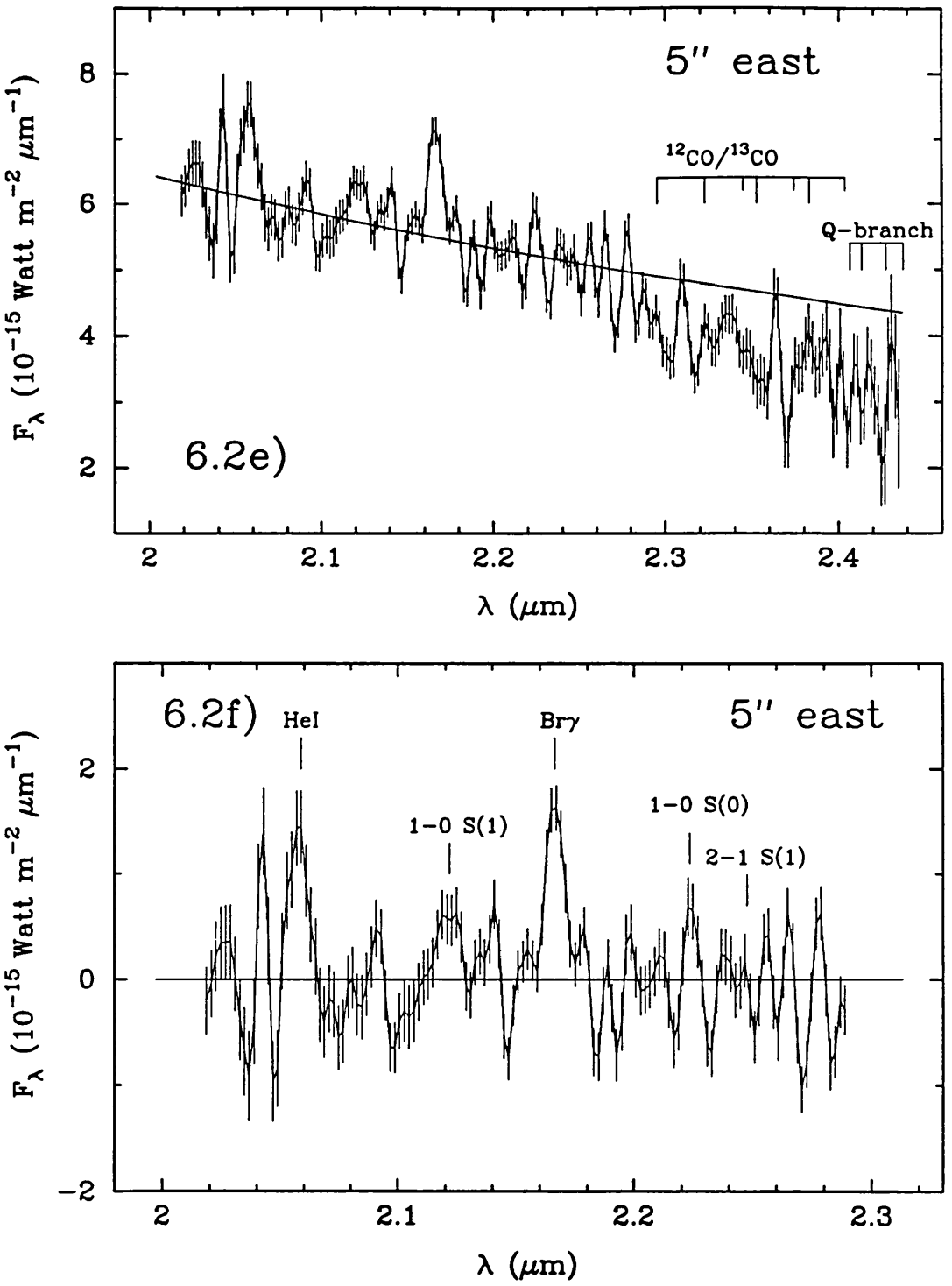

Figure 6.2— K-window spectra of NGC 3256: a)–b) nucleus; c)–d) 5″ south and e)–f) 5″ east of the nucleus. The spectra are shown in the restframe of the galaxy. Each spectral point is plotted with an error bar of $\pm 1\sigma$. The solid lines shown in a), c) and e) are the best fit to a power-law spectrum ($F_\lambda \propto \lambda^\beta$) fitted from featureless sections of the continuum taken between 2.0 and 2.29 μm. The spectra shown in b), d) and f) are continuum-subtracted versions of the 2.0-2.29 μm spectral region of a), c) and e), respectively. Except for a) and b), all spectra have been smoothed with a three-point triangular filter. Note however that the fluxes given in Table 6.1 have been estimated from unsmoothed spectra.

Table 6.1
Line Fluxes and Identifications in NGC 3256

Observed[1] wavelength (μm)	Integrated Flux (10^{-17} W m^{-2}) observed	dereddened	Identification[2]
	NUCLEUS		
1.255(1)	3.3 ± 1	12.9	HeI $3^3S - 4^3P^0$ 1.2531
1.259(1)	3.2 ± 1	12.3	[FeII] $a^6D_1 - a^4d_7$ 1.2573
1.282	14.2 ± 1	52.3	Paβ 1.2822
1.644	4.5 ± 0.1	10.4	[FeII] $a^4F_5 - a^4D_1$ 1.644
2.030(1)	1.1 ± 0.3	2.0	?
2.036(3)	0.8 ± 0.3	1.4	H_2 1-0 S(2) 2.0338
2.058(<1)	1.8 ± 0.2	3.2	HeI $2^1S - 2^1P^0$ 2.0587
2.067(2)	0.4 ± 0.2	0.7	?
2.092(2)	0.4 ± 0.1	0.7	? [FeII] $a^4G_7 - b^2G_7$ 2.091
2.122(< 1)	1.8 ± 0.1	3.1	H_2 1-0 S(1) 2.1218
2.166	5.4 ± 0.1	9.1	Brγ 2.1661
2.196(1)	0.6 ± 0.1	1.0	?
2.215(1)	0.7 ± 0.1	1.2	?
2.224(1)	0.5 ± 0.1	0.8	H_2 1-0 S(0) 2.2233
2.247(1)	0.7 ± 0.1	1.2	H_2 2-1 S(1) 2.2477
2.275(2)	0.5 ± 0.1	0.8	?
2.427(< 1)	1.6 ± 0.5	2.5	H_2 1-0 Q(3) 2.4237
	5″ SOUTH		
2.057(2)	0.9 ± 0.3	—	HeI $2^1S - 2^1P^0$ 2.0587
2.122	2.1 ± 0.2	—	H_2 1-0 S(1) 2.1218
2.167(1)	1.5 ± 0.2	—	Brγ 2.1661
2.218(1)	1.1 ± 0.2	—	?
2.247(3)	0.6 ± 0.3	—	H_2 2-1 S(1) 2.2477
2.256(1)	1.1 ± 0.3	—	? [FeII] $a^2G_7 - a^2H_9$ 2.254
2.412(<)	2.3 ± 0.3	—	? 1-0 Q(1) 2.407
	5″ EAST		
2.057(1)	1.4 ± 0.3	—	HeI $2^1S - 2^1P^0$ 2.0587
2.122(2)	0.7 ± 0.2	—	H_2 1-0 S(1) 2.1218
2.166	1.7 ± 0.2	—	Brγ 2.1661
2.223(2)	0.6 ± 0.2	—	H_2 1-0 S(0) 2.2233

[1] Restframe wavelengths as measured from the spectra relative to the following lines (assumed to be correctly identified): Paβ and Brγ for the nucleus, 1-0 S(1) for the southern spectrum and Brγ for the eastern spectrum. The number in parenthesis gives the error in units of 0.001 μm. No error is given for reference lines.

[2] Unidentified lines are annotated by the symbol '?'. Possible identifications are noted by a '?' followed by the suggested transition.

The relative strengths of the emission lines on the nucleus and the southern position strongly suggest that the H_2 is much more extended than the Brγ emission. Indeed, while the 1-0 S(1) flux remains nearly constant going from the nuclear to the southern position, Brγ decreases by a factor of 3.5. That the H_2 is relatively more extended than Brγ is a similar result that has been previously noted in other mergers based on multi-aperture spectroscopic measurements (Joseph *et al.* 1987; Prestwich 1989).

Other transitions of H_2 were also detected on the nucleus (see Figure 6.2b). These includes the 1-0 S(2) (2.0338 μm), 1-0 S(0) (2.2233 μm), 2-1 S(1) (2.2477 μm) and the first three transitions of the 1-0 Q-branch. Probably the most striking feature of the nucleus spectrum is the strength of the 2-1 S(1). The 2-1 S(1)/1-0 S(1) line ratio was measured to be 0.39 ± 0.06 *which is much stronger than expected for a thermal spectrum (ratio typically 0.1) and very suggestive of non-thermal excitation.* We shall come back to this point later. The 2-1 S(1) is marginally detected in the southern spectrum and seemed to be blended with a stronger line at 2.256 μm. We derived a 2-1 S(1)/1-0 S(1) line ratio of 0.26 ± 0.08 for this position. The identification of the 2-1 S(1) at this position is strengthened by the detection of the 1-0 S(0) which is found at 2.218 μm, only half a resolution element away from the expected wavelength of the 1-0 S(0) transition.

The spectra of the nucleus obtained in the J and H bands are shown in Figure 6.3a and 6.3b, respectively. We identify the strongest emission line in the J spectrum with Paβ (1.2822 μm). The emission feature at ≈ 1.26 μm is probably a blend of two transitions of HeI (1.253 μm) and [FeII] (1.257 μm). Fluxes for these lines are given in Table 6.1. The emission line around 1.27 μm is coincident with the expected position of Paβ blueshifted by the systemic velocity of NGC 3256. We thus associate this line with Paβ absorption in the standard star which appears in our spectrum as a spurious emission line after ratioing the galaxy spectrum with that of the standard.

We identify the strong emission line in the middle of the H spectrum with the transition of [FeII] at 1.644 μm. This line is also very close to a transition of [SiI] at 1.6459 μm and although our wavelength scale is not accurate enough to exclude that possibility, we dismiss this identification on the basis that we also detected a transition of [FeII] in the J-window (see above). Furthermore, if the line at 1.644 μm is [SiI] then we would expect to detect another [SiI]

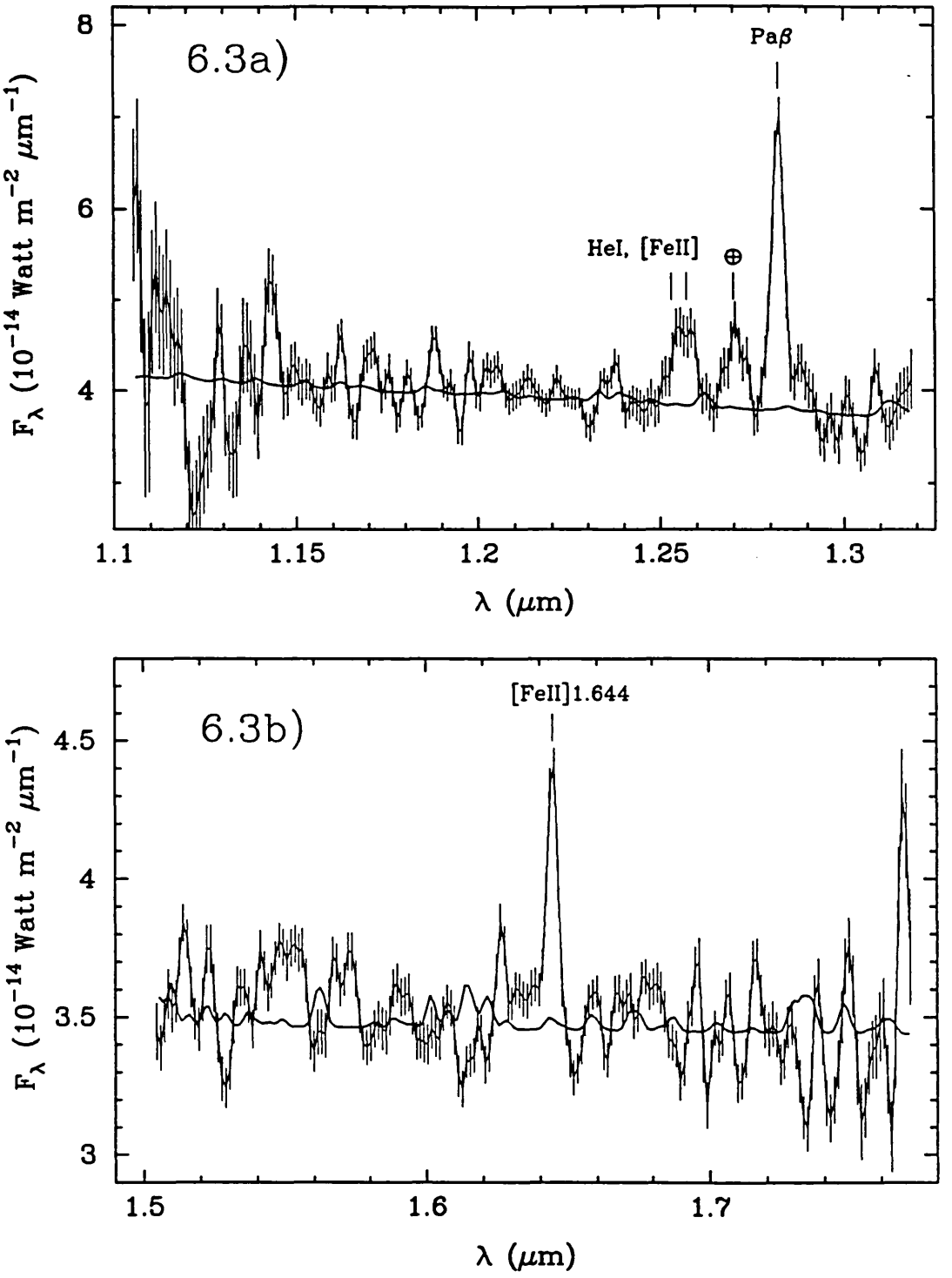

Figure 6.3a,b— J and H spectra of NGC 3256 obtained on the nucleus. As in Figure 6.2, the spectra are shown in the restframe. The emission feature marked by the symbol '⊕' in the J spectrum is probably spurious and due to Paβ absorption in the standard star, used to ratio the raw galaxy spectrum. The thick solid line superimposed on both spectra is a synthetic non-thermal H_2 spectrum added to the continuum of the galaxy. This spectrum was calculated using the extinction-corrected line ratios of Black & Van dishoeck (1987) (model 14) and Gaussian profiles with FWHM as measured from the galaxy spectra.

line at 1.607 μm which should be a factor of three weaker than the 1.6459 μm transition (Graham, Wright & Longmore 1987). Such a strong line should have been detected in our spectrum, given the signal-to-noise of the 1.644 μm line, but this is clearly not the case (see Figure 6.3b).

6.3.2 Absorption lines

The spectrum of the nucleus also shows a number of absorption lines. The strongest of these features is the CO band longward of 2.29 μm. The strength of the CO band was quantified by a *spectroscopic* CO index defined as follows:

$$CO_{sp} = -2.5 \log\langle R_{2.36} \rangle \tag{6.1}$$

where $\langle R_{2.36} \rangle$ is the average of the rectified spectrum R_λ between 2.31 and 2.40 μm in the restframe of the galaxy. The rectified spectrum is obtained by ratioing the observed spectrum with a power-law continuum fitted from featureless sections of the spectrum. The choice of a power-law is motivated by the fact that stars and non-thermal sources are well represented by such a continuum.

Unlike the usual photometric CO index (*e.g.* Frogel *et al.* 1978), which is defined as the difference in magnitude of two narrow-band filters centred on the CO dip and the nearby continuum at 2.2 μm, the spectroscopic CO index is independent of the slope of the continuum. This is very important because the K continuum can be severely affected by reddening and contaminated by non-stellar sources such as hot dust and free-free emission in starburst galaxies. The accuracy of this spectroscopic approach for measuring the depth of the CO band is discussed in Appendix A along with spectroscopic CO indices of all the stars observed by Kleinmann and Hall (1986).

Spectroscopic CO indices and power-law indices for all positions are given in Table 6.2. Note that the errors given for CO_{sp} include the uncertainties in placing the continuum level. For comparison purpose, we also give the spectroscopic CO index of a K5III star which characterizes, to good approximation, the overall energy distribution of ellipticals and bulges of late-type spirals (Frogel *et al.* 1978; Arnaud & Gilmore 1986; Frogel 1985). Furthermore, this star has a spectroscopic CO index of 0.20 which corresponds—after transformation (see Appendix A)—to a photometric CO index of 0.15 *i.e.* identical to the mean photometric CO index observed in bulges of late-type spirals (Frogel 1985). In

Table 6.2
Continuum Slopes and Absorption Line Strengths

Spectrum	β^1	NaI (Å)	CaI (Å)	CO_{sp}
Nucleus	-2.16 ± 0.04	1.9 ± 0.4	1.8 ± 0.5	0.23 ± 0.01
5″ south	-2.49 ± 0.09	—	—	0.11 ± 0.02
5″ east	-2.00 ± 0.17	—	—	0.24 ± 0.03
γ Dra (K5III)	-3.58	3.3	2.9	0.20

[1] Power-law index ($F_\lambda \propto \lambda^\beta$) fitted to the continuum between 2.0 and 2.3 μm.

the rest of the chapter, it will be assumed that a normal stellar population is characterized by a spectroscopic CO index of 0.20.

With a spectroscopic CO index of 0.23 ± 0.01 (see Table 6.2), the nucleus of NGC 3256 has a CO band stronger than expected for a normal stellar population, a result significant at the 3σ level. However, the observed spectroscopic CO index is only a lower limit estimate of the intrinsic CO band strength because of the possible contamination of the stellar K light by non-stellar sources such as hot dust and free-free emission. Since these sources have a featureless continuum, they will dilute the luminosity of late-type stars, hence reducing the depth of the CO band. This effect is not negligible in NGC 3256. The K continuum is contaminated by hot dust as suggested by the strong $K-L$ excess ($\sim$ 0.8) observed within the central 15″ of the nucleus (Wright *et al.* 1991; in preparation). Assuming a dust temperature of 500 K and an emissivity varying linearly with frequency, it can be estimated that 4-5% of the 2.2 μm continuum is associated with hot dust. The free-free contribution can be calculated from the Brγ flux using the theoretical Brγ to free-free continuum ratio of Joy and Lester (1988). The Brγ flux given in Table 6.1 and the observed 2.2 μm flux density yield 4% for the contribution of free-free emission to the 2.2 μm continuum. Thus, an overall contribution of $\sim$ 10% of the K luminosity is associated with featureless continuum. Correcting for this contribution gives a new spectroscopic CO index of 0.26 for the nucleus.

Although the signal-to-noise is not as good as on the nucleus, the CO band is clearly detected in the eastern spectrum. Correcting for the continuum contamination of free-free and hot dust emission (see Table 6.3) yields a spec-

troscopic CO index 0.27±0.03, consistent with the nuclear value. The southern position differs from the others with a spectroscopic CO index of 0.12 ± 0.04 which is significantly lower than typical giant stars.

Absorption features due to transitions of NaI (~2.206 μm) and CaI (~2.263 μm) are also identified in the nuclear spectrum. As given in Table 6.2, the NaI and CaI absorption features have an average equivalent width of 1.9 ± 0.4 Å but this value increases to 2.9 ± 0.4 Å after correction for the 10% contribution of featureless continuum discussed above. This latter value is similar to the average equivalent width measured in the K5III star spectrum. Finally, we suggest that the local depression of the continuum near 2.1 μm is due to absorption lines of AlI and MgI.

These absorption lines are common features in spectra of late-type stars (*cf.* Kleinmann & Hall 1986) and provide strong evidence that *most of the 2.2 μm continuum observed in NGC 3256 has a stellar origin.*

6.3.3 Unidentified emission features

A number of "unidentified" emission lines were found in the K spectrum of the nucleus, unidentified in the sense that none of these lines has been reported in the literature before. These features are annotated in Table 6.1 by an interrogation mark. The observed wavelength (in the vacuum) of these lines and their respective detection level are: 2.030 (3.7σ), 2.068 (2σ), 2.092 (4σ), 2.196 (6σ), 2.215 (7σ), and 2.275 μm (5σ). We do not suggest that all these features are genuine as some of them are marginally detected but we note however that such a high number of 3σ features in one spectrum is difficult to explain just by statistical fluctuations of the noise only, and suggests that some of these features are real.

Before attempting any identifications, it is important to consider first whether some of these features could be due to bad cancellation of the atmosphere when ratioing the galaxy spectrum with the standard. To test this possibility, we examined the ratio of two spectra of the same standard star observed 2 hours apart. Most of the resulting spectrum (not shown here) is flat with typical fluctuations of the order of ~1% which is less than the size of the one σ error bars shown in the spectrum of Figure 6.2a and 6.2b. The only spectral regions that seem to be affected (still at the 2% level) by the atmosphere are around 2.03-2.04 μm and 2.275 μm. We suggest that the line found at 2.275 μm is probably spurious and that perhaps a third of the blend

(including the 1-0 S(2)) observed at 2.03-2.04 μm is due to bad cancellation of the atmosphere. Thus, only one line out of the six mentioned above can be attributed to atmospheric effects.

Interestingly, the lines at 2.030, 2.092 and 2.196 μm are, within the errors, coincident with some transitions of H_3^+ recently detected in Jupiter (Drossart *et al.* 1989; Trafton, Lester & Thompson 1989). Assuming an excitation temperature of 1100 K as observed in Jupiter, we should expect another strong H_3^+ blend around 2.038 μm. Given the strength of the line at 2.092 μm, this blend should be as strong as Brγ observed in our spectrum which is clearly not the case. The identification of these lines with H_3^+ is therefore unlikely.

We tentatively suggest that the line at 2.092 μm is a transition of [FeII]. This line and several other high-excitation transitions of [FeII] have already been detected in η Carinae (Allen, Jones & Hyland 1985). Interestingly, there is also an emission feature at 1.625 μm in the H-window spectrum of the nucleus (see Figure 6.3b) which is coincident with another high-excitation line of [FeII]. As pointed out by Allen *et al.*, these lines would require very high temperatures to be thermally excited and they are probably excited by a fluorescence mechanism (Netzer and Wills 1983; Johansson and Jordan 1984).

The identification of these lines obviously needs to be secured with higher resolution observations but if true, a fluorescent [FeII] spectrum would have important implications for the interpretation of the H_2 spectrum because some of the high-excitation transitions of [FeII] (2.224, 2.240, 2.245, 2.254 μm) are very close in wavelength to the 1-0 S(0) and the 2-1 S(1) and could potentially contaminate these important diagnostic H_2 lines in medium resolution spectra such as those presented in this work. However, given the strength of the 2.092 μm line in our spectrum and assuming the same [FeII] line ratios observed in η Carinae, we estimate that the contribution of non-thermal [FeII] lines to the 2-1 S(1) is less than 6% which is insufficient to affect the interpretation of the H_2 spectrum.

Finally, the line at 2.068 μm could be the same line detected by Allen *et al.* at 2.065 μm in η Carinae, for which they did not provide an identification. The most significant of all the features mentioned above, the line at 2.196 μm, remains unidentified. It is worthwhile to mention that this line has also been detected in NGC 4102 by Tim Hawarden (private communication) at UKIRT using CGS2. Higher resolution observations are urgently needed to assess the

nature of these lines.

6.3.4 EXTINCTION

Our spectra provide three independent methods for determining the extinction towards the nucleus of the galaxy. The most accurate one is probably provided by the ratio of Paβ to Brγ. Assuming the validity of case B for the observed recombination spectrum, the intrinsic Paβ/Brγ line ratio is expected to be 5.89 for $T_e = 10^4$ K and $n_e = 10^4 \mathrm{cm}^{-3}$ (Hummer & Storey 1987). We observed a ratio of 2.7$\pm$0.3 on the nucleus corresponding to a relative extinction of 0.89 mag. Assuming an extinction law that varies as $\lambda^{-1.75}$ (Draine 1989), this corresponds to an absolute extinction at 2.2 μm of 0.55$\pm$0.09 mag ($A_V = 5.5$). We can also use the ratio of [FeII]1.257 to [FeII]1.644. The extinction derived from these lines has the major advantage of being independent on temperature since the two transitions arise from the same upper level. From the Einstein coefficients of Nussbaumer and Storey (1988), we derive an intrinsic [FeII]1.257/[FeII]1.644 line ratio of 1.36. The line fluxes given in Table 6.1 imply $A_K = 0.7 \pm 0.3$.

Finally, the extinction can be derived from the slope of the continuum in the K spectrum. One has to make the assumption that the integrated light of the galaxy is well approximated by giant stars, which is a very good approximation as discussed earlier. It is obvious from Table 6.2 that the nucleus has a flatter continuum than the K5III star suggesting the 2.2 μm continuum of the galaxy is affected by extinction. It can be shown that the relative slopes of the galaxy and the star correspond to an absolute extinction at 2.2 μm of 0.8 ± 0.1. This figure is certainly an upper limit since the continuum is contaminated by warm dust, as discussed in section 6.3.2. Correcting the spectrum with 4% contribution of a grey body spectrum yields $A_K = 0.6$.

It thus seems that within the errors, the extinction derived from the ionized gas and the stars is the same in NGC3256. A similar result was found by Lester *et al.* (1990) in M82. It is important to note that our reddening estimates were derived under the assumption that the stars and the ionized gas are affected by *foreground* extinction only, that there is no dust between the emitting sources. There is growing evidence that this assumption is probably too simplistic. Using relative line ratios of Paβ, Brγ and Brα, Puxley and Brand (private communication) showed that more than 80% of the extinction towards the ionized gas in NGC253 is due to *internal* reddening. If internal reddening is important, then the extinction derived under the assumption that it is foreground will be

much lower. Whether internal reddening is important in NGC3256 needs to be assessed with a measurement of Brα, and for rest of the paper, an extinction of $A_K = 0.55$ mag will be assumed, bearing in mind that this value could well be a lower limit.

6.4 Modelling the Line and Continuum Emission

As discussed in the Introduction, there is compelling evidence that the nuclear region of NGC 3256 is experiencing a burst of star formation. We show in the next section that our spectroscopic observations strengthen this interpretation. The observational properties of the galaxy will then be used along with an evolutionary starburst model to constrain both the age of the burst and the parameters of the IMF.

6.4.1 Evidence for starburst activity in NGC 3256

Except for a ~10% contribution of hot dust and free-free emission, most of the K continuum is due to radiation from late-type stars with no evidence for a significant contribution from an active galactic nucleus (AGN). Therefore, it is natural to suppose that the activity observed in this galaxy is associated with an episode of vigorous star formation.

In this context, the ionization observed in NGC 3256 is most likely associated with young OB stars. At a distance of 37 Mpc, the nuclear Brγ flux corresponds to a luminosity (corrected for extinction) of 3.8×10^6 $L_\odot$ or an ionization rate of 1.14×10^{54} s^{-1} for the central 600 pc, similar to the value inferred in the archetypal starburst M82 within the same physical region (Puxley *et al.* 1989). Such a high ionization rate can only be maintained by massive star formation.

As discussed earlier in Chapter 3, the HeIλ2.06μm/Brγ line ratio can be used to determine the average spectral type of the hot stellar population. We showed that this ratio has a steep dependence on effective temperature. This relation is shown in Figure 3.2 of Chapter 3. The ratio of 0.35 ± 0.04 observed on the nucleus implies an effective temperature of $\sim$ 35000 K which corresponds to an O8 main sequence star. Representing all the ionizing stars in the nucleus by this average spectral type, 6.9×10^5 such stars are required to explain the Brγ luminosity observed in the central 600 pc. This population of young stars has a total mass of 1.5×10^7 $M_\odot$ and a bolometric luminosity of 9.2×10^{10} $L_\odot$, very

close to 8.7×10^{10} $L_{\odot}$ as derived from the small aperture 10 μm measurement of Graham *et al.* 1987, calculated using the extrapolation $L_{IR} = 15 L_{10\mu m}$ (Scoville *et al.* 1983; Telesco & Gatley 1984) after correction for an extinction 0.26 mag at 10 μm. This luminosity can account for a third of the total 3×10^{11} $L_{\odot}$ deduced from the *IRAS* and 10 μm data (Sargent, Sanders and Phillips 1989; Graham *et al.* 1984, 1987).

The detection of Brγ outside the nucleus (see Figure 6.2d and 6.2f) demonstrates that star formation is also active at these positions but the level of this activity is uncertain because the extinction is not well determined for these regions. Inspection of Figure 6.1 suggests that the region 5″ south is probably affected by strong reddening as there is little optical emission at this position relative to the nucleus. The visual extinction at this position could well be as much as 5 to 10 magnitudes higher than that on the nucleus, implying that most of the ionizing stars are still embedded in molecular clouds.

The He Iλ2.06μm line is also detected outside the nucleus. Taking the average of the two off-nuclear spectra and assuming the same extinction as measured on the nucleus, we have an He Iλ2.06μm/Brγ of 0.73 ± 0.14 which is higher (at the 2-3σ level) than the ratio measured on the nucleus. This high ratio provides strong evidence that massive stars are being formed outside the central 600 pc. Integrating the Brγ flux observed in our spectra and representing the hot stellar population by a single spectral type (O8V), we infer a luminosity within the central kpc that can account only for half of the total bolometric luminosity. Unless we have underestimated the reddening towards the ionized gas, this suggests that the starburst is probably extended on scales of several kpc. This interpretation is consistent with the very extended 10 μm map observed in NGC 3256 (Graham *et al.* 1987; Wright *et al.* 1991, in preparation).

The anomalously strong CO band is further compelling evidence for starburst activity as it implies the existence of a young population of red supergiants. As shown in the next section, the strength of the CO band reaches a maximum between 15 and 40 million years with a spectroscopic CO index of $\sim$ 0.28. This increase of about 0.1 mag relative to normal galaxies is due to the sudden occurrence of red supergiants in the stellar population. Making the conservative assumption that the starburst is at a stage near its peak, then the spectroscopic CO index of 0.26 observed in NGC 3256 implies that, *at least*, 75% of the 2.2 μm continuum is associated with a starburst population.

It is often argued that the interpretation of the CO band is complicated by the fact that its strength also depends on metallicity, the higher the metal abundance the stronger the depth of the CO band. This effect has been measured in globular clusters and a calibration between the photometric CO index and metallicity has been established by these observations (Frogel *et al.* 1983). Using this calibration and the transformation between photometric and spectroscopic CO indices (see Appendix A) we have $\Delta CO_{sp} = 0.11\Delta[Fe/H]$ where $[Fe/H]$ is the logarithm of the metal abundance relative to the sun. In this context, the strong CO band observed in NGC 3256 could be accounted for if the metal abundance in this galaxy is more than three times higher than the average metallicity of normal spirals which can reasonably be assumed to be solar.

However, there are two reasons to believe that a metallicity effect is not responsible for the strong CO band observed in NGC 3256. First, the calibration used to relate the CO band strength and metallicity has been determined from observations of globular clusters, most of them with metal abundances below solar. It is far from clear whether the extrapolation of this calibration is valid beyond solar metallicity. It should be remembered that the main reason why the CO band is stronger in supergiants compared with giants is because the former have a higher microturbulent velocity which is strong evidence that the CO absorption band is made of many saturated lines (McGregor 1987). Thus, if most of the CO lines are saturated, increasing the metallicity will have little effect on the strength of the molecular band.

Finally, if the stellar population in NGC 3256 is normal, except for its high metallicity, then its absolute K magnitude should be comparable to other galaxies. On the nucleus, we measured an absolute K magnitude (corrected for extinction) of -22.6 (see Table 6.3) which is six times brighter than the most luminous Sc spirals (Devereux, Becklin & Scoville 1987). This means that less than 20% of the K continuum is contributed by an old population. Clearly, another source must be responsible for this high 2.2 μm luminosity and the most plausible candidate is a population of young red supergiants.

One can estimate the number of red supergiants given the observed 2.2 μm luminosity and assuming that their progenitors are O8V stars (20 $M_{\odot}$) that will eventually become K4 supergiants after 10 million years (Maeder & Meynet 1988; see also Table B.12 of Appendix B) with an absolute K magnitude of

-10.8. Depending on whether a preexisting population is contributing at K, we estimate that $(3-5) \times 10^4$ red supergiants are required to account for the 2.2 μm luminosity in NGC 3256. Comparing with the number of O8V stars derived earlier, we have a O8V to red supergiant ratio between 14 and 23. These values are roughly consistent with the blue-to-red supergiant ratio of 10 to 40 observed in our own galaxy (Humphreys 1978). Although such comparison is only approximate, the purpose of this simple analysis is to demonstrate that the both the ionization state and 2.2 μm luminosity are consistent with the hypothesis that there are numerous OB stars and red supergiants present in the nucleus of NGC 3256. In the following, we use an evolutionary model to put more quantitative constraints on the age of the burst and the parameters of the initial mass function.

6.4.2 The age of the burst

In order to constrain the age of the burst, observable quantities have to be related to a stellar population model. The results presented in this thesis were obtained using an evolutionary model based on a set of new evolutionary tracks (Maeder & Meynet 1988) with masses ranging from 0.85 to 120 $M_\odot$. Unlike previous models, these tracks include the effect of mass loss in the stellar evolution, which allows stars to come back to the left of the HR diagram after the red supergiant phase. The modelling procedure employed is similar to the one described by Huchra *et al.* (1977), a model used later by Rieke *et al.* (1980) in their study of the starburst galaxies M82 and NGC 253. A detailed description of the model used here is given in Appendix B.

The basic ingredients of the model are: the IMF, defined as the number of stars formed per unit mass interval, the star formation rate (SFR) and the age of the burst. The IMF is parametrized by a power-law of the mass with an index α ($\psi(m) \propto m^{-\alpha}$) and a lower and an upper mass limit, m_l and m_u. For instance, the Salpeter (1955) IMF is characterized by $\alpha = 2.35$ whereas Scalo (1986) parametrizes the IMF with three power-law segments, the upper end having $\alpha \sim 2.85$. Three time-dependences were investigated for the SFR: constant, exponential ($SFR \propto \exp(-t/\tau_0)$) and "delayed" ($SFR \propto t\exp(-t/\tau_0)$ where τ_0 is the time-scale of the burst, arbitrarily set to 20 million years. The model can predict the bolometric and 2.2 μm luminosity, ionization rates for photons with energy above 13.6 and 24.6 eV, spectroscopic CO index and other quantities that will be discussed later. Note that the model does not incorporate the effect

of an old preexisting population nor does it predict the contribution of nebular continuum from free-free and hot dust emission.

Ideally, one would like to constrain the model with quantities that are distance-independent and weakly dependent on extinction. We can define four near-infrared parameters that can satisfy the first requirement but not necessarily the second one. These are: the Brγ equivalent width, $W_{Br\gamma}$, defined as the negative ratio of the integrated Brγ flux to the local flux density F_λ, the spectroscopic CO index, CO_{sp}, the He Iλ2.06μm/Brγ ratio and the ratio of the ionization rate to the bolometric luminosity, N_{Lyc}/L_{IR}, the ionization rate being derived from the Brγ flux. These quantities are given in Table 6.3 for the nuclear region of NGC 3256. The total luminosity, L_{IR}, was estimated from a 10 μm measurement made in a 3.5$''$ aperture (see §6.4.1) and corrected for extinction. Both $W_{Br\gamma}$ and CO_{sp} were corrected for the contribution of free-free and hot dust emission to the K continuum since these two types of emission were not treated in the model. The fraction of the K luminosity contributed by hot dust and free-free emission were estimated as described in section 6.3.2 and are given in Table 6.3 as f_K^{HD} and f_K^{ff}, respectively.

The time-dependence of the four quantities described above is shown in Figure 6.4. This was calculated using a Salpeter IMF with lower and upper mass limits of 0.1 and 26 $M_\odot$ respectively. Although all these quantities could be used in principle for constraining the age, the spectroscopic CO index and the Brγ equivalent width are probably best suited for that purpose since they show a sharp variation on a short time scale. The strong time-dependence of CO_{sp} and $W_{Br\gamma}$ is easy to understand. Before 8 million years, the stellar population is dominated by young OB stars which produce strong ionization but little K continuum. This results in a large Brγ equivalent width and a negligible CO band. The near discontinuity in both CO_{sp} and $W_{Br\gamma}$ at 8-9 million years is due to a sudden increase of the K luminosity associated with the first red supergiants appearing in the stellar population.

The spectroscopic CO index of 0.26 and the logarithmic Brγ equivalent width of 1.40 observed on the nucleus of NGC 3256 (see Table 6.3) imply a very narrow range for the age of the burst, between 9 and 14 million years, depending on the detailed shape of the SFR (see Figure 6.4). The observed and predicted values for the He Iλ2.06μm/Brγ ratio and $\log N_{Lyc}/L_{IR}$ are also consistent with this age interval. The effect of a possible preexisting old population is negli-

Table 6.3

Observational Properties in the Nuclear Region of NGC 3256†

	Nucleus	5″ south	5″ east
M_K^{tot}	-22.64 ± 0.05	-21.77 ± 0.05	-21.12 ± 0.05
M_K^{corr} ‡	-22.55 ± 0.1	-21.68 ± 0.1	-20.97 ± 0.1
CO_{sp}^{corr} ‡	0.26 ± 0.01	0.12 ± 0.02	0.27 ± 0.03
$\log N_{Lyc}(s^{-1})$	54.06 ± 0.04	53.50 ± 0.07	53.55 ± 0.05
$\log \lvert W_{Br\gamma}\rvert$(Å) ‡	1.40 ± 0.02	1.21 ± 0.06	1.52 ± 0.04
$HeI2.06\mu m/Br\gamma$	0.35± 0.04	0.6 ± 0.2	0.8± 0.2
$\log N_{Lyc}/L_{IR}$	43.12 ± 0.08	—	—
f_K^{HD} *	>0.05	>0.05	>0.05
f_K^{ff} *	0.04	0.03	0.09

† All quantities have been corrected for extinction when appropriate.
‡ Corrected for free-free and hot dust emission.
* Fraction of the K continuum contributed by hot dust (f_K^{HD}) and free-free (f_K^{ff}) emission, calculated as described in the text.

gible on this result. Indeed, assuming very conservatively that 50% of the K continuum is associated with a giant-dominated population, characterized by negligible Brγ emission and a CO_{sp} of 0.2, then the intrinsic logarithmic Brγ equivalent width and the spectroscopic CO index should *increase* to 1.7 and 0.32 respectively. As shown in Figure 6.4, it is difficult to have such a strong CO band and large Brγ equivalent width *at the same time*, perhaps suggesting that 50% is too high for the contribution of an old population to the K continuum. This interpretation is consistent with our earlier suggestion that 20% is a more likely figure for this contribution. In any case, the new Brγ equivalent width, derived after correction for the old population contribution, still implies an age within the range given above.

Although an accurate determination of the age requires a detailed knowledge of the time-dependence of the SFR, *the Brγ equivalent width and the spectroscopic CO index provide a simple and powerful tool for estimating the the age of the burst.* In the following, we investigate how the four near-infrared quantities defined above can be used to further constrain the age, and also the

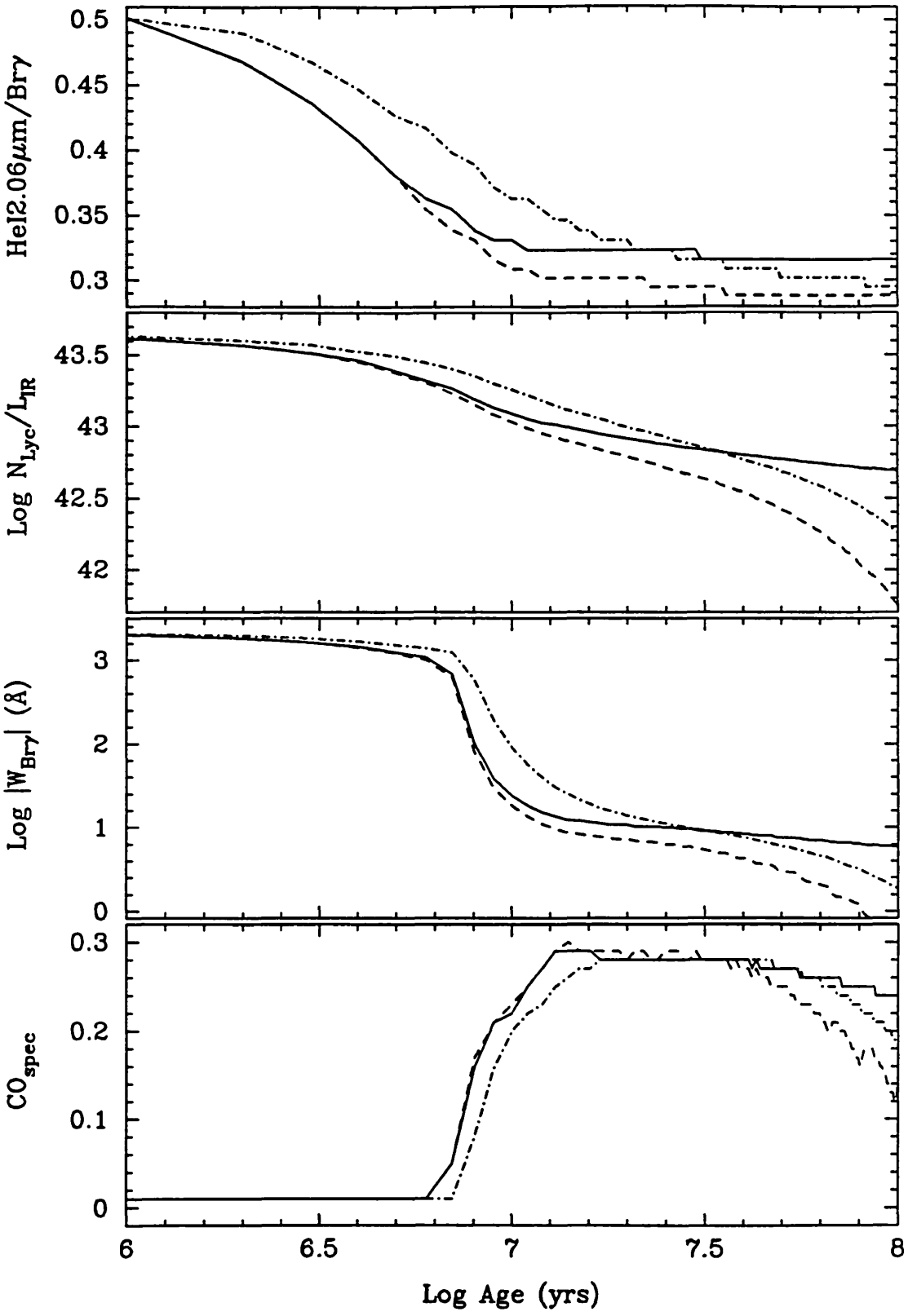

Figure 6.4— Continuum and emission line evolution of a young stellar population (the quantities are defined in the text), calculated with a population synthesis model, using a Salpeter IMF with $m_l = 0.1$ and $m_u = 26\ M_\odot$. The three lines of each plot correspond to different star formation rates: constant (solid line), exponential (dashed line) and "delayed" (dashed-dotted line).

parameters of the IMF.

6.4.3 The initial mass function

Whether the IMF in starbursts is significantly different from that in the solar neighbourhood is probably the most important question that has been raised by recent studies of these galaxies. Over the past few years, evidence has accumulated to suggest that galaxies with vigorous star formation activity are deficient in low-mass stars, a result usually referred as the lower mass limit being anomalously high or the IMF index significantly flatter than observed in the solar neighborhood (see Scalo (1989) for a review of the subject). There is already some evidence for a "top-heavy" IMF in NGC 3256. In their infrared study of interacting galaxies, Wright *et al.* (1988) showed that the small mass-to-light ratio in NGC 3256 can be accounted for only if the Miller-Scalo IMF (1979) is truncated at the lower end around 6 $M_{\odot}$. We shall show in this section that the IR spectroscopic properties of NGC 3256 are consistent with that conclusion.

Basically, there are three parameters to constrain: the IMF index, α and the lower and upper mass limits, m_l and m_u. The upper mass limit is probably the least constrained parameters and values between 30 and 100 $M_{\odot}$ are usually assumed in starburst models. It is however possible to constrain this parameter using the He Iλ2.06μm/Brγ ratio. Since the ionization potential of helium is twice that of hydrogen, the He Iλ2.06μm/Brγ ratio provides some information about the slope of the ultraviolet spectrum, more specifically about the relative number of massive stars. This technique has already been described in Chapter 3. It was shown there that the He Iλ2.06μm/Brγ ratio has a strong dependence on spectral type, a dependence which also translates to the upper mass limit. The dependence of this ratio on m_u is shown in Figure 3.6 of Chapter 3. The ratio of 0.35 ± 0.04 observed on the nucleus of NGC 3256 (see Table 6.3) implies an upper mass limit of $\sim$26 $M_{\odot}$.

It is difficult to constrain the IMF index without making some assumption about the age of the burst. Although we could use the age estimate derived in the previous section, the inferred age may depend on the IMF parameters. Therefore, to avoid this potential problem we choose to constrain both the age and the IMF index at the same time using the following χ^2 analysis. Using the population synthesis model described earlier, a set of five observables (CO_{sp}, $\log |W_{Br\gamma}|$, $\log N_{Lyc}/L_{IR}$, the He Iλ2.06μm/Brγ ratio and the absolute

K magnitude M_K) are calculated for several combinations of α and age, assuming $m_l = 0.1\ M_\odot$ and $m_u = 26\ M_\odot$ and a given time-dependence for the SFR. For a given set of observables x_i, each with an uncertainty σ_i, and X_i the corresponding quantity predicted by the model, the goodness of a given solution may be defined by the following χ^2 expression:

$$\chi^2(t_0, \alpha, M_*) = \sum_i \left(\frac{x_i - X_i(t_0, \alpha, M_*)}{\sigma_i} \right)^2 \qquad (6.2)$$

where t_0 is the age of the burst, α is the IMF index and M_* is the total mass participating in the burst. Good models are characterized by small values of χ^2. Given an estimate of M_*, a χ^2 is calculated for each pair (α-Age). In principle, if there is a unique solution to the problem, one should find a minimum χ^2 in the plane (α-Age).

The dynamical mass in NGC 3256 can be determined from the rotation curve of Feast and Robertson (1978). Within the central 3.5″ of the optical nucleus, we derive a mass of $1.3 \times 10^8\ M_\odot$, assuming a distance of 37 Mpc. This value should be regarded as highly uncertain since there is evidence that the dynamical center of this galaxy is offset from the optical and 2.2 μm nucleus by $\sim$5″ to the west. One can also estimate the mass participating in the starburst from the amount of molecular gas in the nucleus. Using the CO map of Sargent, Sanders and Phillips (1989) and assuming that the molecular gas is distributed as an exponential disk, we derive a total H_2 mass of $1.8 \times 10^8\ M_\odot$ within the central 3.5″. It is probably conservative to assume that the mass M_* participating in the starburst is not higher than the amount of molecular material available. This is especially true if the starburst is relatively young, which is the case of NGC 3256, as shown earlier. We thus adopt a mass of $1.8 \times 10^8\ M_\odot$ as a probable mass participating in the starburst.

Figure 6.5 show three contour maps of the reciprocal χ^2 ($1/\chi^2$), calculated for different SFR history. These figures show without doubt that, for a given time-dependence of the SFR and a mass, *the age and the IMF index are uniquely defined in the plane (α-Age).* One can get a quantitative estimate of the uncertainty in α and the age by looking at the extent of the contours in Figure 6.5. These were drawn on a logarithmic scale, each one separated by "one sigma" *i.e.* by a factor of $e^{1/2}$. The extent of the highest contour yields a one sigma uncertainty of $\sim$ 0.2 for the IMF index and half a million years for the age.

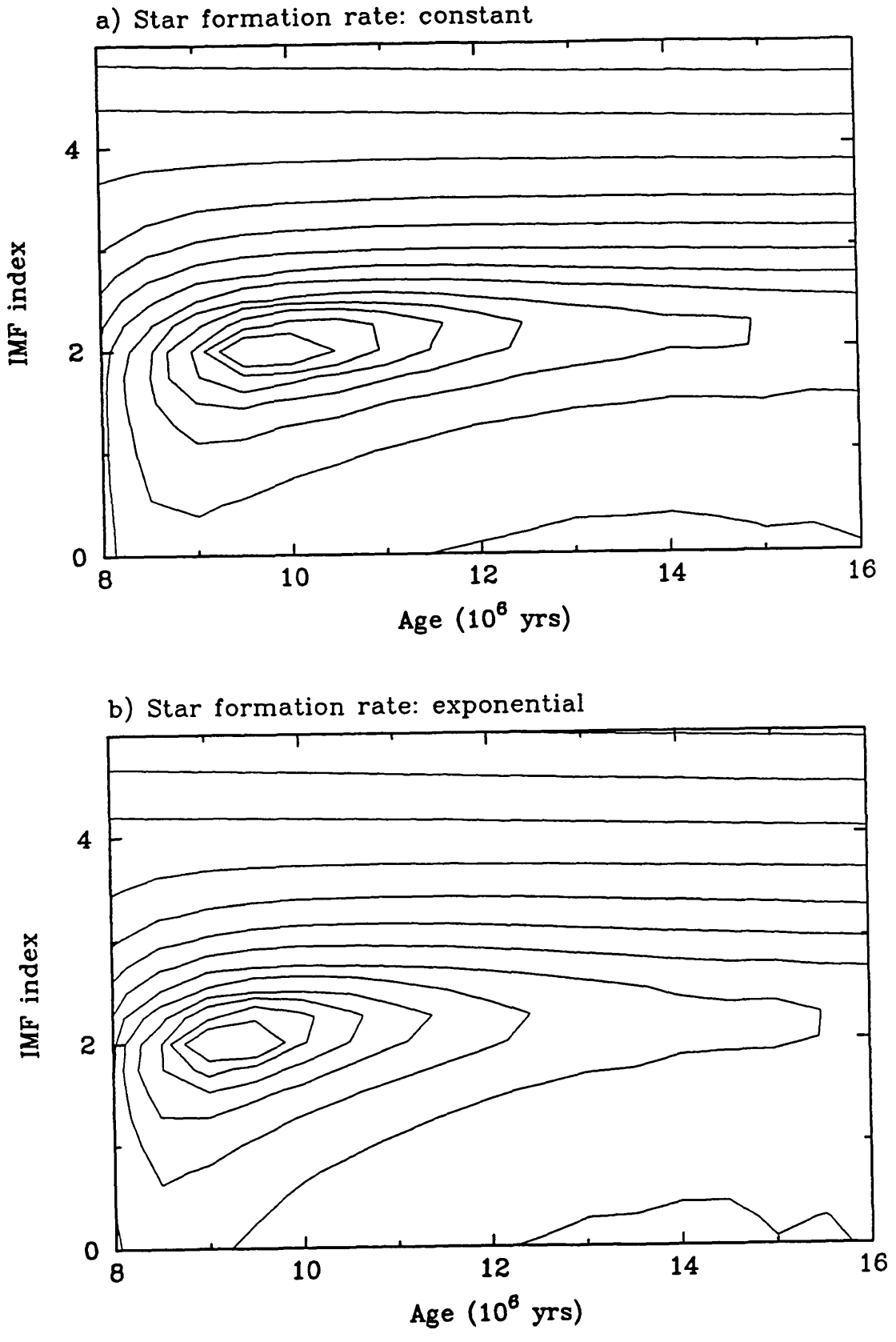
a) Star formation rate: constant
IMF index
0
2
4
8
10
12
14
16
Age (10^6 yrs)
b) Star formation rate: exponential
IMF index
0
2
4
8
10
12
14
16
Age (10^6 yrs)

Figure 6.5

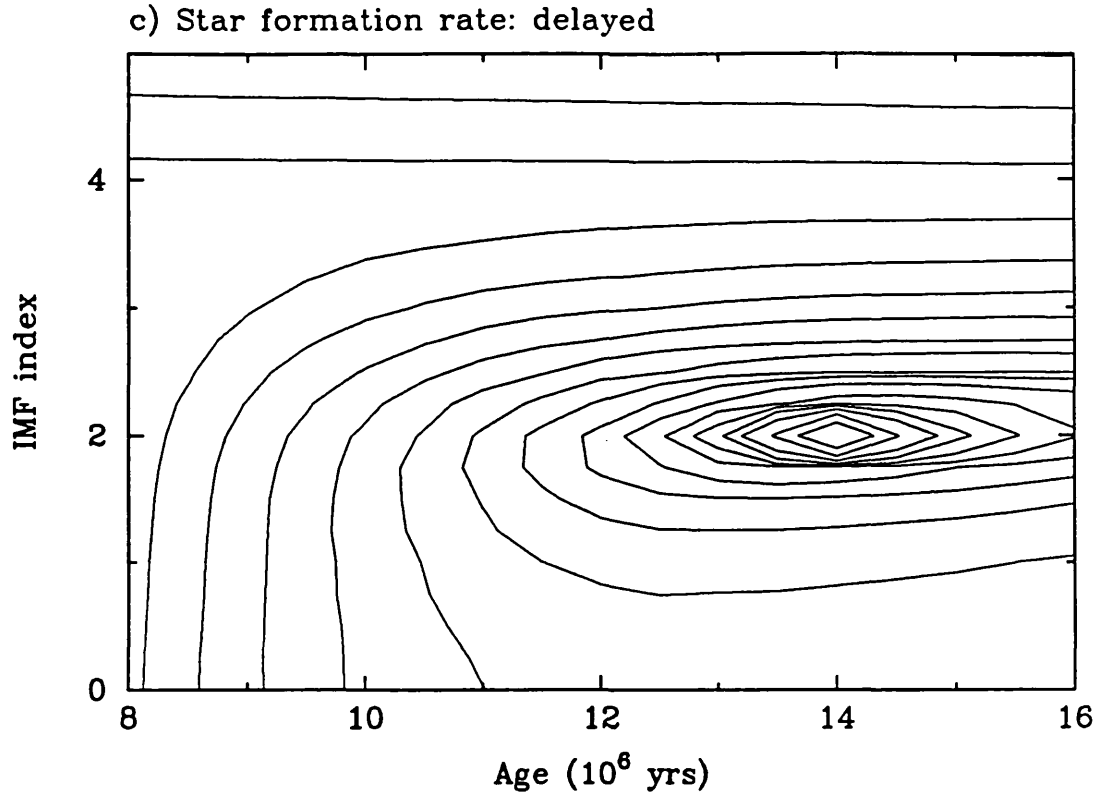

Figure 6.5— Reciprocal χ^2 diagram in the (α-Age) plane for three different star formation rate histories: a) constant, b) exponential with a time scale of 20×10^6 years and c) "delayed" with the same time scale as in b). The contours are drawn on a logarithmic scale, each one separated by "one sigma", *i.e.* by a factor of $e^{1/2}$. The highest contour is drawn one sigma away from the peak.

To complement the χ^2 analysis, a model summary is given in Table 6.4. The predictions of the "best" models, inferred from the analysis above, are given in the third line of each SFR history. For comparison, models calculated with a Salpeter and Scalo IMF are also presented (the same age inferred from the "best" model was assumed). Judging from the absolute χ^2 values given in Table 6.4, the "delayed" model seems to provide a much better fit to the observations compared with the constant and exponentially decreasing SFR. The latter birthrate functions tend to predict CO bands and Brγ equivalent widths which are too small. Since the delayed SFR model reaches a maximum at 20 million years, the age of 14 million years inferred from this model suggests that the SFR is still rising in NGC 3256.

For the three models investigated, the minimum χ^2 was found with an IMF index of 2.0 which is significantly flatter than either the Salpeter or Scalo solar neighbourhood IMF. As seen in Table 6.4, models with a Scalo IMF can

Table 6.4
Model Summary for the Nucleus of NGC 3256[†]

Age (10^6 yrs)	α[‡]	M_K (mag)	CO_{sp}	log $W_{Br\gamma}$ (Å)	log N_{Lyc} (s^{-1})	log N_{Lyc}/L_{IR} (s^{-1} $L_\odot^{-1}$)	HeI/Brγ	χ^2
				$SFR = const$				
10.0	Scalo	-20.66	0.22	1.39	53.24	43.03	0.31	376
10.0	2.35	-21.61	0.22	1.38	53.61	43.04	0.33	107
10.0	2.00	-22.75	0.22	1.37	54.06	43.11	0.34	22
				Exponential: $SFR \propto \exp(-t/\tau_0)$, $\tau_0 = 2 \times 10^7$ years				
9.5	Scalo	-20.67	0.21	1.36	53.22	43.00	0.30	386
9.5	2.35	-21.63	0.22	1.35	53.59	43.05	0.32	108
9.5	2.00	-22.79	0.22	1.34	54.04	43.08	0.33	31
				Delayed: $SFR \propto t\exp(-t/\tau_0)$, $\tau_0 = 2 \times 10^7$ years				
14.0	Scalo	-20.67	0.26	1.39	53.25	43.06	0.32	371
14.0	2.35	-21.58	0.26	1.40	53.62	43.12	0.35	110
14.0	2.00	-22.70	0.26	1.40	54.07	43.15	0.36	2.4
Target values.....		-22.55±0.1	0.26±0.01	1.40±0.02	54.06±0.04	43.12±0.08	0.35±0.04	

[†] All model are calculated with a mass M_* of 1.8×10^8 $M_\odot$.
[‡] IMF index ($\psi(m) \propto m^{-\alpha}$) with $m_l = 0.1$ $M_\odot$ and $m_u = 26$ $M_\odot$. "Scalo" refers to the solar neighbourhood IMF of Scalo (1986).

reproduce less than 20% of the observed ionization rate and 2.2 luminosity. It is interesting to note that a similar result is obtained even when the mass is excluded from the analysis. Indeed, if we omit M_K in the χ^2 expression, both the age and the IMF index remain uniquely defined. Again, the best solution is found for a delayed SFR with the same age as inferred previously but with an IMF index of 2.25 ± 0.2. Thus, compared with the solar neighbourhood IMF of Scalo, the analysis above provides strong evidence that *the IMF in NGC 3256 is biased against the formation of low-mass stars, a result which is independent of the knowledge of the mass participating in the burst.*

Since the age and the shape of the IMF can be determined independently of the mass, it should be possible to constrain the mass participating in the starburst. Varying the mass yields different solutions in the χ^2 diagram and those can be discriminated from their χ^2. Figure 6 shows the dependence of the χ^2 on the mass, calculated assuming a "delayed" SFR. Although there are several local minima, the best solution is found at a mass of $3.2 \times 10^8\ M_\odot$. This solution yields the same age of 14 million years previously inferred but an IMF index of 2.25, still flatter than the Scalo IMF. If we constrain the mass participating in the burst to be less than the current amount of molecular gas ($\sim 2 \times 10^8\ M_\odot$), then the best solution is found at $M_* = 1.6 \times 10^8\ M_\odot$ with an IMF index of 2.

It is also instructive to attack the problem with another approach, which consists of fixing both the IMF index and the age, and to determine the most likely combination of the mass limits, m_l and m_u, that satisfy the observations. Using the same χ^2 analysis as described before, we calculated a χ^2 for several combination of m_l and m_u, using a Scalo IMF, a delayed star formation rate, an age of 14×10^6 years (as suggested by Figure 6.5c) and a mass of $1.6 \times 10^8\ M_\odot$. The resulting reciprocal χ^2 diagram is shown in Figure 6.7. Like Figure 6.5, there is a unique solution, this time at $m_l \sim 2.5\ M_\odot$ and $m_u \sim 26.5\ M_\odot$. This mass range is consistent, at least qualitatively, with the flat IMF inferred above.

It thus seems that whatever approach we choose to constrain the stellar IMF parameters, it is difficult to avoid the conclusion that the IMF is biased against the formation of low-mass stars in NGC 3256. Whether the relatively high lower mass limit found earlier by fixing the IMF index to that of the solar neighbourhood corresponds to some physical reality in the stellar population, is far from clear. Perhaps it is more natural to assume that low-mass stars as

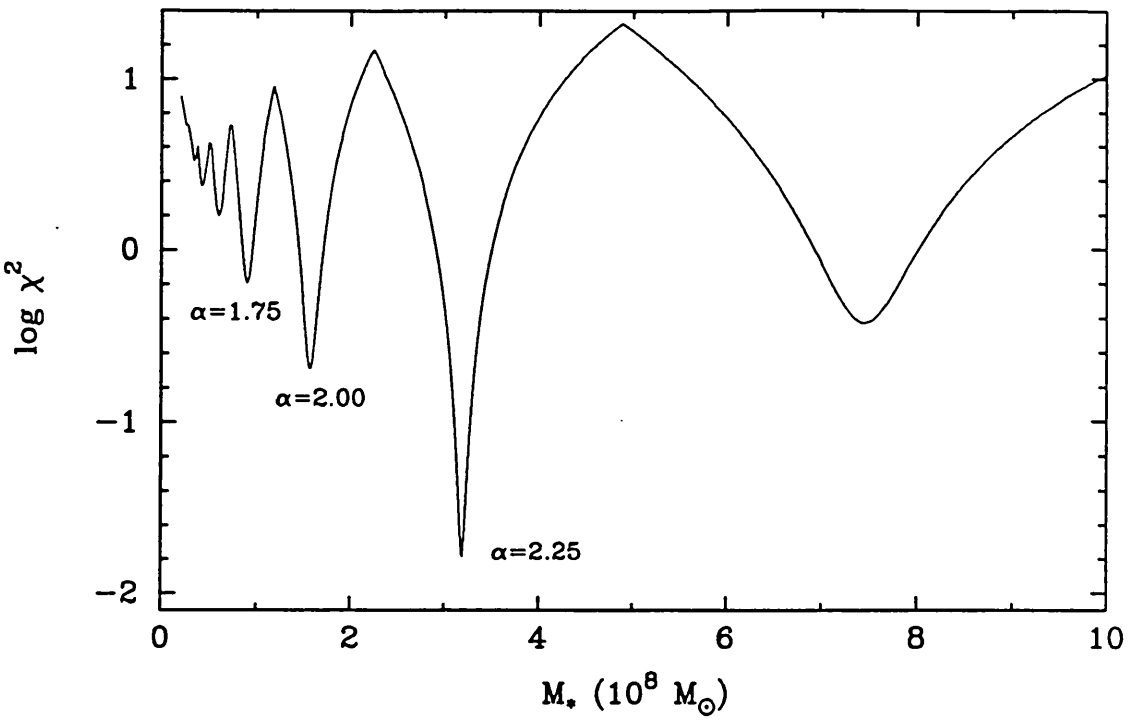

Figure 6.6— χ^2 *vs* the mass participating in the burst. The corresponding IMF index is indicated for some local minimum. The best solution is found for a mass of 3.2×10^8 $M_\odot$.

low as 0.1 $M_\odot$ *do* form in starburst galaxies, only with an IMF flatter than the one measured in the solar neighbourhood.

Interestingly, we inferred an IMF index of ~2 which is not too far from 1.5, the observed mass spectrum index of clumps in molecular cloud (Blitz, Long and Stark, private communication). Zinnecker (1988) has suggested that the IMF could be related to the mass spectrum of clumps *via* a "initial-final mass relation" and presented some directions on how theory could constrain the form of this relation. Although this suggestion is still very speculative, the flat IMF observed in starburst galaxies could be interpreted, in this context, as given by the clump mass spectrum without much modification by the initial-final mass relation. Further determinations of the IMF index in other starburst galaxies are needed to test this hypothesis.

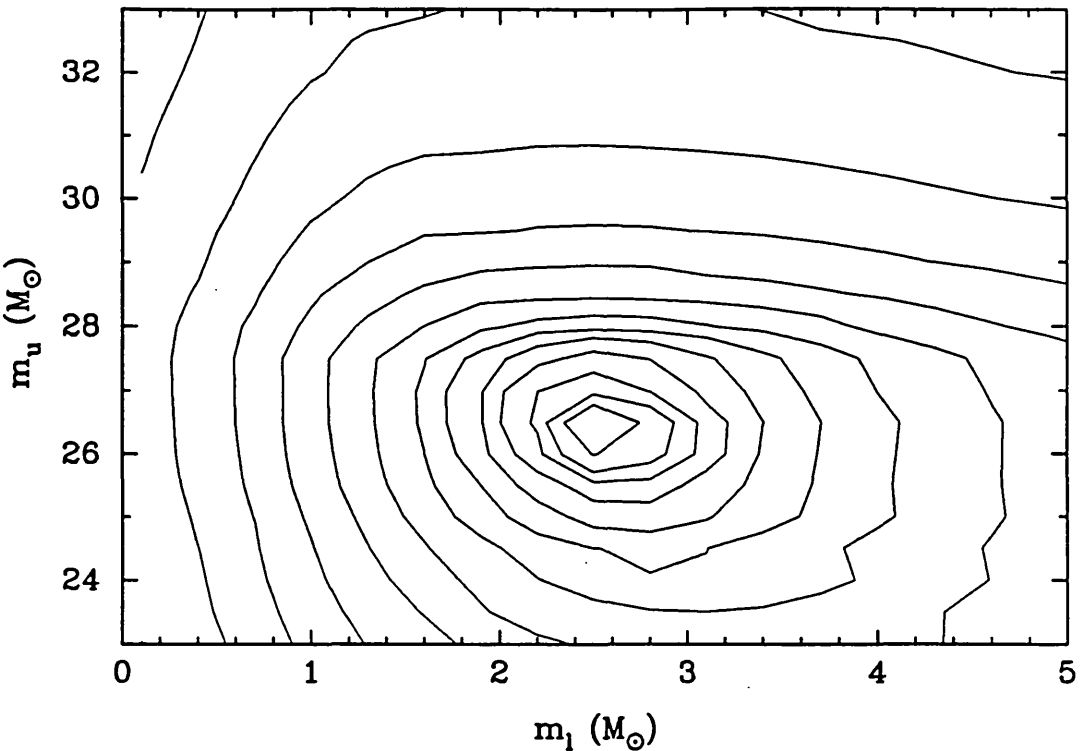

Figure 6.7— Reciprocal χ^2 diagram in the $(m_u - m_l)$ plane, calculated using a Scalo IMF, a delayed star formation rate, an age of 14×10^6 years and a mass M_* of 1.6×10^8 $M_\odot$. The contours were drawn in the same way as described in Figure 6.5.

6.5 Excitation Mechanism of the H_2 Emission

Strong H_2 emission is a characteristic feature of starburst galaxies and NGC 3256 is no exception to this rule. After Brγ, the 1-0 S(1) transition of H_2 is the strongest emission line in the K-window spectrum of the nucleus (see Figure 6.2a, 6.2b). In the following, we try to constrain the excitation mechanism at the origin of the H_2 emission, to determine whether the gas is shock or fluorescently-excited. We will show that UV fluorescence provides the most likely mechanism.

6.5.1 Constraints from the line ratios

The H_2 line ratios observed on the nucleus of NGC 3256 are presented in Table 6.5 and compared with predictions from typical shock and low-density fluorescent models. This table shows that it is difficult to explain the strength of the 2-1 S(1) by a shock model; its intensity is more consistent with UV excitation. On the hand, the UV fluorescence model predicts a 2-1 S(3) which is twice as

Table 6.5
H_2 Line Ratios in NGC 3256

Line	λ^a (μm)	I/I_0^b	Model		
			shock[c]	UV[c]	mixed[d]
1-0 S(2)	2.0338	0.45 ± 0.13	0.37	0.50	0.44
2-1 S(3)	2.0735	< 0.17	0.08	0.35	0.22
1-0 S(1)	2.1218	1.00	1.00	1.00	1.00
2-1 S(2)	2.1542	< 0.17	0.03	0.28	0.16
1-0 S(0)	2.2233	0.26 ± 0.05	0.21	0.46	0.34
2-1 S(1)	2.2477	0.39 ± 0.06	0.08	0.56	0.32

[a] Wavelength in vacuum.
[b] Corrected for extinction. 3σ upper limits are given for undetected lines.
[c] Shock and UV line ratios from Black & Van Dishoeck (1987) model S2 and model 14.
[d] Expected line ratios assuming equal contribution from shock and UV excited H_2 gas.

strong as our 3σ upper limit. In fact, if we exclude the 2-1 S(1), the other line ratios are consistent with the shock model. It thus seems difficult to fit the observed line ratios with a single mechanism. If we assume instead a "mixed" model in which half of the H_2 emission is radiatively-excited and the rest excited by shock, then a better fit is obtained. As shown in Table 6.5, a mixed model is more consistent with the both undetected 2-1 S(3) and 1-0 S(2) and the equally strong 2-1 S(1) and 1-0 S(0).

Since the only evidence for low-density fluorescence relies on the correct identification and detection of the 2-1 S(1), some remarks are in order about this line. First, we can rule out the possibility that we have overestimated the strength of the 2-1 S(1) by misplacing the local continuum. Although the resolution of our spectra corresponds to an improvement of a factor of three over the CVF, there are still uncertainties in the assignment of the continuum. Nevertheless, our resolution is high enough to detect the NaI and CaI absorptions next to the 1-0 S(0) and 2-1 S(1) lines (see Figure 6.2b). We showed in §6.3.2 that the strength of the CO band implies that 2.2 μm luminosity is dominated by late-type stars, an interpretation which is confirmed by the fact that the NaI and CaI lines have equivalent widths very similar to that observed in late-type

giants. This shows that our estimate of the continuum is very reasonable.

One could also argue that given the unidentified features found in our spectra (see §6.3.3), perhaps the 2-1 S(1) is misidentified or blended with something else. We cannot rule out this possibility, but this suggestion, however, remains *ad hoc* and given the fact that we detected other H_2 lines, we believe without further evidence to the contrary that the emission line found at 2.247 ± 0.001 μm is correctly identified with the 2-1 S(1) (2.2477 μm). The evidence for low-density fluorescence from the strong 2-1 S(1) is obviously marginal and confirmation of this result from a higher resolution spectrum is certainly needed.

An important test of low-density fluorescence is to look for high vibrational H_2 lines in the J and H windows. These lines are predicted to have intensities similar to the K-window transitions (Black & Van Dishoeck 1987; Sternberg & Dalgarno 1989). Using the theoretical line ratios of Black and Van Dishoeck (1987), we have calculated synthetic J and H H_2 spectra using Gaussian profiles of the same widths as the strong emission lines observed in these bands. The line intensities were scaled with the observed strength of the 1-0 S(1) and corrected for reddening assuming an absolute extinction at 2.2 μm of 0.55 mag and the extinction law of Draine (1989). The resulting spectra, superimposed on the galaxy spectra, are shown in Figure 6.3a and 6.3b. Unfortunately, the signal-to-noise of our spectra is not good enough and the synthetic H_2 spectra are virtually buried in the noise. Therefore, no constraints can be put on the excitation mechanism from these spectra. Although J and H H_2 lines provide the best diagnostic for determining the excitation mechanism, in practice, these transitions can be very difficult to detect because of the extinction.

Finally, we note that there is another alternative to the two-component or mixed model suggested above for explaining the "unusual" H_2 line ratios. All the H_2 emission could be fluorescently-excited if the density is near the transition between the low and high density regime. As shown in Figure 12 of Sternberg and Dalgarno (1989), this transition is very sharp and occurs at a density of $\sim 3 \times 10^4$ cm^{-3}. The behaviour of the H_2 line ratios at this transition is not well understood. Whether this is the case in NGC 3256 is difficult to assess but this hypothesis could explain why the line ratios are just in between the shock and the fluorescent case. In the following, we investigate how we can constrain, from a theoretical point of view, the amount of H_2 emission excited by shock and UV fluorescence.

6.5.2 H_2 EMISSION CONTRIBUTION FROM A SHOCK COMPONENT

A potential contribution of shock-excited H_2 emission in starburst galaxies is that associated with young stellar objects (YSO) and supernova remnants (SNR). In Chapter 5, we presented a model which predicts the 1-0 S(1)/Brγ as a function of time. Given the age (between 9 and 14 million years) and the IMF parameters inferred earlier for NGC 3256, this model predicts a 1-0 S(1)/Brγ ratio of $\sim$ 0.08, much lower than the ratio of 0.34 ± 0.02 observed on the nucleus. This implies that less than 25% of the H_2 emission at this position is contributed by YSOs and SNRs. The same conclusion is valid for the strong H_2 emission observed 5″ south of the nucleus. Although the large 1-0 S(1)/Brγ of 1.8 observed at this position could be explained by a starburst of $\sim$ 80 million years old (see Figure 5.1 in Chapter 5), this age would imply a Brγ equivalent width less than 3 Å (see Figure 6.4) which is 5 times less than that. On the basis of these calculations we conclude that YSOs and SNRs are unlikely to be the main sources of H_2 emission in NGC 3256.

This interpretation challenges the idea that the strong H_2 and [FeII] emission observed in starburst galaxies is shock-excited by SNRs (*e.g.* Moorwood & Oliva 1988). The reason why the [FeII] emission is generally thought to be shock-excited in galaxies is because the observed [FeII]1.644/Brγ line ratio of $\sim$1 is much stronger than the ratio of 0.06 predicted for photodissociation regions (Graham, Wright & Longmore 1987). However, the situation is far from clear since this ratio is 0.6 in the nebula illuminated by the star ηCarinae (Allen, Jones & Hyland 1985). Such a hot and young object is likely to be present in starbursts and could contribute significantly to the [FeII] emission. We note also that the [FeII] emission could be fluorescently-excited as suggested earlier. Finally, in their recent IR study of the Crab nebula, Graham, Wright & Longmore (1990) suggested that the observed [FeII] emission is excited in a warm photodissociation region, photo-ionized by power-law synchrotron emission. This seriously questions the idea that the [FeII] emission is shock-excited in galaxies.

Another possible source of collisionally-excited H_2 emission is that associated with large scale shocks driven by the merger of the two parent galaxies in NGC 3256. This mechanism is probably responsible for the strong H_2 emission observed in the merger NGC 6240. Recent line imaging of this galaxy (Herbst *et al.* 1990) has revealed that the peak of the H_2 emission is displaced from the

two infrared nuclei, a feature that was interpreted as evidence that large scale shocks are responsible for the excitation of the H_2 gas. Interestingly, we found that the H_2 emission in NGC 3256 is equally strong on the nucleus and 5″ south. Although detailed mapping of this galaxy is needed to accurately determine the relative extent of the H_2 emission and the continuum, our observations are very suggestive that, like NGC 6240, the H_2 peak is not exactly coincident with the infrared nucleus. This interpretation is reinforced by the possibility that the extinction is higher 5″ south than on the nucleus (see argument in section 6.4.1). Finally, the fact that the 1-0 S(1) is stronger than Brγ at this position could also be argued as evidence for shock excitation.

6.5.3 H_2 EMISSION CONTRIBUTION FROM UV FLUORESCENCE

Puxley, Hawarden & Mountain (1990) showed (see also Chapter 5) that OB stars associated with a young stellar population emit enough UV radiation to excite the surrounding molecular H_2 gas and produce fluorescent H_2 emission, in quantity which can explain a wide range of 1-0 S(1)/Brγ ratios observed in starburst galaxies. In this section, we follow a different approach than that adopted in Chapter 5 to show that UV fluorescence provides a viable mechanism for explaining a significant fraction of the H_2 emission observed in NGC 3256.

We suppose that the emitting region of the starburst is made of N_{cl} spherical molecular clouds of mass $M_{H_2}^{cl}$ and density n. These clouds are bathed in a diffuse UV radiation field produced by recently formed OB stars which are assumed to be located in the diffuse interstellar medium, outside their parent molecular clouds. This geometry corresponds to "model C" of Puxley, Hawarden and Mountain (1990) and is justified by the fact that the nucleus of NGC 3256 is relatively evolved, even if the starburst is not older than 15 million years. The fact that galactic O stars spend only 15% of their lifetime embedded in their parent molecular clouds (Wood & Churchwell 1989b) suggests this geometry is probably a good representation of the interstellar medium of the nuclear region of NGC 3256.

The UV radiation field impinging on molecular clouds produces fluorescent H_2 emission. For an observer at a distance D, the integrated H_2 flux emitted in the 1-0 S(1) line from all the clouds in the beam is given by:

$$F_{S(1)} = 4\pi R_{cl}^2 \left(\frac{M_{H_2}^{tot}}{M_{H_2}^{cl}} \right) I_{S(1)} D^{-2} \qquad (6.3)$$

where R_{cl} is the radius of the clouds, $M_{H_2}^{tot}$ the total H_2 mass in the beam and $I_{S(1)}$, the intensity of the fluorescent 1-0 S(1) line in units of $erg\ s^{-1}\ cm^{-2}\ sr^{-1}$. The following analytical expression can be used for this intensity (Sternberg 1989):

$$I_{S(1)} = 5.1 \times 10^{-10}(\frac{\sigma_0}{\sigma})(\frac{R}{R_0})n \ln\left[90(\frac{\sigma_0}{\sigma})^{1/2}(\frac{R}{R_0})(\frac{\chi}{n}) + 1\right] \qquad (6.4)$$

where χ is the photon flux between 912 and 1108 Å, relative to mean background of 2.7×10^{11} $photons\ s^{-1}\ m^{-2}$ measured in the solar neighbourhood (Draine 1978, as quoted in Black & Van Dishoeck 1987). The parameter R is the molecular formation rate coefficient and σ the effective dust continuum cross section at 1000 Å, with $R_0 = 3 \times 10^{17}\ cm^3\ s^{-1}$ and $\sigma_0 = 1.9 \times^{-21}\ cm^2$. After substitution of equation 6.4 in 6.3, assuming $R_{cl} = (3M_{H_2}^{cl}/4\pi n m_H)^{1/3}$ (m_H is the mass of a hydrogen atom), $R = R_0$ and $\sigma = \sigma_0$, we have

$$F_{S(1)} = 1.35 \times 10^{-12}\left(\frac{M_{H_2}^{tot}}{10^8\ M_\odot}\right)\left(\frac{M_{H_2}^{cl}}{10^5\ M_\odot}\right)^{-1/3}\left(\frac{n}{10^4\ cm^{-3}}\right)^{1/3}$$
$$\left(\frac{D}{Mpc}\right)^{-2} \ln\left[90(\frac{\chi}{n_H}) + 1\right]\ erg\ s^{-1}\ cm^{-2}. \qquad (6.5)$$

The three unknown quantities in this equation are the mass of individual clouds $M_{H_2}^{cl}$, the density n and the intensity of the UV field χ. For the total H_2 mass in the beam, $M_{H_2}^{tot}$, we adopt the estimate of $1.8 \times 10^8\ M_\odot$ derived from the CO map of Sargent, Sanders and Phillips (1989) (see also section 6.4.3). Given the observed H_2 flux (corrected for extinction) and a distance of 37 Mpc, the values of n and χ are constrained by the implicit equation

$$\left(\frac{M_{H_2}^{cl}}{10^5\ M_\odot}\right)^{-1/3}\left(\frac{n}{10^4\ cm^{-3}}\right)^{1/3} \ln\left[90(\frac{\chi}{n}) + 1\right] = 17.45f \qquad (6.6)$$

where f is the fraction of the total H_2 emission excited by fluorescence. This constraint is graphically displayed in Figure 6.8 for $f = 1$ (solid lines) and $f = 0.5$ (dashed lines), calculated with molecular cloud masses of 10^3, 10^4 and $10^5\ M_\odot$.

Although it is difficult to constrain the density, one can still put an upper limit on this parameter from the the 2-1 S(1)/1-0 S(1) line ratio. If we assume that all the H_2 emission is fluorescently-excited, then this ratio will vary from 0.56 in the low-density regime ($\sim 10^4$ cm^{-3}) to 0.1 when the density reaches $\sim 10^5\ cm^{-3}$ (Sternberg & Dalgarno 1989). The ratio of 0.4 observed on the

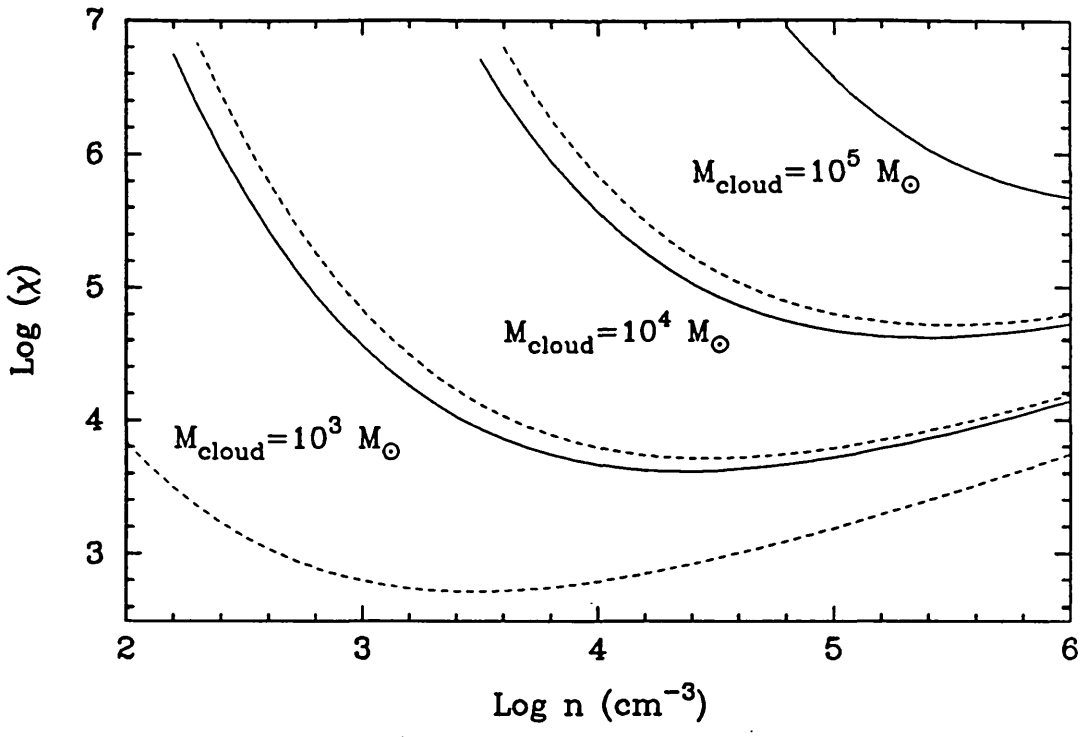

Figure 6.8— Constraint on the intensity of the UV field χ and the density n for producing all (solid line) or half (dashed line) of the observed H_2 flux by fluorescence, each case calculated with three different molecular cloud mass.

nucleus of NGC 3256 implies an excitation temperature of $\sim 4500\ K$, and from Figure 12 of Sternberg & Dalgarno (1989), this corresponds to a density of $(2-3) \times 10^4$ cm^{-3} ($\log n = 4.4$).

It follows from Figure 6.8 that the minimum intensity of the UV field that could produce half of the total H_2 emission is $\log \chi = 2.7$ assuming that the average molecular cloud in the center of NGC 3256 has a mass of $10^3\ M_\odot$. Overall, cloud masses between 10^3 and $10^4\ M_\odot$ and $\log \chi = 3-5$ could easily explain at least half if not all of the observed H_2 emission.

We now try to estimate the UV intensity in the center of NGC 3256. The UV intensity χ at a distance d from a star with effective temperature T_{eff} is given by

$$\chi = 310 \left(\frac{N_{NUV}(T_{eff})}{10^{48}\ s^{-1}} \right) \left(\frac{d}{pc} \right)^{-2} \tag{6.7}$$

where $N_{NUV}(T_{eff})$ is the production rate of non-ionizing photons between 912 and 1108 Å. Puxley, Hawarden & Mountain (1990) have calculated this parameter for stars of different effective temperatures by integrating under Kurucz (1979) atmosphere models. For an O8V star ($T_{eff} \sim 35000\ K$), which is the

average spectral type of the ionizing stars in NGC 3256 (see section 6.4.1), $N_{NUV} = 4 \times 10^{48}\ s^{-1}$.

One can obtain a lower limit on χ by evaluating equation 6.7 at one-half the mean separation of ionizing stars. Assuming that the stars are uniformly distributed, this separation is

$$\frac{d_*}{2} = 0.62\rho_*^{-1/3}\ pc \tag{6.8}$$

where ρ_* is the number of ionizing stars per cubic parsec. From the number of O8V stars estimated in section 6.4.1, $\rho_* = 0.01$ or $0.02\ pc^{-3}$ depending on whether the total volume is a sphere of 300 pc in radius or a disk of the same diameter with a thickness of 100 pc. This yields a one-half mean separation of 2-3 pc, corresponding to $\log\chi = 2.1 - 2.5$.

A more realistic estimate of χ is obtained by integrating the UV intensity of all the stars in the nucleus. One must take into account the effect of dust absorption in the interstellar medium. At a distance d from a star, the UV intensity is simply given by: $\chi(d) = \chi_0 \exp(-n_H^{ism}\sigma_0 d)$, where χ_0 is the UV intensity if there were no dust and n_H^{ism} is the neutral density of the diffuse ISM. For instance, for a typical ISM density of 1 cm^{-3}, an optical depth of one corresponds to a distance of 170 pc. Thus, there is clearly more than one star contributing to the UV intensity at a given point in the nucleus. Integrating over large distances and taking into account the effect of dust absorption, we then have

$$\chi = 13000\left(\frac{\overline{N}_{NUV}}{10^{48}\ s^{-1}}\right)\left(\frac{\rho_*}{10^{-2}\ pc^3}\right)\left(\frac{n_H^{ism}}{1\ cm^{-3}}\right)^{-1}\left(\frac{\sigma_0}{10^{-21}\ cm^2}\right)^{-1} \tag{6.9}$$

where $\overline{N}_{NUV}$ is the average number of non-ionizing photons per star. This expression is valid as long as the obscuration is dominated by dust and not by molecular clouds. Assuming that the H_2 clouds have an average mass of $10^4\ M_\odot$, then the total H_2 mass in the nucleus implies a one-half mean cloud separation of 7-10 pc, three times the separation of the stars. Assuming a cloud density of 10^4 cm^{-3}, these clouds would have a radius of 2 pc. In such condition, only 2% of the volume would be filled by molecular clouds. We can quantify the obscuration effect due to molecular clouds by estimating the distance beyond which the total solid angle of the clouds is greater than 2π steradian *i.e.* when they cover half the sky from a any location in the nucleus. This distance is given by $r_0 = 1/2\pi\rho_{N_{cl}}R_{cl}^2$ where $\rho_{N_{cl}}$ is the number of molecular cloud per

cubic parsec. Using the numbers above, this distance is $\sim 100 - 200$ pc. This is of the same order as the distance at which the dust optical depth is one, and shows that it is reasonable to assume that the obscuration is dominated by dust.

Equation 6.9 shows that UV intensities of the order of 10^4 are certainly possible in the nucleus of NGC 3256, and as shown in Figure 6.8, such intensity is high enough to produce more than half of the observed H_2 emission. In fact, this estimate could well be underestimated since we have assumed a uniform stellar distribution. In reality, young stars are usually found closer to their parent molecular clouds, resulting in strong radiation field at their surface. The best example of such situation is the Orion nebula where the UV intensity near the photodissociation region (the Orion bar) is estimated to be 10^5 times the Galactic background (Burton and Puxley 1989).

This simple analysis shows that UV fluorescence is a viable mechanism for explaining the H_2 emission observed in the nucleus of NGC 3256, provided that the neutral density in molecular clouds is high enough ($\sim 10^4$ cm^{-3}) and that their masses are $\lesssim 10^4$ $M_\odot$, a requirement which is very reasonable. Whether this excitation mechanism is also responsible for the strong H_2 emission observed 5″ south of the nucleus remains to be shown. The smaller molecular mass and the fewer number of ionizing stars at this position would probably require a different geometry for explaining the high 1-0 S(1)/Brγ ratio of 1.4 ± 0.2 measured in the southern spectrum. The possibility that this region suffers from high extinction perhaps suggests that the stars are still embedded in their parent molecular clouds. Puxley, Hawarden and Mountain (1990) have shown that large 1-0 S(1)/Brγ line ratios can result from such geometry. Thus, UV fluorescence is, in principle, a viable excitation mechanism for the H_2 emission outside the nucleus. However, this question is far from settled since it can also be argued that the strong H_2 emission and the large 1-0 S(1)/Brγ ratio are good evidence for shock excitation.

In summary, both the observed line ratios and the physical conditions inferred in the nuclear region NGC 3256 are in favour of UV fluorescence as the most likely excitation mechanism of the H_2 gas. Although a thermal component cannot be excluded, we have shown that Orion-type objects and supernova remnants are unlikely to produce significant H_2 emission. If as much as 50% of the H_2 gas is collisionally-excited on the nucleus, then interaction-driven shocks

are the most likely cause of this emission.

6.6 Summary and Conclusions

We have presented near-infrared spectra of the nuclear region of the merging system NGC 3256. The spectra shows strong molecular hydrogen emission, recombination lines of hydrogen, helium and [FeII]. The relative strength of these lines and the strong CO band absorption are interpreted as evidence that NGC 3256 is experiencing an episode of vigorous star formation activity.

We have used a stellar population synthesis model to determine the age of the burst and the parameters of the initial mass function. The results of this modelling shows that the Brγ equivalent width provides a simple and powerful tool for constraining the age of the burst. With this technique, we derived an age of 9 to 14 million years for the nucleus, depending on the detailed shape of the star formation rate. A χ^2 analysis technique was used to constrained both the age and the slope of the initial mass function in a unique way. Assuming that the IMF is extended down to 0.1 $M_\odot$ and up to 26 $M_\odot$, the observational properties of the galaxy are best fitted with an IMF index of 2 ± 0.2. This is significantly flatter than the IMF in the solar neighbourhood and suggests that low-mass stars are deficient in NGC 3256. This result is independent of the knowledge of the mass participating in the starburst.

The strength of the 2-1 S(1)/1-0 S(1) line ratio shows that at least half if not all of the H_2 emission observed on the nucleus of NGC 3256 is fluorescently-excited by UV photons. From a simple geometrical representation of the inter-stellar medium, in which molecular clouds are bathed in a diffuse UV radiation field, we showed that there are enough OB stars and molecular material in the center of the galaxy to reproduce the observed H_2 flux.

A number of unidentified emission features were found on the K-window spectrum of the nucleus, the strongest one was measured at 2.196 ± 0.001 μm (in the vacuum). We tentatively identified an emission line at 2.092 μm with a high excitation transition of [FeII].

Chapter 7

Summary and Conclusions

7.1 Summary

A near-infrared spectroscopic study of several interacting and merging galaxies exhibiting vigorous star formation activity has been presented in this dissertation. The main results are summarized below.

New near-infrared spectroscopic observations of interacting and merging galaxies was presented in Chapter 2 and 6. Most of the spectra were obtained in the K window (2.0-2.5 μm) at a resolving power between 200 and 300, an improvement of a factor of two to three compared with most of previous studies of this kind. Although all spectra show strong recombination lines including Brγ, Paβ, He Iλ2.06μm and also several transitions of molecular hydrogen (H_2), the relative strengths of these lines vary considerably from one galaxy to another.

The 2.2 μm luminosity of these objects is typically a factor of four stronger than observed in normal spiral galaxies. This 2.2 μm excess is interpreted as arising from an unusually high population of red supergiants presumably produced during a vigorous episode of star formation activity. The existence of red supergiants is strengthened by the detection, in some galaxies, of unusually strong stellar CO band absorption at 2.3 μm, a characteristic spectral feature of such stars. This, combined with the detection of other absorption lines such as NaI (~2.206 μm), CaI (~2.265 μm) and AlI/MgI (2.09-2.10 μm) provide strong evidence that the bulk of the 2.2 μm luminosity of these galaxies has

a stellar origin. If an AGN-like source is present in these systems, its contribution at 2.2 μm is probably no more than 20%. A vigorous episode of star formation provides the most likely mechanism for explaining the near-infrared observational properties of these galaxies.

An analysis of the He Iλ2.06μm/Brγ ratio observed in both Galactic H II regions and starburst galaxies was presented. It was shown theoretically that this ratio is steeply dependent on the effective temperature of the exciting star in the H II region. The effects of collisional excitation and dust within the H II regions on the ratio was also investigated. Preliminary observations of compact H II regions show that their He Iλ2.06μm/Brγ ratios are in reasonable agreement with those predicted theoretically. The steep dependence of the He Iλ2.06μm/Brγ on spectral type is a property that can be used to constrain the upper mass limit of the initial mass function in starburst galaxies. This method is valid for upper mass limits less than $\sim$40 $M_{\odot}$. Some galaxies, including the classical starbursts M82 and NGC 253, are found to have a relatively low upper mass limit, between 25 and 30 $M_{\odot}$. The relatively low He Iλ2.06μm/Brγ ratio observed in these galaxies suggests that the average electron density in the photo-dissociation zones is probably less than 10^3 cm^{-3}.

A stellar synthesis model has been constructed to predict the observational properties of a young stellar population characteristic of starburst galaxies. The dependence of several near-infrared observables on the stellar IMF parameters, the age of the burst and the star formation rate history were investigated. These observables include the 2.2 μm luminosity, the spectroscopic CO index, the Brγ equivalent width, the He Iλ2.06μm/Brγ ratio and the ratio of the ionization rate to the bolometric luminosity. Combined with a simple χ^2 analysis technique, this model allows the age and the stellar parameters of the IMF of a given galaxy to be constrained in a unique way. The age of the burst inferred for the galaxies investigated in this thesis are between 10 and 60 million years. NGC 3256 and NGC 2798 have an IMF unusually deficient in low-mass stars *i.e.* stars less massive than 2 $M_{\odot}$ are not formed in these galaxies if their IMF has the same shape as that in the solar neighbourhood. This result is independent of the knowledge of the mass participating in the starburst.

Evidence for non-thermal or fluorescent excitation was found from the H_2 spectra of IC 694, NGC 1614 and NGC 3256. Simple models of star forming regions were presented to show that the copious production of UV photons by

an ensemble of young OB stars interacting with the surrounding molecular gas provides a viable scenario for explaining both the observed fluorescent H_2 line ratios and the 1-0 S(1)/Brγ ratio. The H_2 emission in ARP 220 and NGC 6240 is thermally-excited. Further models were presented suggesting that the contribution of shock-excited H_2 emission from Orion-like objects and supernova remnants is usually not more than 10-20% of the total H_2 emission. In particular, the contribution of SNRs is expected to be important only if the burst is older than ~60 million years which is usually not the case for the galaxies investigated in this study. If a thermal component is contributing significantly to the total H_2 emission, it is probably produced by interaction-driven large scale shocks. This mechanism could be responsible for the strong H_2 emission observed outside the nuclear region of the merger NGC 1614 and NGC 3256.

7.1 Suggestions for Further Research

The galaxies investigated in this dissertation represent only a small fraction of all starburst galaxies in the local universe (redshifts less than 10000 km s^{-1}). To what extent the near-infrared spectroscopic properties of these objects are representative of "typical" starburst galaxies is far from clear. Since these galaxies were selected because they are relatively bright, it is likely that we are victim of an obvious selection effect *i.e.* we are studying only galaxies at the bright end of the luminosity function. Thus, there is a clear need for establishing the near-infrared spectroscopic properties of starburst galaxies from a more meaningful and complete sample of such objects. Such a statistical study is probably the only way of constraining the average lifetime of the burst, for example by determining the relative fraction of galaxies showing unusually strong CO bands. This project would have been impossible a few years ago but the recent advent of infrared array spectrometers (*e.g.* CGS4 on UKIRT) will make such observing programs within the capabilities of a 4-meter telescope.

We have shown that the strength of the CO band is an important tool for studying the stellar content of starburst galaxies. The results presented in this dissertation are critically dependent on an accurate calibration of the spectroscopic CO indices of red supergiants. Although the calibration used in this work covers a wide range of effective temperatures, it is based on five stars only. A more accurate calibration from more stars is clearly needed Further, it would be particularly interesting to determine the dependence of the spectroscopic

CO index on metallicity. Although there are good reasons to believe that the strength of the CO band should be weakly affected by elemental abundance at high metallicity (near solar), this hypothesis has never been tested observationally. This problem could be addressed by measuring the strength of the first bandhead of CO at 2.29 μm at relatively high resolution (R$\sim$1000) for a large number of late-type stars with known metallicity. It would also be of interest to investigate whether other absorption lines in the K window such as AlI and MgI could be used as metallicity indicators.

The mass participating in the burst is certainly a very important parameter in starburst models, particularly for constraining the stellar parameters of the IMF. Unfortunately, the mass is poorly constrained in most galaxies but could be determined from the rotation curve and/or the velocity dispersion inferred from high resolution spectra of the CO band. Such measurements would not suffer from high extinction which usually plagues optical measurements. Furthermore, unlike emission lines which sample the gas, the CO band arises from *stars* and, thus, the rotation curve derived from this absorption feature is not affected by potential non-gravitational motions. This technique has already been used successfully to measure the mass distribution in the Galactic centre (McGinn *et al.* 1989) and could easily be applied to nearby starbursts.

Except for nearby objects such as M82 and NGC 253, the study of starburst galaxies is usually restricted to relatively large physical areas covering several kpc. With the advent of infrared long-slit spectrometers, it will be possible to increase dramatically the spatial resolution of the measurements, allowing for instance to study the spatial dependence of the excitation mechanism of the H_2 emission or to investigate whether the stellar IMF parameters depend on physical conditions.

There is no doubt that the current revolution in infrared technology reserves a bright future for the study of star formation activity in extragalactic systems.

References

Allen, D. 1989, *"FIGS User's Manual"*, Anglo-Australian Observatory, p. 47.

Allen, D.A., Jones, T.J. & Hyland, A.R. 1985, *Astrophys. J.*, **291**, 280.

Allen, D.A., Wright, A.E. & Goss, W.M. 1976, *Mon. Not. R. astr. Soc.*, **177**, 91.

Armus, L., Heckman, T.M. & Miley, G.K. 1988, *Astrophys. J.*, **326**, L45.

Arnaud, K.A. & Gilmore, G. 1986, *Mon. Not. R. astr. Soc.*, **220**, 759.

Augarde, R. & Lequeux, J. 1985, *Astr. Astrophys.*, **147**, 273.

Bailey, J., Barton, J.R., Conroy,P., Davies, H., Hillier, D.J., Hyland, A.R., Jones, T.J., Shortridge, K. & Whithard, D. 1988, *Publs. astr. Soc. Pacif.*, **100**, 1178.

Beck, S.C., Turner, J.L. & Ho, P.T.P. 1986, *Astrophys. J.*, **309**, 70.

Black, J.H. & Dalgarno, A. 1976, *Astrophys. J.*, **203**, 132.

Black, J.H. & van Dishoeck, E.F. 1987, *Astrophys. J.*, **322**, 412.

Brand, P.W.J.L., Moorhouse, A., Burton, M.G., Geballe, T.R., Bird, M. & Wade, R. 1988, *Astrophys. J.*, **334**, L103.

Brocklehurst, M 1972, *Mon. Not. R. astr. Soc.*, **157**, 211.

Bruzual, G.A. 1983, *Astrophys. J.*, **273**, 105.

Burton, M.G., Geballe, T.R., Brand, P.W.J.L. & Webster, A.S. 1988, *Mon. Not. R. astr. Soc.*, **231**, 617.

Burton, M.G. & Puxley, P.J. 1989, in *The Interstellar Medium in Galaxies*, 2nd Wyoming Conference, eds Hollenbach & Thronson, NASA publications in press.

Bushouse, H.A. 1986, *Astr. J.*, **91**, 255.

Chini, R., Krügel, E. & Wargau, W. 1987, *Astr. Astrophys.*, **181**, 378.

Churchwell, E., Wolfire, M.G. & Wood, D.O.S. 1990, *Astrophys. J.*, **354**, 247.

Condon, J.J., Condon, M.A., Gisler, G. & Pushell, J.J. 1982, *Astrophys. J.*, **252**, 102.

Crawford, M.K., Genzel, R., Townes, C.H., & Watson, D.M., 1985, *Astrophys. J.*, **291**, 755.

Cutri, R.M. & McAlary, C.W. 1985, *Astrophys. J.*, **296**, 90.

DePoy, D.L., Becklin, E.E. & Geballe, T.R. 1987, *Astrophys. J.*, **316**, L63.

DePoy, D.L., Becklin, E.E. & Wynn-Williams 1986, *Astrophys. J.*, **307**, 116.

de Vaucouleurs, G., de Vaucouleurs, A. & Corwin, H.G. 1976, *Second Reference Catalogue of Bright Galaxies*, University of Texas Press, Austin.

Devereux, N.A. 1989, *Astrophys. J.*, **346**, 126.

Devereux, N.A., Becklin, E.E. & Scoville, N. 1987, *Astrophys. J.*, **312**, 529.

Dinerstein, H.L., Lester, D.F., Carr, J.S. & Harvey, P.M. 1988, *Astrophys. J.*, **327**, L27.

D'Odorico, S., Rosa, M. & Wampler, E.J. 1983, *Astr. Astrophys. Suppl.*, **53**, 97.

Doyon, R., Joseph, R.D. & Wright, G.S. 1989, in *Infrared Spectroscopy in Astronomy*, 22nd Eslab Symposium, ed. B. H. Kaldeich, p477.

Doyon, R., Joseph, R.D. & Wright, G.S. 1991, to appear in *Astrophysics with Infrared Arrays*, conference held in Tucson, February 1990 .

Doyon, R. & Nadeau, D. 1988, *Astrophys. J.*, **334**, 883.

Draine, B.T. 1978, *Astrophys. J. Suppl.*, **36**, 595.

Draine, B.T. 1985, *Astrophys. J. Suppl.*, **57**, 587.

Draine, B.T. 1989, in *Infrared Spectroscopy in Astronomy*, 22nd Eslab Symposium, ed. B. H. Kaldeich, p93.

Draine, B.T. & Lee, H.M. 1984, *Astrophys. J.*, **285**, 89.

Drossart, P., Maillard, J.-P., Caldwell, K.S.J., Watson, J.K.G., Majewski, W.A., Tennyson, J., Miller, S., Atreya, S.K., Clarke, J.T., Waite Jr, J.H. & Wagener, R. 1989, *Nature*, **340**, 539.

Elias, J.H. 1980, *Astrophys. J.*, **241**, 728.

Elias, J.A., Frogel, J.A. & Humphreys, R.M. 1985, *Astrophys. J. Suppl.*, **57**, 91.

Elston, R. & Maloney, P. 1990, *Astrophys. J.*, **357**, 91.

Feast, M.W. & Robertson, B.S.C. 1978, *Mon. Not. R. astr. Soc.*, **185**, 31.

Fischer, J., Geballe, T.R., Smith, H.A., Simon, M. & Storey, J.W.V. 1987, *Astrophys. J.*, **320**, 667.

Fischer, J., Sanders, D.B., Simon, M, & Solomon, P.M. 1985, *Astrophys. J.*, **293**, 508.

Fischer, J., Simon, M., Benson, J. & Solomon, P.M. 1983, *Astrophys. J.*, **273**, L27.

Frogel, J.A. 1985, *Astrophys. J.*, **298**, 528.

Frogel, J.A., Cohen, J.G. & Persson, S.E. 1983, *Astrophys. J.*, **275**, 773.

Frogel, J.A., Persson, S.E., Aaronson, M. & Matthews, K. 1978, *Astrophys. J.*, **220**, 75.

Garden, R., Geballe T.R., Gatley, I. & Nadeau, D. 1986, *Mon. Not. R. astr. Soc.*, **220**, 203.

Gatley, I., Hasegawa, T., Suzuki, H., Garden, R., Brand, P., Lightfoot, J., Glenncross, W., Okuda, H., Nagata, T. 1987, *Astrophys. J.*, **318**, L73.

Gatley, I., Jones, T.J., Hyland, A.R., Beattie, D.H. & Lee, T.J. 1984, *Mon. Not. R. astr. Soc.*, **210**, 565.

Gauthier III, T.N., Fink, U., Treffers, R. & Larson, H.P 1976, *Astrophys. J.*, **207**, L209.

Geballe, T.R., Russell, R.W. & Nadeau, D. 1982, *Astrophys. J.*, **259**, L47.

Gehrz, R.D., Sramek, R.A. & Weedman, D.W. 1983, *Astrophys. J.*, **267**, 551.

Glass, I.S. & Moorwood, A.F.M 1985, *Mon. Not. R. astr. Soc.*, **214**, 429.

Graham, J.R., Carico, D.P., Matthews, K., Neugebauer, G. Soifer, B.T. & Wilson, T.D. 1990, *Astrophys. J.*, **354**, L5.

Graham, J.R., Wright, G.S., Joseph, R.D., Frogel, J.A., Phillips, M.M. & Meikle, W.P.S. 1987, in *Star Formation in Galaxies*, ed. C.J. Persson (Washington, D.C.: US Government Printing Office), p517.

Graham, J.R., Wright, G.S. & Longmore, A.J. 1987, *Astrophys. J.*, **313**, 847.

Graham, J.R., Wright, G.S. & Longmore, A.J. 1990, to appear in *The Astrophysical Journal*, preprint.

Graham, J.R., Wright, G.S., Meikle, W.P.S., Joseph, R.D. & Bode, M.F. 1984, *Nature*, **310**, 2313.

Hall, D.N.B., Kleinmann, S.G., Scoville, N.Z. & Ridgway, S.T. 1981, *Astrophys. J.*, **248**, 898.

Hayashi, M., Hasegawa, T. Geballe, T.R., Garden, R. & Kaifu, N. 1985, *Mon. Not. R. astr. Soc.*, **215**, 31p.

Heckman, T.M., Armus, L. & Miley, G.K. 1987, *Astr. J.*, **93**, 276.

Herbst, T.M., Graham, J.R., Beckwith, S., Tsutsui, K., Soifer, B.T. & Matthews, K. 1990, to appear in *The Astronomical Journal*, preprint.

Hoffleit, D. & Jascheck, C. 1982, *The Bright Star Catalogue*, Yale University Observatory.

Hollenbach, D. & McKee, C.F. 1989, *Astrophys. J.*, **342**, 306.

Hollenbach, D. & Shull, J.M. 1977, *Astrophys. J.*, **216**, 419.

Huchra, J.P. 1977, *Astrophys. J.*, **217**, 928.

Hummer, D.G. & Storey, P.J. 1987, *Mon. Not. R. astr. Soc.*, **224**, 801.

Humphreys, R. 1978, *Astrophys. J. Suppl.*, **38**, 309.

Humphreys, R. M. & McElroy, D.B. 1984, *Astrophys. J.*, **284**, 565.

Iben, I. 1967, *Ann. Rev. Astr. Astrophys.*, **5**, 571.

Israel, F.P., Hawarden, T.G., Wade, R., Geballe, T.R. & Van Dishoeck, E.F 1989, *Mon. Not. R. astr. Soc.*, **236**, 89.

Johansson, S. & Jordan, C. 1984, *Mon. Not. R. astr. Soc.*, **210**, 339.

Johnson, H.L. 1966, *Ann. Rev. Astr. Astrophys.*, **4**, 193.

Joseph, R.D. 1989, in *Infrared Spectroscopy in Astronomy*, 22nd Eslab Symposium, ed. B. H. Kaldeich, p439.

Joseph, R.D., Meikle, W.P.S., Robertson, N.A. & Wright, G.S. 1984, *Mon. Not. R. astr. Soc.*, **209**, 111.

Joseph, R.D. & Wright, G.S. 1985, *Mon. Not. R. astr. Soc.*, **214**, 87.

Joseph, R.D., Wright, G.S. & Wade, R. 1984, *Nature*, **311**, 132.

Joseph, R.D., Wright, G.S., Wade, R., Graham, J.R., Gatley, I. & Prestwich, A.H 1987, in *Star Formation in Galaxies*, ed. C.J. Persson (Washington, D.C.: US Government Printing Office), p421.

Joy, M.J. & Lester, D.F. 1988, *Astrophys. J.*, **331**, 145.

Joy, M.J., Lester, D.F., Harvey, P.M. & Frueh, M. 1986, *Astrophys. J.*, **307**, 110.

Joy, M., Lester, D.F., Harvey, P.M., Telesco, C.M. & Decher, R. 1989, *Astrophys. J.*, **339**, 100.

Kawara, K., Nishida, M. Gregory, B. 1987, *Astrophys. J.*, **321**, L35.

Keel, W.C., Kennicutt, R.C., Hummel, E. & van der Hulst, J.M. 1985, *Astr. J.*, **90**, 708.

Kennicutt, R.C. & Keel, W.C. 1984, *Astrophys. J.*, **279**, L25.

Kennicutt, R.L., Keel, V.C., van der Hulst, J.M., Hummel, E. & Roettiger, K.A. 1987, *Astr. Astrophys.*, **93**, 1011.

Kleinmann, S.G. & Hall, D.N.B. 1986, *Astrophys. J. Suppl.*, **62**, 501.

Kurucz, R.L. 1979, *Astrophys. J. Suppl.*, **40**, 1.

Landini, M., Natta, A., Oliva, E., Salinari, P. & Moorwood, A.F.M. 1984, *Astr. Astrophys.*, **134**, 284.

Landolt-Börnstein 1982, *Astronomy & Astrophysics*, **2b**, Star & Star Clusters, eds K. Schiaffers & Voigt, H.H..

Lane, A.P. & Bally, J. 1986, *Astrophys. J.*, **310**, 820.

Lester, D.F., Carr, J.S., Joy, M. & Gaffney, N. 1990, *Astrophys. J.*, **352**, 544.

Lester, D.F., Harvey, P.M. & Carr, J.S. 1988, *Astrophys. J.*, **329**, 641.

Lonsdale, C.J., Persson, S.E. & Matthews, K. 1984, *Astrophys. J.*, **287**, 95.

Maeder, A. 1990, to appear in *Astronomy & Astrophysics, Supplement Series.*

Maeder, A. & Meynet, G. 1988, *Astr. Astrophys. Suppl.*, **76**, 411.

Mateo, M. 1988, *Astrophys. J.*, **331**, 261.

Mathis, J.S. 1986, *Publs. astr. Soc. Pacif.*, **98**, 995.

Mathis, J.S., Rumpl, W. & Nordsieck, K.H. 1977, *Astrophys. J.*, **244**, 483.

McGinn, M.T., Sellgren, K., Becklin, E.E. & Hall, D.N.B. 1989, *Astrophys. J.*, **338**, 824.

McGregor, P.J. 1987, *Astrophys. J.*, **312**, 195.

Miller, G.E. & Scalo, J.M. 1979, *Astrophys. J. Suppl.*, **41**, 513.

Moneti, A. & Moorwood, A.F.M. 1989, in *Infrared Spectroscopy in Astronomy*, 22nd Eslab Symposium, ed. B. H. Kaldeich, p299.

Moorwood, A.F.M. & Oliva, E. 1988, *Astr. Astrophys.*, **203**, 278.

Moorwood, A.F.M. & Oliva, E. 1989, in *Infrared Spectroscopy in Astronomy*, 22nd Eslab Symposium, ed. B. H. Kaldeich, p507.

Nakagawa, T., Nagata, T., Geballe, T.R., Okuda, H., Shibai, H. & Matsuhara, H. 1989, *Astrophys. J.*, **340**, 729.

Neff, S.G., Hutchings, J.B., Stanford, S.A. & Unger, S.W. 1990, *Astr. J.*, **99**, 1088.

Netzer, H. & Wills, B.J. 1983, *Astrophys. J.*, **275**, 445.

Neugebauer, G., Elias, J., Matthews, K., McGill, J., Scoville, N. & Soifer, B.T. 1987, *Astr. J.*, **93**, 1057.

Norman, C. & Scoville, N.Z. 1988, *Astrophys. J.*, **332**, 124.

Nussbaumer, H. & Storey, P.J. 1988, *Astr. Astrophys.*, **193**, 327.

Oliva, E. & Moorwood, A.F.M 1986, *Astr. Astrophys.*, **164**, 104.

Oliva, E. Moorwood, A.F.M, & Danziger, I.J. 1989, *Astr. Astrophys.*, **214**, 307.

Olofsson, K. 1989, *Astr. Astrophys. Suppl.*, **80**, 317.

Osterbrock, D.E. 1989, *Astrophysics of Gaseous Nebulae and Active Galactic Nuclei*, University Science Books, p29.

Panagia, N. 1973, *Astr. J.*, **78**, 9.

Panagia, N. 1974, *Astrophys. J.*, **192**, 221.

Parkes, C.G.E., Culhane, J.L. & Ives, J.C. 1977, *Mon. Not. R. astr. Soc.*, **179**, 55.

Peimbert, M. & Torres-Peimbert, S. 1971, *Bol. Obs. Ton. y Tac.*, **6**, 21.

Prestwich, A.H 1989, Ph.D. thesis, Imperial College, University of London.

Puxley, P.J. 1988, PhD thesis, University of Edinburgh.

Puxley, P.J., Brand, P.W.J.L, Moore, T.J.T., Mountain, C.M. Nakai, N. & Yamashita, T. 1989, *Astrophys. J.*, **345**, 163.

Puxley, P.J., Hawarden, T.G. & Mountain, M.C. 1988, *Mon. Not. R. astr. Soc.*, **234**, 29p.

Puxley, P.J., Hawarden, T.G. & Mountain, C.M. 1990, *Astrophys. J.*, to appear in the November 20 issue.

Rieke, G.H., Cutri, R.M., Black, J.H., Kailey, W.F., McAlary, C.W., Lebofsky, M,.J. & Elston, R. 1985, *Astrophys. J.*, **290**, 116.

Rieke, G.H. & Lebofsky, M.J. 1985, *Astrophys. J.*, **288**, 618.

Rieke, G.H., Lebofsky, M.J., Thompson, R.I., Low, F.J. & Tokunaga, A.T. 1980, *Astrophys. J.*, **238**, 24.

Rieke, G.H., Lebofsky, M.J. & Walker, C.E. 1988, *Astrophys. J.*, **325**, 679.

Salpeter, E.E. 1955, *Astrophys. J.*, **121**, 161.

Salpeter, E.E. 1977, *Ann. Rev. Astr. Astrophys.*, **15**, 267.

Sanders, D.B., Scoville, N.Z., Young, J.S., Soifer, B.T., Schloerb, F.P., Rice, W.L. & Danielson, G.E. 1986, *Astrophys. J.*, **305**, L45.

Sargent, A.I., Sanders, D.B. & Phillips, T.G. 1989, *Astrophys. J.*, **346**, L9.

Sargent, A.I., Sanders, D.B., Scoville, N.Z. & Soifer, B.T. 1987, *Astrophys. J.*, **312**, L35.

Sanders, D.B., Scoville, N.Z., Young, J.S., Soifer, B.T., Schloerb, F.P., Rice, W.L. & Danielson, G.E. 1986, *Astrophys. J.*, **305**, L45.

Sanders, D.B., Soifer, B.T., Elias, J.H., Madore, B.F., Matthews, K., Neugebauer, G. & Scoville, N.Z. 1988, *Astrophys. J.*, **325**, 74.

Scalo, J.M. 1986, *Fund. Cosmic Phys.*, **11**,1.

Scalo, J.M. 1987, in *Starbursts and Galaxy Evolution*, eds T.X. Thuan, T. Montmerle & J. Tran Tranh Van, Editions Frontières, p445.

Scalo, J. 1989, to appear in *Windows on Galaxies*, eds A. Renzini, G. Fabianno, and J.S. Gallagher (Kluwer), preprint.

Schweizer, F. 1986, *Science*, **231**, 227.

Scoville, N.Z., Becklin, E.E., Young, J.S. & Capps, R.W. 1983, *Astrophys. J.*, **271**, 512.

Scoville, N.Z. & Norman, C. 1988, *Astrophys. J.*, **332**, 163.

Scoville, N.Z., Sanders, D.B., Sargent, A.I., Soifer, B.T., Scott, S.L. & Lo, K.Y. 1986, *Astrophys. J.*, **311**, L47.

Scoville, N.Z., Sanders, D.B., Sargent, A.I., Soifer, B.T. & Tinney, C.G. 1989, *Astrophys. J.*, **345**, L25.

Sekiguchi, K. & Anderson, K.S. 1987, *Astr. J.*, **94**, 644.

Sellgren, K. 1986, *Astrophys. J.*, **305**, 399.

Soifer, B.T. 1984, *Astrophys. J.*, **283**, L1.

Sternberg, A. 1989, in *Infrared Spectroscopy in Astronomy*, 22nd Eslab Symposium, ed. B. H. Kaldeich, p269.

Sternberg, A. & Dalgarno, A. 1989, *Astrophys. J.*, **338**, 197.

Storey, J.W.V. 1983, *Mon. Not. R. astr. Soc.*, **202**, 105.

Telesco, C.M., Decher, R. & Gatley, I. 1985, *Astrophys. J.*, **299**, 896.

Telesco, C. M. & Gatley, I. 1984, *Astrophys. J.*, **284**, 557.

Thompson, R.I., Lebofsky, M.J. & Rieke, G.H. 1978, *Astrophys. J.*, **222**, L49.

Thompson, R.I. & Tokunaga, A.T. 1980, *Astrophys. J.*, **235**, 889.

Thronson, H.A., Majewski, S., Descartes, L. & Herald, M. 1990, *Astrophysical Journal*, submitted.

Tielens, A.G.G.M. & de Jong 1979, *Astr. Astrophys.*, **75**, 326.

Tinsley, B. 1968, *Astrophys. J.*, **151**, 547.

Tinsley, B. 1972, *Astr. Astrophys.*, **20**, 383.

Toomre, A. & Toomre, J. 1972, *Astrophys. J.*, **178**, 623.

Trafton, L., Lester, D.F. & Thompson, K.L. 1989, *Astrophys. J.*, **343**, L73.

Treffers, R.R., Fink, U., Larson, H.P. & Gauthier III, T.N. 1976, *Astrophys. J.*, **209**, 793.

Ulrich, M. 1972, *Astrophys. J.*, **178**, 113.

Wood, D.O.S. & Churchwell, E. 1989a, *Astrophys. J. Suppl.*, **69**, 831.

Wood, D.O.S. & Churchwell, E. 1989b, *Astrophys. J.*, **340**, 265.

Wright, G.S., James, P.A., Joseph, R.D. & McLean, I.S. 1990, *Nature*, **344**, 417.

Wright, G.S., Joseph, R.D. & Meikle, W.P.S. 1984, *Nature*, **309**, 430.

Wright, G.S, Joseph, R.D., Robertson, N.A., James, P.A. & Meikle, W.P.S. 1988, *Mon. Not. R. astr. Soc.*, **233**, 1.

Wynn-Williams, C.G., Becklin, E.E., Matthews, K. & Neugebauer, G. 1978, *Mon. Not. R. astr. Soc.*, **183**, 237.

Zinnecker, H. 1987, in *Evolution of Galxies*, Proc. 10th European Regional Astronomy Meeting of the IAU, Vol 4, ed L. Palous, p77.

Zinnecker, H. 1988, in *Evolutionary Phenomena in Galaxies*, eds J.E. Beckman & B.E.J. Pagel (Cambridge University Press: Cambridge), p115.

Appendix A

A Spectroscopic Determination of the 2.3 μm CO Band Strength in Stars

The spectroscopic calibration used to quantify the strength of the stellar CO band absorption at 2.3 μm is described and discussed in this appendix.

A.1 Limitations of the Photometric CO Index

A few representative K-window spectra of late-type stars, taken from the stellar atlas of Kleinmann & Hall (1986), are shown in Figure A1. The CO absorption band longward of 2.3 μm is clearly the most prominent feature in these spectra. It is also obvious that the depth of the CO band increases with decreasing temperature (later spectral type) and increasing luminosity (from dwarfs to supergiants). This property makes the CO band a powerful tool for studying the stellar content of stellar systems, to determine the relative contribution from dwarf, giant and supergiant stars to the infrared luminosity.

In their pioneering study of early-type galaxies, Frogel *et al.* (1978) established a photometric system for measuring the strength of the CO band based on two narrow band ($\Delta\lambda = 0.08$ μm) filters centred on the CO dip at 2.36 μm and the nearby continuum at 2.2 μm. They defined a photometric "CO index" as the difference in magnitudes of the two filters relative to αLyrae, an A0V star which has no trace of CO absorption in its spectrum. The CO index is defined such that high values correspond to strong CO bands. Frogel *et al.* showed that the spectroscopic dependence of the CO absorption feature on temperature and luminosity is well represented by the CO index.

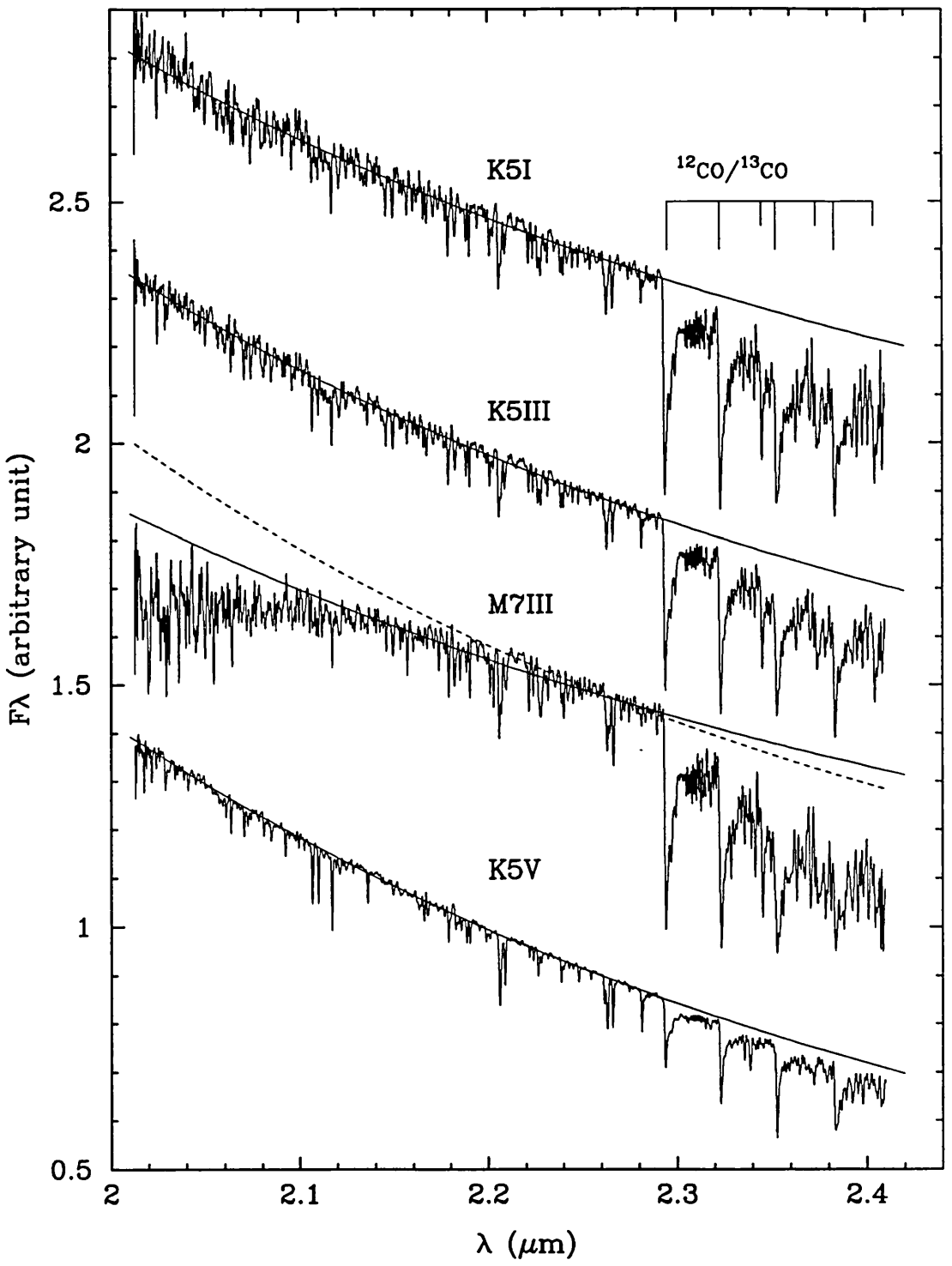

Figure A1— High-resolution K-window spectra of selected late-type stars taken from the stellar atlas of Kleinmann & Hall (1986). The solid line superimposed on each spectrum is the best power-law continuum fitted to featureless sections of the spectrum between 2.1 to 2.29 μm. A power-law continuum fails to fit the energy distribution of the very late-type giant M7III because of the strong water absorption band at 2.0 μm. The dashed line shows the possible range for the power-law continuum of this star.

There are, however, several disadvantages with the photometric CO index. First, since the CO index is sensitive to the slope of the spectrum between 2.2 and 2.36 μm, this technique has serious limitations for measuring the depth of the CO band in such diverse systems as active galactic nuclei (AGN) and starburst galaxies, where the slope of the K continuum is very often affected by high extinction and contaminated by non-stellar sources such as hot dust ($600 - 1000$ K) and non-thermal emission. Extinction and contamination from non-stellar sources make the spectrum redder than normal and thus, artificially *decrease* the CO index. This effect has been shown to be very important in starburst galaxies (Doyon, Joseph & Wright 1989; Doyon, Joseph & Wright 1991).

Second, because the CO and continuum filters have a fixed wavelength, the CO index is redshift-dependent. Above a redshift of 3000 km s^{-1}, the K-correction on the CO index becomes unreliably large (*cf.* Arnaud & Gilmore 1986). Finally, the continuum filter used to define the CO index can be contaminated by Brγ emission. This contamination is small (< 0.02 mag) in starbursts and AGN where the K continuum is relatively strong but potentially important in weak continuum systems such as blue compact galaxies.

All of these problems can be avoided by measuring the strength of the CO band spectroscopically.

A.2 Definition of the Spectroscopic CO Index

Measuring the depth of the CO band spectroscopically requires the local continuum above the absorption feature to be properly defined. Although the assessment of the continuum near isolated lines is unambiguous, this is not the case for the CO band which extends outside the 2.2 μm atmospheric window. In this case, the continuum must be extrapolated from the shorter part (<2.29 μm) of the spectrum by fitting a "typical" stellar energy distribution.

As shown in Figure A.1, except for very late-type stars (*e.g.* the M7III in Figure A.1) which are affected by strong intrinsic water absorption around 2 μm, a power-law continuum ($F_\lambda \propto \lambda^\beta$) always provides a very good fit to the spectrum shortward of 2.29 μm. This is not surprising given the approximate Rayleigh-Jeans nature ($F_\lambda \propto \lambda^{-4}$) of stellar spectra in the infrared. Thus, representing the stellar energy distribution by a power-law not only provides a good fit the spectrum but the choice of such continuum is physically justified.

Once the stellar spectrum is fitted with a power-law continuum, the strength of the CO band may be calculated from the rectified spectrum using the following *spectroscopic* CO index:

$$CO_{sp} \equiv -2.5 \log\langle R_{2.36} \rangle \qquad (A.1)$$

where $\langle R_{2.36} \rangle$ is the average of the rectified spectrum between 2.31 and 2.40 μm. This definition was specifically chosen to be similar to the photometric CO index in order to allow a meaningful comparison between the two indices. Like the photometric CO index, CO_{sp} is defined such that the index is larger for deeper CO features.

Spectroscopic CO indices have been calculated for all 26 stars in the Kleinmann & Hall (1986) atlas. The spectra given in this atlas are ratioed with αLyrae or other A0 stars. In order to uncover the original energy distribution of the stars, the spectra were multiplied by a power-law continuum in the form $F_\lambda \propto \lambda^{-3.94}$ which is the closest representation of an A0 star (Kurucz 1979; as quoted from McGregor 1987). The resulting spectrum was then fitted with a power-law continuum which was used to rectify the spectrum and calculate the spectroscopic CO index using Eqn. A.1. Spectroscopic CO indices and fitted power-law indices are given in Table A.1.

The dependence of the spectroscopic CO index on effective temperature is shown in Figure A.2. Average temperatures were estimated from spectral types using the calibration given in Landolt-Börnstein (1982). The well known strengthening of CO absorption with decreasing temperature and increasing luminosity is clearly reproduced in this figure. Within an accuracy of 0.015 mag, the following analytical expressions may be used to derive the spectroscopic CO index from the effective temperature:

$$\begin{aligned} \text{Dwarfs:} \quad & CO_{sp} = 0.866 - 2.95\,T_4 + 2.55\,T_4^2, \\ \text{Giants:} \quad & CO_{sp} = 1.530 - 5.01\,T_4 + 4.10\,T_4^2, \\ \text{Supergiants:} \quad & CO_{sp} = 1.353 + 2.80\,T_4, \end{aligned} \qquad (A.2)$$

where T_4 is the effective temperature in units of 10^4 K. These expressions are valid at any temperature as long as CO_{sp} is positive. The spectroscopic CO index should be set to zero when the expressions above yield a negative value.

Average photometric CO indices taken from Frogel *et al.* (1978) are also given in Table A.1. These indices are averages based on several measurements

Table A.1
Spectroscopic CO Index of Late-Type Stars

Name	Spectral Type	T_{eff} (K)	β [1]	CO_{PH} [2]	CO_{SP}
HR 8752	G5 0-Ia	4850	-3.3	—	-0.01
RW Cep	K0 0-Ia	4420	-3.1	—	0.11
BS 8726	K5 Ib	3850	-3.4	—	0.27
μ Cep	M2 Ia	3450	-2.8	—	0.40
SU Per	M3-M4 Iab	3090	-2.9	—	0.48
ν Peg	F8 III	6150	-3.9	—	-0.01
31 Com	G0 IIIp	5850	-3.9	—	0.00
84 Her	G2 IIIb	5450	-3.9	—	0.01
o U Ma	G5 IIIa	5150	-3.6	0.03	0.05
ϵ Vir	G8 IIIab	4900	-3.7	0.04	0.06
ι Cep	K0- III	4750	-3.9	0.07	0.09
κ Oph	K2 III	4420	-3.7	0.11	0.12
39 Cyg	K3 III	4200	-3.8	0.12	0.13
γ Dra	K5 III	3950	-3.6	0.15	0.20
γ Sge	M0- III	3800	-3.7	0.17	0.20
χ Peg	M1 III	3720	-3.6	0.18	0.21
R Lyr	M5 III	3330	-3.3	0.23	0.32
BK Vir	M7- III	3150	-3.0	0.25	0.38
SW Vir	M7 III:	3150	-2.9	0.25	0.36
16 Cyg A	G3 V	5830	-3.7	—	0.03
16 Cyg B	G4 V	5800	-4.3	—	-0.01
σ Dra	K0 V	5250	-3.6	0.02	0.03
61 Cyg A	K5 V	4350	-3.7	0.04	0.07
Gl 411	M2+ V	3580	-2.1	0.03	0.12
Wolf 359	M5.8 V	3090	-1.3	-0.03	0.21

[1] Index of the power-law continuum ($F_\lambda \propto \lambda^\beta$) fitted to the spectrum shortward of 2.29 μm.
[2] Average photometric CO index for the corresponding spectral type. From Frogel *et al.* (1978).

of different stars of the same spectral type. The true CO index of the stars listed in Table A.1 is not necessarily the same as these averages but should not differ by more than 0.02 mag.

Photometric and spectroscopic CO indices are compared in Figure A.3. Main sequence stars were excluded from this comparison because the water

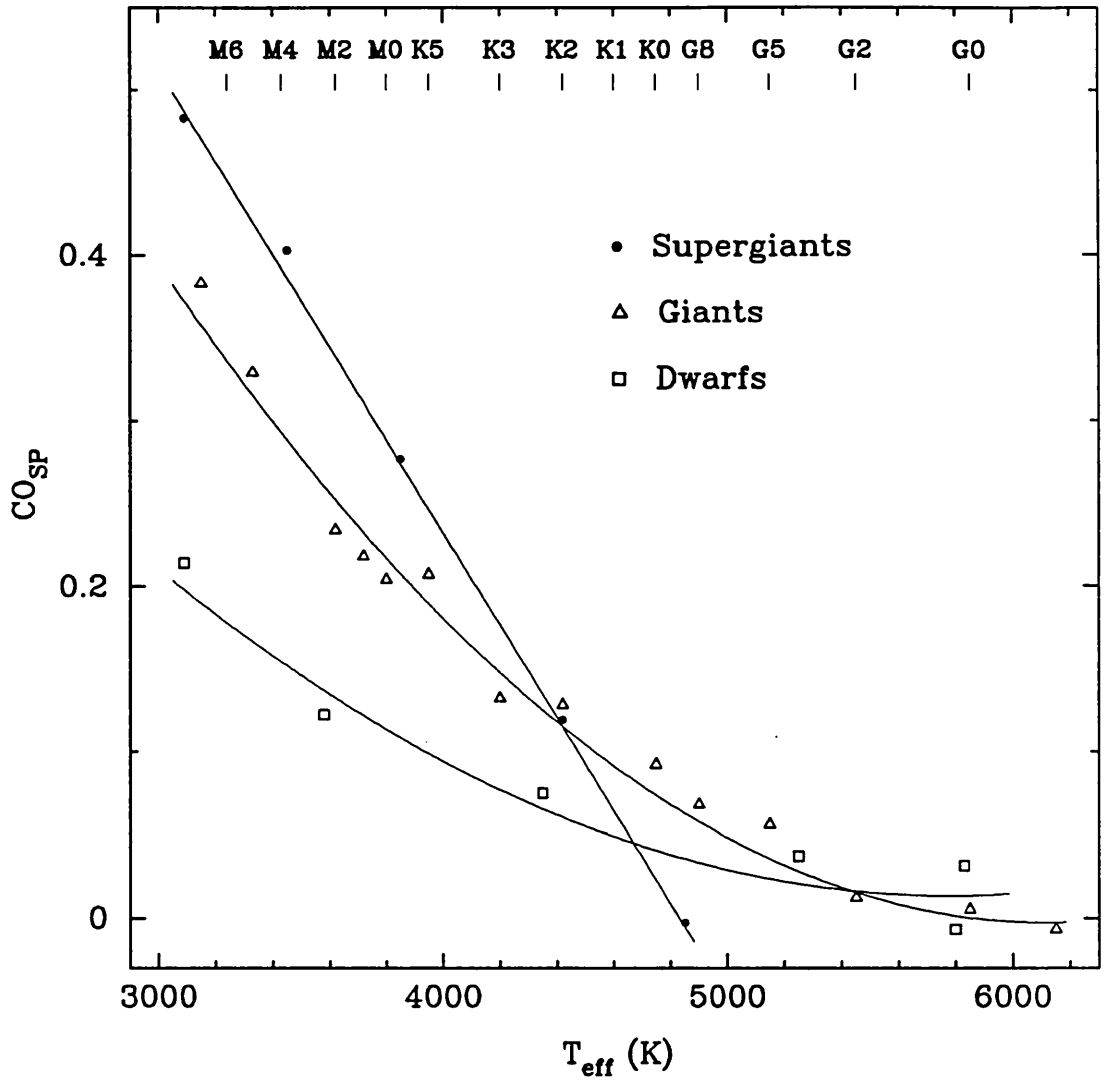

Figure A.2— Dependence of the spectroscopic CO index on effective temperature and luminosity. The spectral type sequence of giant stars is indicated at the top of the figure. The solid lines are graphical representations of Eqns A.2.

absorption at 2 μm is strong enough to contaminate the continuum filter significantly. As a result, the photometric CO index of dwarfs is not very representative of the true CO absorption in their spectrum. It is seen that the two indices are well correlated. The following transformation may be used between them:

$$CO_{SP} = 1.46\,CO_{PH} - 0.02 \qquad (A.3)$$

where CO_{PH} is the photometric CO index. The scatter in the plot is probably due to the fact that we have used average values for the photometric CO index. Estimating the photometric CO index from the Kleinmann & Hall (1986)

spectra, using synthetic (software) filters to simulate the photometric system of Frogel *et al.* (1978), yields a much tighter correlation (not shown here) between the two indices.

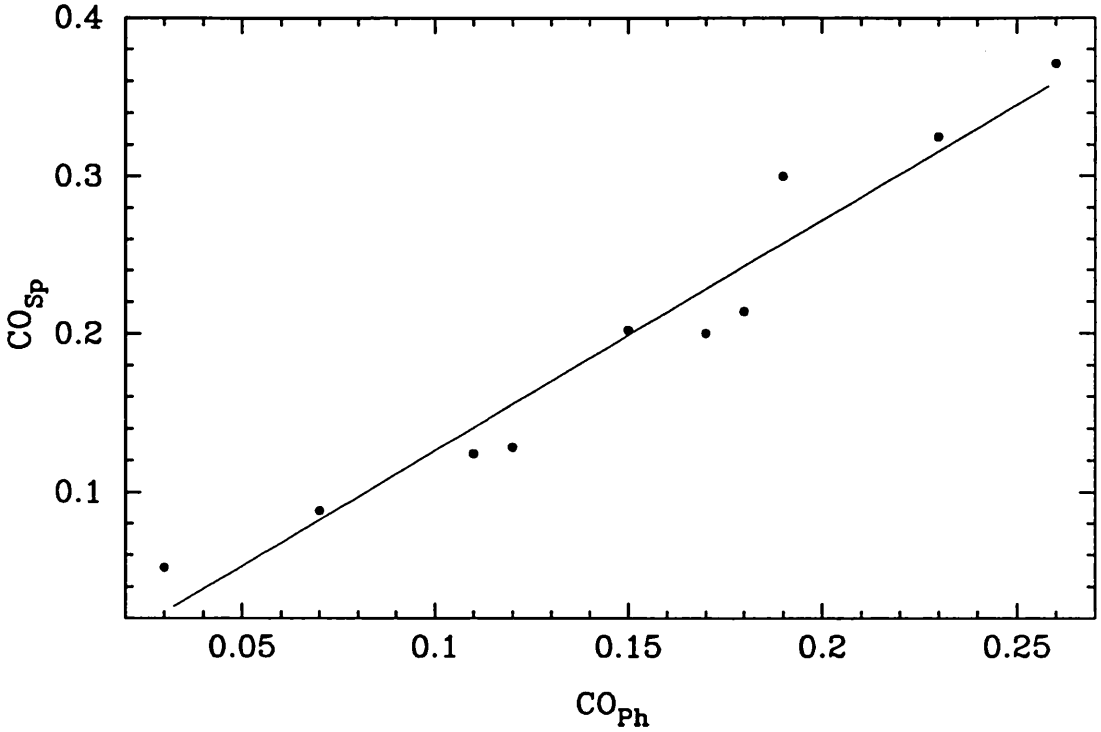

Figure A.3— Comparison of the spectroscopic CO indices with filter photometric indices. The solid is a graphical representation of Eqn A.3, the best fit of a straight line to the data points.

A.3 Uncertainties

The accuracy of the spectroscopic CO index is limited by two factors: 1) the uncertainty associated with the power-law continuum fit and 2) the signal-to-noise of the spectrum. When the spectrum is not affected by strong water absorption, the uncertainty in fitting the power-law continuum is essentially limited by the signal-to-noise of the data. In practice, the error on the power-law index has a negligible (<0.01 mag) effect on the spectroscopic CO index. Only the error on the normalization constant of the power-law fit is translated into a significant uncertainty on CO_{SP}. The error in percentage of the normalization constant corresponds roughly to the same uncertainty in magnitude for the spectroscopic CO index. For instance, with a resolving power of 300 and an

average signal-to-noise per point of 20, one can achieve an accuracy of 0.02 mag for the spectroscopic CO index if the spectrum is oversampled by a factor of two. Thus, in practice, an accuracy better than 0.01 mag can easily be obtained.

If the spectrum is strongly affected by water absorption, a common feature in very late-type stars (later than ~M5), the error on CO_{SP} is then dominated by the systematic uncertainty in fitting the power-law continuum, even if the signal-to-noise is very high. This effect is illustrated in Figure A.1 for the giant M7. Because of the strong water absorption in the spectrum, more than one power-law spectrum can be fitted depending of the wavelength range used for fitting the power-law. In this particular case, the two power-law spectra shown on figure A.1 (dashed and solid lines) yield spectroscopic CO indices that differ by 0.04 mag, relatively small compared with the index of 0.37 measured for this star (see Table A.1). Although this a potential problem, it is not expected to be too serious for measuring the strength of the CO band in galaxies which usually show small water absorption in their spectra.

In the near future, when infrared spectra with resolving power >1000 become available, the uncertainty in assessing the continuum level could be minimized by measuring only the strength of the first bandhead of CO at 2.29 μm. This method was used by Kleinmann & Hall (1986) to quantify the strength of the CO band in their spectra. This technique is not appropriate for relatively low resolution spectra such as those presented in this thesis. The approach described above of averaging over the whole CO band (2.31 to 2.40 μm) was adopted in order to increase the signal-to-noise.

In summary, the spectroscopic CO index described in this appendix is only subject to small uncertainties and it is possible to measure the strength of the CO band with an accuracy of ~0.02 mag. For population synthesis purpose, such precision is very satisfactory.

Appendix B

Continuum and Line Modelling of Starbursts

The details of the evolutionary model used throughout this thesis are presented in this appendix. The relevant equations and the general procedure of the model are derived and discussed in the first part, followed by a brief presentation of some results.

B.1 Procedure and Formulation of the Model

The model is similar to that used by Tinsley (1968, 1972), Huchra (1977) and Bruzual (1983). The technique consists of following the evolution of stars in the Hertzsprung-Russell (HR) diagram according to known evolutionary tracks, for a given initial mass function (IMF) and a star formation rate (SFR). The tracks provide the bolometric luminosity L and the effective temperature T_{eff} as a function of time. Let $N(m,t)$ be the number of stars with progenitor mass m at the evolutionary stage t. After a time t_0, the number of stars in the interval $[t, t+dt]$ is given by

$$dN(m,t,t_0) = R_N(t_0 - t)\,\psi(m)\,dm\,dt, \qquad t < t_0 \qquad (B.1)$$

where $\psi(m)$ is the IMF, the number of stars formed per unit mass interval. R_N is the SFR in units of stars per year. The total mass, $dM(t,t_0)$, of all the stars at the evolutionary stage $[t, t+dt]$, can be obtained by multiplying the right side of Eqn B.1 by m and integrating over the mass, from m_l to m_u, the lower

and upper mass limits of the IMF, respectively. Let $R_M(t)$ be the SFR in units of mass per year and defined as $dM(t)/dt$. It follows from Eqn B.1 that R_M and R_N are related by the following expression

$$R_M(t) = R_N(t) \int_{m_l}^{m_u} \psi(m)\, m\, dm. \qquad (B.2)$$

The lifetime t_0 of the model under consideration is divided up into a large number n (usually 1000) of time steps of equal duration $\Delta\tau$ such that $t_0 = n\Delta\tau$. Let $f(m_i,t)$ be the flux [1] of a star with progenitor mass m_i at the evolutionary stage t. If there are a number l of evolutionary tracks available, then the total flux $F(t_0)$ contributed by stars of all types after a time t_0 is given by

$$F(t_0) = \frac{1}{\int_{m_l}^{m_u} \psi(m)\, m\, dm} \sum_{j=0}^{n-1} \sum_{i=1}^{l} \int_{m_1}^{m_2} \psi(m)\, dm \int_{(n-j-1)\Delta\tau}^{(n-j)\Delta\tau} R_M(t_0 - t)\, f(m_i,t)\, dt \qquad (B.3)$$

with $m_1 = (m_{l-1}\, m_l)^{1/2}$ and $m_2 = (m_l\, m_{l+1})^{1/2}$, as in Tinsley (1972). The normalization of Eqn B.3 is such that

$$\int_{m_l}^{m_u} \psi(m)\, dm = 1$$

and

$$\int_0^{t_0} R_M(t)\, dt = M_0 \qquad (B.4)$$

where M_0 is the total mass of stars ever formed since the beginning of the burst.

The IMF is characterized by a power-law of the mass ($\psi(m) \propto m^{-\alpha}$). For instance, the IMF derived by Salpeter (1955) is described by a power-law index $\alpha = 2.35$. A more recent determination (Scalo 1986) favours a three-segment power-law but in practice, two segments provide also a good approximation to the data. We adopted the same parametrization used by Puxley (1988) to describe the Scalo IMF *i.e.*

$$\begin{aligned} \psi(m) &= k\, m^{-1.25} \qquad 0.1 \leq M/M_\odot < 0.7, \\ \psi(m) &= 0.565k\, m^{-2.85} \qquad 0.7 \leq M/M_\odot < 100 \end{aligned} \qquad (B.5)$$

[1] The use of the term "flux" is very general and refers to any physical quantity associated with a star (*e.g.* bolometric luminosity, band flux, ionization rate, etc...)

where k is a normalization constant.

Three different SFR histories were investigated: constant, exponential ($R_M(t) \propto \exp(-t/\tau_0)$) and "delayed" ($R_M(t) \propto t \exp(-t/\tau_0)$) where τ_0 is the time-scale of the burst. The delayed model is very similar to the exponential one with the exception that the SFR starts from zero and reaches a maximum after a time τ_0.

B.1.1 Evolutionary Tracks

The evolutionary tracks used in the model were taken from Maeder and Meynet (1988). These models include 21 masses ranging from 0.85 to 120 $M_\odot$, calculated for a solar metallicity ($Z = 0.02$). The location of these tracks in the HR diagram is shown in Figure B.1. The new feature of these models compared with previous ones (*e.g.* Iben 1967) is the introduction of mass loss in the stellar evolution. This allows stars to come back to the left in the HR diagram after the red supergiant phase (see Figure B.1).

In order to increase the mass resolution, additional models were interpolated from the original 21 tracks. Because of the digital nature of the model, it is crucial to include as many tracks as possible, otherwise the model will behave erratically. The interpolation between evolutionary tracks is particularly critical. As pointed out by Maeder & Meynet (1988), the interpolation must be based on points of corresponding evolutionary status. The models calculated by these authors have this major advantage of providing $\log L$ and $\log T_{eff}$ at a time when all the stars are in the same evolutionary stage in terms of internal structure. For instance, point 8 in all models (see Figure B.1) corresponds to the central exhaustion of hydrogen in the star. This feature makes the interpolation procedure very easy. For a given mass, a new track was calculated using a cubic spline interpolation (on a logarithmic scale) from the data provided by the three nearest available tracks.

A set of 14 unevolved models (dwarf stars) with masses $< 0.85\ M_\odot$ were also added to the evolutionary tracks in order to cover the lower main sequence. These models were assumed not to evolve on the time scale of a Hubble time. The HR diagram of these models is shown in Figure B.2. A list of all the masses used in the model is given in Table B.1.

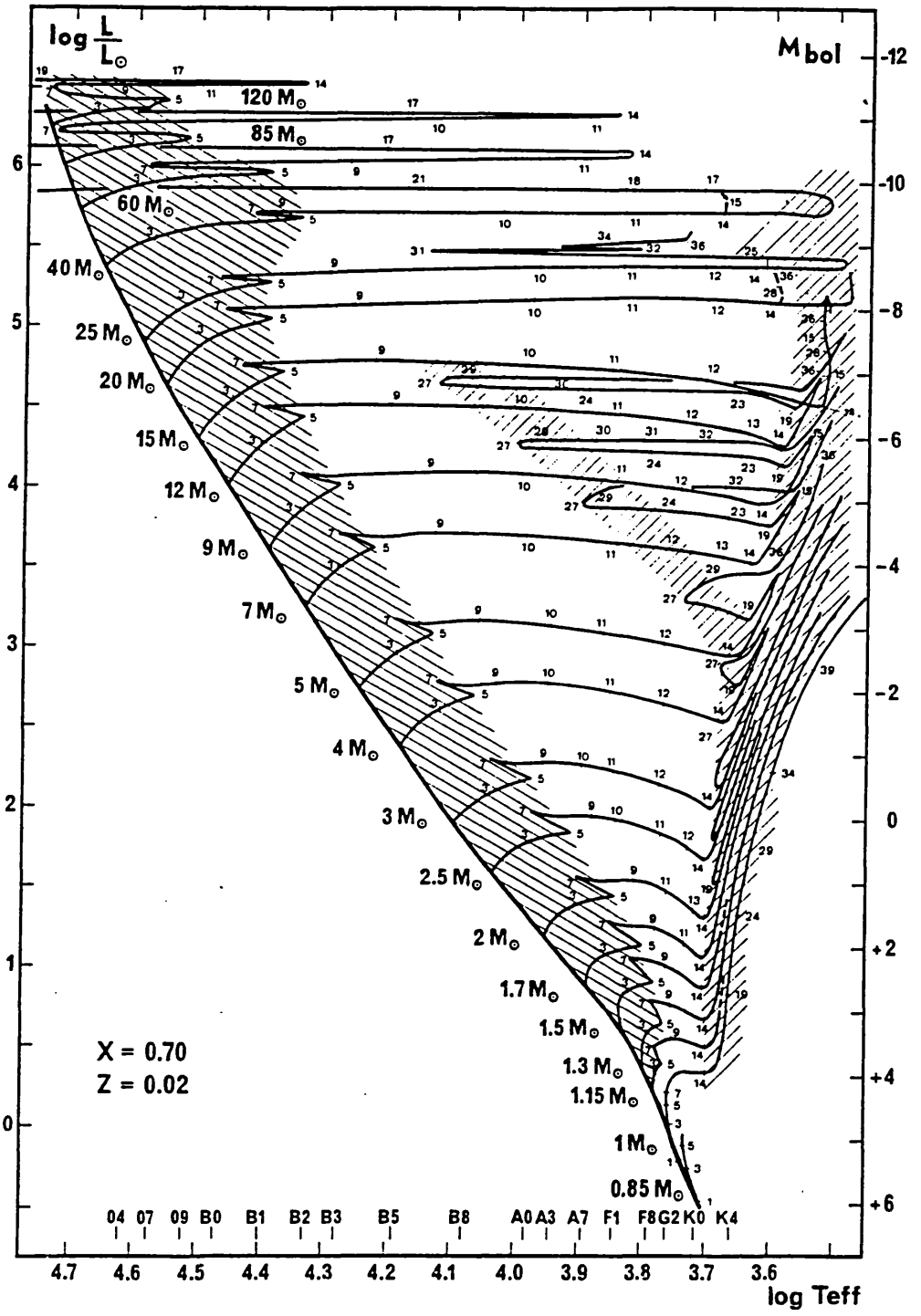

Figure B.1— HR diagram of the original evolutionary tracks used in the model. The locations of some models are indicated according to their numbering in tables B.7 to B.27. The hatched areas indicate the slow phases of nuclear burning. Reproduced from Maeder & Meynet (1988).

Table B.1
Stellar Masses ($M_\odot$)

0.06†	0.64†	1.13*	1.40	1.65*	2.25*	6.50*	13.0*	23.0*	36.0*
0.12†	0.67†	1.15	1.43*	1.68*	2.50*	7.00	14.0*	24.0*	38.0*
0.17†	0.69†	1.18*	1.46*	1.70	2.75*	7.50*	15.0	25.0	40.0
0.21†	0.72†	1.20*	1.48*	1.72*	3.00	8.00*	16.0*	26.0*	45.0*
0.27†	0.85	1.23*	1.50	1.74*	3.50*	8.50*	17.0*	27.0*	50.0*
0.33†	1.00	1.26*	1.52*	1.76*	4.00	9.00	18.0*	28.0*	60.0
0.40†	1.03*	1.30	1.55*	1.78*	4.50*	9.50*	19.0*	29.0*	70.0*
0.46†	1.06*	1.32*	1.58*	1.80*	5.00	10.0*	20.0	30.0*	85.0
0.51†	1.08*	1.35*	1.60*	1.90*	5.50*	11.0*	21.0*	32.0*	100.0*
0.61†	1.10*	1.38*	1.62*	2.00	6.00*	12.0	22.0*	34.0*	120.0

* Interpolated.
† Unevolved.

B.1.2 The Stellar Data

In order for the model to predict observable quantities, all points in the $\log L - \log T_{eff}$ plane of the theoretical evolutionary tracks must be converted into age-flux tables. In practice, this procedure requires determining the spectral type and luminosity class of all the points in the HR diagram.

For simplicity, it was assumed that all stars in the HR diagram can be described either as a dwarf (main sequence star), giant or supergiant star. Although a Wolf-Rayet (WR) stage is predicted by the theoretical evolutionary tracks for the most massive stars ($> 30\ M_\odot$), the observational properties of WR stars were not included in the model because of their relatively short lifetime ($\sim 10^5$ years). Instead, their properties were approximated either as hot main sequence or supergiant stars. The exclusion of WR stars should have little effect on the prediction of broad-band colours and ionization rates provided that the model under consideration is older than ~5 million years.

The calibration between effective temperature and spectral type was taken from the compilation of stellar properties of Landolt-Börnstein (1982). From the same reference, the bolometric luminosity was converted into absolute V magnitude (M_V) using the following relations:

$$\begin{aligned} M_{bol} &= \log L/L_\odot + 4.64, \\ BC &= M_{bol} - M_V \end{aligned} \qquad (B.6)$$

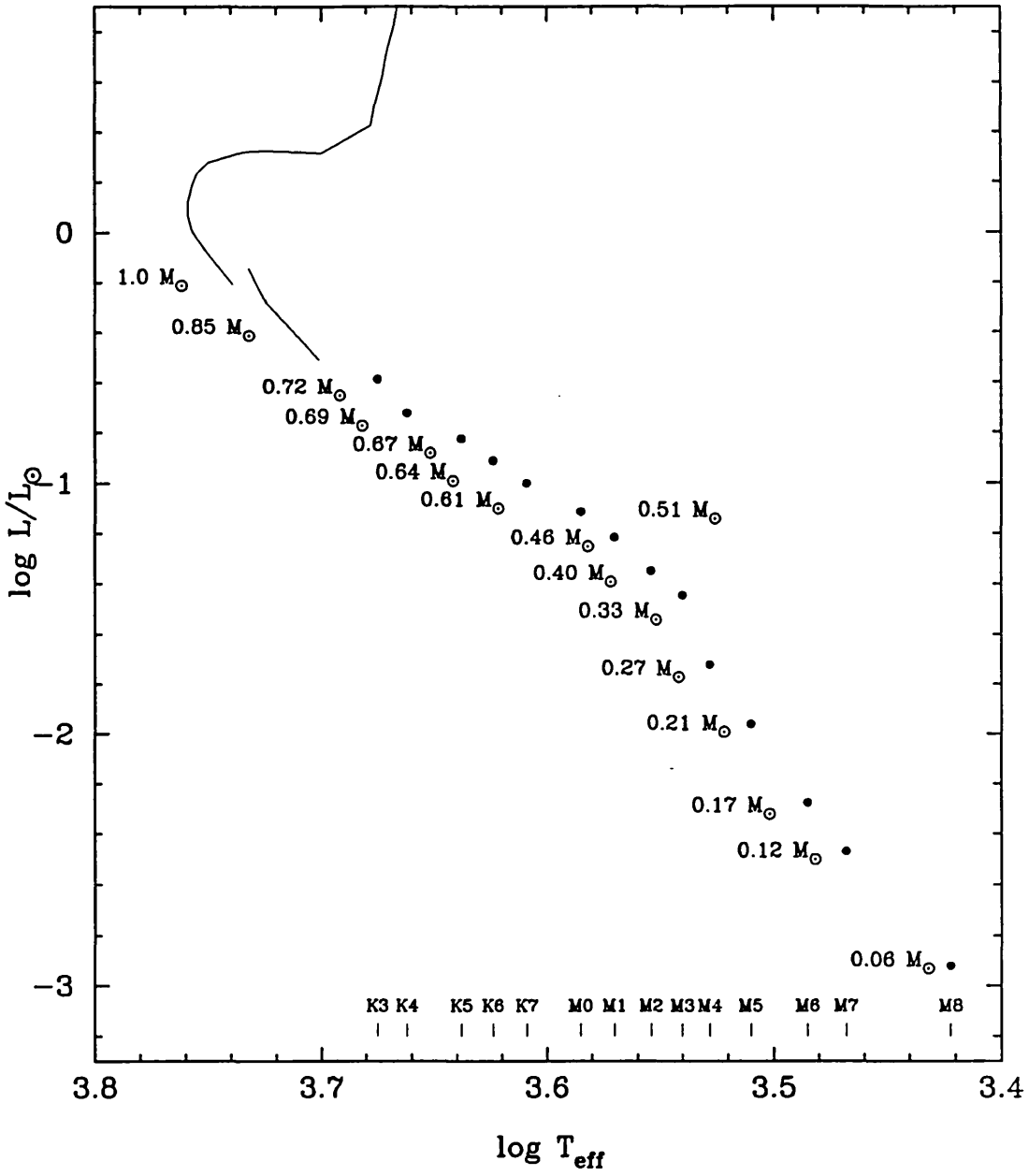

Figure B.2— HR diagram of unevolved models. The solid lines show the location of the lowest main sequence evolutionary tracks. The spectral type sequence for dwarf stars is indicated at the bottom.

where BC is the bolometric correction. The "flux" in a filter i, for a star of type k is defined as

$$F_i^k \equiv 10^{-M_i^k/2.5}, \qquad (B.7)$$

where M_i^k is the absolute magnitude in the filter i of a star of type k. The sources of colours and ionization rates are given below.

B.1.2.1 Colours

UVB colours were taken from Landolt-Börnstein (1982) for all spectral types and luminosity classes. Near-infrared JHK and $V-K$ colours were taken from Frogel *et al.* (1978) for dwarfs and giants later than G5 and from Johnson (1966) for earlier stars. Johnson did not provide $VJHK$ colours for early-type giants. It was assumed that these stars have the same colours as early-type dwarfs. Comparison of their UBV colours shows that this is a very good approximation for stars earlier than F5. Colours of giants with spectral type between F5 and G5 were interpolated smoothly from those of Johnson and Frogel *et al.*. For consistency, the same interpolation procedure was applied to dwarfs with spectral type between F5 and G5.

Because Johnson's $J-K$ colours are systematically redder compared with Frogel's, the former were converted into the Frogel *et al.* (or CIT) system using a transformation derived from the colours of giants given in Frogel *et al.* (1978) and Johnson (1966):

$$(J-K)_{Frogel} = 0.92\,(J-K)_{Johnson} + 0.001. \qquad (B.8)$$

Since $J-H$ colours are not available for stars earlier than G5, the latter were calculated by interpolating from Johnson's IJK colours assuming a power-law for the stellar energy distribution between I and K. $VJHK$ colours of supergiants later than K3 were taken from Elias, Frogel & Humphreys (1985). Other spectral types were interpolated from Johnson's IJK colours as described above.

Spectroscopic CO indices were calculated from the effective temperature using the analytical expressions given in Appendix A. The flux in the CO filter of a star of type k is defined as

$$F^k_{CO} \equiv F^k_K\, 10^{-CO^k_{SP}/2.5}, \qquad (B.9)$$

where CO^k_{SP} is the spectroscopic CO index and F^k_K the flux in the 2.2 μm filter.

B.1.2.2 Ionization rates

The production rate of ionizing photons is the basic ingredient for predicting the strength of recombination lines. Ionization rates for photons with energy greater than 13.6 eV (the ionization potential of hydrogen), $N^H_{Lyc}(T_{eff})$, were taken from Puxley (1988; see also Puxley, Hawarden & Mountain 1990) for

Table B.2
Effective Temperature, Mass, Radius and Surface Gravity of Stars

	Dwarfs			Giants			Supergiants		
T_{eff} (K)	Mass ($M_\odot$)	Radius ($R_\odot$)	$\log g$[1]	Mass ($M_\odot$)	Radius ($R_\odot$)	$\log g$[1]	Mass ($M_\odot$)	Radius ($R_\odot$)	$\log g$[1]
5500	0.8	0.88	4.5	1.0	7.40	3.0	10.0	119.2	1.5
6000	1.0	1.08	4.5	1.1	5.96	3.0	10.0	113.5	1.5
6500	1.3	1.32	4.5	1.5	5.85	3.0	10.0	106.0	1.5
7000	1.5	1.45	4.5	1.8	5.72	3.0	10.3	97.3	1.5
7500	1.7	1.56	4.5	2.2	5.61	3.0	11.5	84.6	1.5
8000	1.9	1.66	4.5	2.5	5.49	3.0	12.5	71.0	1.5
8500	2.2	1.86	4.5	2.9	5.38	3.0	13.0	60.0	2.0
9000	2.5	2.12	4.5	3.2	5.26	3.0	14.6	60.0	2.0
9500	2.9	2.39	4.5	3.6	5.14	3.0	15.7	60.0	2.0
10000	3.1	2.52	4.5	3.9	5.02	3.0	16.4	59.1	2.0
11000	3.5	2.77	4.5	4.6	5.55	3.0	17.4	56.4	2.0
12000	3.9	3.03	4.5	5.2	6.16	3.5	18.2	54.4	2.0
13000	4.5	3.28	4.5	5.8	6.78	3.5	19.2	52.0	2.5
14000	5.1	3.54	4.5	6.4	7.39	3.5	20.3	48.8	2.5
15000	5.7	3.80	4.5	7.0	8.00	3.5	20.9	46.3	2.5
16000	6.2	4.06	4.5	7.9	8.50	3.5	21.8	42.6	2.5
17000	6.7	4.34	4.5	8.9	9.00	3.5	22.3	40.6	2.5
18000	7.2	4.61	4.5	9.8	9.50	3.5	22.8	38.9	2.5
20000	8.5	5.12	4.5	11.6	10.50	3.5	23.7	35.4	2.5
22500	10.3	5.72	4.5	14.0	11.75	3.5	24.3	32.7	3.0
25000	12.6	6.31	4.5	16.3	13.00	3.5	24.8	30.8	3.0
30000	17.5	7.40	4.5	—	—	—	25.9	27.0	3.2
35000	21.9	8.30	4.5	—	—	—	31.2	21.3	—
40000	32.3	10.19	4.5	—	—	—	63.1	28.8	—
45000	63.8	12.19	4.5	—	—	—	89.7	30.0	—
50000	101.3	14.06	4.5	—	—	—	—	—	—

[1] Log of surface gravity in CGS units. No value is given when no Kurucz model is available for this surface gravity.

main sequence stars. Those were calculated by integrating under Kurucz (1979) atmosphere models.

For consistency, the ionization rates of giants and supergiants were calculated in a similar way from Kurucz's models using a program kindly provided by Phil Puxley. Adopted stellar properties (mass, radius and surface gravity) were taken from Landolt-Börnstein (1982). Those quantities are compiled in

Table B.2. Note that the surface gravities given in this table are only approximate (±0.2 dex) and correspond to the nearest surface gravity available in Kurucz's models. Because giant and supergiant models with effective temperatures >30000 K are not available from Kurucz, the ionization rates of these stars were estimated from those of main sequence stars of the same temperature assuming the ionization rate ratios (giants/dwarf, supergiant/dwarf) derived from the data of Panagia (1973). In order to calculate the strength of helium recombination lines, a second ionization rate, $N_{Lyc}^{He}(T_{eff})$, was also calculated in the same way by integrating Kurucz models beyond the ionization potential of helium (24.6 eV).

Bolometric luminosities, bolometric corrections, broad-band colours, spectroscopic CO indices and ionization rates of dwarf, giant and supergiant stars are compiled in table B.4, B.5 and B.6, respectively. The following entries are listed in these tables.

Column (1) Spectral type in the MK system.

Column (2) Effective temperature of the star in Kelvin.

Column (3) Logarithm of the bolometric luminosity in solar units.

Column (4) Bolometric correction as defined in Eqn B.6.

Column (5-9) $UBVJHK$ colours.

Column (10) Spectroscopic CO index.

Column (11) Logarithm of the production rate (in s^{-1}) of ionizing photons with energy greater than 13.6 eV.

Column (12) Logarithm of the production rate (in s^{-1}) of ionizing photons with energy greater than 24.6 eV.

B.1.2.3 Flux-Age tables

Tables B.4 to B.6 were used to determine the spectral type and the corresponding stellar properties for all points on the theoretical evolutionary tracks. Because of the large number of points involved (86 tracks times ~40 points), a simple algorithm was developed to carry out this procedure automatically. The resulting flux-age tables are presented in tables B.7 to B.27. Only the original 21 tracks of Maeder & Meynet (1988) are given to save space, but an additional 79 tracks (of which 14 are unevolved) were also calculated.

The entries of Table B.7 to B.27 have the same meaning as those in Table B.4 to B6, except for the following columns:

Column (1) Evolutionary stage according to the numbering given in Figure B.1.

Column (2) Age of the star in millions of years.

Column (13) Approximate spectral type and luminosity class of the star at this evolutionary stage. An interrogation mark means that the classification is uncertain because the effective temperature or/and the bolometric luminosity in the theoretical evolutionary track is outside the range of temperature and luminosity given in table B.4 to B.6. This is usually the case when the star is in the Wolf-Rayet stage.

B.2 Some results: colours of early-type galaxies

Previous studies on stellar population synthesis have mostly been devoted to modelling the present energy distribution of elliptical galaxies. The rationale for such programs is to determine the star formation history of these galaxies on the time scale of a Hubble time, in order to make predictions of their energy distributions at earlier times, or equivalently, at higher redshifts. One important goal of such programs is to correct the value of q_0—the deceleration parameter—derived from the Hubble diagram. In this section we will use the model described in this appendix to predict the colours of elliptical galaxies based on parameters (SFR, IMF) used in previous studies. The purpose of this exercise is to test the validity of the model developed here.

Previous infrared studies of elliptical galaxies (Frogel *et al.* 1978) have clearly established that the luminosity is dominated by late-type giants. These provide a constraint on the age of these stellar systems. Theoretically, giant stars should appear in the stellar population after ~10 Gyr (see Table B.26). Thus, a requirement for the stellar synthesis model is to reproduce the energy distribution of early-type galaxies at an age near 10 Gyr. Moreover, the fact that ellipticals are dominated by giants puts some constraint on the star formation history. In order to produce an excess of giant stars, the star formation rate must have been higher in the past. This can be modelled with an exponentially decreasing star formation rate.

We have calculated several stellar synthesis models, assuming a Salpeter IMF extending from 0.08 to 30 $M_\odot$ and an exponentially decreasing star formation rate with a time scale of 2.5 Gyr. Predicted optical and near-infrared colours are given in Table B.3 for different ages. Also given in this table are

the average colours of elliptical and lenticular galaxies (Frogel *et al.* 1978). It can be seen that ages between 10 and 12 Gyr reproduce the observed colours, especially in the near-infrared. The predicted mass-to-light ratio is ~3, in very good agreement with the infrared population synthesis of Arnaud & Gilmore (1986) based on empirical dwarf and giant luminosity functions.

The time scale adopted here is slightly higher than the value of 1 Gyr adopted by Bruzual (1983). Given the uncertainties in comparing both models (different evolutionary tracks, different procedure), we do not regard this discrepancy as significant. In fact, both models and the observations are in reasonably good agreement.

Table B.3
Stellar Synthesis Models[1]

Age (Gyr)	U-V	V-K	J-H	H-K	CO_{SP}	$M/L_{\odot\ bol}$
1	0.03	1.80	0.44	0.14	0.18	0.2
3	0.26	1.80	0.43	0.13	0.14	0.6
5	0.37	1.79	0.41	0.13	0.12	1.2
7	0.54	2.09	0.48	0.16	0.14	2.0
9	0.78	2.60	0.58	0.19	0.18	2.6
10	0.97	3.12	0.67	0.21	0.23	2.6
11	1.07	3.24	0.69	0.22	0.23	3.1
12	1.16	3.32	0.69	0.22	0.23	3.6
13	1.40	3.74	0.75	0.23	0.26	3.2
14	1.42	3.67	0.74	0.23	0.25	4.3
15	1.43	3.59	0.72	0.22	0.24	5.6
17	1.49	3.46	0.69	0.21	0.22	8.7
20	1.72	3.42	0.65	0.19	0.18	14.4
Observed Colours of E and S0 Galaxies[2]						
	1.48±0.16	3.25±0.24	0.68±0.04	0.20±0.03	0.20±0.02	2.5-5.0

[1] Calculated with a Salpeter IMF (α = 2.35) from 0.08 to 30 $M_{\odot}$ and an exponentially decreasing star formation rate with a time-scale of 2.5 Gyr.
[2] From Frogel *et al.* (1978). The error quoted is one standard deviation from the mean. The range of mass-to-light ratio is from Arnaud & Gilmore (1986).

Table B.4
Stellar Properties of Main Sequence Stars

Sp	T_{eff}	$\log L$	BC	U-B	B-V	V-K	J-K	J-H	CO_{Sp}	N^{H}_{Lyc}	N^{He}_{Lyc}
O3	52500	6.146	-4.75	-1.22	-0.33	-0.94	-0.19	-0.07	0.00	49.84	49.36
O4	48000	5.996	-4.45	-1.20	-0.33	-0.94	-0.19	-0.07	0.00	49.68	49.17
O5	44500	5.897	-4.40	-1.19	-0.33	-0.94	-0.19	-0.07	0.00	49.42	48.85
O6	41000	5.623	-3.93	-1.17	-0.33	-0.94	-0.19	-0.07	0.00	49.13	48.46
O7	38000	5.415	-3.68	-1.15	-0.32	-0.94	-0.19	-0.07	0.00	48.80	47.83
O8	35800	5.230	-3.54	-1.14	-0.32	-0.94	-0.19	-0.07	0.00	48.49	47.21
O9	33000	4.987	-3.33	-1.12	-0.31	-0.94	-0.19	-0.07	0.00	47.94	46.28
B0	30000	4.716	-3.16	-1.08	-0.30	-0.93	-0.21	-0.08	0.00	47.41	45.46
B1	25400	4.204	-2.70	-0.95	-0.26	-0.81	-0.18	-0.07	0.00	46.04	43.09
B2	22000	3.756	-2.35	-0.84	-0.24	-0.74	-0.17	-0.07	0.00	45.01	41.38
B3	18700	3.278	-1.94	-0.71	-0.20	-0.61	-0.15	-0.06	0.00	43.85	39.51
B5	15400	2.919	-1.46	-0.58	-0.17	-0.47	-0.11	-0.05	0.00	42.25	36.88
B6	14000	2.699	-1.21	-0.50	-0.15	-0.41	-0.10	-0.04	0.00	41.43	35.27
B7	13000	2.505	-1.02	-0.43	-0.13	-0.35	-0.09	-0.04	0.00	40.81	34.16
B8	11900	2.255	-0.80	-0.34	-0.11	-0.24	-0.06	-0.03	0.00	40.00	32.46
B9	10500	1.978	-0.51	-0.20	-0.07	-0.14	-0.05	-0.03	0.00	38.82	30.19
A0	9520	1.732	-0.30	-0.02	-0.02	-0.03	-0.02	-0.01	0.00	37.47	27.73
A1	9230	1.544	-0.23	0.02	0.01	0.05	0.00	0.00	0.00	36.98	27.30
A2	8970	1.415	-0.20	0.05	0.05	0.13	0.02	0.00	0.00	36.36	26.38
A3	8720	1.322	-0.17	0.08	0.08	0.21	0.04	0.01	0.00	35.63	25.58
A5	8200	1.146	-0.15	0.10	0.15	0.36	0.08	0.03	0.00	34.42	24.10
A7	7850	1.021	-0.12	0.10	0.20	0.46	0.10	0.04	0.00	0.00	0.00
A8	7580	0.934	-0.10	0.09	0.25	0.57	0.13	0.06	0.00	0.00	0.00
F0	7200	0.813	-0.09	0.03	0.30	0.79	0.19	0.09	0.00	0.00	0.00
F2	6890	0.462	-0.11	0.00	0.35	0.93	0.23	0.11	0.00	0.00	0.00
F5	6440	0.505	-0.14	-0.02	0.44	1.07	0.26	0.12	0.00	0.00	0.00
F8	6200	0.322	-0.16	0.02	0.52	1.12	0.27	0.14	0.00	0.00	0.00
G0	6030	0.176	-0.18	0.06	0.58	1.16	0.28	0.15	0.00	0.00	0.00
G2	5860	0.041	-0.20	0.12	0.63	1.20	0.29	0.15	0.01	0.00	0.00
G5	5770	-0.102	-0.21	0.20	0.68	1.25	0.30	0.26	0.01	0.00	0.00
G8	5570	-0.180	-0.40	0.30	0.74	1.50	0.37	0.32	0.01	0.00	0.00
K0	5250	-0.377	-0.31	0.45	0.81	1.75	0.43	0.37	0.02	0.00	0.00
K1	5080	-0.432	-0.37	0.54	0.86	2.00	0.49	0.42	0.03	0.00	0.00
K2	4900	-0.538	-0.42	0.64	0.91	2.25	0.55	0.47	0.03	0.00	0.00
K3	4730	-0.585	-0.50	0.80	0.96	2.50	0.61	0.52	0.04	0.00	0.00
K4	4590	-0.721	-0.55	0.94	1.06	2.75	0.66	0.56	0.05	0.00	0.00
K5	4360	-0.824	-0.72	1.08	1.15	3.00	0.69	0.59	0.06	0.00	0.00
K7	4060	-1.000	-1.01	1.21	1.33	3.15	0.73	0.61	0.09	0.00	0.00
M0	3850	-1.114	-1.38	1.22	1.40	3.25	0.76	0.63	0.11	0.00	0.00
M1	3720	-1.215	-1.62	1.21	1.46	3.50	0.79	0.65	0.12	0.00	0.00
M2	3580	-1.347	-1.89	1.18	1.49	3.75	0.81	0.65	0.14	0.00	0.00
M3	3470	-1.444	-2.15	1.16	1.51	4.00	0.84	0.63	0.15	0.00	0.00
M4	3370	-1.721	-2.38	1.15	1.54	4.25	0.82	0.60	0.16	0.00	0.00
M5	3240	-1.959	-2.73	1.24	1.64	4.50	0.81	0.57	0.18	0.00	0.00
M6	3050	-2.276	-3.21	1.32	1.73	4.75	0.79	0.54	0.20	0.00	0.00
M7	2940	-2.469	-3.46	1.40	1.80	5.00	0.79	0.53	0.22	0.00	0.00
M8	2640	-2.921	-4.10	1.53	1.93	5.25	0.80	0.52	0.26	0.00	0.00

Table B.5
Stellar Properties of Giant Stars

Sp	T_{eff}	$\log L$	BC	U-B	B-V	V-K	J-K	J-H	CO_{Sp}	N^{H}_{Lyc}	N^{He}_{Lyc}
O3	50000	6.322	-4.58	-1.22	-0.32	-0.94	-0.19	-0.07	0.00	49.84	49.36
O4	45500	6.176	-4.28	-1.20	-0.32	-0.94	-0.19	-0.07	0.00	49.68	49.17
O5	42500	5.996	-4.05	-1.18	-0.32	-0.94	-0.19	-0.07	0.00	49.42	48.85
O6	39500	5.813	-3.80	-1.17	-0.32	-0.94	-0.19	-0.07	0.00	49.23	48.56
O7	37000	5.643	-3.58	-1.14	-0.32	-0.94	-0.19	-0.07	0.00	48.99	48.02
O8	34700	5.531	-3.39	-1.13	-0.31	-0.94	-0.19	-0.07	0.00	49.80	47.52
O9	32000	5.342	-3.13	-1.12	-0.31	-0.94	-0.19	-0.07	0.00	48.40	46.74
B0	29000	5.041	-2.88	-1.08	-0.29	-0.93	-0.21	-0.08	0.00	47.72	45.77
B1	24000	4.591	-2.43	-0.97	-0.26	-0.81	-0.18	-0.07	0.00	46.39	43.44
B2	20300	4.230	-2.02	-0.91	-0.24	-0.74	-0.17	-0.07	0.00	45.98	42.50
B3	17100	3.699	-1.60	-0.74	-0.20	-0.61	-0.15	-0.06	0.00	44.37	39.84
B5	15000	3.255	-1.30	-0.58	-0.17	-0.47	-0.11	-0.05	0.00	43.28	38.09
B6	14100	3.041	-1.13	-0.51	-0.15	-0.41	-0.10	-0.04	0.00	42.76	37.17
B7	13200	2.845	-0.97	-0.44	-0.13	-0.35	-0.09	-0.04	0.00	42.20	36.09
B8	12400	2.663	-0.82	-0.37	-0.11	-0.24	-0.06	-0.03	0.00	41.72	35.12
B9	11000	2.380	-0.71	-0.20	-0.07	-0.14	-0.05	-0.03	0.00	40.68	33.01
A0	10100	2.025	-0.42	-0.07	-0.03	-0.03	-0.02	-0.01	0.00	39.93	31.27
A1	9480	1.892	-0.29	0.07	0.01	0.05	0.00	0.00	0.00	38.84	29.00
A2	9000	1.813	-0.20	0.06	0.05	0.13	0.02	0.00	0.00	37.53	26.71
A3	8600	1.724	-0.17	0.10	0.08	0.21	0.04	0.01	0.00	36.47	25.82
A5	8100	1.633	-0.14	0.11	0.15	0.36	0.08	0.03	0.00	35.44	23.73
A7	7650	1.462	-0.10	0.11	0.22	0.46	0.10	0.04	0.00	0.00	0.00
A8	7450	1.415	-0.10	0.10	0.25	0.57	0.13	0.06	0.00	0.00	0.00
F0	7150	1.301	-0.11	0.08	0.30	0.79	0.19	0.09	0.00	0.00	0.00
F2	6870	1.230	-0.11	0.08	0.35	0.93	0.23	0.11	0.00	0.00	0.00
F5	6470	1.230	-0.14	0.09	0.43	1.07	0.26	0.12	0.00	0.00	0.00
F8	6150	1.411	-0.16	0.10	0.54	1.37	0.34	0.16	0.00	0.00	0.00
G0	5850	1.531	-0.20	0.21	0.65	1.58	0.39	0.18	0.00	0.00	0.00
G2	5450	1.602	-0.27	0.39	0.77	1.78	0.44	0.20	0.02	0.00	0.00
G5	5150	1.633	-0.34	0.56	0.86	2.08	0.52	0.47	0.04	0.00	0.00
G8	4900	1.708	-0.42	0.70	0.94	2.16	0.55	0.49	0.06	0.00	0.00
K0	4750	1.778	-0.50	0.84	1.00	2.35	0.59	0.51	0.07	0.00	0.00
K1	4600	1.839	-0.55	1.01	1.07	2.48	0.63	0.54	0.09	0.00	0.00
K2	4420	1.898	-0.61	1.16	1.16	2.59	0.66	0.56	0.12	0.00	0.00
K3	4200	2.041	-0.76	1.39	1.27	2.92	0.74	0.62	0.15	0.00	0.00
K4	4000	2.230	-0.94	1.66	1.39	3.24	0.81	0.68	0.18	0.00	0.00
K5	3950	2.342	-1.02	1.81	1.50	3.67	0.88	0.73	0.19	0.00	0.00
K7	3850	2.447	-1.17	1.83	1.53	3.71	0.89	0.73	0.21	0.00	0.00
M0	3800	2.519	-1.25	1.87	1.56	3.74	0.90	0.74	0.22	0.00	0.00
M1	3720	2.633	-1.44	1.88	1.58	3.90	0.93	0.76	0.23	0.00	0.00
M2	3620	2.740	-1.62	1.89	1.60	4.16	0.95	0.77	0.25	0.00	0.00
M3	3530	2.845	-1.87	1.88	1.61	4.63	0.99	0.79	0.27	0.00	0.00
M4	3430	2.944	-2.22	1.73	1.62	5.34	1.04	0.81	0.29	0.00	0.00
M5	3330	2.968	-2.48	1.58	1.63	6.20	1.12	0.86	0.32	0.00	0.00
M6	3240	3.029	-2.73	1.16	1.52	7.20	1.19	0.89	0.34	0.00	0.00

Table B.6
Stellar Properties of Supergiant Stars

Sp	T_{eff}	$\log L$	BC	U-B	B-V	V-K	J-K	J-H	CO_{Sp}	N^{H}_{Lyc}	N^{He}_{Lyc}
O3	47300	6.342	-4.41	-1.21	-0.31	-0.94	-0.19	-0.07	0.00	49.84	49.36
O4	44100	6.204	-4.17	-1.19	-0.31	-0.94	-0.19	-0.07	0.00	49.68	49.17
O5	40300	6.041	-3.87	-1.17	-0.31	-0.94	-0.19	-0.07	0.00	49.48	48.91
O6	39000	5.954	-3.74	-1.16	-0.31	-0.94	-0.19	-0.07	0.00	49.44	48.77
O7	35700	5.851	-3.48	-1.14	-0.31	-0.94	-0.19	-0.07	0.00	49.31	48.34
O8	34200	5.792	-3.35	-1.13	-0.29	-0.94	-0.19	-0.07	0.00	49.20	47.92
O9	32600	5.724	-3.18	-1.13	-0.27	-0.94	-0.19	-0.07	0.00	48.74	47.08
B0	26000	5.415	-2.49	-1.06	-0.23	-0.79	-0.16	-0.07	0.00	48.08	45.64
B1	20800	5.176	-1.87	-1.00	-0.19	-0.60	-0.12	-0.04	0.00	46.92	43.06
B2	18500	5.041	-1.58	-0.93	-0.17	-0.45	-0.08	-0.03	0.00	46.33	41.66
B3	16200	4.881	-1.26	-0.83	-0.13	-0.36	-0.06	-0.02	0.00	45.33	39.95
B5	13600	4.716	-0.95	-0.72	-0.10	-0.22	-0.02	0.01	0.00	43.88	37.23
B6	13000	4.690	-0.88	-0.69	-0.08	-0.16	0.00	0.01	0.00	43.56	36.47
B7	12200	4.643	-0.78	-0.63	-0.05	-0.10	0.02	0.02	0.00	43.22	35.38
B8	11200	4.602	-0.66	-0.55	-0.03	-0.03	0.05	0.04	0.00	42.46	33.62
B9	10300	4.544	-0.52	-0.49	-0.02	0.03	0.06	0.04	0.00	41.59	31.70
A0	9730	4.544	-0.41	-0.38	-0.01	0.10	0.08	0.05	0.00	40.95	30.46
A1	9230	4.544	-0.32	-0.29	0.02	0.16	0.09	0.05	0.00	40.25	29.12
A2	9080	4.556	-0.28	-0.25	0.03	0.22	0.11	0.06	0.00	39.99	28.68
A3	8770	4.544	-0.21	-0.14	0.06	0.27	0.12	0.07	0.00	39.29	27.83
A5	8510	4.544	-0.13	-0.08	0.09	0.37	0.13	0.07	0.00	38.65	27.04
A7	8150	4.519	-0.06	0.00	0.12	0.47	0.15	0.08	0.00	37.90	25.46
A8	7950	4.505	-0.03	0.11	0.14	0.53	0.14	0.07	0.00	0.00	0.00
F0	7700	4.505	-0.01	0.15	0.17	0.63	0.17	0.09	0.00	0.00	0.00
F2	7350	4.491	0.00	0.18	0.23	0.75	0.19	0.09	0.00	0.00	0.00
F5	6900	4.505	-0.03	0.27	0.32	0.93	0.24	0.12	0.00	0.00	0.00
F8	6100	4.491	-0.09	0.41	0.56	1.21	0.33	0.16	0.00	0.00	0.00
G0	5550	4.477	-0.15	0.52	0.76	1.44	0.38	0.18	0.00	0.00	0.00
G2	5200	4.462	-0.21	0.63	0.87	1.67	0.43	0.21	0.00	0.00	0.00
G5	4850	4.462	-0.33	0.83	1.02	1.95	0.48	0.22	0.00	0.00	0.00
G8	4600	4.462	-0.42	1.07	1.14	1.99	0.56	0.36	0.06	0.00	0.00
K0	4420	4.462	-0.50	1.17	1.25	2.16	0.62	0.45	0.11	0.00	0.00
K1	4330	4.477	-0.56	1.28	1.32	2.29	0.65	0.50	0.14	0.00	0.00
K2	4250	4.462	-0.61	1.32	1.36	2.44	0.67	0.54	0.16	0.00	0.00
K3	4080	4.519	-0.75	1.60	1.46	2.90	0.70	0.59	0.21	0.00	0.00
K4	3950	4.531	-0.90	1.70	1.53	3.20	0.73	0.60	0.25	0.00	0.00
K5	3850	4.580	-1.01	1.80	1.60	3.50	0.75	0.61	0.27	0.00	0.00
K7	3700	4.613	-1.20	1.84	1.63	3.62	0.78	0.63	0.32	0.00	0.00
M0	3650	4.613	-1.29	1.90	1.67	3.80	0.83	0.66	0.33	0.00	0.00
M1	3550	4.643	-1.38	1.90	1.69	3.90	0.85	0.66	0.36	0.00	0.00
M2	3450	4.740	-1.62	1.95	1.71	4.10	0.87	0.66	0.39	0.00	0.00
M3	3200	4.748	-2.13	1.95	1.69	4.60	0.90	0.67	0.46	0.00	0.00
M4	2980	5.204	-2.75	2.00	1.76	5.20	0.96	0.71	0.52	0.00	0.00
M5	2800	5.477	-3.47	1.60	1.80	5.20	0.96	0.71	0.57	0.00	0.00
M6	2600	5.653	-3.90	1.60	1.80	5.20	0.96	0.71	0.62	0.00	0.00

Table B.7
Star Model with an Initial Mass of 120.00 $M_{\odot}$

#	Age	$\log L$	BC	U-B	B-V	V-K	J-K	J-H	CO_{Sp}	N^{H}_{Lyc}	N^{He}_{Lyc}	Sp
1	0.1180	6.254	-4.75	-1.22	-0.33	-0.94	-0.19	-0.07	0.00	49.84	49.36	O?V
2	1.0034	6.310	-4.58	-1.22	-0.32	-0.94	-0.19	-0.07	0.00	49.84	49.36	O?III
3	1.4872	6.341	-4.21	-1.19	-0.31	-0.94	-0.19	-0.07	0.00	49.71	49.20	O4I
4	1.8274	6.364	-3.68	-1.16	-0.31	-0.94	-0.19	-0.07	0.00	49.42	48.70	O7I?
5	2.4814	6.417	-3.49	-1.14	-0.31	-0.94	-0.19	-0.07	0.00	49.31	48.36	O7I?
6	2.7175	6.435	-3.74	-1.16	-0.31	-0.94	-0.19	-0.07	0.00	49.44	48.77	O7I?
7	2.9379	6.501	-4.41	-1.21	-0.31	-0.94	-0.19	-0.07	0.00	49.84	49.36	O?I?
9	2.9390	6.507	-4.00	-1.18	-0.31	-0.94	-0.19	-0.07	0.00	49.55	49.03	O5I?
10	2.9401	6.507	-3.88	-1.17	-0.31	-0.94	-0.19	-0.07	0.00	49.48	48.92	O5I?
11	2.9412	6.511	-3.10	-1.13	-0.26	-0.94	-0.19	-0.07	0.00	48.54	46.73	B0I?
12	2.9423	6.514	-2.61	-1.08	-0.24	-0.83	-0.17	-0.07	0.00	48.14	45.84	B0I?
13	2.9434	6.515	-2.40	-1.05	-0.23	-0.77	-0.16	-0.07	0.00	47.99	45.42	B1I?
14	2.9445	6.516	-1.99	-1.02	-0.20	-0.65	-0.13	-0.05	0.00	47.18	43.67	B1I?
17	2.9456	6.517	-3.39	-1.13	-0.30	-0.94	-0.19	-0.07	0.00	49.26	48.07	O8I?
18	2.9467	6.516	-4.41	-1.21	-0.31	-0.94	-0.19	-0.07	0.00	49.84	49.36	O?I?
19	2.9748	6.520	-4.41	-1.21	-0.31	-0.94	-0.19	-0.07	0.00	49.84	49.36	O?I?
20	2.9869	6.515	-4.41	-1.21	-0.31	-0.94	-0.19	-0.07	0.00	49.84	49.36	O?I?
21	3.0038	6.510	-4.41	-1.21	-0.31	-0.94	-0.19	-0.07	0.00	49.84	49.36	O?I?
22	3.0377	6.499	-4.41	-1.21	-0.31	-0.94	-0.19	-0.07	0.00	49.84	49.36	O?I?
23	3.0606	6.500	-4.41	-1.21	-0.31	-0.94	-0.19	-0.07	0.00	49.84	49.36	O?I?
24	3.0798	6.498	-4.41	-1.21	-0.31	-0.94	-0.19	-0.07	0.00	49.84	49.36	O?I?
25	3.1150	6.500	-4.41	-1.21	-0.31	-0.94	-0.19	-0.07	0.00	49.84	49.36	O?I?
26	3.1372	6.502	-4.41	-1.21	-0.31	-0.94	-0.19	-0.07	0.00	49.84	49.36	O?I?
27	3.1434	6.502	-4.41	-1.21	-0.31	-0.94	-0.19	-0.07	0.00	49.84	49.36	O?I?
28	3.1795	6.502	-4.41	-1.21	-0.31	-0.94	-0.19	-0.07	0.00	49.84	49.36	O?I?
29	3.2207	6.500	-4.41	-1.21	-0.31	-0.94	-0.19	-0.07	0.00	49.84	49.36	O?I?
30	3.2590	6.499	-4.41	-1.21	-0.31	-0.94	-0.19	-0.07	0.00	49.84	49.36	O?I?
31	3.2846	6.500	-4.41	-1.21	-0.31	-0.94	-0.19	-0.07	0.00	49.84	49.36	O?I?
32	3.3190	6.500	-4.41	-1.21	-0.31	-0.94	-0.19	-0.07	0.00	49.84	49.36	O?I?
33	3.3445	6.500	-4.41	-1.21	-0.31	-0.94	-0.19	-0.07	0.00	49.84	49.36	O?I?
34	3.3734	6.502	-4.41	-1.21	-0.31	-0.94	-0.19	-0.07	0.00	49.84	49.36	O?I?
35	3.4122	6.507	-4.41	-1.21	-0.31	-0.94	-0.19	-0.07	0.00	49.84	49.36	O?I?
36	3.4511	6.539	-4.41	-1.21	-0.31	-0.94	-0.19	-0.07	0.00	49.84	49.36	O?I?
37	3.4517	6.552	-4.41	-1.21	-0.31	-0.94	-0.19	-0.07	0.00	49.84	49.36	O?I?
38	3.4521	6.562	-4.41	-1.21	-0.31	-0.94	-0.19	-0.07	0.00	49.84	49.36	O?I?

Table B.8
Star Model with an Initial Mass of 85.00 $M_{\odot}$

#	Age	$\log L$	BC	U-B	B-V	V-K	J-K	J-H	CO_{Sp}	N^{H}_{Lyc}	N^{He}_{Lyc}	Sp
1	0.1036	6.004	-4.75	-1.22	-0.33	-0.94	-0.19	-0.07	0.00	49.84	49.36	O4V
2	1.1758	6.071	-4.46	-1.20	-0.33	-0.94	-0.19	-0.07	0.00	49.70	49.19	O4V
3	2.0700	6.131	-3.86	-1.17	-0.31	-0.94	-0.19	-0.07	0.00	49.48	48.90	O6I
4	2.3545	6.150	-3.44	-1.14	-0.30	-0.94	-0.19	-0.07	0.00	49.29	48.23	O8I
5	2.6081	6.171	-3.24	-1.13	-0.28	-0.94	-0.19	-0.07	0.00	48.90	47.36	O9I
6	3.3236	6.237	-4.58	-1.22	-0.32	-0.94	-0.19	-0.07	0.00	49.84	49.36	O?IV
7	3.3245	6.245	-4.75	-1.22	-0.33	-0.94	-0.19	-0.07	0.00	49.84	49.36	O?V
8	3.3266	6.267	-4.04	-1.18	-0.31	-0.94	-0.19	-0.07	0.00	49.58	49.07	O5I
9	3.3282	6.289	-2.42	-1.05	-0.23	-0.77	-0.16	-0.07	0.00	48.01	45.46	B1I
10	3.3292	6.305	-0.97	-0.73	-0.10	-0.24	-0.03	0.01	0.00	43.98	37.44	B5I
11	3.3298	6.311	-0.02	0.15	0.16	0.59	0.16	0.08	0.00	0.00	0.00	F0I
12	3.3301	6.312	0.00	0.16	0.20	0.70	0.18	0.09	0.00	0.00	0.00	F2I
13	3.3310	6.314	0.00	0.20	0.25	0.79	0.20	0.09	0.00	0.00	0.00	F5I
14	3.3328	6.320	-0.02	0.25	0.30	0.89	0.23	0.11	0.00	0.00	0.00	F5I
17	3.3393	6.315	-1.09	-0.77	-0.12	-0.31	-0.05	0.00	0.00	44.58	38.63	B5I
18	3.3394	6.341	-4.75	-1.22	-0.33	-0.94	-0.19	-0.07	0.00	49.84	49.36	O?V
19	3.3458	6.336	-4.75	-1.22	-0.33	-0.94	-0.19	-0.07	0.00	49.84	49.36	O?V
20	3.3535	6.331	-4.75	-1.22	-0.33	-0.94	-0.19	-0.07	0.00	49.84	49.36	O?V
21	3.3628	6.332	-4.75	-1.22	-0.33	-0.94	-0.19	-0.07	0.00	49.84	49.36	O?V
22	3.3880	6.311	-4.75	-1.22	-0.33	-0.94	-0.19	-0.07	0.00	49.84	49.36	O?V
23	3.4162	6.280	-4.75	-1.22	-0.33	-0.94	-0.19	-0.07	0.00	49.84	49.36	O?V
24	3.4408	6.267	-4.75	-1.22	-0.33	-0.94	-0.19	-0.07	0.00	49.84	49.36	O?V
25	3.4803	6.260	-4.75	-1.22	-0.33	-0.94	-0.19	-0.07	0.00	49.84	49.36	O?V
26	3.5049	6.259	-4.75	-1.22	-0.33	-0.94	-0.19	-0.07	0.00	49.84	49.36	O?V
27	3.5123	6.258	-4.75	-1.22	-0.33	-0.94	-0.19	-0.07	0.00	49.84	49.36	O?V
28	3.5509	6.254	-4.75	-1.22	-0.33	-0.94	-0.19	-0.07	0.00	49.84	49.36	O?V
29	3.5923	6.246	-4.75	-1.22	-0.33	-0.94	-0.19	-0.07	0.00	49.84	49.36	O?V
30	3.6357	6.241	-4.75	-1.22	-0.33	-0.94	-0.19	-0.07	0.00	49.84	49.36	O?V
31	3.6660	6.237	-4.75	-1.22	-0.33	-0.94	-0.19	-0.07	0.00	49.84	49.36	O?V
32	3.7034	6.233	-4.75	-1.22	-0.33	-0.94	-0.19	-0.07	0.00	49.84	49.36	O?V
33	3.7302	6.230	-4.75	-1.22	-0.33	-0.94	-0.19	-0.07	0.00	49.84	49.36	O?V
34	3.7580	6.229	-4.75	-1.22	-0.33	-0.94	-0.19	-0.07	0.00	49.84	49.36	O?V
35	3.7948	6.232	-4.75	-1.22	-0.33	-0.94	-0.19	-0.07	0.00	49.84	49.36	O?V
36	3.8243	6.262	-4.75	-1.22	-0.33	-0.94	-0.19	-0.07	0.00	49.84	49.36	O?V
37	3.8255	6.280	-4.75	-1.22	-0.33	-0.94	-0.19	-0.07	0.00	49.84	49.36	O?V
38	3.8261	6.303	-4.75	-1.22	-0.33	-0.94	-0.19	-0.07	0.00	49.84	49.36	O?V

Table B.9
Star Model with an Initial Mass of 60.00 $M_{\odot}$

#	Age	$\log L$	BC	U-B	B-V	V-K	J-K	J-H	CO_{Sp}	N^{H}_{Lyc}	N^{He}_{Lyc}	Sp
1	0.1675	5.731	-4.50	-1.20	-0.33	-0.94	-0.19	-0.07	0.00	49.74	49.25	O4V
2	1.4753	5.813	-4.44	-1.19	-0.33	-0.94	-0.19	-0.07	0.00	49.52	48.97	O5V
3	2.4897	5.881	-3.80	-1.16	-0.31	-0.94	-0.19	-0.07	0.00	49.46	48.84	O6II
4	3.1071	5.927	-3.00	-1.12	-0.26	-0.92	-0.19	-0.07	0.00	48.36	46.41	B0I
5	3.4489	5.960	-2.32	-1.04	-0.22	-0.74	-0.15	-0.06	0.00	47.86	45.14	B1I
6	3.5812	5.973	-2.52	-1.06	-0.23	-0.80	-0.16	-0.07	0.00	48.10	45.70	B0I
7	3.7108	5.999	-3.68	-1.16	-0.31	-0.94	-0.19	-0.07	0.00	49.41	48.69	O7I
8	3.7135	6.022	-2.83	-1.11	-0.24	-0.89	-0.18	-0.07	0.00	48.20	46.07	B0I
9	3.7149	6.034	-1.58	-0.93	-0.17	-0.45	-0.08	-0.03	0.00	46.33	41.66	B3I
10	3.7160	6.045	-0.47	-0.44	-0.02	0.06	0.07	0.05	0.00	41.32	31.16	A0I
11	3.7165	6.054	-0.01	0.15	0.16	0.60	0.16	0.08	0.00	0.00	0.00	F0I
12	3.7166	6.057	-0.01	0.22	0.27	0.83	0.21	0.10	0.00	0.00	0.00	F5I
13	3.7168	6.061	-0.04	0.28	0.33	0.95	0.25	0.13	0.00	0.00	0.00	F8I
14	3.7172	6.070	-0.05	0.32	0.39	1.03	0.27	0.14	0.00	0.00	0.00	F8I
15	3.7179	6.085	-0.04	0.30	0.36	0.99	0.26	0.13	0.00	0.00	0.00	F8I
16	3.7180	6.094	-0.02	0.24	0.29	0.87	0.22	0.11	0.00	0.00	0.00	F5I
18	3.7397	6.103	-1.31	-0.85	-0.14	-0.37	-0.06	-0.02	0.00	45.53	40.28	B3I
19	3.7601	6.106	-2.05	-1.02	-0.20	-0.67	-0.14	-0.05	0.00	47.32	43.98	B1I
20	3.7804	6.111	-4.06	-1.18	-0.31	-0.94	-0.19	-0.07	0.00	49.59	49.08	O5II
21	3.8008	6.108	-4.75	-1.22	-0.33	-0.94	-0.19	-0.07	0.00	49.84	49.36	O?V
22	3.8349	6.092	-4.75	-1.22	-0.33	-0.94	-0.19	-0.07	0.00	49.84	49.36	O?V
23	3.8612	6.063	-4.75	-1.22	-0.33	-0.94	-0.19	-0.07	0.00	49.84	49.36	O?V
24	3.8915	6.026	-4.75	-1.22	-0.33	-0.94	-0.19	-0.07	0.00	49.84	49.36	O?V
25	3.9350	6.016	-4.75	-1.22	-0.33	-0.94	-0.19	-0.07	0.00	49.84	49.36	O?V
26	3.9562	6.010	-4.75	-1.22	-0.33	-0.94	-0.19	-0.07	0.00	49.84	49.36	O?V
27	3.9659	6.008	-4.75	-1.22	-0.33	-0.94	-0.19	-0.07	0.00	49.84	49.36	O?V
28	4.0060	5.998	-4.75	-1.22	-0.33	-0.94	-0.19	-0.07	0.00	49.84	49.36	O?V
29	4.0529	5.979	-4.75	-1.22	-0.33	-0.94	-0.19	-0.07	0.00	49.84	49.36	O?V
30	4.1008	5.963	-4.75	-1.22	-0.33	-0.94	-0.19	-0.07	0.00	49.84	49.36	O?V
31	4.1342	5.951	-4.75	-1.22	-0.33	-0.94	-0.19	-0.07	0.00	49.84	49.36	O?V
32	4.1766	5.935	-4.75	-1.22	-0.33	-0.94	-0.19	-0.07	0.00	49.84	49.36	O?V
33	4.2067	5.923	-4.75	-1.22	-0.33	-0.94	-0.19	-0.07	0.00	49.84	49.36	O?V
34	4.2401	5.911	-4.75	-1.22	-0.33	-0.94	-0.19	-0.07	0.00	49.84	49.36	O?V
35	4.2847	5.899	-4.75	-1.22	-0.33	-0.94	-0.19	-0.07	0.00	49.84	49.36	O?V
36	4.3193	5.928	-4.75	-1.22	-0.33	-0.94	-0.19	-0.07	0.00	49.84	49.36	O?V
37	4.3210	5.962	-4.75	-1.22	-0.33	-0.94	-0.19	-0.07	0.00	49.84	49.36	O?V
38	4.3211	5.974	-4.75	-1.22	-0.33	-0.94	-0.19	-0.07	0.00	49.84	49.36	O?V
39	4.3212	6.017	-4.75	-1.22	-0.33	-0.94	-0.19	-0.07	0.00	49.84	49.36	O?V

Table B.10
Star Model with an Initial Mass of 40.00 $M_{\odot}$

#	Age	$\log L$	BC	U-B	B-V	V-K	J-K	J-H	CO_{Sp}	N^{H}_{Lyc}	N^{He}_{Lyc}	Sp
1	0.2148	5.374	-4.42	-1.19	-0.33	-0.94	-0.19	-0.07	0.00	49.45	48.89	O5V
2	1.9384	5.478	-4.07	-1.18	-0.33	-0.94	-0.19	-0.07	0.00	49.22	48.59	O6V
3	3.2721	5.560	-3.62	-1.14	-0.32	-0.94	-0.19	-0.07	0.00	48.94	48.12	O7IV
4	4.0724	5.611	-3.07	-1.13	-0.26	-0.93	-0.19	-0.07	0.00	48.49	46.65	B0I
5	4.6979	5.667	-1.98	-1.02	-0.20	-0.65	-0.13	-0.05	0.00	47.17	43.64	B1I
6	4.7902	5.699	-2.46	-1.06	-0.23	-0.78	-0.16	-0.07	0.00	48.06	45.58	B1I
7	4.7912	5.702	-2.50	-1.06	-0.23	-0.79	-0.16	-0.07	0.00	48.09	45.65	B0I
9	4.7928	5.691	-2.21	-1.04	-0.21	-0.72	-0.15	-0.06	0.00	47.67	44.72	B1I
10	4.7948	5.709	-0.59	-0.53	-0.02	0.00	0.05	0.04	0.00	41.98	32.54	B9I
11	4.7952	5.711	-0.04	0.29	0.34	0.96	0.25	0.13	0.00	0.00	0.00	F8I
12	4.7955	5.707	-0.11	0.44	0.63	1.28	0.35	0.16	0.00	0.00	0.00	G0I
13	4.7956	5.696	-0.17	0.55	0.80	1.50	0.40	0.19	0.00	0.00	0.00	G2I
14	4.7960	5.709	-0.37	0.94	1.07	1.97	0.51	0.27	0.02	0.00	0.00	G8I
15	4.8015	5.825	-0.38	0.98	1.09	1.97	0.52	0.29	0.03	0.00	0.00	G8I
16	4.8493	5.840	-0.28	0.73	0.96	1.87	0.46	0.20	-0.01	0.00	0.00	G5I
17	4.8873	5.847	-0.23	0.66	0.90	1.74	0.44	0.21	0.00	0.00	0.00	G5I
18	4.9028	5.850	-0.20	0.61	0.85	1.63	0.42	0.21	0.00	0.00	0.00	G2I
19	4.9101	5.853	-0.17	0.56	0.81	1.53	0.40	0.20	0.00	0.00	0.00	G2I
20	4.9271	5.856	-0.03	0.28	0.33	0.95	0.25	0.12	0.00	0.00	0.00	F8I
21	4.9300	5.856	-1.12	-0.78	-0.12	-0.32	-0.05	-0.01	0.00	44.74	38.92	B5I
22	4.9399	5.854	-2.86	-1.11	-0.25	-0.90	-0.18	-0.07	0.00	48.22	46.12	B0I
23	4.9539	5.849	-3.46	-1.14	-0.31	-0.94	-0.19	-0.07	0.00	49.30	48.28	O8I
24	4.9708	5.846	-3.91	-1.18	-0.32	-0.94	-0.19	-0.07	0.00	49.35	48.71	O6III
25	4.9849	5.838	-4.57	-1.21	-0.33	-0.94	-0.19	-0.07	0.00	49.78	49.29	O4V
26	5.0017	5.823	-4.75	-1.22	-0.33	-0.94	-0.19	-0.07	0.00	49.84	49.36	O?V
27	5.0309	5.764	-4.75	-1.22	-0.33	-0.94	-0.19	-0.07	0.00	49.84	49.36	O?V
28	5.0836	5.713	-4.75	-1.22	-0.33	-0.94	-0.19	-0.07	0.00	49.84	49.36	O?V
29	5.1398	5.670	-4.75	-1.22	-0.33	-0.94	-0.19	-0.07	0.00	49.84	49.36	O?V
30	5.2010	5.620	-4.75	-1.22	-0.33	-0.94	-0.19	-0.07	0.00	49.84	49.36	O?V
31	5.2401	5.585	-4.75	-1.22	-0.33	-0.94	-0.19	-0.07	0.00	49.84	49.36	O?V
32	5.2866	5.538	-4.75	-1.22	-0.33	-0.94	-0.19	-0.07	0.00	49.84	49.36	O?V
33	5.3204	5.501	-4.75	-1.22	-0.33	-0.94	-0.19	-0.07	0.00	49.84	49.36	O?V
34	5.3605	5.452	-4.75	-1.22	-0.33	-0.94	-0.19	-0.07	0.00	49.84	49.36	O?V
35	5.4057	5.396	-4.75	-1.22	-0.33	-0.94	-0.19	-0.07	0.00	49.84	49.36	O?V
36	5.4307	5.404	-4.75	-1.22	-0.33	-0.94	-0.19	-0.07	0.00	49.84	49.36	O?V
37	5.4347	5.467	-4.75	-1.22	-0.33	-0.94	-0.19	-0.07	0.00	49.84	49.36	O?V
38	5.4351	5.476	-4.75	-1.22	-0.33	-0.94	-0.19	-0.07	0.00	49.84	49.36	O?V
39	5.4355	5.516	-4.75	-1.22	-0.33	-0.94	-0.19	-0.07	0.00	49.84	49.36	O?V

Table B.11
Star Model with an Initial Mass of 25.00 $M_{\odot}$

#	Age	$\log L$	BC	U-B	B-V	V-K	J-K	J-H	CO_{Sp}	N^{H}_{Lyc}	N^{He}_{Lyc}	Sp
1	0.2663	4.897	-3.72	-1.15	-0.32	-0.94	-0.19	-0.07	0.00	48.89	48.01	O7V
2	2.9395	5.030	-3.60	-1.14	-0.32	-0.94	-0.19	-0.07	0.00	48.63	47.49	O8V
3	4.8642	5.138	-3.36	-1.12	-0.31	-0.94	-0.19	-0.07	0.00	48.04	46.43	O9V
4	5.9393	5.198	-2.96	-1.10	-0.30	-0.94	-0.20	-0.08	0.00	47.83	46.15	B0III
5	6.8972	5.258	-2.35	-1.05	-0.22	-0.75	-0.15	-0.07	0.00	47.92	45.25	B1I
6	7.0837	5.284	-2.73	-1.09	-0.24	-0.86	-0.17	-0.07	0.00	48.17	45.96	B0II
7	7.0887	5.300	-2.84	-1.11	-0.25	-0.89	-0.18	-0.07	0.00	48.21	46.09	B0II
8	7.0894	5.301	-2.83	-1.11	-0.25	-0.89	-0.18	-0.07	0.00	48.21	46.08	B0II
9	7.0954	5.329	-1.77	-0.98	-0.18	-0.55	-0.11	-0.04	0.00	46.71	42.55	B2I
10	7.0995	5.360	-0.35	-0.32	0.01	0.13	0.08	0.05	0.00	40.44	29.48	A1I
11	7.1006	5.369	-0.03	0.28	0.33	0.95	0.25	0.12	0.00	0.00	0.00	F8I
12	7.1021	5.366	-0.23	0.66	0.90	1.75	0.44	0.21	0.00	0.00	0.00	G5I
13	7.1027	5.356	-0.46	1.12	1.20	2.08	0.60	0.42	0.09	0.00	0.00	K0I
14	7.1032	5.360	-0.60	1.31	1.35	2.41	0.67	0.53	0.16	0.00	0.00	K2I
15	7.1585	5.405	-0.73	1.57	1.45	2.84	0.70	0.59	0.20	0.00	0.00	K3I
16	7.1826	5.407	-0.72	1.55	1.44	2.82	0.69	0.58	0.20	0.00	0.00	K3I
17	7.2067	5.411	-0.72	1.55	1.44	2.82	0.69	0.58	0.20	0.00	0.00	K3I
18	7.2260	5.414	-0.72	1.55	1.44	2.82	0.69	0.58	0.20	0.00	0.00	K3I
19	7.2383	5.416	-0.72	1.55	1.44	2.82	0.69	0.58	0.20	0.00	0.00	K3I
20	7.2557	5.418	-0.71	1.53	1.44	2.79	0.69	0.58	0.20	0.00	0.00	K3I
21	7.2774	5.419	-0.70	1.52	1.43	2.77	0.69	0.58	0.19	0.00	0.00	K3I
22	7.2861	5.420	-0.70	1.52	1.43	2.77	0.69	0.58	0.19	0.00	0.00	K3I
23	7.2991	5.423	-0.69	1.50	1.42	2.74	0.69	0.58	0.19	0.00	0.00	K3I
24	7.3468	5.427	-0.68	1.46	1.41	2.68	0.69	0.57	0.18	0.00	0.00	K3I
25	7.3685	5.430	-0.67	1.44	1.41	2.66	0.68	0.57	0.18	0.00	0.00	K3I
26	7.4140	5.436	-0.65	1.41	1.39	2.60	0.68	0.56	0.18	0.00	0.00	K3I
27	7.7382	5.463	-0.47	1.13	1.22	2.10	0.60	0.43	0.10	0.00	0.00	K0I
28	7.8431	5.473	-0.41	1.05	1.13	1.98	0.55	0.35	0.05	0.00	0.00	G8I
29	7.9105	5.482	-0.17	0.56	0.81	1.53	0.40	0.20	0.00	0.00	0.00	G2I
30	7.9601	5.479	-0.61	-0.54	-0.03	-0.01	0.05	0.04	0.00	42.15	32.92	B9I
31	7.9628	5.473	-0.98	-0.73	-0.11	-0.24	-0.03	0.01	0.00	44.02	37.52	B5I
32	7.9856	5.484	-0.06	0.34	0.42	1.06	0.29	0.15	0.00	0.00	0.00	F8I
33	8.0978	5.491	-0.01	0.21	0.26	0.82	0.20	0.10	0.00	0.00	0.00	F5I
34	8.1688	5.500	-0.01	0.21	0.27	0.82	0.21	0.10	0.00	0.00	0.00	F5I
35	8.2049	5.506	-0.06	0.34	0.41	1.06	0.28	0.14	0.00	0.00	0.00	F8I
36	8.2605	5.536	-0.15	0.53	0.77	1.46	0.38	0.18	0.00	0.00	0.00	G2I
37	8.2622	5.555	-0.16	0.55	0.79	1.50	0.39	0.19	0.00	0.00	0.00	G2I
38	8.2669	5.591	-0.17	0.55	0.80	1.50	0.40	0.19	0.00	0.00	0.00	G2I
39	8.2676	5.609	-0.16	0.55	0.79	1.50	0.39	0.19	0.00	0.00	0.00	G2I

Table B.12
Star Model with an Initial Mass of 20.00 $M_{\odot}$

#	Age	$\log L$	BC	U-B	B-V	V-K	J-K	J-H	CO_{Sp}	N^{H}_{Lyc}	N^{He}_{Lyc}	Sp
1	0.2413	4.643	-3.53	-1.14	-0.32	-0.94	-0.19	-0.07	0.00	48.46	47.16	O9V
2	3.9227	4.792	-3.39	-1.13	-0.31	-0.94	-0.19	-0.07	0.00	48.12	46.56	O9V
3	6.2329	4.907	-3.24	-1.10	-0.30	-0.94	-0.20	-0.08	0.00	47.65	45.84	B0V
4	7.4842	4.977	-2.82	-1.07	-0.28	-0.92	-0.21	-0.08	0.00	47.61	45.48	B1III
5	8.5661	5.041	-2.33	-1.05	-0.22	-0.75	-0.15	-0.06	0.00	47.88	45.19	B1II
6	8.7930	5.064	-2.64	-1.08	-0.24	-0.83	-0.17	-0.07	0.00	48.15	45.87	B0II
7	8.8064	5.086	-2.88	-1.08	-0.29	-0.93	-0.21	-0.08	0.00	47.72	45.76	B1III
8	8.8068	5.086	-2.87	-1.08	-0.29	-0.93	-0.21	-0.08	0.00	47.71	45.73	B1III
9	8.8156	5.125	-1.54	-0.92	-0.17	-0.44	-0.08	-0.03	0.00	46.24	41.49	B3I
10	8.8208	5.147	-0.38	-0.35	0.00	0.11	0.08	0.05	0.00	40.72	30.01	A1I
11	8.8231	5.158	-0.03	0.28	0.33	0.95	0.25	0.12	0.00	0.00	0.00	F8I
12	8.8255	5.155	-0.25	0.68	0.92	1.79	0.44	0.20	-0.01	0.00	0.00	G5I
13	8.8264	5.145	-0.47	1.12	1.21	2.09	0.60	0.42	0.09	0.00	0.00	K0I
14	8.8273	5.135	-0.81	1.65	1.49	3.01	0.71	0.59	0.23	0.00	0.00	K4I
15	8.8301	5.162	-1.00	1.79	1.59	3.47	0.75	0.61	0.27	0.00	0.00	K5I
16	8.8330	5.172	-1.01	1.80	1.60	3.49	0.75	0.61	0.27	0.00	0.00	K5I
17	8.8378	5.175	-0.99	1.78	1.59	3.45	0.75	0.61	0.26	0.00	0.00	K5I
18	8.9624	5.189	-0.96	1.75	1.57	3.37	0.74	0.61	0.26	0.00	0.00	K5I
19	8.9745	5.191	-0.97	1.76	1.58	3.40	0.74	0.61	0.26	0.00	0.00	K5I
20	8.9943	5.193	-0.96	1.75	1.57	3.37	0.74	0.61	0.26	0.00	0.00	K5I
21	9.0339	5.195	-0.95	1.74	1.56	3.34	0.74	0.60	0.26	0.00	0.00	K5I
24	9.0669	5.199	-0.95	1.74	1.56	3.34	0.74	0.60	0.26	0.00	0.00	K5I
25	9.1301	5.206	-0.95	1.74	1.56	3.34	0.74	0.60	0.26	0.00	0.00	K5I
26	9.2371	5.216	-0.94	1.73	1.55	3.31	0.74	0.60	0.26	0.00	0.00	K5I
27	9.4000	5.233	-0.99	1.78	1.59	3.45	0.75	0.61	0.26	0.00	0.00	K5I
28	9.6968	5.256	-0.93	1.72	1.55	3.28	0.74	0.60	0.25	0.00	0.00	K5I
29	9.8907	5.271	-0.87	1.68	1.52	3.14	0.72	0.60	0.24	0.00	0.00	K4I
30	9.9063	5.274	-0.88	1.69	1.52	3.16	0.73	0.60	0.25	0.00	0.00	K4I
31	9.9496	5.280	-0.87	1.68	1.52	3.14	0.72	0.60	0.24	0.00	0.00	K4I
32	9.9848	5.286	-0.87	1.68	1.52	3.14	0.72	0.60	0.24	0.00	0.00	K4I
33	9.9943	5.287	-0.86	1.68	1.51	3.12	0.72	0.60	0.24	0.00	0.00	K4I
34	10.0078	5.289	-0.88	1.69	1.52	3.16	0.73	0.60	0.25	0.00	0.00	K4I
35	10.0322	5.297	-0.88	1.69	1.52	3.16	0.73	0.60	0.25	0.00	0.00	K4I
36	10.0638	5.339	-0.85	1.67	1.51	3.09	0.72	0.60	0.24	0.00	0.00	K4I
37	10.0662	5.355	-0.86	1.68	1.51	3.12	0.72	0.60	0.24	0.00	0.00	K4I
38	10.0717	5.410	-0.91	1.70	1.53	3.22	0.73	0.60	0.25	0.00	0.00	K5I
39	10.0727	5.423	-0.90	1.70	1.53	3.19	0.73	0.60	0.25	0.00	0.00	K4I
40	10.0728	5.423	-0.90	1.70	1.53	3.19	0.73	0.60	0.25	0.00	0.00	K4I

Table B.13
Star Model with an Initial Mass of 15.00 $M_{\odot}$

#	Age	$\log L$	BC	U-B	B-V	V-K	J-K	J-H	CO_{Sp}	N^{H}_{Lyc}	N^{He}_{Lyc}	Sp
1	0.5500	4.305	-3.24	-1.10	-0.31	-0.94	-0.20	-0.08	0.00	47.68	45.88	B0V
2	5.2736	4.444	-3.17	-1.08	-0.30	-0.93	-0.21	-0.08	0.00	47.45	45.53	B0V
3	8.6693	4.566	-3.00	-1.03	-0.29	-0.89	-0.21	-0.08	0.00	46.92	44.63	B1V
4	10.4476	4.644	-2.60	-1.01	-0.27	-0.86	-0.20	-0.08	0.00	46.88	44.20	B1III
5	11.7507	4.706	-2.37	-0.96	-0.26	-0.80	-0.18	-0.07	0.00	46.30	43.27	B2III
6	12.0252	4.727	-2.47	-0.98	-0.26	-0.82	-0.18	-0.07	0.00	46.49	43.60	B1III
7	12.1052	4.757	-2.72	-1.04	-0.28	-0.89	-0.21	-0.08	0.00	47.28	44.86	B1III
8	12.1149	4.763	-2.52	-0.99	-0.26	-0.83	-0.19	-0.07	0.00	46.61	43.78	B1III
9	12.1240	4.776	-1.34	-0.86	-0.14	-0.38	-0.06	-0.02	0.00	45.63	40.44	B3I
10	12.1290	4.752	-0.40	-0.37	-0.01	0.10	0.08	0.05	0.00	40.89	30.35	A1I
11	12.1304	4.727	-0.01	0.22	0.28	0.84	0.21	0.10	0.00	0.00	0.00	F5I
12	12.1313	4.666	-0.25	0.68	0.92	1.78	0.44	0.20	-0.01	0.00	0.00	G5I
13	12.1317	4.593	-0.71	1.53	1.44	2.79	0.69	0.58	0.20	0.00	0.00	K3I
14	12.1320	4.511	-1.82	1.96	1.71	4.27	0.88	0.66	0.41	0.00	0.00	M3I
15	12.1451	4.933	-1.77	1.96	1.71	4.23	0.88	0.66	0.41	0.00	0.00	M3I
16	12.1520	4.930	-1.77	1.96	1.71	4.23	0.88	0.66	0.41	0.00	0.00	M3I
17	12.1613	4.926	-1.77	1.96	1.71	4.23	0.88	0.66	0.41	0.00	0.00	M3I
18	12.3315	4.879	-2.00	1.95	1.69	4.45	0.89	0.66	0.44	0.00	0.00	M3I
19	12.3511	4.874	-2.00	1.95	1.69	4.45	0.89	0.66	0.44	0.00	0.00	M3I
20	12.3642	4.874	-2.00	1.95	1.69	4.45	0.89	0.66	0.44	0.00	0.00	M3I
21	12.3903	4.871	-2.00	1.95	1.69	4.45	0.89	0.66	0.44	0.00	0.00	M3I
24	12.4100	4.872	-2.00	1.95	1.69	4.45	0.89	0.66	0.44	0.00	0.00	M3I
25	12.5352	4.869	-1.99	1.95	1.70	4.44	0.89	0.66	0.44	0.00	0.00	M3I
26	12.5935	4.863	-1.99	1.95	1.70	4.44	0.89	0.66	0.44	0.00	0.00	M3I
27	12.9061	4.849	-1.98	1.95	1.70	4.42	0.89	0.66	0.44	0.00	0.00	M3I
28	13.2739	4.850	-1.94	1.95	1.70	4.38	0.89	0.66	0.43	0.00	0.00	M3I
29	13.5260	4.865	-1.94	1.95	1.70	4.38	0.89	0.66	0.43	0.00	0.00	M3I
30	13.5458	4.868	-1.94	1.95	1.70	4.38	0.89	0.66	0.43	0.00	0.00	M3I
31	13.6076	4.879	-1.94	1.95	1.70	4.38	0.89	0.66	0.43	0.00	0.00	M3I
32	13.6541	4.890	-1.94	1.95	1.70	4.38	0.89	0.66	0.43	0.00	0.00	M3I
33	13.6623	4.893	-1.92	1.95	1.70	4.37	0.89	0.66	0.43	0.00	0.00	M3I
34	13.6740	4.897	-1.92	1.95	1.70	4.37	0.89	0.66	0.43	0.00	0.00	M3I
35	13.6983	4.910	-1.91	1.96	1.70	4.35	0.89	0.66	0.43	0.00	0.00	M3I
36	13.7381	5.038	-1.75	1.96	1.71	4.21	0.88	0.66	0.41	0.00	0.00	M3I
37	13.7471	5.071	-1.73	1.96	1.71	4.20	0.88	0.66	0.40	0.00	0.00	M3I
38	13.7533	5.169	-1.55	1.93	1.71	4.04	0.86	0.66	0.38	0.00	0.00	M2I
39	13.7534	5.165	-1.57	1.94	1.71	4.06	0.87	0.66	0.39	0.00	0.00	M2I
40	13.7536	5.173	-1.55	1.93	1.71	4.04	0.86	0.66	0.38	0.00	0.00	M2I

Table B.14
Star Model with an Initial Mass of 12.00 $M_{\odot}$

#	Age	$\log L$	BC	U-B	B-V	V-K	J-K	J-H	CO_{Sp}	N^{H}_{Lyc}	N^{He}_{Lyc}	Sp
1	0.1200	4.005	-3.03	-1.04	-0.29	-0.90	-0.21	-0.08	0.00	47.02	44.80	B1V
2	8.1554	4.157	-2.89	-1.00	-0.28	-0.86	-0.20	-0.08	0.00	46.60	44.07	B1V
3	12.7422	4.283	-2.70	-0.95	-0.26	-0.81	-0.18	-0.07	0.00	46.04	43.10	B1V
4	15.2120	4.364	-2.37	-0.96	-0.26	-0.80	-0.18	-0.07	0.00	46.30	43.27	B2IV
5	16.8879	4.426	-2.17	-0.94	-0.25	-0.77	-0.17	-0.07	0.00	46.17	42.92	B2III
6	17.3730	4.453	-2.33	-0.96	-0.26	-0.79	-0.17	-0.07	0.00	46.26	43.19	B2III
7	17.4530	4.487	-2.52	-0.99	-0.26	-0.83	-0.19	-0.07	0.00	46.61	43.78	B1IV
8	17.4571	4.479	-2.46	-0.98	-0.26	-0.82	-0.18	-0.07	0.00	46.46	43.55	B1III
9	17.4736	4.505	-1.22	-0.82	-0.13	-0.35	-0.06	-0.02	0.00	45.16	39.67	B5I
10	17.4812	4.481	-0.47	-0.44	-0.02	0.06	0.07	0.05	0.00	41.32	31.16	A0I?
11	17.4840	4.446	-0.01	0.21	0.26	0.81	0.20	0.10	0.00	0.00	0.00	F5I
12	17.4855	4.384	-0.20	0.61	0.85	1.62	0.42	0.21	0.00	0.00	0.00	G2I
13	17.4860	4.332	-0.56	1.28	1.32	2.28	0.65	0.50	0.14	0.00	0.00	K1I
14	17.4867	4.255	-0.99	1.78	1.59	3.45	0.75	0.61	0.26	0.00	0.00	K5I
15	17.4983	4.682	-1.83	1.96	1.71	4.29	0.88	0.66	0.42	0.00	0.00	M3I
16	17.5593	4.643	-1.78	1.96	1.71	4.24	0.88	0.66	0.41	0.00	0.00	M3I
17	17.6196	4.604	-1.71	1.96	1.71	4.18	0.88	0.66	0.40	0.00	0.00	M3I
18	17.7293	4.545	-1.57	1.94	1.71	4.06	0.87	0.66	0.39	0.00	0.00	M2I
19	17.9016	4.498	-1.33	1.91	1.69	3.87	0.85	0.67	0.34	0.00	0.00	M1I
20	17.9183	4.500	-1.32	1.91	1.68	3.86	0.85	0.67	0.34	0.00	0.00	M1I
21	17.9561	4.532	-1.16	1.82	1.62	3.57	0.76	0.62	0.31	0.00	0.00	K7I
22	17.9615	4.580	-0.82	1.66	1.49	3.03	0.71	0.60	0.23	0.00	0.00	K4I
23	17.9632	4.595	-0.46	1.12	1.20	2.08	0.60	0.42	0.09	0.00	0.00	K0I
24	17.9756	4.597	-0.01	0.15	0.16	0.61	0.16	0.09	0.00	0.00	0.00	F0I
25	18.0566	4.610	-0.58	-0.52	-0.02	0.00	0.05	0.04	0.00	41.91	32.38	B9I
26	18.1235	4.617	-0.73	-0.59	-0.04	-0.07	0.03	0.03	0.00	42.93	34.65	B8I
27	18.4777	4.640	-0.92	-0.71	-0.09	-0.20	-0.01	0.01	0.00	43.75	36.94	B6I
28	18.9509	4.657	-0.88	-0.69	-0.08	-0.16	0.00	0.01	0.00	43.57	36.51	B6I
29	19.7770	4.680	-0.80	-0.64	-0.06	-0.11	0.02	0.02	0.00	43.30	35.61	B7I
30	19.8769	4.680	-0.24	-0.19	0.04	0.25	0.12	0.07	0.00	39.63	28.22	A3I
31	19.9941	4.676	-0.01	0.15	0.18	0.67	0.18	0.09	0.00	0.00	0.00	F2I
32	20.0614	4.654	-0.52	1.21	1.28	2.21	0.63	0.47	0.12	0.00	0.00	K1I
33	20.0690	4.622	-1.13	1.82	1.61	3.55	0.76	0.61	0.31	0.00	0.00	K7I
34	20.0728	4.596	-1.37	1.90	1.69	3.90	0.85	0.66	0.36	0.00	0.00	M1I
35	20.0804	4.626	-1.64	1.95	1.71	4.12	0.87	0.66	0.39	0.00	0.00	M3I
36	20.1519	4.716	-1.88	1.96	1.71	4.33	0.89	0.66	0.42	0.00	0.00	M3I
37	20.1637	4.850	-2.16	1.96	1.69	4.64	0.90	0.67	0.46	0.00	0.00	M4I
38	20.1742	4.945	-2.35	2.01	1.71	4.88	0.93	0.69	0.49	0.00	0.00	M4I
39	20.1764	4.926	-2.39	2.02	1.72	4.93	0.93	0.69	0.49	0.00	0.00	M4I
40	20.1765	4.946	-2.43	2.02	1.72	4.97	0.94	0.69	0.49	0.00	0.00	M4I

Table B.15
Star Model with an Initial Mass of 9.00 $M_{\odot}$

#	Age	$\log L$	BC	U-B	B-V	V-K	J-K	J-H	CO_{Sp}	N^{H}_{Lyc}	N^{He}_{Lyc}	Sp
1	0.7301	3.603	-2.61	-0.92	-0.25	-0.79	-0.18	-0.07	0.00	45.77	42.63	B2V
2	13.6010	3.756	-2.49	-0.89	-0.25	-0.77	-0.17	-0.07	0.00	45.42	42.06	B2V
3	20.8916	3.873	-2.35	-0.84	-0.24	-0.74	-0.17	-0.07	0.00	45.00	41.37	B3V
4	24.9419	3.949	-2.03	-0.91	-0.24	-0.74	-0.17	-0.07	0.00	46.01	42.56	B2IV
5	28.0809	4.015	-1.85	-0.86	-0.23	-0.70	-0.17	-0.07	0.00	45.47	41.62	B3III
6	28.6125	4.048	-2.05	-0.92	-0.24	-0.74	-0.17	-0.07	0.00	46.03	42.60	B2IV
7	28.6985	4.079	-2.19	-0.94	-0.25	-0.77	-0.17	-0.07	0.00	46.18	42.96	B2IV
8	28.7123	4.065	-2.07	-0.92	-0.24	-0.75	-0.17	-0.07	0.00	46.07	42.69	B2IV
9	28.7402	4.093	-1.00	-0.74	-0.11	-0.26	-0.03	0.01	0.00	44.13	37.74	B5I?
10	28.7532	4.069	-0.44	-0.41	-0.01	0.09	0.08	0.05	0.00	41.14	30.82	A0I?
11	28.7604	4.026	-0.03	0.26	0.31	0.91	0.23	0.12	0.00	0.00	0.00	F5I
12	28.7631	3.992	-0.15	0.52	0.77	1.45	0.38	0.18	0.00	0.00	0.00	G2I
13	28.7655	3.910	-0.58	1.30	1.34	2.35	0.66	0.52	0.15	0.00	0.00	K2I
14	28.7663	3.876	-0.70	1.52	1.43	2.77	0.69	0.58	0.19	0.00	0.00	K3II
15	28.7991	4.321	-1.59	1.94	1.71	4.08	0.87	0.66	0.39	0.00	0.00	M2II
16	29.0837	4.264	-1.45	1.91	1.70	3.95	0.85	0.66	0.37	0.00	0.00	M2II
17	29.2705	4.224	-1.37	1.90	1.69	3.90	0.85	0.66	0.36	0.00	0.00	M1II
18	29.5215	4.175	-1.31	1.91	1.68	3.84	0.84	0.67	0.33	0.00	0.00	M1II
19	30.0669	4.127	-1.12	1.81	1.61	3.54	0.75	0.61	0.30	0.00	0.00	K7II
20	30.0925	4.128	-1.11	1.81	1.61	3.54	0.75	0.61	0.30	0.00	0.00	K7II
21	30.1693	4.145	-1.00	1.79	1.59	3.47	0.75	0.61	0.27	0.00	0.00	K5I
22	30.2035	4.176	-0.75	1.60	1.46	2.89	0.70	0.59	0.21	0.00	0.00	K3I
23	30.2163	4.190	-0.48	1.14	1.22	2.11	0.61	0.43	0.10	0.00	0.00	K0I
24	30.2805	4.207	-0.08	0.39	0.52	1.17	0.32	0.16	0.00	0.00	0.00	F8I
25	30.4156	4.222	-0.01	0.21	0.26	0.81	0.20	0.10	0.00	0.00	0.00	F5I?
26	30.6307	4.246	-0.33	-0.30	0.02	0.15	0.09	0.05	0.00	40.31	29.23	A1I?
27	30.9072	4.260	-0.47	-0.44	-0.02	0.07	0.07	0.05	0.00	41.29	31.12	A0I?
28	31.5993	4.282	-0.38	-0.35	0.00	0.11	0.08	0.05	0.00	40.75	30.07	A1I?
29	32.2453	4.298	-0.38	-0.35	0.00	0.11	0.08	0.05	0.00	40.75	30.07	A1I?
30	32.6257	4.302	0.00	0.16	0.19	0.68	0.18	0.09	0.00	0.00	0.00	F2I
31	33.0151	4.305	-0.07	0.37	0.48	1.13	0.31	0.15	0.00	0.00	0.00	F8I
32	33.0947	4.294	-0.30	0.75	0.98	1.90	0.46	0.20	-0.01	0.00	0.00	G5I
33	33.1212	4.287	-0.56	1.28	1.32	2.30	0.65	0.50	0.14	0.00	0.00	K2I
34	33.1522	4.247	-1.13	1.82	1.61	3.55	0.76	0.61	0.31	0.00	0.00	K7I
35	33.2606	4.282	-1.37	1.90	1.69	3.90	0.85	0.66	0.36	0.00	0.00	M1I
36	33.3071	4.339	-1.59	1.94	1.71	4.08	0.87	0.66	0.39	0.00	0.00	M2I
37	33.3263	4.493	-1.94	1.95	1.70	4.38	0.89	0.66	0.43	0.00	0.00	M3I
38	33.3601	4.640	-2.19	1.96	1.69	4.68	0.91	0.67	0.47	0.00	0.00	M4I
39	33.3626	4.639	-2.21	1.97	1.69	4.71	0.91	0.68	0.47	0.00	0.00	M4I
40	33.3643	4.639	-2.24	1.98	1.70	4.75	0.91	0.68	0.47	0.00	0.00	M4I

Table B.16
Star Model with an Initial Mass of 7.00 $M_{\odot}$

#	Age	$\log L$	BC	U-B	B-V	V-K	J-K	J-H	CO_{Sp}	N^{H}_{Lyc}	N^{He}_{Lyc}	Sp
1	1.0301	3.235	-2.29	-0.82	-0.23	-0.72	-0.17	-0.07	0.00	44.83	41.09	B3V
2	22.7217	3.381	-2.15	-0.78	-0.22	-0.68	-0.16	-0.07	0.00	44.46	40.48	B3V
3	34.9626	3.498	-1.85	-0.86	-0.23	-0.70	-0.17	-0.07	0.00	45.47	41.62	B3IV
4	41.0831	3.569	-1.68	-0.78	-0.21	-0.64	-0.16	-0.06	0.00	44.73	40.40	B3IV
5	45.1874	3.619	-1.54	-0.71	-0.19	-0.58	-0.14	-0.06	0.00	44.11	39.44	B5III
6	47.0624	3.664	-1.71	-0.79	-0.21	-0.65	-0.16	-0.06	0.00	44.85	40.60	B3IV
7	47.2741	3.697	-1.85	-0.86	-0.23	-0.70	-0.17	-0.07	0.00	45.47	41.62	B3IV
8	47.3028	3.690	-1.79	-0.83	-0.22	-0.68	-0.16	-0.07	0.00	45.22	41.20	B3IV
9	47.3535	3.718	-0.93	-0.71	-0.09	-0.20	-0.01	0.01	0.00	43.76	36.98	B6I?
10	47.3866	3.687	-0.40	-0.36	-0.01	0.10	0.08	0.05	0.00	40.83	30.24	A1I?
11	47.4042	3.636	-0.02	0.26	0.31	0.90	0.23	0.11	0.00	0.00	0.00	F5I?
12	47.4108	3.603	-0.13	0.49	0.71	1.37	0.36	0.17	0.00	0.00	0.00	G0I
13	47.4152	3.564	-0.37	0.94	1.07	1.97	0.51	0.27	0.02	0.00	0.00	G8II
14	47.4197	3.509	-0.59	1.30	1.34	2.37	0.66	0.52	0.15	0.00	0.00	K2II
15	47.5229	3.965	-1.32	1.91	1.68	3.86	0.85	0.67	0.34	0.00	0.00	M1II
16	48.0133	3.909	-1.24	1.86	1.64	3.69	0.80	0.64	0.32	0.00	0.00	M0II
17	48.5216	3.837	-1.08	1.81	1.61	3.54	0.75	0.61	0.29	0.00	0.00	K7II
18	48.8327	3.795	-1.02	1.81	1.60	3.52	0.75	0.61	0.27	0.00	0.00	K7II
19	49.6012	3.743	-0.85	1.67	1.51	3.09	0.72	0.60	0.24	0.00	0.00	K4II
20	49.7659	3.749	-0.81	1.65	1.49	3.01	0.71	0.59	0.23	0.00	0.00	K4II
21	49.8757	3.760	-0.74	1.58	1.45	2.87	0.70	0.59	0.21	0.00	0.00	K3II
22	49.9443	3.779	-0.64	1.37	1.38	2.55	0.68	0.56	0.17	0.00	0.00	K3II
23	50.0266	3.807	-0.40	1.03	1.11	1.97	0.54	0.33	0.04	0.00	0.00	G8I
24	50.2325	3.835	-0.10	0.44	0.62	1.27	0.34	0.16	0.00	0.00	0.00	G0I
25	50.4520	3.859	-0.02	0.25	0.30	0.89	0.23	0.11	0.00	0.00	0.00	F5I?
26	50.6716	3.878	-0.03	0.13	0.14	0.55	0.14	0.07	0.00	0.00	0.00	F0I?
27	50.8637	3.886	-0.05	0.03	0.13	0.49	0.15	0.08	0.00	37.78	25.17	A8I?
28	52.9691	3.940	-0.01	0.15	0.18	0.67	0.18	0.09	0.00	0.00	0.00	F2I?
29	55.4558	3.997	-0.01	0.21	0.26	0.81	0.20	0.10	0.00	0.00	0.00	F5I?
30	55.9054	4.000	-0.11	0.45	0.65	1.30	0.35	0.16	0.00	0.00	0.00	G0I
31	56.2869	3.998	-0.19	0.60	0.85	1.61	0.42	0.21	0.00	0.00	0.00	G2I
32	56.3625	3.997	-0.38	0.99	1.09	1.97	0.53	0.30	0.03	0.00	0.00	G8I
33	56.4488	3.988	-0.63	1.34	1.37	2.50	0.67	0.55	0.17	0.00	0.00	K3I
34	56.6754	3.969	-1.11	1.81	1.61	3.54	0.75	0.61	0.30	0.00	0.00	K7II
35	56.8804	4.011	-1.28	1.89	1.67	3.78	0.82	0.66	0.33	0.00	0.00	M0II
36	56.9802	4.060	-1.34	1.91	1.69	3.88	0.85	0.67	0.34	0.00	0.00	M1II
37	57.0049	4.202	-1.64	1.95	1.71	4.12	0.87	0.66	0.39	0.00	0.00	M3II
38	57.0833	4.415	-2.09	1.95	1.69	4.55	0.90	0.67	0.45	0.00	0.00	M3I
39	57.0863	4.374	-2.13	1.95	1.69	4.60	0.90	0.67	0.46	0.00	0.00	M4II

Table B.17
Star Model with an Initial Mass of 5.00 $M_{\odot}$

#	Age	log L	BC	U-B	B-V	V-K	J-K	J-H	CO_{Sp}	N^{H}_{Lyc}	N^{He}_{Lyc}	Sp
1	1.2500	2.720	-1.78	-0.67	-0.19	-0.56	-0.14	-0.06	0.00	43.34	38.73	B5V
2	48.9990	2.851	-1.64	-0.63	-0.18	-0.52	-0.12	-0.06	0.00	42.87	37.98	B5V
3	75.6450	2.958	-1.46	-0.58	-0.17	-0.47	-0.11	-0.05	0.00	42.26	36.90	B5V
4	88.6760	3.019	-1.17	-0.52	-0.15	-0.42	-0.10	-0.04	0.00	42.87	37.38	B6III
5	96.3650	3.065	-0.94	-0.72	-0.10	-0.21	-0.02	0.01	0.00	43.82	37.09	B6II
6	98.4220	3.110	-1.19	-0.53	-0.16	-0.43	-0.10	-0.04	0.00	42.95	37.52	B6III
7	98.8100	3.156	-1.39	-0.62	-0.18	-0.51	-0.12	-0.05	0.00	43.55	38.54	B5IV
8	98.8420	3.130	-1.30	-0.58	-0.17	-0.47	-0.11	-0.05	0.00	43.28	38.09	B6IV
9	98.9770	3.166	-0.69	-0.56	-0.03	-0.04	0.05	0.04	0.00	42.64	34.02	B8I?
10	99.0740	3.131	-0.23	-0.16	0.05	0.26	0.12	0.07	0.00	39.44	27.99	A3I?
11	99.1220	3.084	0.00	0.19	0.24	0.78	0.19	0.09	0.00	0.00	0.00	F5I?
12	99.1580	3.023	-0.12	0.46	0.66	1.31	0.35	0.16	0.00	0.00	0.00	G0II
13	99.1760	2.979	-0.24	0.67	0.91	1.77	0.44	0.20	0.00	0.00	0.00	G5II
14	99.2010	2.924	-0.42	1.07	1.14	1.99	0.56	0.36	0.06	0.00	0.00	K0II
15	99.4970	3.454	-0.99	1.78	1.59	3.45	0.75	0.61	0.26	0.00	0.00	K5II
16	101.0550	3.361	-0.84	1.67	1.50	3.07	0.72	0.60	0.24	0.00	0.00	K4II
17	101.7250	3.304	-0.78	1.63	1.47	2.96	0.70	0.59	0.22	0.00	0.00	K4II
18	102.8980	3.218	-0.68	1.48	1.42	2.71	0.69	0.58	0.19	0.00	0.00	K3II
19	104.4570	3.160	-0.59	1.31	1.35	2.39	0.66	0.53	0.15	0.00	0.00	K2II
20	104.7750	3.157	-0.58	1.30	1.34	2.35	0.66	0.52	0.15	0.00	0.00	K2II
21	105.1320	3.159	-0.56	1.28	1.32	2.28	0.65	0.50	0.14	0.00	0.00	K1II
22	105.4000	3.168	-0.53	1.23	1.29	2.22	0.64	0.47	0.13	0.00	0.00	K1II
23	105.4900	3.171	-0.52	1.20	1.27	2.19	0.63	0.46	0.12	0.00	0.00	K1II
24	105.6680	3.178	-0.49	1.15	1.24	2.14	0.61	0.44	0.10	0.00	0.00	K0II
25	105.8470	3.187	-0.47	1.12	1.21	2.09	0.60	0.42	0.09	0.00	0.00	K0II
26	106.0250	3.196	-0.45	1.10	1.18	2.05	0.59	0.40	0.08	0.00	0.00	K0II
27	107.2590	3.272	-0.16	0.53	0.78	1.47	0.39	0.19	0.00	0.00	0.00	G2II
28	114.1190	3.355	-0.31	0.79	1.00	1.93	0.47	0.21	0.00	0.00	0.00	G5II
29	121.8660	3.451	-0.39	1.01	1.10	1.97	0.53	0.31	0.04	0.00	0.00	G8II
30	121.9800	3.450	-0.42	1.06	1.13	1.98	0.56	0.35	0.06	0.00	0.00	G8II
31	122.6690	3.458	-0.42	1.07	1.14	1.99	0.56	0.36	0.06	0.00	0.00	K0II
32	123.4610	3.460	-0.47	1.12	1.21	2.09	0.60	0.42	0.09	0.00	0.00	K0II
33	124.2980	3.453	-0.63	1.36	1.38	2.52	0.68	0.55	0.17	0.00	0.00	K3II
34	124.9960	3.455	-0.76	1.61	1.46	2.91	0.70	0.59	0.21	0.00	0.00	K4II
35	125.5420	3.486	-0.86	1.68	1.51	3.12	0.72	0.60	0.24	0.00	0.00	K4II
36	125.9880	3.553	-1.01	1.80	1.60	3.49	0.75	0.61	0.27	0.00	0.00	K5II
37	126.1790	3.852	-1.53	1.93	1.70	4.02	0.86	0.66	0.38	0.00	0.00	M2II
38	126.3460	4.102	-2.05	1.94	1.69	4.50	0.89	0.67	0.45	0.00	0.00	M3II
39	126.3560	4.152	-1.86	1.96	1.71	4.31	0.89	0.66	0.42	0.00	0.00	M3II
40	126.3570	4.130	-1.85	1.96	1.71	4.30	0.88	0.66	0.42	0.00	0.00	M3II

Table B.18
Star Model with an Initial Mass of 4.00 $M_{\odot}$

#	Age	$\log L$	BC	U-B	B-V	V-K	J-K	J-H	CO_{Sp}	N^{H}_{Lyc}	N^{He}_{Lyc}	Sp
1	2.3000	2.366	-1.43	-0.57	-0.17	-0.46	-0.11	-0.05	0.00	42.14	36.67	B6V
2	87.2710	2.487	-1.27	-0.52	-0.16	-0.42	-0.10	-0.04	0.00	41.62	35.63	B6V
3	133.3250	2.583	-1.08	-0.45	-0.14	-0.37	-0.09	-0.04	0.00	41.01	34.53	B7V
4	156.1370	2.638	-0.81	-0.36	-0.11	-0.23	-0.06	-0.03	0.00	41.66	34.99	B9III
5	169.6260	2.677	-0.71	-0.58	-0.04	-0.06	0.04	0.03	0.00	42.80	34.36	B8II
6	173.3850	2.726	-0.82	-0.37	-0.11	-0.24	-0.06	-0.03	0.00	41.69	35.07	B9III
7	173.9740	2.777	-1.01	-0.46	-0.13	-0.37	-0.09	-0.04	0.00	42.32	36.33	B7IV
8	173.9930	2.763	-0.98	-0.44	-0.13	-0.35	-0.09	-0.04	0.00	42.23	36.14	B7IV
9	174.2030	2.782	-0.59	-0.53	-0.02	0.00	0.05	0.04	0.00	42.01	32.60	B9I?
10	174.3990	2.762	-0.25	-0.21	0.04	0.25	0.12	0.07	0.00	39.73	28.33	A3I?
11	174.5660	2.697	-0.01	0.23	0.28	0.86	0.22	0.10	0.00	0.00	0.00	F5I?
12	174.6500	2.629	-0.11	0.45	0.65	1.30	0.35	0.16	0.00	0.00	0.00	G0II
13	174.7050	2.560	-0.22	0.65	0.89	1.71	0.44	0.21	0.00	0.00	0.00	G5II
14	174.7750	2.516	-0.37	0.94	1.07	1.97	0.51	0.27	0.02	0.00	0.00	G8II
15	175.3930	3.103	-0.79	1.64	1.48	2.98	0.71	0.59	0.22	0.00	0.00	K4II
16	178.0120	2.992	-0.66	1.42	1.40	2.63	0.68	0.57	0.18	0.00	0.00	K3II
17	180.0110	2.879	-0.59	1.30	1.34	2.37	0.66	0.52	0.15	0.00	0.00	K2II
18	183.0210	2.756	-0.49	1.15	1.24	2.14	0.61	0.44	0.10	0.00	0.00	K0II
19	184.1150	2.740	-0.46	1.12	1.20	2.08	0.60	0.42	0.09	0.00	0.00	K0II
20	184.6620	2.737	-0.46	1.11	1.19	2.06	0.59	0.41	0.08	0.00	0.00	K0II
21	185.0730	2.737	-0.45	1.10	1.18	2.04	0.58	0.40	0.08	0.00	0.00	K0II
22	185.4830	2.740	-0.44	1.09	1.17	2.02	0.58	0.39	0.07	0.00	0.00	K0II
23	189.2280	2.800	-0.37	0.94	1.07	1.97	0.51	0.27	0.02	0.00	0.00	G8II
24	191.8870	2.822	-0.37	0.94	1.07	1.97	0.51	0.27	0.02	0.00	0.00	G8II
25	194.5980	2.845	-0.37	0.93	1.07	1.97	0.51	0.27	0.02	0.00	0.00	G8II
26	198.4600	2.873	-0.37	0.94	1.07	1.97	0.51	0.27	0.02	0.00	0.00	G8II
27	202.4780	2.900	-0.37	0.95	1.08	1.97	0.51	0.28	0.02	0.00	0.00	G8II
28	208.3430	2.924	-0.41	1.05	1.13	1.98	0.55	0.35	0.05	0.00	0.00	G8II
29	212.1550	2.928	-0.47	1.13	1.22	2.10	0.60	0.43	0.10	0.00	0.00	K0II
30	212.6830	2.929	-0.49	1.15	1.24	2.14	0.61	0.44	0.10	0.00	0.00	K0II
31	213.2110	2.932	-0.51	1.19	1.26	2.18	0.62	0.46	0.11	0.00	0.00	K1II
32	213.9140	2.941	-0.54	1.24	1.29	2.24	0.64	0.48	0.13	0.00	0.00	K1II
35	215.1460	2.992	-0.61	1.32	1.36	2.43	0.67	0.54	0.16	0.00	0.00	K2II
36	216.0710	3.051	-0.67	1.44	1.41	2.66	0.68	0.57	0.18	0.00	0.00	K3II
37	216.6050	3.353	-1.03	1.81	1.61	3.53	0.75	0.61	0.28	0.00	0.00	K7II
38	217.0660	3.645	-1.35	1.90	1.69	3.89	0.85	0.66	0.35	0.00	0.00	M1II
39	217.3450	3.851	-1.05	1.81	1.61	3.54	0.75	0.61	0.28	0.00	0.00	K7II

Table B.19
Star Model with an Initial Mass of 3.00 $M_{\odot}$

#	Age	log L	BC	U-B	B-V	V-K	J-K	J-H	CO_{Sp}	N^{H}_{Lyc}	N^{He}_{Lyc}	Sp
1	4.9250	1.886	-0.91	-0.39	-0.12	-0.30	-0.08	-0.04	0.00	40.41	33.33	B8V
2	200.6710	2.002	-0.77	-0.33	-0.11	-0.23	-0.06	-0.03	0.00	39.91	32.28	B9V
3	305.3290	2.086	-0.59	-0.25	-0.08	-0.16	-0.05	-0.03	0.00	39.21	30.99	B9V
4	356.3390	2.128	-0.47	-0.44	-0.02	0.07	0.07	0.05	0.00	41.29	31.12	A0I?
5	388.8830	2.163	-0.36	-0.33	0.01	0.11	0.08	0.05	0.00	40.57	29.72	A1I
6	396.5820	2.212	-0.47	-0.45	-0.02	0.06	0.07	0.04	0.00	41.34	31.21	A0I?
7	398.5070	2.273	-0.69	-0.19	-0.07	-0.13	-0.05	-0.03	0.00	40.62	32.87	A0III
8	398.8030	2.251	-0.47	-0.45	-0.02	0.06	0.07	0.04	0.00	41.34	31.21	A0I?
9	399.1730	2.269	-0.27	-0.24	0.03	0.23	0.11	0.06	0.00	39.90	28.56	A3I
10	399.6920	2.251	-0.03	0.13	0.14	0.55	0.14	0.07	0.00	0.00	0.00	F0I
11	400.0620	2.217	-0.02	0.24	0.29	0.88	0.22	0.11	0.00	0.00	0.00	F5I
12	400.4320	2.149	-0.10	0.43	0.61	1.26	0.34	0.16	0.00	0.00	0.00	G0II
13	400.6540	2.072	-0.28	0.41	0.78	1.82	0.45	0.23	0.02	0.00	0.00	G5III
14	400.9500	1.970	-0.39	0.66	0.92	2.12	0.54	0.49	0.06	0.00	0.00	G8III
15	403.0450	2.714	-0.65	1.39	1.39	2.57	0.68	0.56	0.17	0.00	0.00	K3II
16	406.0490	2.501	-0.64	1.21	1.19	2.66	0.68	0.57	0.13	0.00	0.00	K3III
17	409.0740	2.248	-0.55	1.02	1.07	2.48	0.63	0.54	0.09	0.00	0.00	K2III
18	411.9920	2.131	-0.50	0.85	1.00	2.36	0.59	0.51	0.07	0.00	0.00	K1III
19	415.4660	2.098	-0.46	0.76	0.97	2.24	0.57	0.49	0.06	0.00	0.00	K0III
20	425.4970	2.122	-0.46	0.76	0.97	2.24	0.57	0.49	0.06	0.00	0.00	K0III
21	435.4880	2.148	-0.46	0.76	0.97	2.24	0.57	0.49	0.06	0.00	0.00	K0III
22	446.9760	2.179	-0.46	0.77	0.97	2.25	0.57	0.50	0.06	0.00	0.00	K0III
23	455.1460	2.200	-0.46	0.77	0.97	2.25	0.57	0.50	0.06	0.00	0.00	K0III
24	474.0380	2.250	-0.48	0.79	0.98	2.29	0.58	0.50	0.07	0.00	0.00	K0III
25	493.9520	2.300	-0.50	0.84	1.00	2.35	0.59	0.51	0.07	0.00	0.00	K0III
26	510.6050	2.350	-0.54	0.96	1.05	2.45	0.62	0.53	0.08	0.00	0.00	K1III
27	514.5750	2.402	-0.56	1.05	1.09	2.50	0.64	0.54	0.10	0.00	0.00	K2III
28	514.9720	2.412	-0.57	1.06	1.10	2.50	0.64	0.55	0.10	0.00	0.00	K2III
29	526.4990	2.467	-0.58	1.10	1.12	2.53	0.65	0.55	0.11	0.00	0.00	K2III
30	526.6200	2.478	-0.59	1.11	1.13	2.53	0.65	0.55	0.11	0.00	0.00	K2III
31	526.7420	2.490	-0.59	1.12	1.13	2.54	0.65	0.55	0.11	0.00	0.00	K2III
32	526.8630	2.501	-0.60	1.14	1.15	2.56	0.65	0.56	0.12	0.00	0.00	K2III
35	527.2880	2.558	-0.63	1.19	1.18	2.65	0.67	0.57	0.13	0.00	0.00	K3III
36	527.7590	2.565	-0.63	1.19	1.18	2.65	0.67	0.57	0.13	0.00	0.00	K3III
37	529.3760	2.805	-0.68	1.46	1.41	2.68	0.69	0.57	0.18	0.00	0.00	K3II
38	530.3480	3.025	-0.90	1.70	1.53	3.19	0.73	0.60	0.25	0.00	0.00	K4II
39	532.1680	3.529	-1.57	1.94	1.71	4.06	0.87	0.66	0.39	0.00	0.00	M2II
40	535.2880	3.955	-2.41	2.02	1.72	4.95	0.93	0.69	0.49	0.00	0.00	M4II

Table B.20
Star Model with an Initial Mass of 2.50 $M_{\odot}$

#	Age	$\log L$	BC	U-B	B-V	V-K	J-K	J-H	CO_{Sp}	N^{H}_{Lyc}	N^{He}_{Lyc}	Sp
1	13.9600	1.572	-0.58	-0.25	-0.08	-0.16	-0.05	-0.03	0.00	39.16	30.90	B9V
2	396.4160	1.687	-0.47	-0.17	-0.06	-0.13	-0.05	-0.03	0.00	38.59	29.68	A0V
3	580.2480	1.764	-0.30	-0.02	-0.02	-0.03	-0.02	-0.01	0.00	37.45	27.71	A1V
4	665.6170	1.800	-0.18	0.08	0.07	0.18	0.03	0.00	0.00	36.84	26.13	A3III
5	717.8360	1.826	-0.07	-0.02	0.12	0.46	0.15	0.08	0.00	38.01	25.72	A7II
6	730.9460	1.886	-0.18	0.07	0.06	0.16	0.03	0.00	0.00	37.06	26.28	A3III
7	732.8660	1.949	-0.37	-0.34	0.00	0.11	0.08	0.05	0.00	40.66	29.89	A1II
8	733.5860	1.932	-0.14	-0.09	0.09	0.35	0.13	0.07	0.00	38.75	27.18	A5II
9	734.4500	1.929	0.00	0.16	0.19	0.67	0.18	0.09	0.00	0.00	0.00	F2II
10	735.1030	1.910	-0.02	0.26	0.31	0.90	0.23	0.11	0.00	0.00	0.00	F5II
11	736.1780	1.842	-0.19	0.18	0.63	1.55	0.38	0.18	0.00	0.00	0.00	G0III
12	736.9460	1.734	-0.29	0.43	0.79	1.86	0.46	0.27	0.02	0.00	0.00	G5III
13	737.2530	1.676	-0.33	0.54	0.85	2.06	0.51	0.44	0.04	0.00	0.00	G5III
14	737.5450	1.649	-0.37	0.61	0.89	2.11	0.53	0.50	0.05	0.00	0.00	G8III
15	743.3030	2.543	-0.74	1.37	1.26	2.91	0.73	0.62	0.15	0.00	0.00	K3III
16	744.3790	2.364	-0.64	1.21	1.19	2.66	0.68	0.57	0.13	0.00	0.00	K3III
17	747.0370	2.146	-0.57	1.07	1.10	2.51	0.64	0.55	0.10	0.00	0.00	K2III
18	754.2060	1.798	-0.46	0.76	0.97	2.24	0.57	0.49	0.06	0.00	0.00	K0III
19	757.7910	1.769	-0.43	0.72	0.95	2.18	0.56	0.49	0.06	0.00	0.00	K0III
20	815.9800	1.858	-0.44	0.74	0.96	2.21	0.56	0.49	0.06	0.00	0.00	K0III
21	835.7860	1.890	-0.45	0.75	0.96	2.22	0.56	0.49	0.06	0.00	0.00	K0III
22	884.0740	1.982	-0.48	0.80	0.98	2.30	0.58	0.50	0.07	0.00	0.00	K0III
23	896.5070	2.000	-0.48	0.79	0.98	2.29	0.58	0.50	0.07	0.00	0.00	K0III
24	909.0850	2.021	-0.48	0.79	0.98	2.29	0.58	0.50	0.07	0.00	0.00	K0III
25	925.5660	2.050	-0.49	0.81	0.99	2.32	0.58	0.50	0.07	0.00	0.00	K0III
26	939.1560	2.079	-0.50	0.84	1.00	2.35	0.59	0.51	0.07	0.00	0.00	K0III
27	947.8310	2.112	-0.52	0.90	1.02	2.41	0.61	0.52	0.08	0.00	0.00	K1III
28	957.6620	2.136	-0.53	0.92	1.03	2.43	0.61	0.53	0.08	0.00	0.00	K1III
29	960.6980	2.165	-0.54	0.97	1.05	2.46	0.62	0.53	0.08	0.00	0.00	K1III
30	964.0230	2.197	-0.55	1.02	1.07	2.48	0.63	0.54	0.09	0.00	0.00	K2III
31	965.0350	2.232	-0.56	1.05	1.09	2.50	0.64	0.55	0.10	0.00	0.00	K2III
32	965.3240	2.244	-0.57	1.06	1.10	2.50	0.64	0.55	0.10	0.00	0.00	K2III
33	965.7580	2.266	-0.57	1.08	1.11	2.51	0.64	0.55	0.10	0.00	0.00	K2III
34	966.1910	2.293	-0.58	1.10	1.12	2.53	0.65	0.55	0.11	0.00	0.00	K2III
35	966.6250	2.330	-0.59	1.13	1.14	2.55	0.65	0.55	0.11	0.00	0.00	K2III
36	967.7820	2.425	-0.62	1.18	1.17	2.63	0.67	0.57	0.12	0.00	0.00	K3III
37	970.2390	2.474	-0.65	1.23	1.20	2.70	0.68	0.58	0.13	0.00	0.00	K3III

Table B.21
Star Model with an Initial Mass of 2.00 $M_{\odot}$

#	Age	log L	BC	U-B	B-V	V-K	J-K	J-H	CO_{Sp}	N^{H}_{Lyc}	N^{He}_{Lyc}	Sp
1	105.4000	1.177	-0.20	0.05	0.05	0.14	0.02	0.00	0.00	36.31	26.32	A3V
2	974.2500	1.290	-0.17	0.08	0.08	0.21	0.04	0.01	0.00	35.60	25.55	A5V
3	1374.3199	1.364	-0.14	0.11	0.15	0.37	0.08	0.03	0.00	35.39	23.59	A7IV
4	1551.4100	1.395	-0.10	0.10	0.26	0.61	0.14	0.07	0.00	0.00	0.00	F0III
5	1647.8000	1.415	-0.11	0.08	0.34	0.90	0.22	0.11	0.00	0.00	0.00	F2III
6	1673.7300	1.482	-0.10	0.10	0.25	0.55	0.12	0.06	0.00	0.00	0.00	A8III
7	1677.2500	1.543	-0.14	0.11	0.16	0.37	0.08	0.03	0.00	35.35	23.49	A7III
8	1679.8800	1.535	-0.01	0.23	0.28	0.85	0.21	0.10	0.00	0.00	0.00	F5II
9	1681.6400	1.525	-0.06	0.34	0.43	1.07	0.29	0.15	0.00	0.00	0.00	F8II
10	1683.3900	1.503	-0.16	0.11	0.56	1.41	0.35	0.17	0.00	0.00	0.00	G0III
11	1685.1500	1.465	-0.21	0.24	0.67	1.61	0.40	0.17	0.00	0.00	0.00	G2III
12	1686.5601	1.415	-0.25	0.34	0.74	1.71	0.42	0.16	0.01	0.00	0.00	G2III
13	1688.2400	1.327	-0.31	0.50	0.83	1.99	0.49	0.38	0.03	0.00	0.00	G5III
14	1689.8199	1.283	-0.36	0.61	0.89	2.11	0.53	0.50	0.05	0.00	0.00	G8III
15	1710.2300	2.437	-0.79	1.43	1.27	2.89	0.74	0.62	0.16	0.00	0.00	K4III
16	1710.9900	2.118	-0.62	1.18	1.17	2.63	0.67	0.57	0.12	0.00	0.00	K3III
17	1711.1400	1.800	-0.55	1.00	1.06	2.47	0.63	0.54	0.09	0.00	0.00	K1III
18	1712.0000	1.561	-0.48	0.80	0.98	2.30	0.58	0.50	0.07	0.00	0.00	K0III
19	1753.1000	1.498	-0.44	0.74	0.96	2.21	0.56	0.49	0.06	0.00	0.00	K0III
20	1758.7200	1.501	-0.44	0.74	0.96	2.21	0.56	0.49	0.06	0.00	0.00	K0III
21	1771.4399	1.503	-0.44	0.73	0.95	2.20	0.56	0.49	0.06	0.00	0.00	K0III
22	1786.5200	1.506	-0.44	0.73	0.95	2.20	0.56	0.49	0.06	0.00	0.00	K0III
23	1798.9700	1.511	-0.44	0.73	0.95	2.20	0.56	0.49	0.06	0.00	0.00	K0III
24	1832.3300	1.532	-0.43	0.72	0.95	2.18	0.56	0.49	0.06	0.00	0.00	K0III
25	1867.3700	1.562	-0.44	0.73	0.95	2.20	0.56	0.49	0.06	0.00	0.00	K0III
26	1961.2800	1.659	-0.46	0.77	0.97	2.25	0.57	0.50	0.06	0.00	0.00	K0III
27	1976.9100	1.705	-0.48	0.80	0.98	2.30	0.58	0.50	0.07	0.00	0.00	K0III
28	1996.7300	1.733	-0.49	0.81	0.99	2.32	0.58	0.50	0.07	0.00	0.00	K0III
29	1999.9399	1.766	-0.50	0.84	1.00	2.35	0.59	0.51	0.07	0.00	0.00	K0III
30	2002.2300	1.803	-0.52	0.90	1.02	2.41	0.61	0.52	0.08	0.00	0.00	K1III
31	2003.5200	1.833	-0.53	0.94	1.04	2.44	0.61	0.53	0.08	0.00	0.00	K1III
32	2004.2700	1.866	-0.54	0.97	1.05	2.46	0.62	0.53	0.08	0.00	0.00	K1III
33	2004.8700	1.902	-0.55	1.00	1.06	2.47	0.63	0.54	0.09	0.00	0.00	K1III
34	2005.2200	1.933	-0.55	1.03	1.08	2.49	0.63	0.54	0.09	0.00	0.00	K2III
35	2005.6600	1.985	-0.56	1.05	1.09	2.50	0.64	0.55	0.10	0.00	0.00	K2III
36	2006.5699	2.067	-0.59	1.11	1.13	2.53	0.65	0.55	0.11	0.00	0.00	K2III
37	2023.3400	2.367	-0.72	1.34	1.25	2.88	0.73	0.61	0.14	0.00	0.00	K3III
38	2027.4301	2.675	-0.93	1.63	1.37	3.17	0.80	0.67	0.18	0.00	0.00	K4III
39	2029.2800	2.976	-1.43	1.88	1.58	3.89	0.93	0.76	0.23	0.00	0.00	M1III
40	2030.7400	3.377	-2.51	1.54	1.62	6.31	1.13	0.86	0.32	0.00	0.00	M6III

Table B.22
Star Model with an Initial Mass of 1.70 $M_{\odot}$

#	Age	log L	BC	U-B	B-V	V-K	J-K	J-H	CO_{Sp}	N^{H}_{Lyc}	N^{He}_{Lyc}	Sp
1	35.0000	0.858	-0.10	0.10	0.24	0.53	0.12	0.05	0.00	0.00	0.00	A8V
2	2012.2400	0.997	-0.10	0.09	0.25	0.56	0.13	0.06	0.00	0.00	0.00	A8V
3	2774.3899	1.075	-0.11	0.08	0.30	0.80	0.19	0.09	0.00	0.00	0.00	F2IV
4	3073.4399	1.102	-0.13	0.09	0.40	1.00	0.24	0.11	0.00	0.00	0.00	F5III
5	3231.1299	1.121	-0.15	0.09	0.49	1.22	0.30	0.14	0.00	0.00	0.00	F8III
6	3271.2400	1.201	-0.12	0.09	0.38	0.97	0.24	0.11	0.00	0.00	0.00	F5III
7	3275.4800	1.261	-0.11	0.08	0.31	0.81	0.20	0.09	0.00	0.00	0.00	F2III
8	3278.6499	1.244	-0.14	0.09	0.43	1.08	0.26	0.12	0.00	0.00	0.00	F8III
9	3282.8799	1.233	-0.18	0.14	0.59	1.48	0.37	0.18	0.00	0.00	0.00	G0III
10	3289.2300	1.189	-0.23	0.29	0.71	1.65	0.41	0.16	0.01	0.00	0.00	G2III
11	3293.4700	1.129	-0.28	0.41	0.78	1.81	0.45	0.22	0.02	0.00	0.00	G5III
12	3296.6399	1.073	-0.32	0.51	0.83	2.00	0.50	0.39	0.03	0.00	0.00	G5III
13	3297.7000	1.057	-0.33	0.53	0.84	2.05	0.51	0.43	0.04	0.00	0.00	G5IV
14	3300.8799	1.036	-0.37	0.61	0.89	2.11	0.53	0.50	0.05	0.00	0.00	G8IV
15	3308.2800	1.139	-0.43	0.71	0.94	2.17	0.55	0.49	0.06	0.00	0.00	K0III
16	3312.5200	1.232	-0.46	0.77	0.97	2.25	0.57	0.50	0.06	0.00	0.00	K0III
17	3316.7500	1.327	-0.49	0.81	0.99	2.32	0.58	0.50	0.07	0.00	0.00	K0III
18	3320.9800	1.426	-0.51	0.87	1.01	2.38	0.60	0.52	0.07	0.00	0.00	K1III
19	3325.2200	1.528	-0.53	0.92	1.03	2.43	0.61	0.53	0.08	0.00	0.00	K1III
20	3329.4500	1.629	-0.55	1.00	1.06	2.47	0.63	0.54	0.09	0.00	0.00	K1III
21	3333.6799	1.733	-0.56	1.05	1.09	2.50	0.64	0.55	0.10	0.00	0.00	K2III
22	3336.8601	1.836	-0.59	1.11	1.13	2.53	0.65	0.55	0.11	0.00	0.00	K2III
23	3340.5601	1.934	-0.62	1.17	1.17	2.61	0.66	0.56	0.12	0.00	0.00	K3III
24	3342.1499	2.000	-0.64	1.21	1.19	2.66	0.68	0.57	0.13	0.00	0.00	K3III
25	3343.4700	2.038	-0.65	1.23	1.20	2.70	0.68	0.58	0.13	0.00	0.00	K3III
26	3345.5901	2.079	-0.66	1.25	1.21	2.74	0.69	0.58	0.13	0.00	0.00	K3III
27	3349.2700	1.877	-0.59	1.12	1.13	2.54	0.65	0.55	0.11	0.00	0.00	K2III
28	3352.0500	1.970	-0.62	1.18	1.17	2.63	0.67	0.57	0.12	0.00	0.00	K3III
29	3354.1201	2.048	-0.65	1.23	1.20	2.70	0.68	0.58	0.13	0.00	0.00	K3III
30	3356.7000	2.148	-0.70	1.31	1.24	2.84	0.71	0.60	0.14	0.00	0.00	K3III
31	3358.1001	2.203	-0.73	1.36	1.26	2.90	0.73	0.61	0.15	0.00	0.00	K3III
32	3360.3201	2.302	-0.77	1.41	1.27	2.91	0.74	0.62	0.15	0.00	0.00	K4III
33	3362.4099	2.401	-0.84	1.48	1.28	2.88	0.75	0.63	0.16	0.00	0.00	K4III
34	3364.2000	2.501	-0.92	1.61	1.36	3.11	0.79	0.66	0.18	0.00	0.00	K4III
35	3365.8000	2.601	-1.04	1.83	1.52	3.74	0.89	0.74	0.19	0.00	0.00	K7III
36	3367.1499	2.700	-1.18	1.83	1.53	3.71	0.89	0.73	0.21	0.00	0.00	M0III
37	3367.7300	2.750	-1.23	1.86	1.55	3.72	0.90	0.74	0.22	0.00	0.00	M0III
38	3368.3501	2.800	-1.33	1.88	1.57	3.80	0.91	0.75	0.22	0.00	0.00	M1III
39	3368.8601	2.850	-1.45	1.88	1.58	3.91	0.93	0.76	0.23	0.00	0.00	M2III
40	3369.3799	2.900	-1.54	1.88	1.59	4.02	0.94	0.77	0.24	0.00	0.00	M2III
41	3369.8201	2.950	-1.62	1.89	1.60	4.15	0.95	0.77	0.25	0.00	0.00	M2III
42	3370.2700	3.000	-1.69	1.90	1.60	4.29	0.96	0.78	0.26	0.00	0.00	M3III
43	3370.5801	3.035	-1.81	1.89	1.61	4.52	0.98	0.79	0.27	0.00	0.00	M3III
44	3370.9099	3.071	-1.98	1.84	1.61	4.83	1.00	0.80	0.28	0.00	0.00	M4III

Table B.23
Star Model with an Initial Mass of 1.50 $M_{\odot}$

#	Age	log L	BC	U-B	B-V	V-K	J-K	J-H	CO_{Sp}	N^{H}_{Lyc}	N^{He}_{Lyc}	Sp
1	8.5000	0.577	-0.13	-0.02	0.40	1.02	0.25	0.12	0.00	0.00	0.00	F5V
2	3338.4399	0.758	-0.11	0.08	0.36	0.94	0.23	0.11	0.00	0.00	0.00	F5IV
3	4585.6099	0.845	-0.13	0.09	0.40	1.01	0.25	0.12	0.00	0.00	0.00	F5IV
4	5075.8701	0.872	-0.15	0.09	0.51	1.28	0.32	0.15	0.00	0.00	0.00	F8IV
5	5332.6201	0.891	-0.17	0.14	0.59	1.47	0.37	0.18	0.00	0.00	0.00	G0IV
6	5389.6401	0.976	-0.15	0.09	0.48	1.19	0.29	0.14	0.00	0.00	0.00	F8IV
7	5396.6802	1.037	-0.13	0.09	0.41	1.02	0.25	0.12	0.00	0.00	0.00	F5III
8	5403.7100	1.021	-0.17	0.12	0.57	1.44	0.36	0.17	0.00	0.00	0.00	G0IV
9	5415.4302	1.002	-0.22	0.25	0.68	1.62	0.40	0.17	0.00	0.00	0.00	G2IV
10	5424.8101	0.968	-0.25	0.34	0.74	1.70	0.42	0.16	0.01	0.00	0.00	G2IV
11	5431.8501	0.920	-0.29	0.44	0.80	1.88	0.46	0.28	0.03	0.00	0.00	G5IV
12	5436.5400	0.883	-0.32	0.51	0.83	2.01	0.50	0.40	0.03	0.00	0.00	G5IV
13	5441.2300	0.855	-0.35	0.58	0.87	2.09	0.53	0.48	0.04	0.00	0.00	G8IV
14	5444.5098	0.848	-0.37	0.61	0.89	2.11	0.53	0.50	0.05	0.00	0.00	G8IV
15	5459.9399	0.940	-0.43	0.72	0.95	2.18	0.56	0.49	0.06	0.00	0.00	K0IV
16	5470.2700	1.046	-0.46	0.77	0.97	2.25	0.57	0.50	0.06	0.00	0.00	K0IV
17	5479.9302	1.147	-0.49	0.81	0.99	2.32	0.58	0.50	0.07	0.00	0.00	K0IV
18	5488.7500	1.242	-0.51	0.86	1.01	2.37	0.60	0.51	0.07	0.00	0.00	K1III
19	5497.5698	1.340	-0.53	0.92	1.03	2.43	0.61	0.53	0.08	0.00	0.00	K1III
20	5506.7202	1.443	-0.54	0.97	1.05	2.46	0.62	0.53	0.08	0.00	0.00	K1III
21	5515.4702	1.541	-0.55	1.02	1.07	2.48	0.63	0.54	0.09	0.00	0.00	K2III
22	5523.2002	1.642	-0.57	1.07	1.10	2.51	0.64	0.55	0.10	0.00	0.00	K2III
23	5530.2998	1.741	-0.59	1.13	1.14	2.55	0.65	0.55	0.11	0.00	0.00	K2III
24	5534.7798	1.791	-0.60	1.15	1.15	2.57	0.66	0.56	0.12	0.00	0.00	K2III
25	5538.1499	1.841	-0.62	1.17	1.17	2.61	0.66	0.56	0.12	0.00	0.00	K3III
26	5542.4399	1.888	-0.64	1.21	1.19	2.66	0.68	0.57	0.13	0.00	0.00	K3III
27	5547.4102	1.734	-0.59	1.11	1.13	2.53	0.65	0.55	0.11	0.00	0.00	K2III
28	5552.5200	1.831	-0.61	1.16	1.16	2.60	0.66	0.56	0.12	0.00	0.00	K3III
29	5557.3101	1.932	-0.65	1.23	1.20	2.70	0.68	0.58	0.13	0.00	0.00	K3III
30	5561.5698	2.033	-0.69	1.29	1.23	2.82	0.71	0.60	0.14	0.00	0.00	K3III
31	5565.4702	2.133	-0.74	1.37	1.26	2.91	0.73	0.62	0.15	0.00	0.00	K3III
32	5568.5898	2.231	-0.79	1.42	1.27	2.90	0.74	0.62	0.16	0.00	0.00	K4III
33	5571.2100	2.332	-0.86	1.51	1.30	2.92	0.76	0.64	0.17	0.00	0.00	K4III
34	5573.5098	2.432	-0.94	1.66	1.39	3.24	0.81	0.68	0.18	0.00	0.00	K5III
35	5575.3501	2.531	-1.04	1.83	1.52	3.74	0.89	0.74	0.19	0.00	0.00	K7III
36	5576.9502	2.631	-1.20	1.84	1.54	3.71	0.89	0.73	0.21	0.00	0.00	M0III
37	5578.2998	2.731	-1.41	1.88	1.58	3.87	0.93	0.76	0.23	0.00	0.00	M1III
38	5579.4102	2.831	-1.53	1.88	1.59	4.00	0.94	0.76	0.24	0.00	0.00	M2III
39	5580.4199	2.931	-1.78	1.90	1.61	4.47	0.98	0.78	0.26	0.00	0.00	M3III
40	5581.2900	3.031	-2.18	1.75	1.62	5.24	1.03	0.81	0.29	0.00	0.00	M4III
41	5582.0298	3.131	-2.39	1.66	1.64	5.87	1.09	0.84	0.31	0.00	0.00	M5III
42	5582.4800	3.200	-2.59	1.42	1.59	6.64	1.15	0.88	0.33	0.00	0.00	M6III
43	5582.6499	3.231	-2.68	1.26	1.55	6.98	1.18	0.89	0.34	0.00	0.00	M6III
44	5582.8501	3.263	-2.73	1.16	1.52	7.20	1.19	0.89	0.34	0.00	0.00	M?III

Table B.24
Star Model with an Initial Mass of 1.30 $M_{\odot}$

#	Age	log L	BC	U-B	B-V	V-K	J-K	J-H	CO_{Sp}	N^{H}_{Lyc}	N^{He}_{Lyc}	Sp
1	20.0000	0.401	-0.13	-0.02	0.41	1.04	0.26	0.12	0.00	0.00	0.00	F5V
2	4509.8301	0.477	-0.15	0.01	0.50	1.11	0.27	0.13	0.00	0.00	0.00	F8V
3	6777.4502	0.579	-0.16	0.09	0.53	1.34	0.33	0.16	0.00	0.00	0.00	F8IV
4	7630.1699	0.611	-0.18	0.16	0.61	1.51	0.37	0.18	0.00	0.00	0.00	G0IV
5	8037.9199	0.631	-0.21	0.23	0.66	1.60	0.39	0.18	0.00	0.00	0.00	G2IV
6	8114.0898	0.709	-0.18	0.15	0.60	1.49	0.37	0.18	0.00	0.00	0.00	G0IV
7	8123.0601	0.781	-0.16	0.10	0.53	1.35	0.34	0.16	0.00	0.00	0.00	F8IV
8	8127.5400	0.763	-0.18	0.15	0.60	1.50	0.37	0.18	0.00	0.00	0.00	G0IV
9	8153.2998	0.763	-0.23	0.28	0.70	1.64	0.41	0.16	0.01	0.00	0.00	G2IV
10	8179.0601	0.737	-0.26	0.37	0.76	1.74	0.43	0.18	0.02	0.00	0.00	G2IV
11	8192.5098	0.713	-0.29	0.43	0.79	1.86	0.46	0.27	0.02	0.00	0.00	G5IV
12	8205.9502	0.684	-0.32	0.51	0.83	2.00	0.50	0.39	0.03	0.00	0.00	G5IV
13	8219.3896	0.658	-0.35	0.57	0.87	2.09	0.52	0.48	0.04	0.00	0.00	G8IV
14	8235.0703	0.646	-0.38	0.63	0.90	2.11	0.54	0.50	0.05	0.00	0.00	G8IV
15	8283.2402	0.744	-0.45	0.75	0.96	2.22	0.56	0.49	0.06	0.00	0.00	K0IV
16	8314.6104	0.845	-0.48	0.80	0.98	2.30	0.58	0.50	0.07	0.00	0.00	K0IV
17	8342.6104	0.942	-0.50	0.84	1.00	2.35	0.59	0.51	0.07	0.00	0.00	K0IV
18	8368.3799	1.041	-0.52	0.89	1.02	2.40	0.60	0.52	0.07	0.00	0.00	K1IV
19	8393.0195	1.144	-0.53	0.92	1.03	2.43	0.61	0.53	0.08	0.00	0.00	K1IV
20	8414.2998	1.246	-0.54	0.99	1.06	2.47	0.63	0.54	0.09	0.00	0.00	K1III
21	8433.3496	1.344	-0.55	1.02	1.07	2.48	0.63	0.54	0.09	0.00	0.00	K2III
22	8449.0303	1.448	-0.56	1.05	1.09	2.50	0.64	0.55	0.10	0.00	0.00	K2III
23	8458.5498	1.547	-0.58	1.10	1.12	2.52	0.64	0.55	0.11	0.00	0.00	K2III
24	8469.7500	1.646	-0.60	1.14	1.15	2.56	0.65	0.56	0.12	0.00	0.00	K2III
25	8473.6699	1.700	-0.61	1.16	1.16	2.60	0.66	0.56	0.12	0.00	0.00	K3III
26	8478.1602	1.729	-0.62	1.18	1.17	2.63	0.67	0.57	0.12	0.00	0.00	K3III
27	8483.7598	1.670	-0.60	1.15	1.15	2.57	0.66	0.56	0.12	0.00	0.00	K2III
28	8491.0400	1.768	-0.65	1.23	1.20	2.70	0.68	0.58	0.13	0.00	0.00	K3III
29	8497.2002	1.867	-0.68	1.28	1.23	2.80	0.71	0.59	0.14	0.00	0.00	K3III
30	8502.6602	1.967	-0.73	1.36	1.26	2.90	0.73	0.61	0.15	0.00	0.00	K3III
31	8507.1396	2.066	-0.77	1.40	1.27	2.92	0.74	0.62	0.15	0.00	0.00	K4III
32	8510.9902	2.166	-0.81	1.45	1.28	2.88	0.74	0.63	0.16	0.00	0.00	K4III
33	8514.2803	2.266	-0.90	1.59	1.34	3.06	0.78	0.66	0.18	0.00	0.00	K4III
34	8516.9805	2.366	-1.00	1.78	1.48	3.58	0.86	0.72	0.19	0.00	0.00	K5III
35	8519.3203	2.466	-1.12	1.84	1.53	3.76	0.90	0.74	0.20	0.00	0.00	K7III
36	8521.0703	2.560	-1.22	1.85	1.55	3.72	0.89	0.73	0.22	0.00	0.00	M0III
37	8522.7402	2.660	-1.41	1.88	1.58	3.87	0.93	0.76	0.23	0.00	0.00	M1III
38	8524.2002	2.760	-1.58	1.89	1.60	4.09	0.95	0.77	0.25	0.00	0.00	M2III
39	8525.4404	2.860	-1.78	1.90	1.61	4.47	0.98	0.78	0.26	0.00	0.00	M3III
40	8526.5000	2.960	-2.12	1.78	1.61	5.12	1.02	0.80	0.28	0.00	0.00	M4III
41	8527.3896	3.060	-2.39	1.66	1.64	5.87	1.09	0.84	0.31	0.00	0.00	M5III
42	8528.1504	3.160	-2.73	1.16	1.52	7.20	1.19	0.89	0.34	0.00	0.00	M?III
43	8528.7695	3.260	-2.73	1.16	1.52	7.20	1.19	0.89	0.34	0.00	0.00	M?III
44	8529.2402	3.331	-2.73	1.16	1.52	7.20	1.19	0.89	0.34	0.00	0.00	M?III

Table B.25
Star Model with an Initial Mass of 1.15 $M_{\odot}$

#	Age	log L	BC	U-B	B-V	V-K	J-K	J-H	CO_{Sp}	N^{H}_{Lyc}	N^{He}_{Lyc}	Sp
1	469.7400	0.133	-0.19	0.07	0.59	1.17	0.28	0.13	0.00	0.00	0.00	G2V
2	3740.6201	0.233	-0.18	0.06	0.58	1.16	0.28	0.15	0.00	0.00	0.00	G2V
3	5965.9902	0.321	-0.19	0.07	0.59	1.17	0.28	0.14	0.00	0.00	0.00	G2V
4	7062.0098	0.355	-0.20	0.10	0.62	1.19	0.29	0.13	0.01	0.00	0.00	G2V
5	7578.7500	0.376	-0.21	0.23	0.66	1.60	0.39	0.18	0.00	0.00	0.00	G2IV
6	7751.4302	0.431	-0.19	0.18	0.63	1.55	0.38	0.18	0.00	0.00	0.00	G0IV
7	7785.7900	0.501	-0.17	0.14	0.59	1.47	0.37	0.18	0.00	0.00	0.00	G0IV
8	7877.3599	0.515	-0.19	0.18	0.63	1.55	0.38	0.18	0.00	0.00	0.00	G0IV
9	8314.2402	0.541	-0.24	0.31	0.72	1.67	0.41	0.15	0.01	0.00	0.00	G2IV
10	8433.3896	0.524	-0.28	0.41	0.78	1.81	0.45	0.22	0.02	0.00	0.00	G5IV
11	8473.1104	0.511	-0.30	0.46	0.80	1.90	0.47	0.30	0.03	0.00	0.00	G5IV
12	8539.2998	0.483	-0.34	0.55	0.86	2.07	0.52	0.46	0.04	0.00	0.00	G5IV
13	8565.7803	0.474	-0.35	0.59	0.88	2.10	0.53	0.49	0.04	0.00	0.00	G8IV
14	8618.7305	0.467	-0.39	0.65	0.91	2.12	0.54	0.50	0.05	0.00	0.00	G8IV
15	8777.5996	0.565	-0.46	0.77	0.97	2.25	0.57	0.50	0.06	0.00	0.00	K0IV
16	8857.0303	0.655	-0.48	0.80	0.98	2.30	0.58	0.50	0.07	0.00	0.00	K0IV
17	8923.2197	0.758	-0.50	0.84	1.00	2.35	0.59	0.51	0.07	0.00	0.00	K0IV
18	8962.9404	0.850	-0.51	0.87	1.01	2.38	0.60	0.52	0.07	0.00	0.00	K1IV
19	9002.6602	0.957	-0.52	0.91	1.03	2.42	0.61	0.52	0.08	0.00	0.00	K1IV
20	9029.1299	1.056	-0.53	0.95	1.04	2.45	0.62	0.53	0.08	0.00	0.00	K1IV
21	9052.2998	1.150	-0.54	0.99	1.06	2.47	0.63	0.54	0.09	0.00	0.00	K1IV
22	9070.5098	1.247	-0.55	1.03	1.08	2.49	0.63	0.54	0.09	0.00	0.00	K2III
23	9087.0498	1.347	-0.57	1.06	1.10	2.50	0.64	0.55	0.10	0.00	0.00	K2III
24	9100.2900	1.449	-0.58	1.10	1.12	2.52	0.64	0.55	0.11	0.00	0.00	K2III
25	9111.8799	1.553	-0.60	1.15	1.15	2.57	0.66	0.56	0.12	0.00	0.00	K2III
26	9126.3604	1.669	-0.64	1.21	1.19	2.66	0.68	0.57	0.13	0.00	0.00	K3III
27	9131.7305	1.625	-0.62	1.17	1.17	2.61	0.66	0.56	0.12	0.00	0.00	K3III
28	9139.5898	1.726	-0.65	1.24	1.21	2.72	0.69	0.58	0.13	0.00	0.00	K3III
29	9146.4199	1.825	-0.70	1.31	1.24	2.84	0.71	0.60	0.14	0.00	0.00	K3III
30	9152.4199	1.925	-0.74	1.37	1.26	2.91	0.73	0.62	0.15	0.00	0.00	K3III
31	9157.2803	2.025	-0.79	1.42	1.27	2.90	0.74	0.62	0.16	0.00	0.00	K4III
32	9161.6201	2.126	-0.84	1.48	1.28	2.88	0.75	0.63	0.16	0.00	0.00	K4III
33	9165.0400	2.226	-0.92	1.61	1.36	3.11	0.79	0.66	0.18	0.00	0.00	K4III
34	9168.0400	2.325	-1.01	1.80	1.49	3.65	0.88	0.73	0.19	0.00	0.00	K5III
35	9170.4404	2.425	-1.16	1.83	1.53	3.71	0.89	0.73	0.21	0.00	0.00	K7III
36	9172.6104	2.525	-1.28	1.88	1.57	3.77	0.91	0.74	0.22	0.00	0.00	M1III
37	9174.3301	2.625	-1.51	1.88	1.59	3.98	0.94	0.76	0.24	0.00	0.00	M2III
38	9175.8896	2.725	-1.58	1.89	1.60	4.09	0.95	0.77	0.25	0.00	0.00	M2III
39	9177.1504	2.825	-2.04	1.82	1.61	4.94	1.01	0.80	0.28	0.00	0.00	M4III
40	9178.2998	2.925	-2.29	1.70	1.63	5.54	1.06	0.82	0.30	0.00	0.00	M5III
41	9179.2197	3.025	-2.51	1.54	1.62	6.31	1.13	0.86	0.32	0.00	0.00	M6III
42	9180.0703	3.125	-2.73	1.16	1.52	7.20	1.19	0.89	0.34	0.00	0.00	M?III
43	9180.7803	3.225	-2.73	1.16	1.52	7.20	1.19	0.89	0.34	0.00	0.00	M?III
44	9181.4404	3.326	-2.97	1.90	1.78	5.24	0.97	0.71	0.54	0.00	0.00	M5II

Table B.26
Star Model with an Initial Mass of 1.00 $M_{\odot}$

#	Age	log L	BC	U-B	B-V	V-K	J-K	J-H	CO_{Sp}	N^{H}_{Lyc}	N^{He}_{Lyc}	Sp
1	7.0000	-0.207	-0.41	0.33	0.76	1.58	0.39	0.32	0.01	0.00	0.00	K0V
2	3248.6001	-0.075	-0.34	0.28	0.73	1.41	0.35	0.32	0.01	0.00	0.00	G8V
3	5669.7002	0.006	-0.25	0.24	0.70	1.31	0.32	0.30	0.01	0.00	0.00	G8V
4	7276.5000	0.069	-0.23	0.22	0.69	1.28	0.31	0.29	0.01	0.00	0.00	G8V
5	8447.0996	0.118	-0.23	0.22	0.69	1.28	0.31	0.29	0.01	0.00	0.00	G8V
6	9196.7998	0.156	-0.24	0.23	0.70	1.29	0.31	0.30	0.01	0.00	0.00	G8V
7	9700.7998	0.186	-0.25	0.24	0.70	1.31	0.32	0.30	0.01	0.00	0.00	G8V
8	10386.0000	0.234	-0.23	0.28	0.70	1.64	0.41	0.16	0.01	0.00	0.00	G2IV
9	10981.9004	0.280	-0.24	0.31	0.72	1.67	0.41	0.15	0.01	0.00	0.00	G2IV
10	11577.7998	0.322	-0.28	0.41	0.78	1.81	0.45	0.22	0.02	0.00	0.00	G5IV
11	11726.7002	0.327	-0.30	0.47	0.81	1.93	0.48	0.33	0.03	0.00	0.00	G5IV
12	11905.5000	0.321	-0.35	0.57	0.87	2.09	0.52	0.48	0.04	0.00	0.00	G8IV
13	11965.0996	0.319	-0.36	0.61	0.89	2.11	0.53	0.50	0.05	0.00	0.00	G8IV
14	11994.9004	0.318	-0.38	0.63	0.90	2.11	0.54	0.50	0.05	0.00	0.00	G8IV
15	12263.0000	0.428	-0.49	0.82	0.99	2.33	0.59	0.51	0.07	0.00	0.00	K0IV
16	12352.4004	0.517	-0.50	0.85	1.00	2.36	0.59	0.51	0.07	0.00	0.00	K1IV
17	12426.7998	0.622	-0.52	0.89	1.02	2.40	0.60	0.52	0.07	0.00	0.00	K1IV
18	12479.0000	0.712	-0.52	0.91	1.03	2.42	0.61	0.52	0.08	0.00	0.00	K1IV
19	12531.0996	0.820	-0.53	0.95	1.04	2.45	0.62	0.53	0.08	0.00	0.00	K1IV
20	12568.4004	0.921	-0.54	0.97	1.05	2.46	0.62	0.53	0.08	0.00	0.00	K1IV
21	12601.9004	1.023	-0.55	1.01	1.07	2.48	0.63	0.54	0.09	0.00	0.00	K1IV
22	12626.0996	1.122	-0.56	1.04	1.08	2.49	0.63	0.54	0.09	0.00	0.00	K2IV
23	12648.4004	1.221	-0.57	1.07	1.10	2.51	0.64	0.55	0.10	0.00	0.00	K2III
24	12665.2002	1.321	-0.58	1.10	1.12	2.52	0.64	0.55	0.11	0.00	0.00	K2III
25	12681.0000	1.420	-0.60	1.14	1.15	2.56	0.65	0.56	0.12	0.00	0.00	K2III
26	12702.9004	1.564	-0.65	1.23	1.20	2.70	0.68	0.58	0.13	0.00	0.00	K3III
27	12711.2998	1.517	-0.62	1.18	1.17	2.63	0.67	0.57	0.12	0.00	0.00	K3III
28	12721.0000	1.617	-0.65	1.24	1.21	2.72	0.69	0.58	0.13	0.00	0.00	K3III
29	12729.2002	1.717	-0.70	1.32	1.24	2.85	0.72	0.60	0.14	0.00	0.00	K3III
30	12736.5000	1.815	-0.74	1.37	1.26	2.91	0.73	0.62	0.15	0.00	0.00	K3III
31	12742.7002	1.915	-0.80	1.43	1.27	2.89	0.74	0.62	0.16	0.00	0.00	K4III
32	12747.7002	2.015	-0.84	1.48	1.28	2.88	0.75	0.63	0.16	0.00	0.00	K4III
33	12752.0000	2.115	-0.94	1.66	1.39	3.24	0.81	0.68	0.18	0.00	0.00	K5III
34	12755.7002	2.215	-1.00	1.78	1.48	3.58	0.86	0.72	0.19	0.00	0.00	K5III
35	12758.5996	2.315	-1.11	1.84	1.53	3.77	0.90	0.74	0.20	0.00	0.00	K7III
36	12764.2002	2.560	-1.55	1.88	1.59	4.05	0.94	0.77	0.24	0.00	0.00	M2III
37	12765.9004	2.660	-1.69	1.90	1.60	4.29	0.96	0.78	0.26	0.00	0.00	M3III
38	12767.2998	2.760	-2.09	1.79	1.61	5.06	1.02	0.80	0.28	0.00	0.00	M4III
39	12768.5996	2.860	-2.36	1.68	1.63	5.74	1.08	0.83	0.30	0.00	0.00	M5III
40	12769.5000	2.960	-2.53	1.52	1.62	6.39	1.14	0.87	0.32	0.00	0.00	M6III
41	12770.4004	3.060	-2.73	1.16	1.52	7.20	1.19	0.89	0.34	0.00	0.00	M?III
42	12771.2002	3.160	-2.73	1.16	1.52	7.20	1.19	0.89	0.34	0.00	0.00	M?III
43	12771.9004	3.260	-2.73	1.16	1.52	7.20	1.19	0.89	0.34	0.00	0.00	M?III
44	12772.5000	3.346	-3.49	1.59	1.80	5.20	0.96	0.71	0.57	0.00	0.00	M6II

Table B.27
Star Model with an Initial Mass of 0.85 $M_{\odot}$

#	Age	$\log L$	BC	U-B	B-V	V-K	J-K	J-H	CO_{Sp}	N^{H}_{Lyc}	N^{He}_{Lyc}	Sp
1	24.0000	-0.507	-0.39	0.57	0.88	2.08	0.51	0.44	0.03	0.00	0.00	K2V
2	5832.0000	-0.389	-0.33	0.50	0.83	1.87	0.46	0.40	0.03	0.00	0.00	K1V
3	11016.0000	-0.283	-0.32	0.43	0.80	1.70	0.42	0.36	0.02	0.00	0.00	K0V
4	13608.0000	-0.218	-0.35	0.40	0.79	1.67	0.41	0.35	0.02	0.00	0.00	K0V
5	16119.0000	-0.142	-0.38	0.38	0.78	1.64	0.40	0.33	0.01	0.00	0.00	K0V

Appendix C

Publications

The following research papers, to which I have contributed during the course of this Ph.D., are enclosed:

Doyon, R. & Joseph, R.D. 1989, "Dust Deficiency in Virgo Spirals", *Monthly Notices of the Royal Astronomical Society*, **239**, 347-360.

Doyon, R. & Joseph, R.D. 1989, "Far-Infrared Properties of Virgo Spirals", in *Evolutionary Phenomena in Galaxies*, *Astrophysics and Space Science*, **157**, 211-214.

Doyon, R., Joseph, R.D. & Wright, G.S. 1989, "The Strengths of the 2.3 μm CO Band in Luminous Interacting and Merging Galaxies", in *Infrared Spectroscopy in Astronomy*, 22nd ESLAB Symposium, ed. M. Kestler, p. 477-479.

Doyon, R., Joseph, R.D. & Wright. G.S. 1990, "CO Index Imaging of NGC 253", to appear in *Astrophysics with Infrared Arrays*, conference held in Tucson, February 1990.

Wright, G.S., James, P.A., Joseph, R.D., McLean, I.S. & Doyon, R. 1990, "Infrared Images of Merging Galaxies", to appear in *Interacting Paired*, conference proceeding IAU 124, held in Alabama, December 1989.

Mon. Not. R. astr. Soc. (1989) **239**, 347–360

Dust deficiency in Virgo spirals

René Doyon and R. D. Joseph *Astrophysics Group, Blackett Laboratory, Imperial College, London SW7 2BZ.*

Accepted 1989 January 27. Received 1989 January 27; in original form 1988 September 20

Summary. The results of an analysis of far-infrared (FIR) and 21-cm data for a sample of 102 spiral galaxies in the Virgo cluster are presented. We show that H I deficient galaxies have lower 60- and 100-μm fluxes and cooler far-infrared colour temperatures than those with normal H I content. No reasonable selection or systematic effect can account for these variations. We interpret these results in the context of a two-component model for the far-infrared emission: a warm component associated with star formation and H II regions, and a cool 'cirrus-like' component of dust heated by the interstellar radiation field. We find that, for a typical spiral in the core of the cluster, at least half of the diffuse dust has been stripped and the star formation activity suppressed by a factor of 3, compared to normal field galaxies. The dust stripping confirms the presence of a diffuse dust component in Virgo spirals and the validity of current models for the FIR emission in spiral galaxies.

1 Introduction

The *Infrared Astronomical Satellite* (*IRAS*) has revolutionized our understanding of the infrared emission from spiral galaxies. An estimated 20 000 spiral galaxies were detected in the far-infrared (60 and 100 μm, hereafter FIR). This radiation is generally agreed to be thermal radiation by dust grains which have been heated by starlight. Models for this infrared emission from spiral galaxies have been guided by another *IRAS* discovery, namely 'infrared cirrus' emission in the Galaxy. The 'cirrus' (so called because its wispy, filamentary structure is reminiscent of cirrus clouds in the Earth's atmosphere) is evident at 60 and 100 μm. It is clearly infrared emission by dust associated with interstellar clouds, heated by the general Interstellar Radiation Field (ISRF), and the dust occupies a disc of diameter $\sim$20 kpc and height $\sim$1 kpc (Puget 1988). Models of the infrared emission from other spiral galaxies by various authors (Helou 1986; Crawford & Rowan-Robinson 1986; Lonsdale, Persson & Helou 1987; de Jong & Brink 1987) have all incorporated a component due to 'cirrus' as well as a component due to starburst activity, and in these models the 'cirrus' component is a significant and often dominant fraction of the total FIR luminosity.

The validity of these models has recently been challenged by Leggett, Brand & Mountain (1987). They pointed out that, if there is a significant extended cirrus-type component in spiral

galaxies generally, galaxies in the centre of the Virgo cluster, which have been stripped of much of their neutral hydrogen, should also have lost similar proportions of their dust, and have significantly different FIR properties from field galaxies. Using a sample of 23 galaxies from the Virgo cluster, Leggett *et al.* argued that there was no such effect in this sample, and that the two-component models for the infrared emission from *IRAS* galaxies are incorrect.

The Leggett *et al.* argument has received indirect support from the Burstein & Lebofsky (1986) comparison of the detection rates for face-on and edge-on Sc galaxies in the *IRAS* survey. They conclude that edge-on Sc's are optically thick at 100 μm and the FIR emission is therefore largely confined to a central region $\leqslant 1$ kpc in these galaxies.

There are, however, some serious deficiencies in the Leggett *et al.* study. First, there are over 100 Virgo cluster spirals with well-determined H I and FIR properties, and it is difficult to understand why only 23 galaxies were used in their sample. Secondly, Leggett *et al.* expected to see a simple correlation between H I deficiency and (reduced) FIR flux, if there were an extended dust component which was stripped along with the H I, and they failed to find such a correlation. As we show below, however, the intrinsic scatter in the FIR fluxes of unstripped spirals guarantees that such a simple correlation would not be expected, and so the Leggett *et al.* conclusion was based on a faulty premise. For these reasons, and because the conclusion has fundamental implications for understanding the global dust distribution and star-formation activity in spiral galaxies, we undertook a more thorough investigation of the evidence for dust stripping in Virgo spirals.

2 The sample

Helou *et al.* (1989) have re-coadded the *IRAS* data for 196 galaxies in the Virgo cluster, in the region bounded by $12^h < \alpha < 13^h$, $4° < \delta < 20°.5$. This sample includes 131 bright spirals with morphological types Sa and later, and total corrected blue magnitude $\leqslant 12.80$. With this survey they achieved a sensitivity of 0.14 and 0.34 Jy at 60 and 100 μm, respectively. This is almost a factor 3 better than that of the *Point Source Catalog*. A main advantage of the Helou *et al.* survey is that they obtained good-quality integrated fluxes for galaxies that were resolved by *IRAS*. We have restricted the Helou *et al.* sample to the spiral subset with good 21-cm observations already published in the literature. The resulting sample consists of 102 galaxies, 65 of which are situated within 5° of the core of the cluster.

The H I content of each galaxy is characterized by its H I deficiency (*Def*), which is defined on a logarithmic scale (e.g. Haynes & Giovanelli 1986) as the difference between the observed H I mass and that expected for an isolated galaxy of the same optical linear diameter and morphological type, that is,

$$Def = \langle \log M_{\mathrm{H\,I}}(T, D_{\mathrm{L}}) \rangle - \log M_{H\,\mathrm{I}}(obs), \tag{1}$$

where T is the morphological type and D_{L} is the optical diameter. *Def* values have been taken from Giovanelli & Haynes (1985) and Haynes & Giovanelli (1986) or calculated as prescribed by Haynes & Giovanelli (1983) using published H I fluxes from Helou, Hoffman & Salpeter (1984), Giovanardi *et al.* (1983) and from Fisher & Tully (1981).

The following parameters for the galaxies are listed in Table 1.

Column (1) Entry number from the *Uppsala General Catalogue* (Nilson 1973: UGC).

Column (2) Numerical type code, T, corresponding to $T=0$ for ellipticals; $T=1$ for S0; $T=2$ for S0/a; $T=3$ for Sa; $T=4$ for Sab; $T=5$ for Sb; $T=6$ for Sbc; $T=7$ for Sc; $T=8$ for Scd; $T=9$ for Sd and Sdm; $T=10$ for Sm and Irr.

Column (3) Blue major and minor diameters in arcmin, a and b, from the UGC.

Column (4) Projected distance in degrees from the cluster centre, assumed to be at $\alpha = 12^h 25^m4$ and $\delta = +12°40'$ (van den Bergh 1977).

Column (5), (6) *IRAS* 60- and 100-μm flux densities from Helou *et al.* (1989).

Column (7) H I deficiency of the galaxy as defined in equation (1).

Column (8) Source of 21-cm observations.

Table 1. Properties of the galaxies.

UGC	Type	Diameters a×b	R_{core} (°)	F_{60} (Jy)	F_{100} (Jy)	HI *Def*	Reference[a]
7054	7	4.20×1.80	8.4	3.50	7.31	0.99	2
7169	7	2.20×1.90	5.6	4.60	8.60	0.02	2
7170	7	3.00×0.20	7.8	0.25	0.33	-0.46	5
7182	3	1.70×1.60	8.8	0.75	2.58	0.13	3
7209	5	2.50×1.70	3.9	0.55	1.20	0.08	2
7215	7	5.50×1.70	4.0	4.30	9.89	-0.13	2
7231	5	9.90×2.20	4.3	8.90	23.05	0.09	2
7234	7	2.30×1.10	3.6	1.30	3.70	0.21	3
7235	7	2.70×2.20	3.6	3.80	8.51	0.12	2
7239	9	2.50×2.30	5.8	0.15	0.31	0.69	5
7247	8	3.80×0.60	7.4	2.35	5.25	-0.05	3
7255	7	2.40×0.40	3.6	0.64	1.89	0.05	1
7260	7	5.80×0.90	3.2	1.15	2.49	-0.09	2
7275	7	2.90×1.90	3.4	7.50	16.94	1.10	2
7279	9	2.20×0.20	3.5	<0.10	0.34	-0.22	2
7284	5	8.50×1.70	3.1	3.70	14.19	0.35	2
7291	8	3.10×0.40	3.0	1.20	3.27	0.06	2
7292	3	2.00×0.90	5.7	0.17	0.86	0.51	3
7315	7	2.20×1.40	3.9	3.10	9.03	0.52	2
7326	9	1.80×0.50	2.6	0.20	<0.22	0.14	1
7345	7	5.00×4.70	3.0	44.00	96.32	0.02	2
7361	3	2.20×1.20	6.7	0.20	0.95	0.35	2
7380	7	2.50×1.20	7.3	10.00	20.38	-0.10	3
7407	7	3.00×1.10	1.9	3.17	5.68	-0.21	2
7412	7	3.00×1.70	2.7	3.40	11.44	0.54	2
7414	8	1.70×1.70	1.8	3.00	5.07	-0.13	2
7418	7	5.10×0.90	2.7	4.70	15.22	0.15	2
7420	7	6.60×6.40	8.1	41.00	77.40	0.17	2
7431	7	3.50×0.70	3.7	1.17	4.04	1.21	3
7442	4	4.20×0.90	3.4	2.10	6.19	1.27	3
7445	4	3.50×0.80	1.4	1.10	3.87	1.07	3
7447	6	2.70×0.50	3.3	1.60	5.68	0.38	1
7450	7	6.80×5.80	3.7	31.00	70.52	0.52	2
7451	3	2.10×0.90	7.2	0.41	1.72	0.11	4
7456	9	4.50×0.90	1.6	0.80	3.01	0.73	3
7465	5	2.60×0.70	5.5	1.60	4.04	0.33	3
7470	7	1.90×1.60	1.0	0.60	1.03	0.67	2
7476	7	1.90×1.40	1.0	0.74	2.06	0.54	2
7482	7	2.60×0.50	4.0	0.56	1.46	1.25	1
7497	3	3.30×3.10	7.5	0.50	1.46	-0.06	2
7503	4	3.50×2.20	2.5	0.73	2.92	1.05	3
7507	10	1.80×0.90	4.1	8.50	12.30	-0.39	1

Table 1 – *continued*

UGC	Type	Diameters a×b	R_{core} (°)	F_{60} (Jy)	F_{100}	HI *Def*	Reference[a]
7513	7	3.50×0.40	5.2	2.20	5.42	-0.13	2
7518	7	2.40×0.50	4.9	0.65	1.89	0.37	1
7520	4	6.20×1.70	0.6	11.50	18.06	1.06	2
7523	5	3.60×3.40	5.9	1.15	4.99	0.86	4
7526	7	3.50×1.20	3.3	1.35	3.78	0.27	3
7528	7	3.80×1.10	0.9	6.20	16.34	0.61	2
7537	7	2.30×2.20	3.5	0.30	0.83	0.39	2
7538	6	2.40×1.70	0.4	1.00	3.10	0.80	2
7541	7	1.80×1.60	4.5	1.00	2.75	0.46	3
7546	7	3.20×3.20	3.6	0.40	1.63	0.08	2
7551	3	3.10×1.00	2.7	7.80	16.17	1.06	2
7556	9	2.20×0.35	6.5	0.55	1.20	-0.18	5
7557	8	3.20×2.60	5.1	0.43	0.73	0.12	5
7561	3	3.60×1.90	3.0	3.00	5.50	1.09	2
7563	8	2.10×1.20	3.5	0.15	0.30	0.52	2
7566	7	2.90×2.30	6.1	1.15	3.78	0.58	3
7574	5	9.70×3.90	0.6	1.52	4.30	1.28	2
7594	4	5.50×3.70	4.8	1.80	7.91	1.31	2
7609	5	3.40×2.80	8.8	4.70	8.94	0.81	4
7627	7	1.40×0.90	4.6	1.90	4.04	0.01	3
7647	5	2.50×1.20	8.2	1.40	3.70	0.01	3
7668	7	4.00×3.00	8.5	5.10	9.20	0.06	2
7669	7	3.50×1.70	4.6	1.20	3.70	0.47	2
7675	6	6.70×3.00	2.3	21.00	59.34	0.47	2
7709	7	3.80×2.50	4.0	4.20	6.62	-0.33	2
7711	5	4.20×1.10	3.5	1.70	3.96	0.51	2
7713	9	2.50×2.20	3.1	0.40	1.29	0.14	2
7726	10	3.50×1.20	4.7	10.00	14.88	-0.28	3
7727	7	7.80×7.00	4.5	14.00	31.82	0.17	2
7729	3	3.50×2.30	1.7	0.36	1.72	2.13	3
7742	8	2.10×1.70	3.6	1.40	5.16	0.37	2
7753	5	5.50×4.50	2.8	2.80	10.92	0.86	2
7781	9	3.00×3.00	6.2	0.30	0.52	0.19	5
7784	10	2.50×1.50	2.3	0.54	1.72	0.57	2
7786	4	11.40×4.70	2.3	11.00	24.08	0.99	2
7788	7	4.50×3.70	2.9	1.80	6.02	0.44	2
7794	3	2.60×1.80	7.4	1.20	4.30	1.36	3
7796	4	6.00×5.00	2.5	6.70	18.92	1.01	2
7804	3	3.90×1.20	8.5	0.40	1.72	1.19	3
7826	7	1.70×1.10	4.1	0.90	2.67	0.30	2
7839	3	2.80×1.60	3.3	0.85	2.49	1.83	3
7843	8	3.20×0.70	3.4	3.10	7.91	0.72	1
7875	7	2.60×0.50	4.2	4.50	10.32	0.44	3
7884	5	3.20×2.20	3.8	1.85	4.47	0.16	2
7896	7	2.90×2.40	3.9	6.10	15.57	0.51	2
7901	7	3.90×2.50	5.6	6.30	14.19	-0.16	2
7902	7	5.30×2.90	4.0	14.70	34.40	0.00	2
7920	10	2.70×1.00	4.2	<0.15	<0.34	1.12	1
7943	7	2.50×2.00	8.0	0.20	0.60	0.40	5

Table 1 - *continued*

UGC	Type	Diameters axb	R_{core} (°)	F_{60} (Jy)	F_{100}	HI *Def*	Reference[a]
7961	7	4.40x4.40	9.5	1.25	1.98	0.19	3
7965	7	4.00x3.50	5.1	3.90	9.63	1.06	2
7969	10	3.50x1.60	5.3	1.20	2.92	0.99	4
7970	3	3.50x1.80	6.4	0.63	1.89	0.25	2
7985	7	3.20x2.00	9.0	5.50	10.06	-0.24	3
8007	5	2.20x0.45	6.0	4.70	12.90	-0.21	3
8014	5	3.00x0.80	7.1	1.20	2.58	0.16	3
8022	6	2.10x1.80	7.0	2.20	4.04	0.22	3
8036	7	2.50x2.00	9.6	0.08	0.34	-0.19	3
8054	7	2.60x1.00	10.7	7.30	14.79	-0.64	3
8102	3	6.00x1.30	8.1	0.36	0.77	0.24	2

[a]Source of the 21 cm observations. (1) Haynes & Giovanelli 1986. (2) Giovanelli & Haynes 1985. (3) Helou, Hoffman & Salpeter 1984. (4) Giovanardi *et al.* 1983. (5) Fisher & Tully 1981.

3 Data analysis

3.1 PROPERTIES OF 'NORMAL' AND 'DEFICIENT' GALAXIES

Average properties of all galaxies are presented in Table 2. The sample has been divided into two subsets of 'normal' ($Def < 0.3$) and 'deficient' ($Def \geqslant 0.3$) galaxies. With this definition, the two subsets have average (Def) and standard deviation of 0 ± 0.2 and 0.8 ± 0.4, respectively. Deficient galaxies are generally located close to the centre of the cluster (Haynes & Giovanelli 1986). As illustrated in Table 2, normal galaxies are located at an average projected distance $R_{\rm core}$ of 5°.5 from the centre, whereas deficients are at 3°.8 from the core. By definition, an average field galaxy has a Def of zero. Therefore, as far as the H I content and the location relative to the centre are concerned, H I normal galaxies in Virgo can be assumed to have similar properties to those in the field.

Table 2. Averaged properties of the galaxies.

	Galaxy	Number	$\log(F_{100}/F_{60})$	$\log(F_{60}/a^2)$	$\log(F_{100}/a^2)$	a_{UGC} (′)	R_{core} (°)
	Sa–Sbc	12	0.43(0.03)	−0.81(0.12)	−0.38(0.12)	3.3	6.4
'normal'	Sc–Irr	34	0.34(0.02)	−0.64(0.10)	−0.30(0.10)	3.5	5.2
	All	46	0.36(0.02)	−0.68(0.08)	−0.32(0.08)	3.5	5.5
	Sa–Sbc	25	0.49(0.03)	−0.96(0.08)	−0.47(0.07)	4.5	3.7
'deficient'	Sc–Irr	28	0.43(0.02)	−0.77(0.08)	−0.34(0.08)	3.0	3.9
	All	53	0.46(0.02)	−0.86(0.06)	−0.40(0.06)	3.7	3.8

Numbers in parentheses are standard errors of the mean. Galaxies with upper limit FIR fluxes were excluded.

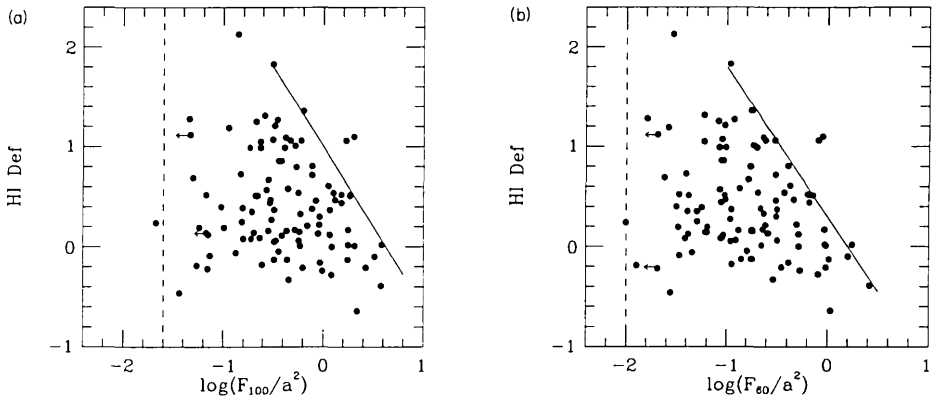

Figure 1. Plots of H I deficiency against the FIR 'surface brightness' at (a) 100 μm and (b) 60 μm. Upper limit fluxes are symbolized by left arrows. Solid lines delimit the upper envelope seen in both figures. Dashed lines represent the corresponding *IRAS* detection limit of each band converted to surface brightness using an average optical diameter of 3.6 arcmin.

To investigate the possible variation of the FIR fluxes with *Def*, we have defined a hybrid FIR 'surface brightness', expressed as the ratio of the *IRAS* band flux $F_\lambda(\lambda = 60$ or 100μm) to the square of the optical diameter a. This parameter reduces to a first approximation the intrinsic scatter introduced by size effects. H I deficiency, *Def*, is plotted against the log of the 60- and 100-μm surface brightness in Fig. 1(a) and (b). We can see from the distribution of normal galaxies ($Def < 0.3$) that, even though the FIR fluxes have been normalized, the intrinsic scatter is still very important. Nevertheless, the two diagrams show a significant upper envelope, suggesting that the surface brightness *decreases* in a systematic way with increasing *Def*. The slopes for these envelopes are in the range between -1 and -2. The vertical dashed line in both figures corresponds to the *IRAS* detection limit. As expected, almost all galaxies fall on the right side of the line. The combined effect of this limit with the large scatter in the FIR fluxes of normal galaxies eliminates any simple anticorrelation between *Def* and surface brightness.

The colour distribution F_{100}/F_{60} for normal and deficient galaxies is plotted in Fig. 2. Average $\langle \log F_{100}/F_{60} \rangle$ ratios are also given in Table 2. Galaxies with upper limits were not

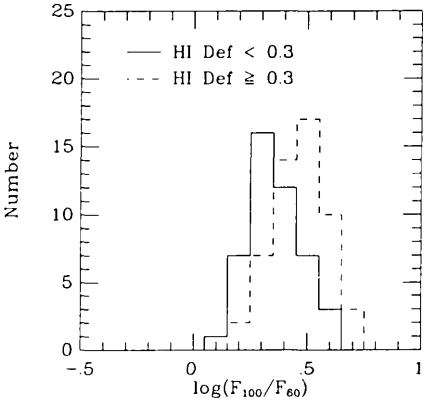

Figure 2. Histograms of the FIR colour distributions of H I normal galaxies (solid line) and deficient galaxies (dashed line). Galaxies with upper limit fluxes were excluded.

included for this comparison. Normal and deficient galaxies have an average $\langle \log F_{100}/F_{60} \rangle$ of 0.36 ± 0.02 and 0.46 ± 0.02, respectively. A Student t-test performed on the two distributions shows that the difference is significant at the 4–5 σ level. Deficient galaxies are apparently 'cooler' than normal galaxies. A similar result has been found at a lower significance (1 or 2 σ) by Bicay & Giovanelli (1987) for a sample of nine clusters excluding Virgo.

3.2 SYSTEMATIC EFFECTS

Before attempting any interpretation of these results, it is important to investigate possible systematic or selection effects which could reproduce the observed envelopes and colour distribution. One obvious bias could be due to morphological stratification. It is well known that the fraction of early-type spirals in Virgo is larger close to the centre than it is in the outer regions. Since deficient galaxies tend to be found near the core of the cluster, a sample of deficient galaxies will naturally be dominated by early-type spirals. This effect is clearly illustrated in Table 2. Consequently, if early-type spirals happen to have intrinsically a lower FIR surface-brightness than late types, this could well explain the observed differences between deficient and normal galaxies. Given the distributions of morphological types in both samples, one can easily estimate that, to explain the observed differences, early- and late-type spirals must differ in intrinsic surface brightness by 0.5–0.6 on a logarithmic scale. A comparison of average FIR surface brightness of early- and late-type spirals in the normal sample (see Table 2) shows that this difference is less than 0.2. Within the error, the FIR surface brightness is independent of morphological type. The same argument applies also for the colour distribution.

Another potential source of bias is the use of optical diameters to normalize FIR fluxes. Although there is no apparent variation in diameter between normal and deficient galaxies (see Table 2), it has been found (Peterson, Strom & Strom 1979) that, when a faint isophotal diameter (to 26.6 mag arcsec^{-2}) is considered, spirals in the core of the cluster appear smaller than field galaxies by a factor of 1.3. Since this effect is more likely to affect deficient galaxies which are more concentrated at the centre, the surface brightness of deficient galaxies could have been *overestimated* by ≈ 0.23 dex. Although this effect cannot explain the existence of the envelopes, it could affect the value of their slopes. A variation in the optical diameter should, however, also affect the value of *Def*, because the first term in equation (1) is determined by a calibration that involves an optical diameter. A smaller diameter leads to an underestimate of *Def*. In a situation where *Def* is anticorrelated with surface brightness, it can be shown that the two effects cancel out. Thus the slope of the envelopes is unlikely to be affected by such a systematic effect.

In summary, it seems that no obvious systematic or selection effect can account for the observed variations of FIR surface brightness with H I deficiency. They must then have a physical origin. We have shown that, when the H I content is taken into account, Virgo spirals do have FIR properties different from field galaxies.

4 Interpretation

In normal galaxies, the FIR emission is generally thought to be thermal emission from dust heated by starlight. The FIR flux is then given by $F_\nu \propto M_d B_\nu(T_d) Q(\nu)$, where M_d is the dust mass, $B_\nu(T_d)$ the Planck function at a dust temperature T_d, and $Q(\nu)$ is the emissivity law. This expression shows that the reduced FIR surface-brightness in deficient galaxies might be due either to a lower dust content (M_d) or to a lower dust temperature T_d. The situation might also

be more complicated if several components at different temperatures are responsible for the integrated spectrum.

Let us first assume that the integrated spectrum is due to a single temperature. Assuming the emissivity to vary as ν^2 and using the F_{100}/F_{60} ratios of the two subsets, we find temperatures for normal and deficient galaxies of 28 and 26 K, respectively. Because of these different temperatures, in a diagram *Def* versus $\log(F_\lambda/a^2)$, the line joining a typical normal galaxy and a typical deficient one should have a negative slope. From the average H I deficiency of the two samples and the temperatures above, we can easily estimate that the value of these slopes should be -5 at 100 μm and -3 at 60 μm. These slopes are too steep to be consistent with those actually observed (≈ -1.5). Therefore, to explain the observed envelopes we must suppose that the dust content of deficient galaxies has been reduced by a factor of about 2.

A single-temperature model is too simple nevertheless, because the dust can be heated in different physical conditions, from the cold interstellar medium (ISM) to the hot environment of an H II region. As discussed in the Introduction, recent models have shown that the FIR spectral distribution of spiral galaxies is best explained by assuming at least two components. These models differ in detail but all have in common both a component due to warm dust heated to a temperature 40–50 K by young OB stars and compact H II regions, and a cool cirrus component due to dust heated at temperature of ≈ 20 K by ISRF. In these models the latter component contributes about 50–70 per cent of the total FIR luminosity. The single-component temperatures of 26–28 K inferred above are too high to be explained by cirrus emission, but also too low to be explained by warm emission above. This indicates that the FIR spectral distribution of Virgo spirals is a composite spectrum of 'cool' and 'warm' emission.

In the following we develop a simple two-component model to disentangle the effects of variations in both components on the integrated spectrum, and to interpret envelopes and colour distributions shown in Figs 1 and 2.

4.1 DESCRIPTION OF THE MODEL

We assume a two-component model for the FIR emission similar to one developed by Lonsdale Persson & Helou (1987): a cool component of dust associated with H I gas, heated by the general ISRF, and a warm component associated with young OB stars and H II regions. The flux density $F_N(\lambda)$ in normal galaxies is thus given by the sum of the cool and the warm component $F_N^c(\lambda)$ and $F_N^w(\lambda)$. Intrinsic colour ratios (temperatures) $F_M^c(100)/F_M^c(60)$ and $F_N^w(100)/F_N^w(60)$ are assumed to be identical for all galaxies and are chosen from previous galactic observations of 'cirrus' (Gauthier 1986) and H II regions (Chini *et al.* 1986b,c). To model the variations in FIR flux with *Def*, we express the cool and the warm component in deficient galaxies as a power law of 'normal' fluxes,

$$\begin{aligned} F_D^c(\lambda) &= F_M^c(\lambda) \times 10^{-\alpha Def} \\ F_N^w(\lambda) &= F_N^w(\lambda) \times 10^{-\beta Def}. \end{aligned} \tag{2}$$

We assume that the variations in flux are not due to temperature effects, in that when a galaxy becomes deficient the temperatures of the cool and the warm dust remain unchanged. This assumption will be discussed later. The value of α is just a measure of the efficiency by which the cold dust is removed compared to the atomic gas. Following the argument of Cox, Krügel & Megzer (1986), the warm component is proportional to the star formation rate (SFR). We have therefore allowed for the possibility that the SFR is dependent on H I deficiency by introducing the free parameter β.

The detailed description of this model is outlined in the Appendix. In summary, we generate a simulated sample of normal Virgo cluster spirals using the observed FIR surface brightness

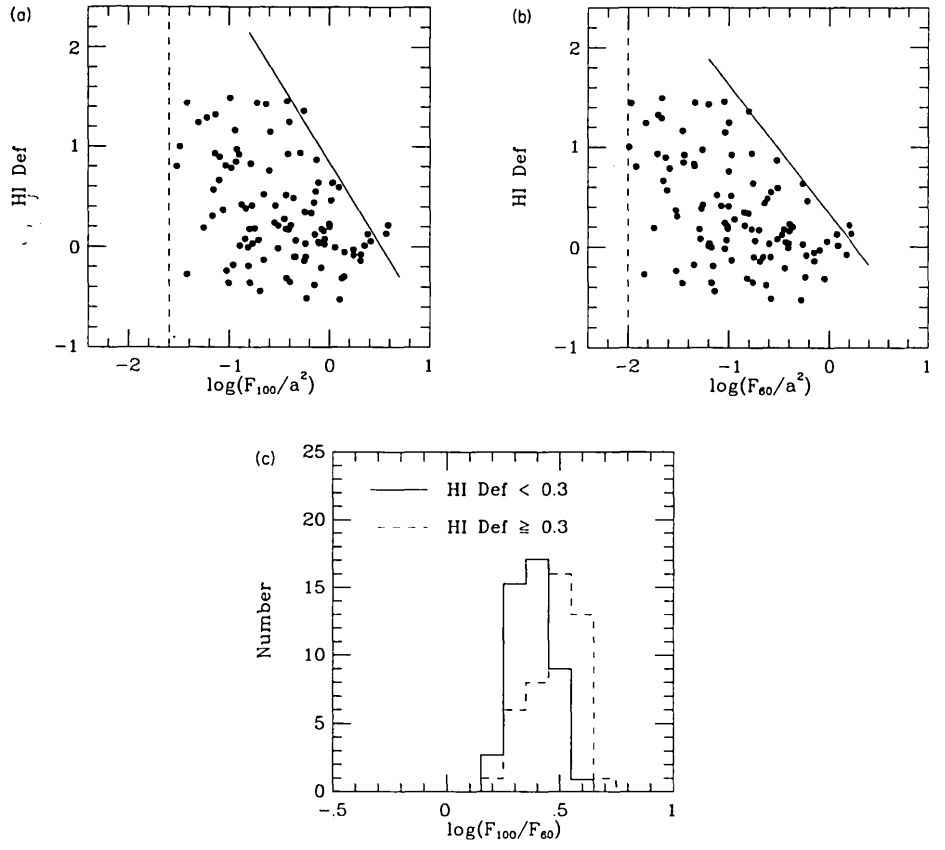

Figure 3. (a) and (b) Modelled diagrams corresponding to Fig. 1(a) and (b), respectively. They were simulated using the model described in the text with the following parameters: $\alpha = 0.5$, $\beta = 1.0$, $F^c_M(100)/F^c_M(60) = 5$ and $F^w_N(100)/F^w_N(60) = 1.0$. The number of points in the model has been set equal to the number of galaxies in the sample. (c) Resulting colour distributions from the model.

and colour distributions. From the observed H I deficiency distribution and equations (2), we calculate the cool and the warm component $F^c_D(\lambda)$ and $F^w_D(\lambda)$ for various combinations of α and β. The model produces envelopes in plots of *Def* versus log F_λ/a^2 with slopes that depend on the values of α and β. The observed colour distributions and envelopes can be used to constrain the two parameters. Naturally, α and β cannot be uniquely determined, because of uncertainties both in the observations and in the choice of intrinsic temperatures for the two components. We have tried several models with different combinations of $F(100)/F(60)$ ratios chosen in the following range: $F^c_M(100)/F^c_D(60) = 5$–10 and $F^w_N(100)/F^w_N(60) = 0.5$–$1.5$. The values of α and β which reproduced the observed envelopes and colour distributions have averages $\alpha = 0.5 \pm 0.1$ and $\beta = 1.0 \pm 0.15$. In Fig. 3(a–c) we have plotted the simulated diagrams which correspond to Figs 1(a), (b) and (2), respectively for a typical model. The agreement between the observations and the model is very good.

The main conclusion is that *both* components must be reduced to explain the observed variations. No model with either α or β equal to zero was found to fit the observed envelopes and colour distributions. This model shows that the cold dust content has been reduced significantly and that star formation has been suppressed in Virgo spirals.

4.2 MODEL VIABILITY

The main assumption in this model is that the temperatures of the cool and the warm component remain unchanged when a galaxy becomes H I deficient. We examine here the validity of this assumption.

A decrease of temperature in the warm component would mean that the Initial Mass Function (IMF) in deficient and normal galaxies is different, in the sense that deficient ones would produce less massive stars, making the effective stellar population look 'cooler'. Although we cannot exclude this possibility, we have no observational or theoretical reasons to believe that such IMF variations occur when a galaxy becomes deficient. It is therefore artificial to suppose that these effects are genuine.

Since the cool component is associated with cold dust heated by the background starlight, any fluctuations in dust temperature will be driven by variations in the ISRF. A diminution of the ISRF is certainly possible, for it has a strong contribution from young massive stars (Mezger, Mathis & Panagia 1982), which are in turn less effectively produced in deficient galaxies, as we have shown. Draine & Anderson (1985) calculated the effect of different ISRF on the dust temperature of cirrus clouds in our Galaxy. They found that, if the ISRF is decreased by a factor of 2, the cold dust temperature is decreased by about 2 K, which causes a 100-μm flux reduction by a factor of 2.4. We have investigated this effect using our model, by assuming that very deficient galaxies ($Def > 0.5$) have an ISRF half of that in other galaxies. The model gives now an average solution with $\alpha = 0.3$ and $\beta = 1.0$. The fact that $\alpha \neq 0$ shows that a reduction of the temperature is not sufficient to reproduce the observations, that is, a certain amount of dust has still to be removed. Moreover, Boulanger & Pérault (1986) estimated that at least half of the cirrus emission in the solar neighbourhood is due to re-radiation of light from the old disc stellar population. Since deficient galaxies have morphological types similar to or earlier than that of our galaxy (Sb), even if their young stellar population are reduced by a factor of 2, the ISRF would not be reduced by more than 1.3, which should have a negligible effect on the cold dust temperature. For these reasons, we believe that the dominant effect responsible for the reduction of the cool component flux is the removal of dust mass.

5 Discussion

We have shown that the FIR properties of spirals in the Virgo cluster are best explained by supposing that a certain amount of cold dust has been removed and that the SFR has been reduced. We now discuss the origin of these variations and their consistency with other observations.

5.1 DUST STRIPPING

5.1.1 Dust removal mechanisms

The removal of atomic gas is thought to be caused by interactions with the intracluster medium (ICM). The following processes have been suggested:

(i) ram pressure stripping (Gunn & Gott 1972);
(ii) thermal evaporation (Cowie & Songaila 1977), and
(iii) turbulent viscous stripping (Nulsen 1982).

In (i) and (iii), the velocity of the galaxy relative to the ICM is responsible for the removal, whereas the high gradient of temperature between the cold ISM and the hot ICM is the physical cause in (ii).

Are these processes consistent with the removal of dust? Dust particles in the ISM are coexistent with the atomic gas. It is easy to show that the time required for the dust to be dynamically in equilibrium with the atomic gas is about 10^5 yr. This is negligible compared to the gas-stripping time-scale (of the order of a crossing time, i.e. $\approx 10^9$ yr). Therefore, any mechanism which can remove the gas will also remove the dust. Because of this dust–gas coupling, however, the dust stripping we find in Virgo spirals cannot be used to identify which of the processes mentioned above dominates.

5.1.2 Spatial distribution of the cold dust

Since the dust is coupled with the H I gas, the masses of dust and H I removed in a deficient galaxy should be directly proportional. In other words, the expected value of α in the model described above should be unity. The model has predicted a value significantly lower, $\alpha = 0.5 \pm 0.1$.

The explanation for so low a value of α is probably related to the spatial distribution of cold dust. In our model we have assumed that the cold dust is coexistent with the atomic gas only, but this is not necessarily true. Cox *et al.* (1986) showed that the FIR spectral distribution in our Galaxy is best explained with four components. One of them is due to very cold dust ($T_D = 14$ K) associated with quiescent molecular cloud. They estimated that the very cold dust accounts for ≈ 10 per cent of the combined luminosity of cold dust (associated with H I gas) and very cold dust. This very cold dust can explain the value of α only if this dust is not stripped. Kenney & Young (1986) showed from the CO emission of 23 Virgo spirals that the molecular content of these galaxies is normal. The mechanism responsible for the gas stripping apparently has no effect on the molecular content. Thus the dust associated with these clouds is not likely to be removed. From the value of α and the average *Def* of deficient galaxies, and assuming that the dust is stripped in the same proportion as the H I, we can estimate the contribution to the total cool component luminosity of very cold dust in molecular clouds. We find that ≈ 20–30 per cent of the total cool luminosity is due to dust in molecular clouds. Given the uncertainties involved in this calculation our estimate is in good agreement with Cox *et al.* (1986). While we have assumed two components for the FIR emission, the results of the model turn out to be consistent with three components.

5.1.3 Observational consequences of dust stripping

An obvious consequence of removing the cold dust is to reduce the internal absorption, which artificially decreases the blue magnitude of the galaxy. This has a direct effect on the blue-light Tully–Fisher relation. Van den Bergh (1984) has drawn attention to this problem for the Virgo cluster. He showed that the deviation of individual galaxies from the mean blue Tully–Fisher relation is a function of inclination, in the sense expected if the galaxies are dust-poor. From his analysis, he was not able to determine precisely by what factor they are dust-poor, but pointed out that *if* the internal absorption in Virgo galaxies were reduced by a factor of 2 then the Virgo distance modulus derived from the blue Tully–Fisher relation would be increased by 0.27 mag. This correction results in a decrease of the Hubble constant by 12 per cent. From the average deficiency of typical galaxies within 5° of the cluster centre, we estimate that they are dust-poor by a factor of 2–3 compared to field galaxies. The dust stripping is thus consistent with van den Bergh's analysis and emphasizes the point of using an infrared Tully–Fisher relation for the extragalactic distance scale, which is less affected by such extinction effects.

The removal of dust should have observable effects in the submillimetre spectral region where cold dust emission is more prominent. Since the cold dust is mainly associated with the extended H I disc, the submillimetre diameter should be affected in deficient galaxies, since a

diminution of the H I disc diameter in these galaxies has already been observed (*cf.* Haynes & Giovanelli 1983). Submillimetre mapping of normal and deficient galaxies could be used to test directly the dust stripping.

5.2 SUPPRESSION OF STAR FORMATION

From the result of our model ($\beta = 1$) we find the SFR is $\propto 10^{-Def}$. This expression shows that a typical galaxy in Virgo with $Def = 0.5$ has an SFR a factor of 3 lower than that in the field. This result is consistent with previous observations. Kennicutt (1983) found from a comparison of Hα data of Virgo cluster and field galaxies that spirals of all types in Virgo are deficient in star formation. De Jong (1985) found also the same result for early-type spirals by comparing the IR excess (L_{IR}/L_B) of Virgo and field galaxies. Suppression of star formation in other clusters has also been suggested by Bicay & Giovanelli (1987).

Although the suppression of star formation in Virgo spirals is unambiguous observationally, its explanation is not straightforward. One possibility is that the star-formation activity is regulated by the amount of atomic gas. This hypothesis might sound paradoxical, for star formation is thought to occur in molecular clouds, but star formation is generally triggered by external processes such as explosions of supernova, propagation of a spiral density wave, or shocks driven by stellar wind from young OB associations. All these processes involve the ISM as a means to transfer energy and momentum to molecular clouds. Any fluctuations in density of the ISM will affect the efficiency by which these processes trigger star formation.

Dopita (1985) has used the basic assumption that the pressure in the ISM is balanced by the pressure due to energetic processes associated with star formation to derive a simple law of star formation. This law states that the rate of star formation per unit of total mass is linearly related to the ratio of gas to the total surface mass densities. For an SFR like that in the Galaxy, this can be approximated simply by SFR $\propto M_{H\,I}$. Dopita found a remarkable agreement of this law with observations, which has been also confirmed independently by Chini *et al.* (1986a).

The Dopita law can be expressed as a function of *Def* using equation (1): SFR $\propto 10^{-Def}$. This corresponds exactly to what we found from our model. Of course, the power law has been *assumed* in the model, but it is still interesting that the model predicts an index which corresponds exactly to Dopita's law. This strongly suggests that the SFR is indeed regulated by the amount of gas via this law.

It is important to note that this discussion is relevant only for the star-formation activity in the disc. The picture discussed above might be quite different in the nucleus. In fact, hydrodynamic calculations (Shaviv & Salpeter 1982) of the effects of interaction for a galaxy with a hot environment suggest the possibility of enhanced star-formation activity near the centre of the galaxy. IR excesses at 10 μm (Becklin *et al.* 1983) and in the near-infrared (Joseph, Hawarden & Gatley 1985), found in the nuclei of Virgo spirals, might support this prediction.

6 Summary and conclusions

We have used a sample of 102 spiral galaxies in the Virgo cluster to show that they have different FIR properties compared to field galaxies. On average, H I-poor galaxies have lower 60- and 100-μm fluxes and cooler F_{100}/F_{60} ratios relative to H I normal (field) galaxies. No reasonable selection or systematic effect can explain the variations observed. We have interpreted these variations in the context of a two-component model for the FIR emission and presented a phenomenological model including cold-dust stripping and suppression of star formation. This simple model can quantitatively reproduce the variations observed. The main results are as follows.

(i) The cold dust associated with H I gas of a typical spiral in the core of the cluster has been stripped in the same proportion as the hydrogen gas; a galaxy within 5° of the centre of the cluster has lost at least half of its cold-dust content. This confirms the existence of a cool diffuse dust component in Virgo spirals and the validity of current models for the FIR emission in spiral galaxies.

(ii) About 20–30 per cent of the cold dust luminosity is due to very cold dust associated with quiescent molecular clouds.

(iii) The star-formation activity in spiral discs has been suppressed by about a factor of 3 compared to field galaxies. On average, the SFR in a Virgo spiral is probably regulated by the amount of gas present in the galaxy.

Acknowledgments

Illuminating discussions from many people have contributed to this work, but we are specially grateful to Philip James and Andrea Prestwich. We thank also Carol Lonsdale who made us aware of the existence of the Helou *et al.* data. RD is financially supported by a Canadian NSERC and an OIDE postgraduate scholarship.

References

Becklin, E. E., Scoville, N. Z., Young, J. S. & Capps, R. W., 1983. *Astrophys. J.*, **271**, 512.
Bicay, M. D. & Giovanelli, R., 1987. *Astrophys. J.*, **321**, 645.
Boulanger, F. & Pérault, M., 1986. In: *Comets to Cosmology, 'Lecture Notes in Physics'*, Vol. 297, p. 122, ed. Lawrence, A., Springer Verlag, Berlin.
Burstein, D. & Lebofsky, M. J., 1986. *Astrophys. J.*, **301**, 683.
Chini, R., Kreysa, E., Krügel, E. & Mezger, P. G., 1986a. *Astr. Astrophys.*, **166**, L8.
Chini, R., Kreysa, E., Mezger, P. G. & Gemünd, H. P., 1986b. *Astr. Astrophys.*, **154**, L8.
Chini, R., Kreysa, E., Mezger, P. G. & Gemünd, H. P., 1988c. *Astr. Astrophys.*, **157**, L1.
Cox, P., Krügel, E. & Mezger, P. G., 1986. *Astr. Astrophys.*, **155**, 380.
Cowie, L. L. & Songaila, A., 1977. *Nature*, **266**, 501.
Crawford, J. & Rowan-Robinson, M., 1986. *Mon. Not. R. astr. Soc.*, **221**, 923.
de Jong, T., 1985. In: *The Virgo Cluster, ESO workshop*, p. 111, eds. Richter, O.-G. & Binggeli, B., ESO, Garching, FRG.
de Jong, T. & Brink, K., 1987. In: *Star Formation in Galaxies*, p. 323, ed. Lonsdale Persson, C. J., NASA Conference Publication 2466.
Dopita, M. A., 1985. *Astrophys. J.*, **295**, L5.
Draine, B. T. & Anderson, N., 1985. *Astrophys. J.*, **292**, 494.
Fisher, J. R. & Tully, R. B., 1981. *Astrophys. J. Suppl.*, **47**, 139.
Gauthier, T. N., III., 1986. In: *Light on Dark Matter*, p. 213, ed. Israel, F. P., Reidel, Dordrecht.
Giovanardi, C., Helou, G., Salpeter, E. E. & Krumm, N., 1983. *Astrophys. J.*, **267**, 35.
Giovanelli, R. & Haynes, M. P., 1985. *Astrophys. J.*, **292**, 404.
Gunn, J. E. & Gott, J. R., 1972. *Astrophys. J.*, **176**, 1.
Haynes, M. P. & Giovanelli, R., 1983. *Astr. J.*, **88**, 881.
Haynes, M. P. & Giovanelli, R., 1986. *Astrophys. J.*, **306**, 466.
Helou, G., 1986. *Astrophys. J.*, **311**, L33.
Helou, G., Hoffman, G. L. & Salpeter, E. E., 1984. *Astrophys. J. Suppl.*, **55**, 433.
Helou, G., Khan, I. R., Malek, L. & Boehmer, L., 1989. *Astrophys. J. Suppl.*, submitted.
Joseph, R. D., Hawarden, T. G. & Gatley, I., 1985. In: *The Virgo Cluster, ESO workshop*, p. 127, ed. Richter, O.G. & Binggeli, B., ESO, Garching, FRG.
Kenney, J. D. & Young, J. S., 1986. *Astrophys. J.*, **301**, L13.
Kennicutt, R. C., 1983. *Astr. J.*, **88**, 483.
Leggett, S. K., Brand, W. J. L. & Mountain, C. M., 1987. *Mon. Not. R. astr. Soc.*, **228**, 11P.
Lonsdale Persson, C. J. & Helou, G., 1987. *Astrophys. J.*, **314**, 513.
Mezger, P. G., Mathis, J. S. & Panagia, N., 1982. *Astr. Astrophys.*, **105**, 372.
Nilson, P., 1973. *Uppsala General Catalogue of Galaxies; Uppsala Astr. Obs. Ann.*, **6**.

Nulsen, P. E. J., 1982. *Mon. Not. R. astr. Soc.*, **198,** 1007.
Peterson, B. M., Strom, S. E. & Strom, K. M., 1979. *Astr. J.*, **84,** 735.
Puget, J. L., 1988. In: *Comets to Cosmology, 'Lecture Notes in Physics'*, Vol. 297, p. 113, ed. Lawrence, A., Springer Verlag, Berlin.
Shaviv, G. & Salpeter, E. E., 1982. *Astr. Astrophys.*, **110,** 300.
van den Bergh, S., 1977. *Vistas Astr.*, **21,** 71.
van den Bergh, S., 1984. *Astr. J.*, **89,** 5.

Appendix: Detailed description of the model

For each model, we first define a sample of N galaxies. Each one is randomly assigned a value of $F_N(100)$ and $F_N(100)/F_N(60)$ according to the observed surface brightness and colour distributions (assumed to be Gaussian) of normal galaxies. As described in Section 4.1, these fluxes are given by the sum of a cool and a warm component $F_N^c(\lambda)$ and $F_N^w(\lambda)$ (λ: 60, 100). An intrinsic colour temperature for the two components is assumed and input by the ratios $F_N^c(100)/F_N^c(60)$ and $F_N^w(100)/F_N^w(60)$. Given these ratios and the fluxes at 60 and 100 μm [$F_N(100)$, $F_N(60)$], we calculate the value of the two components in each band. This step is repeated for all galaxies.

Each galaxy is then assigned an H I *Def*. A good approximation for the H I *Def* distribution is to use two populations (Haynes & Giovanelli 1986), a population of normal and deficient galaxies. The distributions are assumed to be Gaussian and their parameters are chosen from the observed distributions, that is, normal and deficient galaxies have average *Def* and standard deviations of 0 ± 0.2 and 0.8 ± 0.4, respectively. To represent closely the real sample, half of the galaxies have H I *Def* chosen from the normal subset.

At this point, a pair of α and β is chosen. Then, for all galaxies that have $Def \geq 0.2$, new flux densities $F_D(100)$ and $F_D(60)$ are calculated using equation (2). For positive values of α and β, we have $F_D(\lambda) < F_N(\lambda)$. A detection limit is simulated by excluding galaxies which have $F_D(100)$ and/or $F_D(60)$ less than the corresponding *IRAS* detection limit of each band. This operation results in shifting galaxies with $Def \geq 0.2$ to the left in the diagram *Def* versus $\log(F_\lambda/a^2)$. Since this shift is larger for the most H I-deficient galaxies, this produces an envelope. The slope of this envelope was calculated by taking the average of the parameter $Slope(\lambda) = Def/[\log F_D(\lambda) - \log F_N(\lambda)]$ for individual galaxies. With the resulting sample of 'deficient' galaxies ($Def \geq 0.3$) we then calculate $\langle \log[F_D(100)/F_D(60)] \rangle$, $\langle Slope(100) \rangle$ and $\langle Slope(60) \rangle$. A valid solution for the model is obtained if a combination of α and β produces an average colour ratio and slopes of envelope that correspond to observed ones, *i.e.* $0.44 \leq \langle \log[F_D(100)/F_D(60)] \rangle \leq 0.48$, and $-2 \leq \langle Slope(100) \rangle, \langle Slope(60) \rangle \leq -1$. The average values of α and β found for these solutions are $\alpha = 0.5 \pm 0.1$ and $\beta = 1.0 \pm 0.15$.

FAR-INFRARED PROPERTIES OF VIRGO SPIRALS

RENÉ DOYON and R. D. JOSEPH

Astrophysics Group, Blackett Laboratory, Imperial College, London, England

Abstract. Using a sample of 109 spiral galaxies in the Virgo cluster we show that H I deficient galaxies have cooler far-infrared colour temperatures and lower 60 and 100 μm fluxes than those with normal H I content. We suggest that these results can be explained if the dust content of H I deficient galaxies have been reduced by a factor of two compared to field galaxies.

1. Introduction

The discovery by IRAS of extended 100 μm emission ('cirrus') in our Galaxy has led to the development of models for the far-infrared (FIR) emission that include two components (e.g., Lonsdale and Helou, 1987): a warm component that traces young stars and star formation regions and a cool one associated with cold dust heated by the general interstellar radiation field (ISRF). The existence of this cool component in our Galaxy raises questions about the validity of using the FIR flux in extragalactic systems as an estimate of the star formation rate (SFR). It is, therefore, important to determine whether this cool component is present or not in other disc galaxies.

Spirals in the Virgo cluster are good candidates for the investigation of this question. Since the cold dust is thought to be associated with the H I gas which is very deficient in these galaxies (e.g., Haynes and Giovanelli, 1986), they should have a lower dust content and consequently have lower FIR fluxes than H I normal galaxies. Leggett *et al.* (1987) looked for such effects in 23 Virgo spirals and found no correlation between H I deficiency and FIR fluxes. They concluded that current two-component models are inadequate to explain the FIR properties of Virgo spirals.

In this paper we present an analysis of a sample of 109 Virgo galaxies. We find that H I deficient galaxies *do* have lower FIR fluxes but this is not reflected as a correlation because of the combined effect of the IRAS detection limit and the large scatter in the FIR fluxes.

2. Data Analysis

The sample includes all late-type (Sa and later) spirals in the Virgo cluster that have both 21 cm and IRAS FIR data. FIR flux densities were taken from the *Cataloged Galaxies and Quasars in the IRAS Survey* (Lonsdale *et al.*, 1985: CGQ) for point-source galaxies and from the *IRAS Small Extended Source Catalogue* (Helou and Walker, 1986) for

Astrophysics and Space Science **157**: 211–214, 1989.

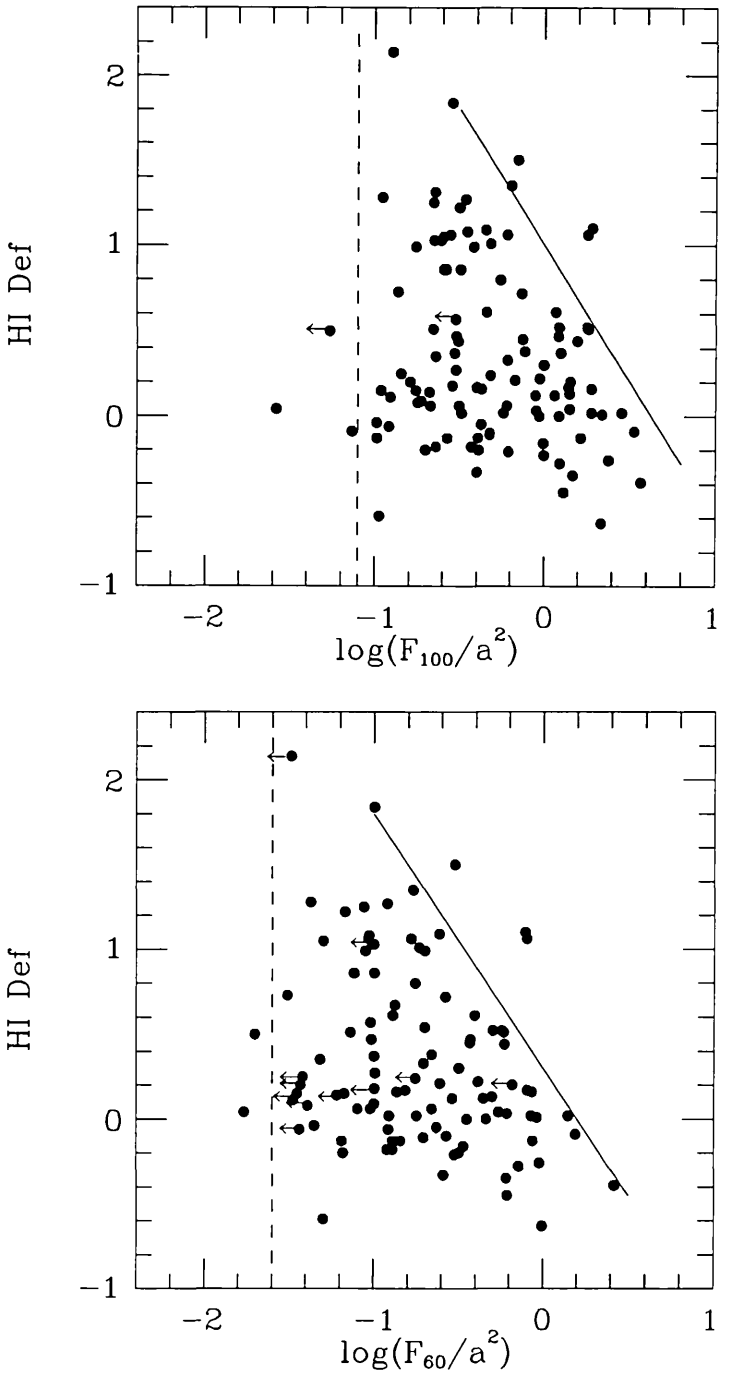

Fig. 1a–b. Plots of H I deficiency against the FIR 'surface brightness' at (a) 100 μm and (b) 60 μm. Upper limit fluxes are symbolized by left arrows. Solid lines delimit the upper envelope seen in both figures. Dashed lines represent the corresponding IRAS detection limit of each band converted to surface brightness using an average optical diameter of 4.6 arc min. The combined effect of this limit with the large scatter in the FIR fluxes of normal galaxies (Def < 0.3) eliminates any simple anticorrelation between Def and surface brightness.

sources that were flagged extended in the CGQ. In Figures 1(a) and 1(b) we have plotted the H I deficiency Def(Def $\equiv \log M_{\rm H\,I}$(expected) – $\log M_{\rm H\,I}$(observed)) against the hybrid 100 and 60 μm 'surface brightness', defined as the ratio of the IRAS band flux F_λ to the square of the optical diameter a (UGC blue major diameter). Both figures show a significant upper envelope suggesting that the FIR flux *decreases* in a systematic way with increasing Def. In Figure 2 the colour ratio $\log(F_{100}/F_{60})$ of H I normal (Def < 0.3) and deficient (Def ≥ 0.3) galaxies are compared. Deficient galaxies are 'cooler' than normal ones at the 5σ level.

3. Interpretation and Discussion

In normal galaxies, the FIR emission is generally thought to be thermal emission from dust heated by starlight. The FIR flux is then given by $F_\nu \sim M_d B_\nu(T_d) Q(\nu)$ where M_d is the dust mass, $B_\nu(T_d)$ the Planck function at a dust temperature T_d, and $Q(\nu)$ is the emissivity law.

The colour distributions of normal and deficient galaxies (see Figures 1(a) and 1(b)) suggest that a temperature effect could be the cause of the envelopes, for a lower temperature in deficient galaxies relative to normal ones shifts the former galaxies to the left in a diagram Def vs $\log(F_\lambda/a^2)$, producing a negative envelope. Assuming the

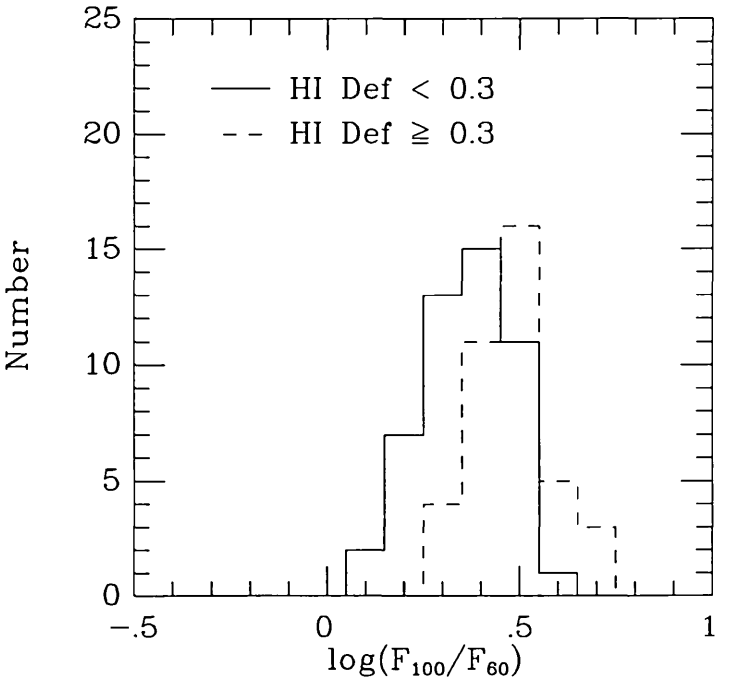

Fig. 2. Comparison of the colour distribution of H I normal (solid line) and deficient galaxies (dashed line). Galaxies with upper limit fluxes were excluded. The mean of the distributions for the normal and deficient sample are 0.36 ± 0.02 and 0.47 ± 0.02, respectively.

emissivity varies as ν^2 and using the F_{100}/F_{60} ratios, we find temperatures for normal and deficient galaxies of 28 and 26 K, respectively. From the average H I deficiency of the two samples and the temperatures above, we can easily estimate that the envelopes at 100 and 60 μm should have a slope of -5 and -3, respectively. These slopes are, however, too steep to be consistent with those actually observed (≈ -1.5). Therefore, to explain the observed envelopes we must suppose that the dust content M_d of deficient galaxies has been reduced by roughly a factor of 2.

This interpretation is based on the assumption that a single temperature is representative of the FIR spectrum. This is not necessarily true. Recent models have shown that the FIR spectral distribution of spiral galaxies is best explained by assuming at least two components: a warm component due to dust heated to a temperature of 40–50 K by young OB stars and compact H II regions and a cool 'cirrus'-like component due to dust heated at temperature of ≈ 20 K by the ISRF, with the latter contributing about 50–70% of the total FIR luminosity. The single-component temperatures of 26–28 K inferred above are too high to be explained by cirrus emission but also too low to be explained by warm emission only. This indicates that the FIR spectral distribution of Virgo spirals is a composite spectrum of 'cool' and warm emission.

In the context of a two-component model for the dust emission, the observed envelopes and colour distributions could be the result of the reduction of the SFR (SFR ~ warm component) and/or the cold dust content (stripping of the cool component). It is difficult to disentangle the two effects without using a model but the simple argument above do suggest that the dust content in Virgo spirals is lower than that in field galaxies.

4. Conclusions

We have shown that Virgo spirals *do* have different FIR properties than normal (field) galaxies. Probably more than one component is responsible for the integrated FIR spectrum of these galaxies. If we assume a single average temperature, the FIR properties of H I deficient galaxies can only be explained if their dust content has been reduced by roughly a factor of two compared to normal galaxies. Fuller investigation, including a two-component model to disentangle the effect of variations in both components has been submitted for publication in *Monthly Notices of the Royal Astronomical Society*.

References

Haynes, M. P. and Giovanelli, R.: 1986, *Astrophys. J.* **306**, 466.

Helou, G. and Walker, D. W.: 1987, *IRAS Small Scale Structure Catalogue*, Government Printing Office, Washington.

Leggett, S. K., Brand, W. J. L., and Mountain, C. M.: 1987, *Monthly Notices Roy. Astron. Soc.* **228**, 11p.

Lonsdale, C. J. and Helou, G.: 1986, *Astrophys. J.* **314**, 513.

Lonsdale, C. J., Helou, G., Good, J. C., and Rice, W.: 1985, *Cataloged Galaxies and Quasars Observed in the IRAS Survey*, Jet Propulsion Laboratory.

THE STRENGTHS OF THE 2.3μm CO BAND IN LUMINOUS INTERACTING AND MERGING GALAXIES

R Doyon, R D Joseph,
Blackett Laboratory, Imperial College, London, SW7 2BZ
and
G S Wright
UK Infrared Telescope, 665 Komohana Street, Hilo, Hawaii.

ABSTRACT

Spectra between 2.0 and 2.5 μm are presented for NGC 1614, NGC 2798, NGC 4565, NGC 6240, NGC 253 and ARP 220. We show that the strength of the CO band at 2.36 μm in the nucleus of ARP 220 is abnormally strong; it is suggested that this anomaly may be the result of starburst activity. However, in the large aperture spectra of ARP 220 and other starburst galaxies, the strength of the CO band is consistent with a normal stellar population typical of a spiral galaxy. This suggests that the stellar continuum associated with the starburst is very diluted by the normal population, a situation consistent with the starburst being mostly localised in the nucleus.

I. INTRODUCTION

Amongs the most prominent spectral features in K-window spectra of galaxies is the absorption due to molecular bands of CO at 2.36 μm. The CO depth has been shown to be strongly dependent on stellar spectral type and luminosity class (*cf.* Kleinmann & Hall 1986) in the sense that it becomes strong in late-type and high luminosity stars. This property has been extensively and successfully used to study stellar populations in stellar systems (Frogel 1985 and references therein).

The CO feature is a powerful diagnostic of stellar luminosity that can also be used to study the stellar population in starburst galaxies. A starburst episode is expected to produce a substantial population of red supergiants. Since these stars have stronger CO strength than giants—which are found in the nuclei of normal galaxies—an unusually strong CO strength should be an indication of starburst activity. In this paper, we analyse 2 μm spectra of some interacting, merging and ultraluminous galaxies in order to measure the CO band strength.

Table 1

Galaxy parameters

Galaxy	Aperture (")	V_0 (km/sec)	Size (Kpc)*	CO Index	A_K (mag)
NGC 4565	7.8	1122	0.9	0.15	—
NGC 4565	12.4	1122	0.6	0.14	—
NGC 1614	19.6	4643	5.9	0.13	—
NGC 2798	19.6	1709	2.2	0.12	—
NGC 253	12.4	259	0.2	0.08	0.5
NGC 6240	19.6	7597	9.6	0.13	—
ARP 220	7.8	5500	2.8	0.07	0.8
ARP 220	19.6	5500	7.0	0.08	0.5

*H_0 = 75 km/sec/Mpc

II. OBSERVATIONS AND DATA REDUCTION

All spectra were taken at UKIRT with the CVF (R≈100) spectrometer. The galaxies were observed with aperture sizes of 7.8, 12.4 and 19.6 arcsec. A list of these galaxies along with the apertures used is given in Table 1. The spectra were ratioed with a solar-type standard to take out atmospheric absorption and instrumental response and then multiplied with a black-body function corresponding to the effective temperature of the standard star. The final spectra, shifted to their restframes and normalized to unity at 2.2 μm are shown in Figure 1.

The sample includes the classical starburst galaxy NGC 253, two ultraluminous *IRAS* galaxies (ARP 220 and NGC 6240), a merger (NGC 1614) and a member of an interacting pair (NGC 2798). All these galaxies show signs of starburst activity (*cf.* Joseph *et al.* 1984; Joseph & Wright 1985). For comparison purpose, we have also included the normal galaxy NGC 4565, an edge-on Sb.

II. ANALYSIS AND DISCUSSION

The CO band is clearly visible in all spectra as a

Proc. 22nd Eslab Symposium on Infrared Spectroscopy in Astronomy, Salamanca, Spain, 7-9 December 1988, ESA SP-290 (September 1989)

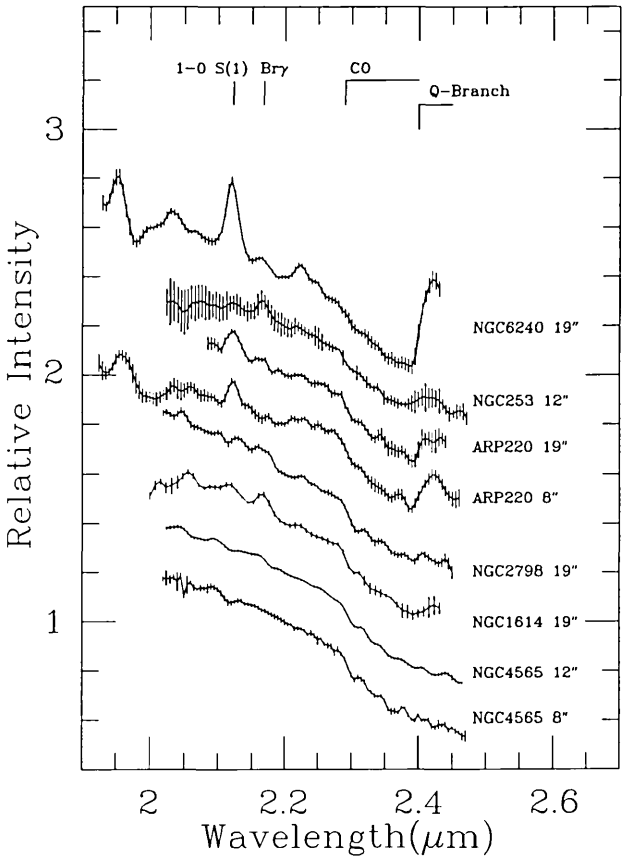

Fig. 1—K-window spectra of the galaxies listed in Table 1. The spectra have been normalized to unity at 2.2 μm and shifted to their restframes. The intensity scale is relative; all spectra are separated by a unit of 0.2. Vertical bars correspond to an error of $+/-1\sigma$.

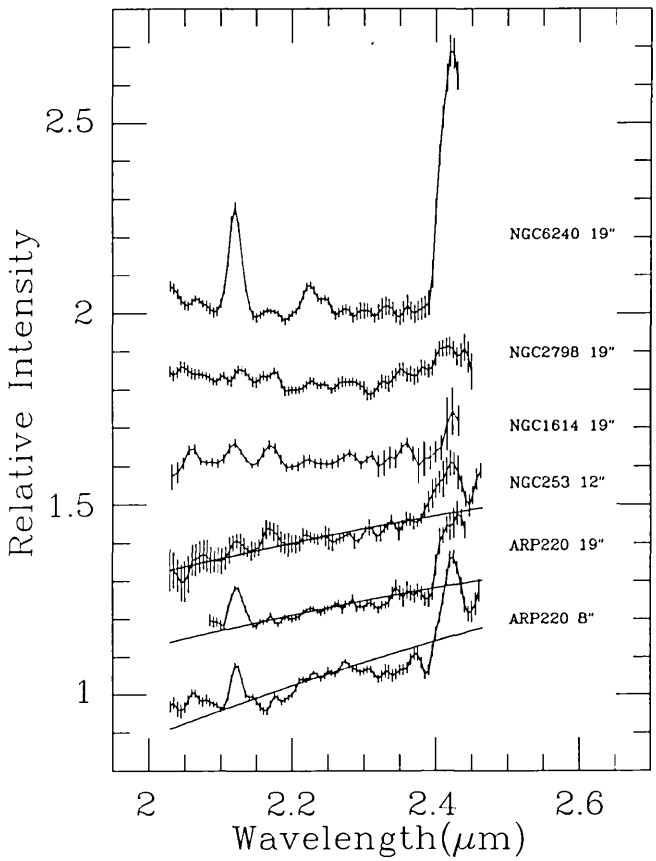

Fig. 2— Spectra of the galaxies ratioed with the spectrum of NGC 4565 (12" aperture). For ARP 220 (8 and 19 arcsec aperture) and NGC 253, the straight lines correspond to absolute extinctions at 2.2 μm of 0.8, 0.5 and 0.5 magnitudes respectively.

depression of the continuum longward of 2.3 μm. The spectra also show prominent emission lines due to molecular hydrogen and Brγ. In previous work on early-type galaxies (*e.g.* Frogel *et al.* 1978), the CO depth was measured photometrically by means of intermediate-band filters centred on the CO dip (2.36 μm) and the adjacent continuum (2.20 μm). The CO index was defined as the difference in magnitudes of the two filters, relative to αLyrae. This photometric method is however limited at high redshift (> 3000 km/sec) since the CO filter is no longer centred on the CO band and the continuum filter can be contaminated by a strong 1-0 S(1) line. A spectroscopic approach is more appropriate here since these problems can be easily obviated with a spectrum.

We have estimated the CO index for all galaxies by ratioing the spectra (in their restframe) with the flux distribution of αLyrae, which is well approximated by $F_\lambda \propto \lambda^{-3.94}$ (Kurucz 1979). The CO index was then calculated using digital filters with the same bandwidth and central wavelength used by Frogel *et al.* (1978). In order to check for systematic differences between the photometric and spectroscopic CO indices, we measured the spectroscopic CO index from 11 stellar spectra taken in Arnaud, Gilmore & Cameron (1988), for which photometric CO indices are available. We have derived a transformation to convert spectroscopic CO indices in the Frogel *et al.* system. The CO indices are given in Table 1.

Except for ARP 220 and NGC 253, all galaxies have CO indices of 0.12-0.15. This value is similar to the average CO index of 0.15 found in nuclei of Sc galaxies (Frogel 1985). The CO indices were not corrected for galactic reddening but such correction should only *increase* the CO index by $\approx$0.005-0.01 magnitudes. No correction was applied for the presence of emission lines (Brγ wing and 1-0 S(0) of H_2) in the continuum filter because their contributions to the continuum are very small. In any case, this small correction should *decrease* the CO index which partially cancels out the galactic reddening correction. Apart from the correction due to internal extinction, we feel that the CO indices given here are free from any systematic effects. As we show below, the small CO indices of ARP 220 and NGC 253 are due to internal reddening.

Another way of estimating the CO strength is to compare the spectra with the spectrum of a normal galaxy. We have used the spectrum of NGC 4565 (edge-on Sb) for this purpose. In Figure 2, we have plotted all spectra ratioed with NGC 4565. In general, the resulting spectrum is flat and shows no residual CO absorption. However, the 8 arcsec aperture spectrum of ARP 220 does show a significant residual of CO. The most simple explanation for this abnormal CO strength is that the nucleus of ARP 220 is affected by starburst activity. Morever, the fact that there is no CO residual in the 19.6 arcsec aperture suggests that the continuum is highly diluted by the normal stellar population

of the disk. Thus, the starburst activity seems to be mostly confined to the nucleus. Since most of the galaxies have been observed with large apertures, this dilution effect and a spatially concentrated starburst could explain why the CO strength is normal in galaxies (*e.g.* NGC 6240) which show other signs of starburst activity.

The positive slope of the ratioed spectra in ARP 220 and NGC 253 shows that these galaxies are affected by internal reddening. From the slope of the continuum and assuming that the extinction varies as $A_\lambda \propto \lambda^{-1.85}$, we have estimated the extinction at 2.2 μm. These values are given in Table 1 and Figure 2. Note that these extinctions are relative to NGC 4565 for which we have assumed to be free of extinction. Thus, our values could be systematically lower that true ones and although no extinction estimates are given for NGC 6240, NGC 2798 and NGC 1614, we can not rule out small values of the order of 0.1 magnitude at K. Using these extinctions, we have derived a corrected CO index of 0.17 for ARP 220 (8 arcsec aperture). This is higher (but only marginally) than the average value found in normal spirals.

III. SUMMARY AND CONCLUSION

We have presented an analysis of K-window spectra of interacting merging and ultraluminous galaxies. The main results are:

1) The CO depth in the nucleus of ARP 220 is abnormally strong compared to a normal galaxy. We suggest that this anomaly is the result of starburst activity. However, this interpretation need be confirmed with a small aperture (5 arcsec) K-window spectrum.

2) The CO strength measured from large aperture spectra is normal even for galaxies that show signs of starburst activity. The case of ARP 220 suggests that the starburst is mostly confined to the nucleus.

3) The CO index is sensitive to extinction. Unless the extinction is well determined, the spectroscopic approach described in this paper is the best way of determining the strength of the CO band.

REFERENCES

Arnaud, K. A., Gilmore, G. & Cameron, A. C. 1988. preprint, .

Frogel, J. A., Persson, S. E., Aaronson, M. & Matthews, K. 1978. *Astrophys. J.*, **220**, 75.

Frogel, J. A. 1985. *Astrophys. J.*, **298**, 528.

Joseph, R. D., Meikle, W. P. S., Robertson, N. A. & Wright, G. S. 1984. *Mon. Not. R. astr. Soc.*, **209**, 111.

Joseph, R. D., Wright, G. S. 1985. *Mon. Not. R. astr. Soc.*, **214**, 87.

Kleinmann, S. G. & Hall, D. N. B. 1986. *Astrophys. J. Suppl.*, **62**, 501.

Kurucz, R. L. 1979. *Astrophys. J. Suppl.*, **40**, 1.

CO INDEX IMAGING OF NGC 253

RENE DOYON, R. D. JOSEPH
Astrophysics Group, The Blackett Laboratory, Imperial College, Prince Consort Road, London, SW7 2BZ, United Kingdom.

G. S. WRIGHT
Joint Astronomy Centre, 665 Komohana Street, Hilo, HI 96720.

ABSTRACT We present J, H, K and narrow-band CO index images of the starburst galaxy NGC 253. The CO index of the nucleus is significantly lower than expected for a giant-dominated nucleus. We show that this low CO index is due to a combination of reddening and hot dust contamination of the 2.2 μm continuum. When these two effects are taken into account, the average CO index within 40 arcsec of the nucleus is typical of red supergiant stars.

INTRODUCTION

The CO absorption band at 2.3 μm is the most prominent feature in K-window spectra of normal galaxies. Because of its strong dependence on spectral type and luminosity class, the CO depth is a powerful tool for investigating the stellar content of galaxies. It has been used in the past to show that ellipticals and bulges of spirals are dominated by giant stars (*eg.* Frogel 1985), and more recently, anomalously strong CO bands— indicative of supergiants—have been used as evidence for starburst activity. To date, CO index studies have been restricted to the nucleus with relatively large apertures. Very little is known about the spatial behaviour of the CO band. In this paper, we present the first CO index image of the starburst galaxy NGC 253.

OBSERVATIONS

The observations were obtained at UKIRT on the nights of 9 and 10 September 1989. Images at J, H, K and narrow-band (FWHM=0.08 μm) filters centred at 2.21 and 2.34 μm were obtained using the 62x58 infrared camera *IRCAM* with a pixel scale of 1.24 arcsec/pixel. After dark subtraction, all images were flatfielded and sky-subtracted using sky frames. The CO indices were transformed into the Frogel *et al.* system. The calibration of the CO index is uncertain by $\approx$0.03 magnitude.

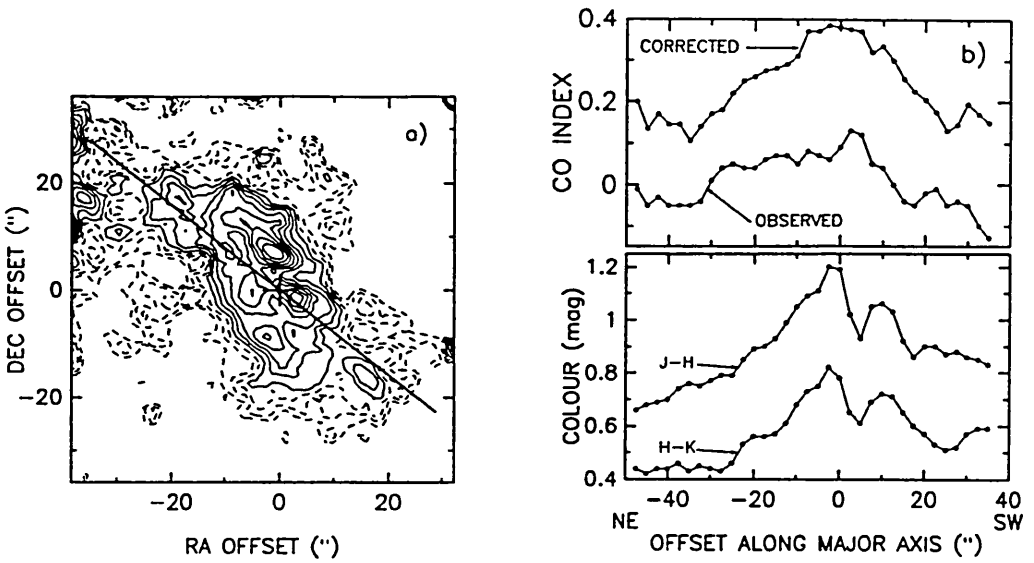

Fig. 1. a) CO index image of NGC253. The contours are in steps of 0.02 mag, the lowest corresponding to a CO index of -0.06. The position of 2.2 μm nucleus and the direction of the major axis are indicated by the cross and the solid line respectively. b) CO index, J-H and H-K colour profiles along the major axis measured with synthetic apertures of 5 arcsec.

RESULTS AND DISCUSSION

A contour map of the CO index image of NGC 253 is shown in Fig. 1a. The average CO index of the nucleus within a circular aperture of 12.4 arcsec is 0.08, in exact agreement with the CO index derived from a CVF spectrum taken with the same aperture (Doyon, Joseph & Wright 1989). This CO index is significantly lower than the average value of 0.15 found in late-type spirals (Frogel 1985). The image also shows a gradient of $\approx$0.1 mag from the nucleus to the outer regions of the disc.

As shown in Fig. 2a, the colours along the major axis are much redder than expected for a normal stellar population. The reddening vector shows that extinction alone cannot account for the H-K excess, that an additional component such as hot dust or free-free emission is required to explain the total reddening. Hot dust at 500-1000 K is the most likely source as Scoville *et al.* (1985) showed that the free-free component is negligible. Evidence for hot dust contamination is also provided by the [CO index – J-K] diagram (see Fig. 2b). Although a normal stellar population with a visual extinction of $\approx$9 mag could account for the observed CO index and J-K colour of the nucleus, such extinction would imply a J-H excess of 0.9 *i.e.* 0.4 magnitude higher than observed. Clearly, a combination of <u>both</u> extinction and emission from hot dust can account for the observed CO index and the near-infrared colours of the nucleus.

One can estimate quantitatively the effect of extinction and hot dust on the CO index assuming that the J-H excess is due to extinction only. In terms of the J-H and H-K excesses, the CO index excess E_{CO} may be expressed as

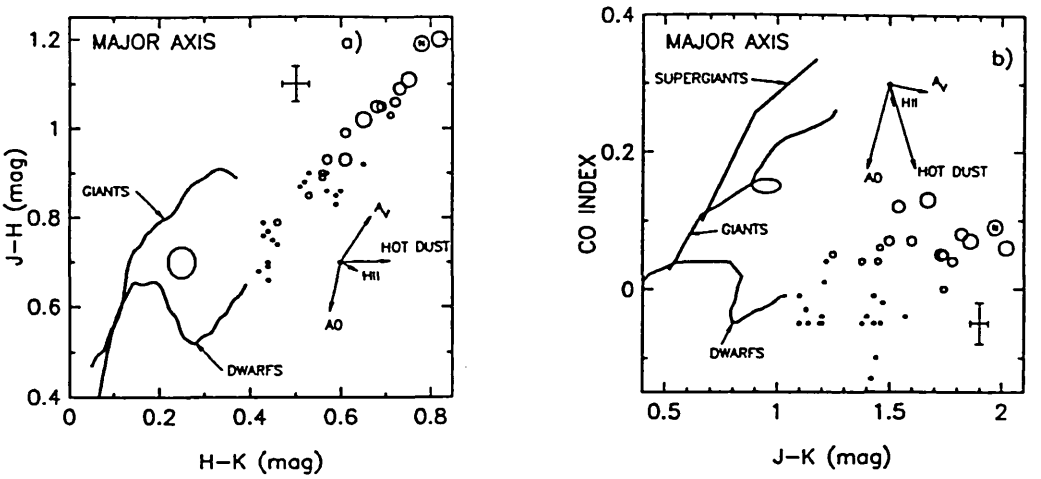

Fig. 2. a) Two-colour diagram and b) CO index *vs* J-K for the positions along the major axis used in Fig. 1b. The size of the symbols is proportional to the brigthness at K. The nucleus is indicated by the letter "N". The solid lines represent the average relationships for dwarf, giant and supergiant stars. The region within the ellipse is that occupied by the nuclei of Sc galaxies. The vectors indicate how the normal galaxy colours are affected by 10% contamination (at 2.2 μm) of blue stars ("A0"), hot dust, free-free emission ("HII") and 1 mag of visual extinction ("A_V").

follows: $E_{CO} \approx -E_{H-K} + 0.5 \times E_{J-H}$. Corrected (intrinsic) CO indices for the major axis are shown in Fig. 1b. The average CO index within 40 arcsec of the nucleus is $\approx$0.3 suggesting that most if not all of the 2.2 μm *stellar* continuum is associated with red supergiant stars. The large spatial extent of strong CO index is puzzling. If there is a significant population of red supergiants 20 arcsec out from the nucleus, strong Brγ emission associated with young OB stars—the progenitors of red supergiants— should be detected at this position but this is not the case: Brγ decreases by an order of magnitude 15 arcsec off the nucleus (Wright & Joseph 1989). However, because the CO index is strongly affected by emission from hot dust, spectroscopic evidence for red supergiants outside the nucleus along with more spatial observations of Brγ are needed to confirm the result above. Fuller analysis along with more CO index observations of other galaxies will be presented in a subsequent paper.

REFERENCES

Doyon, R., Joseph, R. D. & Wright, G. S. 1989, in *Infrared Spectroscopy in Astronomy*, 22nd ESLAB Symposium, ed B. H. Kaldeich, p477.

Frogel, J. A. 1985, *Ap.J.*, **298**, 528.

Scoville, N. Z., Soifer, B. T., Neugebauer, G., Young, J. S., Matthews, K., Yerka, J. 1985, *Ap.J.*, **289**, 129.

Wright, G. S. & Joseph, R. D. 1989, in *Infrared Spectroscopy in Astronomy*, 22nd ESLAB Symposium, ed B. H. Kaldeich, p535.

INFRARED IMAGES OF MERGING GALAXIES

G. S. Wright[1], P. A. James[2], R. D. Joseph[2], I. S. McLean[3], and R. Doyon[4]

1) Joint Astronomy Centre, 665 Komohana Street, Hilo, HI96720.

2) Institute for Astronomy, 2680 Woodlawn Drive, Honolulu, HI96822.

3) Dept. of Astronomy and Physics, UCLA, 405 Hilgard Ave., Los Angeles, CA90024.

4) Blackett Laboratory, Imperial College, London, SW7 2BZ.

1. INTRODUCTION

Infrared imaging of interacting galaxies is especially interesting because their optical appearance is often so chaotic due to extinction by dust and emission from star formation regions, that it is impossible to locate the nuclei or determine the true stellar distribution. However, at near-infrared wavelengths extinction is considerably reduced, and most of the flux from galaxies originates from red giant stars that comprise the dominant stellar component by mass. Thus near infrared images offer the opportunity to study directly components of galactic structure which are otherwise inaccessible. Such images may ultimately provide the framework in which to understand the activity taking place in many of the mergers with high IRAS luminosities.

2. MULTIPLE NUCLEI

Infrared imaging is a powerful tool for the identification of galactic nuclei, since the nuclear regions of many galaxies are often too heavily enshrouded by dust for optical images to show the underlying structure. A well known example of this is Arp220, where the two optical maxima are due to a dust lane which bisects the galaxy and neither of them are associated with galaxy nuclei. We have obtained K ($2.2\,\mu m$) images of two galaxies, Mkn788 and IRAS0857+3912 which have previously been described as the result of galaxy mergers on the basis of two equally bright optical peaks. Our image of Mkn788 (Joseph et al. 1988) shows that the western source is much more sharply peaked and has twice the integrated luminosity of the other. The brightest infrared source is coincident with the VLA source (Kollatschny et al. 1986), suggesting that it is the true nucleus of Mkn788. The broader, lower intensity K source which corresponds to the other "optical nucleus" could be interpreted as a giant extra-nuclear HII region similar to the jumbo HII region in NGC3310 (cf. Telesco & Gatley 1984). In IRAS0857+3912 we find a similar result. The optical image presented by Sanders et al. (1988) shows two almost equally bright optical lobes, whereas in our K image the north-western source has almost an order of magnitude higher peak surface brightness than its neighbour. This extremely red source is quite possibly the nucleus of the IRAS galaxy. However, a third very red source, which is barely apparent even at J ($1.25\ \mu m$) is also clearly detected in the K image of this very disturbed galaxy.

Infrared images have also been useful in identifying double structures in the nuclei of interacting galaxies which have not even been hinted at by optical observations. A striking example of this is given by the K images of Arp220. Graham et al. (1990) have used high resolution imaging to show that it has a double nucleus coincident with the radio sources in the middle of the dust lane.

The results discussed above suggest that caution should be applied in the identification of optical bright spots as multiple nuclei in the absence of other evidence. They also illustrate the advantages of using infrared imaging to study the underlying structure in merging galaxies.

3. SURFACE PHOTOMETRY

We have begun a programme to take near infrared images of galaxies which are believed to be mergers of disk galaxies because they have tidal tails and filaments. In many of these the merger is thought to have induced exceptionally luminous infrared emission (cf. Joseph and Wright 1985, Sanders et al. 1988). Although the optical images of the galaxies show spectacular dust lanes and filaments, the K images all have a very smooth distribution of light with an apparently single nucleus. Several authors (e.g. White 1979, Farouki & Shapiro 1982, Barnes 1989) have predicted that over a period of $\sim 10^9$ yrs mergers should produce a mass distribution indistinguishable from that of an elliptical galaxy, based on n-body simulations of merging disk galaxies. Observational evidence in support of this idea is presented by Schweizer (1982), who showed that the V-light profile of NGC7252 is indeed well fitted by the $r^{1/4}$ de Vaucouleurs law. We have used the K images to test the hypothesis that other mergers are also developing elliptical-like light profiles.

Figure 1a shows profiles for Arp 220 and NGC 2623, in which K surface brightness within elliptical annuli is plotted against radius$^{1/4}$. The characteristic de Vaucouleurs law for elliptical galaxies is a straight line on this plot. The lines shown were obtained by a least-squares fit to all points except for the inner two, which are artificially reduced due to seeing and decentering effects. The lines are clearly a good fit to the data over a range of about 4 magnitudes and linear scales of about 5 kpc in radius, using $H_0 = 50$ km s^{-1} Mpc^{-1}. This similarity with ellipticals is strengthened by the half-light scale lengths for the two mergers. The effective radius containing half the K light is 1.6 kpc for NGC2623, and 3.4 kpc for Arp220, consistent with published values for ellipticals (Kormendy 1982). Unfortunately the limited area covered by these data makes it impossible to rule out absolutely the existence of a more extended disk. We nevertheless conclude, on the basis of our present data, that Arp220 and NGC2623 have stellar light profiles which closely resemble those of elliptical galaxies.

K images for the remaining four galaxies show light profiles which are not those of spiral or elliptical galaxies. Figure 1b shows examples of the kinds of deviation from simple light profiles which we have found. IC883 (shown) and NGC4194 are well fitted by an $r^{1/4}$ law beyond approximately 1 kpc, but the profile is significantly flattened within this radius. NGC6240 and NGC6052 (shown) differ from

ellipticals or spirals over the entire surface brightness range. It is probably significant that these four galaxies all have nuclei substantially offset from the centre of the outer isophotes. The fact that the light profiles of Arp220 and NGC2623 are a much better fit to an $r^{1/4}$ law than the other galaxies we have imaged so far suggests that Arp220 and NGC2623 may be the most dynamically evolved of the merger remnants associated with IRAS sources. In the case of Arp220 it is tempting to speculate that its stage of dynamical evolution is related to other suggestions that Arp220 is one of the "oldest" of the IR luminous mergers, based on scenarios for the evolution of the luminosity source.

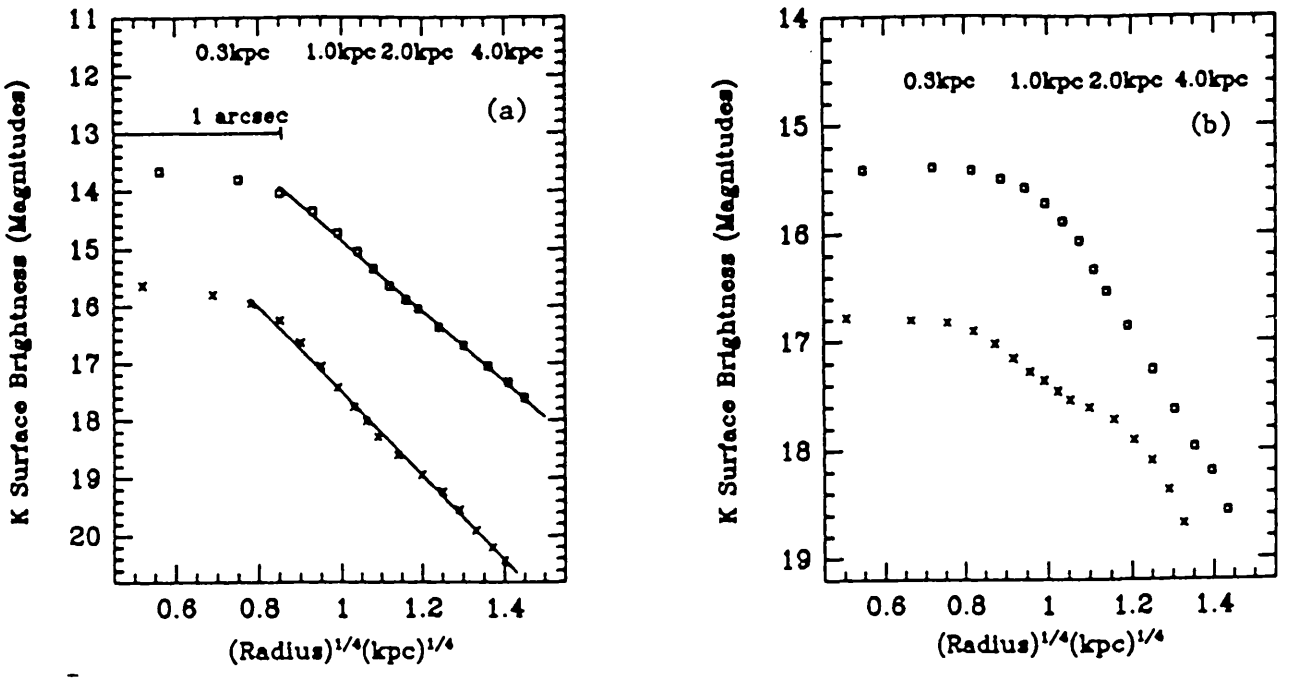

Figure 1 K surface brightness (mag/arcsec^2) plotted vs. the fourth root of the radius for a) Arp220 ( ) and NGC2623 ( ) and b) IC883 ( ) and NGC6052 ( ). The plot for NGC2623 has been offset by +2 magnitudes for clarity. The scale along the top of both plots is radius in kpc, assuming $H_0 = 50$ km s^{-1} Mpc^{-1}.

While Arp220 and NGC2623 may have developed the mass distribution of an elliptical galaxy, they still have much more gas and dust. If merger remnants are actually to evolve into elliptical galaxies there must be some mechanism which removes the interstellar material. The activity which powers the luminous IR emission of these galaxies may play a key role in this process. For example, Graham et al. (1984) argue that a consequence of starbursts is a sufficiently high supernova rate to severely deplete the gas.

Similarly it has been suggested (eg. Carlberg 1989, Efstathiou & Rees 1988) that a quasar-like active nucleus could consume the gas in less than a Hubble time. We suggest therefore that the high IRAS luminosities of merging galaxies provide a clue to the means by which they could become as gas free as ellipticals.

4. CONCLUSIONS

Near infrared images are a much better way to investigate the existence of multiple nuclei than optical images because extinction and the emission from hot young stars are much reduced at $2.2\,\mu m$. Our images of Mkn 788 and IRAS 0857+3912 are strikingly different from optical images in that only one nucleus clearly dominates in the near-IR. This suggests that in the absence of other evidence for interaction care should be taken in classifying potential mergers on the basis of nuclear structure in optical images alone.

$2.2\,\mu m$ surface photometry of several high luminosity mergers of disk galaxies has been used to test the idea that they may be evolving into ellipticals. Arp220 and NGC2623 obey the characteristic de Vaucouleurs law of ellipticals at $2.2\,\mu m$ over several kpc, contrary to the impression given by optical images. We suggest that this provides support for the idea that mergers will evolve into elliptical-like objects. It is clear that the relation between degree of relaxation and other evolutionary processes in mergers is a very important question. By obtaining infrared images of a larger sample of mergers going to fainter isophotes we plan a more definitive study of the evolution of merger remnants with high IRAS luminosities.

REFERENCES

Barnes, J. E. 1989 *Nature* **338**, 123.

Carlberg, R. G. 1989 *Astrophys. J. preprint*

Efstathiou, G. & Rees, M.J. 1988 *Mon. Not. R. astr. Soc.* **230**, 5p.

Farouki, R. T. & Shapiro, S. L. 1982 *Astrophys. J.* **259**, 103.

Graham, J. R., Wright, G. S., Meikle, W. P. S., Joseph, R. D., & Bode, M. F. 1984 *Nature* **310**, 213.

Graham, J. R., Carico, D. P., Matthews, K., Neugebauer, G., Soifer, B. T. & T. D. Wilson 1990 *Astrophys. J. Lett. preprint*

Joseph, R. D. & Wright, G. S. 1985 *Mon. Not. R. astr. Soc.* **214**, 87.

Joseph, R. D., Wright, G. S., James, P. A., & McLean, I. S. 1988 *Mon. Not. R. astr. Soc.* **232**, 7p.

Kollatschny, W., Netzer, H. & Frike, K. J., 1986 *Astr. Astrophys.*, **163**, 31.

Kormendy, J. 1982 *Morphology and Dynamics of Galazies* ed. Martinet, L. *SAAS-FEE* 115.

Sanders, D. B., Soifer, B. T., Elias, J. H., Madore, B. F., Matthews, K., Neugebauer, G. & Scoville, N. Z. 1988 *Astrophys. J.* **325**, 74.

Schweizer, F. 1982 *Astrophys. J.* **252**, 455.

Telesco, C. M., Decher, R. & Gatley, I., 1985. *Astrophys. J.* **299**, 896.

Telesco, C. M. & Gatley, I., 1984 *Astrophys. J.* **284**, 557.

White, S. D. M. 1979 *Mon. Not. R. astr. Soc.* **189**, 831.